Physics and chemistry at the surface of interstellar dust grains: the influence of O-atom diffusion and chemical desorption on a H-N-C-O reaction network.

A DISSERTATION PRESENTED
BY
Marco Minissale

Supervisor **Prof. François Dulieu**
Co-supervisor **Dr. Emanuele Congiu**
Co-supervisor **Prof. Valerio Pironello**

Referee **Prof. Pascal Parneix**
Referee **Prof. Stephen Price**

Examiner **Prof. Paola Caselli**
Examiner **Prof. Cécile Engrand**
Examiner **Prof. Olivier Pluchery**

2012-2014

Abstract

The interstellar medium is the matter that exists in the space between the star systems in a galaxy. It is composed of gas and elongated tiny dust grains. To date, plenty of molecules (> 170) are known to exist in the interstellar medium. The presence of most of them can be understood in terms of gas phase reactions but the synthesis of some key species (i.e., H_2, H_2O, CO_2) need the intervention of solid-state reactions on dust grains surface. The aims of this thesis are to understand what are the relevant physical-chemical processes (i.e., diffusion and desorption) occurring on the surface of interstellar dust grains and how these processes influence synthesis of more and more complex molecules. In particular, the focus of my thesis is the investigation of:

- the role of O-atom diffusion and the oxidation processes in the formation of interstellar ices;

- the thermal and non-thermal processes coupling gas and solid phase.

The reasons of these investigations lie on the realization that, up to now, only hydrogen diffusion and hydrogenation reactions are commonly considered in solid astrochemistry and the role of oxygenation as well as the importance of adsorption and desorption processes are often disregarded. Evidently, a better knowledge of such physical-chemical processes and, in general, of the solid state physical-chemistry could help astronomers to understand the formation of interstellar ices, the increase on molecular complexity, and the equilibrium between gas and solid phase.

To answer these questions, many experiments have been performed with the **FORMOLISM** set-up, i.e., **FOR**mation of **MOL**ecules in the **ISM**, located at the LERMA-Cergy lab (Université de Cergy Pontoise and Observatoire de Paris). Via two triply differentially pumped beams, atoms and molecules were aimed at a cold (>6.5 K) sample held in a Ultra high vacuum chamber. The products were probed using Mass spectroscopy and Reflexion Absorption Infrared Spectroscopy.

To simulate different astrophysical environments, the solid state physical-chemistry has been studied in different experimental conditions: substrate morphology (Amorphous water ice, porous (p) and compact (np), crystalline (c) ice, amorphous silicate, and graphite), species deposited and their relative ratio, coverage of deposited species, and substrate temperature.

Concerning oxidation processes and O-atom reactivity, the results show that oxygen is very reactive with many species (i.e., H, CO, NO, H_2CO, HCOOH); O diffusion appears to be much faster than previously expected and can occur via quantum mechanical tunnelling at temperatures as low as 6.5 K. We compared the experimental values of the diffusion coefficients and found that the rates of diffusion on each surface, based on modelling results, were considerably higher than those expected for heavy atoms such as oxygen. Our findings show that O atoms can scan any available reaction partners (e.g., either another H atom, if available, or a surface radical like O, OH, CO) at a faster rate than that of accretion. In particular, in very dense interstellar clouds, the O/H ratio is such that O becomes one of the dominant reactive partners together with H. This has an impact on the chemistry occurring at the surface of dust grains as either the formation of some species may be enhanced, or at least the relative abundances of the final products will be affected. An important example of how O-atom mobility can modulate the abundances of key species of ices in the ISM is the case of the H_2O/CO_2 ratio via the CO+O and H_2CO+O pathways.

Concerning gas-solid coupling processes (i.e., adsorption, sticking, thermal desorption, chemical desorption), the results show that each processes is influenced in a different way by the substrate (i.e., water ice, silicate or graphite). Moreover, we provide a useful list of binding energies of several species and chemical desorption efficiency for different reactions on different substrates.

Resumé

Le milieu interstellaire est la matière qui existe dans l'espace au sein des galaxies. Cette matière est composée de gaz et de grains de poussière. Jusqu'à présent, les radioastronomes ont identifié plus de 170 molécules différentes dans le milieu interstellaire. La présence de la plupart de ces molécules est expliquée à travers des réactions dans la phase gazeuse, mais la synthèse de beaucoup de ces molécules (comme H_2, H_2O, CO_2) nécessite l'intervention d'un catalyseur, donc des réactions dans la phase solide (par exemple sur la surface des grains de poussière). Les objectifs de cette thèse sont de comprendre quels sont les processus physico-chimiques qui ont lieu (par exemple, la diffusion et de désorption) sur la surface des grains de poussière interstellaire et comment ils conduisent à la synthèse de molécules de plus en plus complexes. En particulier, l'objet de ma thèse est d'étudier:

- le rôle de la diffusion des atomes d'oxygène (noté « O ») et les processus d'oxydation dans la formation des glaces interstellaires ;

- le couplage thermique et non thermique entre la phase gaz et la phase solide.

L'astrochimie ne tend à considérer que la diffusion des atomes d'hydrogène et les réactions d'hydrogénation, ignorant souvent le rôle de l'oxygénation ainsi que l'importance des processus d'adsorption et de désorption, d'où mes recherches approfondies sur ces thématiques délaissées. évidemment, une meilleure connaissance de ces processus physico-chimiques et des surfaces de réactions aiderait les astronomes à comprendre la formation des glaces interstellaires, l'augmentation de la complexité moléculaire, et l'équilibre entre le gaz et la phase solide. Pour répondre à ces questions, de nombreuses expériences ont été réalisées avec le dispositif FORMOLISM, situé au laboratoire LERMA-Cergy (Université de Cergy Pontoise et Observatoire de Paris). Via deux jets de particules avec un pompage différentiel, les atomes et les molécules sont déposés sur un échantillon froid ($> 6{,}5$ K) dans une chambre ultravide. Les produits des réactions sont ensuite sondés en utilisant la spectroscopie de masse et la spectroscopie infrarouge. Pour simuler différents environnements astrophysiques, la physique-chimie de l'état solide a été étudié dans différentes conditions expérimentales: morphologie de substrat (glace d'eau amorphe soit poreuse, soit compacte, glace d'eau cristalline, silicate amorphe ou graphite), espèces déposés et leur rapport relatif, couverture des espèces déposées, et température du substrat.

En ce qui concerne les processus d'oxydation, les résultats montrent que l'oxygène est très réactif avec de nombreuses espèces ; la diffusion des atomes d'oxygène semble être beaucoup plus rapide que prévu et peut se produire par effet tunnel quantique à des températures aussi basses que $6{,}5$ K. Nous avons comparé les valeurs expérimentales des coefficients de diffusion et constaté que les taux de diffusion sur chaque surface, basés sur les résultats de la modélisation, étaient considérablement plus élevés que ceux prévus pour les atomes lourds tels que l'oxygène. Nos résultats montrent que les atomes O peuvent analyser tous les partenaires disponibles de réaction à un taux plus rapide que le taux daccrétion. En particulier, dans les nuages interstellaires très denses, le rapport O/H est telle que O est l'un des partenaires réactifs dominants avec H. Ceci a un impact sur la formation de certaines espèces et sur l'abondance relative des produits formés. En ce qui concerne les processus de couplage solide-gaz (c'est à dire, l'adsorption, désorption thermique, désorption chimique), les résultats montrent que chaque processus est influencé d'une manière différente par le substrat (glace d'eau, de silicate ou graphite). De plus, nous fournissons une liste utile des énergies de liaison de plusieurs espèces et de l'efficacité de désorption chimique des différentes réactions sur ces substrats.

"Now, under this game-scenario,
how might we wish to see the drawings as functioning, here?"
He settled back down with Lenore's help, looked at her.
"The sliding-man drawing, under this scenario,
might say, hey, ho, watch how you go.
Perceive how you-we-perceive Lenore's being ... 'missing'.
Don't just look at it; think about how to look at it.
Maybe it...means the opposite of what you think it does, of the way it...looks."

"The Broom of the System"
David Foster Wallace

"[...] la connaissance du tout et de ses lois, de l'ensemble et de sa structure,
ne saurait être déduite de la connaissance séparée des parties qui le composent :
cela veut dire qu'on peut regarder une pièce d'un puzzle pendant trois jours et croire
tout savoir de sa configuration et de sa couleur sans avoir le moins du monde avancé :
seule compte la possibilité de relier cette pièce à d'autres pièces [...],
considérée isolément une pièce d'un puzzle ne veut rien dire ; [...]
mais à peine a-t-on réussi, au terme de plusieurs minutes d'essais et
d'erreurs, ou en une demi-seconde
prodigieusement inspirée, à la connecter à l'une de ses voisines,
que la pièce disparaît, cesse d'exister en tant que pièce ."

"La vie mode d'emploi"
Georges Perec

Contents

The baryonic matter of our Galaxy, in common with that of all other galaxies in the Universe, is in perpetual evolution. Analogous to the cycle of life on Earth, the birth and death of stars continuously cycles matter. In each new cycle, heavy elements are created in the interior of a star and, upon its death, these elements are expelled into the InterStellar Medium (ISM) (Figure 1). Spectroscopic and photometric observations show that ISM consists of gas and elongated tiny dust grains. Such a medium is not uniformly distributed in our galaxy but condenses in clouds that settle on the galactic plane. To date, plenty of molecules (> 170)
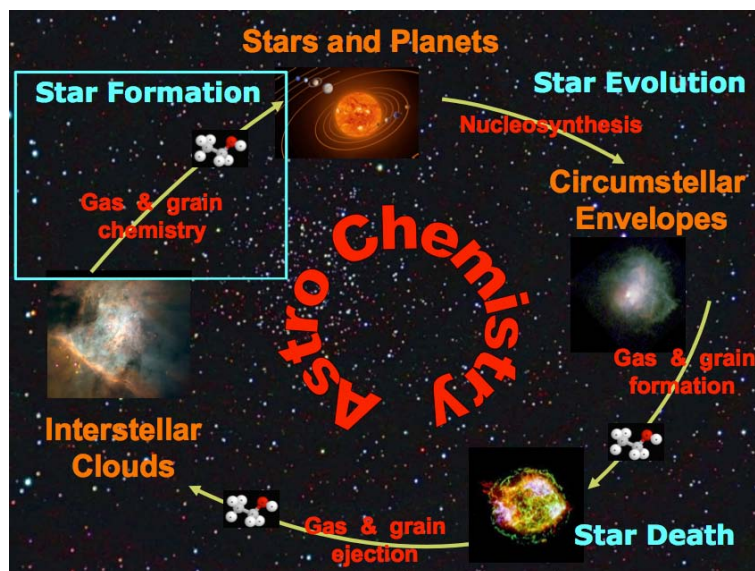
Figure 1: From *ANR project, 2013, MIIA13 Dulieu, Ceccarelli, Theule, et al.*. The cycle of matter. Heavy elements are synthesised in the interiors of stars and expelled, upon their death, into the ISM where they recondense into new stars.

are known to exist in the ISM. The presence and the abundance of most of them can be understood in terms of gas phase reactions but some key species (like molecular hydrogen, the most abundant and important species in the Universe, water and some carbon bearing molecules) are not formed efficiently enough and need the intervention of dust grains, that play the role of catalysts. In fact, although it is in warm regions that the large majority of molecules are seen, these species are not necessarily formed there, at that evolutionary

stage. The synthesis of interstellar molecules is a long and complex process that starts when (and where) the UV photons emitted by galactic stars are shielded by H atoms, in so-called molecular clouds; and chemical complexity increases throughout the star formation process.

The various steps involved in interstellar molecule synthesis can be summed up as follows:

1. Cold gas phase reactions: Neutral - ion chemical reactions at low temperatures (<20 K) in the gas phase form a plethora of molecules at relatively low abundances ($\leq 10^{-7}$ with respect to H nuclei), with the exception of CO. This occurs especially in molecular clouds. Note that the synthesised species can be observed via their rotational lines.

2. Species adsorption: H, O and C atoms not bound in CO, as well as molecules formed in the gas phase stick onto interstellar grains and are adsorbed. The colder and denser the region, the more efficient the process is. The density plays a role because the probability of the atom/molecule encountering interstellar grains increases with density. The temperature is important because, depending on the atom/molecule, it regulates the residence time of the species, i.e. whether it sticks for a long time or just bounces back rapidly into the gas. A key temperature is that at which CO freezes-out, around 23 K. Freeze-out occurs mostly during the, so-called, prestellar core phase, just before the collapse of the cloud, in the very cold (≤ 10 K) and dense ($>10^5$ cm^{-3}) zone. Similar conditions are also found in a large fraction of protoplanetary disks, where planets are eventually formed.

3. Grain surface chemistry: Once on the grain, H atoms diffuse on the surface and react with other frozen species to eventually form new molecules. The most notable example is H_2, which is formed on the grain surface due to the fact that gas phase H_2 formation is extremely slow and, hence, inefficient. Additionally, other polyatomic molecules are formed, notably H_2O, CO_2, H_2CO and CH_3OH, whose key role in astrochemistry will be discussed later. Grain surface chemistry is particularly important in the prestellar core and protoplanetary disk phases. Most of the species synthesised on grain surfaces remain frozen in the, so-called, ice mantles and are only detectable via IR absorption bands in those serendipitous cases where an IR bright source is located behind the cloud or core. It is possible, but not yet proven, that even more complex species are formed during warming up of the grain mantles.

4. Species desorption: When and where the temperature of the dust exceeds the sublimation temperature of the frozen species, the molecules in the icy grain mantles are injected into the gas, where they once again become observable via their rotational lines. In principle, different molecular species desorb at different temperatures; furthermore, the desorption temperature varies in mixed ices. A key desorption temperature is that of water, the major component of the grain mantles, at about 100 K. In the formation route to low mass protostars, the regions where water ice sublimation occurs are called hot corinos.

5. Hot chemistry: Once in the gas phase, the grain mantle components undergo fast neutral-neutral reactions, increasing the chemical complexity of the gas. Molecules are observable via their rotational lines. Regions where hot chemistry plays a dominant role are hot corinos and the warm zones of protoplanetary disks.

Molecules can be simple diatomics or polyatomics, depending on the environment and evolution of the material. Even in the densest regions of the ISM, the gas shows an unsuspected chemical complexity in such harsh environments characterized by extremely low densities and temperatures. In summary, the chemical transformation of matter during the star formation process passes through "bright" periods where gas phase molecules can be directly observed via their rotational lines, and "dark" periods where, except for the most abundant molecules (observable via IR absorption spectra of background stars), molecules are "hidden" in the solid phase. Unfortunately, the birth-place of the molecular complexity is partially hidden and locked in the solid phase. For this reason, freezing and synthesis of complex molecules on micron-sized cold dust particles remain ambiguous. *Pagani et al.* (2012) have shown that CO and N_2 species present very different depletion behaviors, in spite of their similar sticking

probability and desorption efficiency (*Bisschop et al.* 2006). *Bacmann et al.* (2012) have observed unexpected "high" gas-phase abundances of large molecules like CH_3OCH_3 in very cold environments (i.e. pre-stellar cores): such molecules should remain trapped on the solid phase. In other words the solid and gas phase equilibrium is still an open problem and a key point for observations. It could explain origins of solid condensates found in comets and meteorites.

The study of all these processes (species reactivity and diffusion, gas-solid equilibrium) is the challenge of Molecular Astrophysics. Due to its intrinsic difficulties, until fifteen years ago this field of Molecular Astrophysics (often called "Astrochemistry", see i.e. *Caselli&Ceccarelli* (2012)) had been tackled only from a theoretical and observational point of view and only from the second half of the nineties laboratory simulations of the interaction gas-solid have been performed in the conditions and for the surfaces that are encountered in interstellar clouds. Surface reactions on grains constitute today the frontier of astrochemistry, being the youngest and the still less studied field.

In this thesis I will report different results of a laboratory investigation I performed with some colleagues mostly at the LERMA-lab in the University of Cergy-Pontoise. The experimental set-up housed in this laboratory is called **FORMOLISM**, i.e. **FOR**mation of **MOL**ecules in the **ISM**. The purpose of FORMOLISM is to investigate the formation of molecules of Astrophysics interest, as the name of instrument suggests, and to study the interaction of atoms and molecules and the chemical reactions among them on surfaces that simulate those of dust grains under interstellar conditions.

This thesis is organized as follows:

Chapter 1 This chapter presents some theoretical elements of surface physics and surface chemistry. It focus on different mechanisms of catalysis and on the phases that lead to molecules formation on surface: accretion, diffusion, reaction and ejection.

Chapter 2 A quite detailed description of the different parts that form the set-up FORMOLISM (the laboratory equipment in Cergy-Pontoise University) is given in this chapter. Furthermore this chapter describes the experimental methods used to carry out the experiments: TPD (Temperature Programmed Desorption) and DED (During-Exposure Desorption) techniques, methods of flux calibration of each experimental beam and the different methods of water ice growing.

Chapter 3 This chapter carefully presents the rate equation model used to simulate and fit our experimental results. Moreover it explains how model results are linked to physical-chemical quantities.

Chapter 4 The experiments discussed in this chapter study different physical processes occurring on different surfaces. In particular, this chapter focuses on O-atom diffusion, on binding energy of several molecules and atoms, and on chemical desorption process.

Chapter 5 This chapter deals with experiments about molecular synthesis on cold surface: from water to nitrogen dioxide, from carbon dioxide to methanol.

Conclusion This last chapter presents possible applications to astrophysics of our experimental findings. Moreover some of personal perspectives are briefly described.

1

Theoretical background

This thesis is mostly centered around two fields of interest: surface science and its application to Astrophysics, or better Astrochemistry. In this chapter we will present some theoretical elements necessary to understand the results presented in the three last chapter. The chapter is subdivided as follows:

1. Surface Physics

    1.1. From the bulk to the surface

    1.2. Adsorption (and sticking)

    1.3. Desorption

    1.4. Surface migration

2. Gas Phase Chemistry

    2.1. Chemistry in gas phase

    2.2. Exothermicity of reactions

3. Surface Chemistry

    3.1. Eley-Rideal mechanism

    3.2. Langmuir-Hinshelwood mechanism

    3.3. Hot-Atom mechanism

1.1 Surface Physics

1.1.1 Sub-monolayer and multilayer: surface and bulk

Surface physics can be defined as the study of the structure and dynamics of atoms (and their associated electron clouds) in the vicinity of an interface, usually at the boundary between a solid and a low-density gas. There are three main processes concerning solid-gas interfaces and surface physics: adsorption, leading particles from gas to solid phase; surface diffusion; and desorption, leading particles from solid to gas phase. These three processes depend on different parameters: the mass, the polarization, and the energy of the particles, as well as the physical-chemical properties of the surface, i.e. its chemical structure and its temperature. These parameters govern how the energy can be shared (or transferred) from a phase to an other, and as consequence they rule the solid-phase interaction. Generally speaking, a monolayer is defined as a layer of material that is one molecule thick. The dynamics and the reactivity of atoms can be studied in two different regimes: sub-monolayer and multilayer. The regime transition is accompanied by a switch on the physics of the system (*Hörnström et al.* 1958; *Evans et al.* 2007). Actually surface atoms do not experience the same potential as bulk atoms: binding energies change (i.e. *Cuppen&Herbst* 2007), diffusion properties vary (i.e. *Benderskii&Wight* 1996; *Minissale et al.* 2013; *Lee et al.* 2014), reactivity is modified (i.e. *Dulieu et al.* 2010; *Miyauchi et al.* 2008). In other words, the physical-chemical description is quite different in the two regimes. The experiments described in this thesis were performed in a sub-monolayer regime. For this reason, we will describe only surface processes linked to sub-monolayer regimes.

1.1.2 Adsorption

1.1.2.1 Physisorption and chemisorption

The initial step for any surface process is the collision of gas phase species at the surface. The collision depends on the potential interaction between the approaching atom and the surface. The collision of impinging atoms with surface can lead to two different kinds of bonding as shown in Figure 1.1

- Physisorption (physical adsorption) in which the forces involved are intermolecular forces; it is a process in which the electronic structure of the atom or molecule is barely perturbed upon adsorption. The potential describing physisorption is a combination of an attractive and a repulsive part. The attractive potential is due to *van der Waals* forces. The energy of the induced dipole p_{ind} in the electric field of the original atom is negative (attractive interaction) and proportional to r^{-6}. Consequently, atoms attract each other even in the absence of chemical bonding. At smaller distances, Pauli-repulsion between closed shells eventually balances the attractive van-der-Waals interaction. Pauli-repulsion is proportional to the overlap of wave functions and increases therefore exponentially with decreasing distance. For convenience, the exponential dependence is traditionally replaced by an r^{-12}-dependence in analytical calculations. The resulting potential is the Lennard-Jones potential

$$U(r) = D_\epsilon [\underbrace{(\frac{\sigma}{r})^{12}}_{repulsion} - \underbrace{(\frac{\sigma}{r})^{6}}_{attraction}] \qquad (1.1)$$

  where D_ϵ defines the strength of the potential and α is its range. Typical binding energy of physisorption is about 10-400 meV (100-5000 K/k_b[1]).

- Chemisorption (chemical adsorption) in which the forces involved are valence forces of the same kind as those operating in the formation of chemical compounds. New chem-

---

[1]Binding energy can be expressed as a temperature through E=T/k_b; for the sake of simplicity k_b will be omitted hereafter.

ical bonds are generated at the adsorbant surface. The potential describing chemisorption is described through a Morse potential

$$U(r) = D_\epsilon [1 - e^{-\alpha(r-r_e)}] \tag{1.2}$$

where D_ϵ defines the strength of the potential, σ is its range, and r_e the equilibrium distance. Chemisorption usually forms bonds with energy of 1-10 eV. Chemisorption can occur only if: (1) the surface contain chemically active sites; (2) the impinging species are not saturated molecules (i.e., H_2, O_2, or CO_2); (3) impinging species are able to overcome activation barriers for reaction. Except for some particular cases, these three conditions were not present simultaneously in our experiments, and as consequence we can neglect chemisorption in our studies.
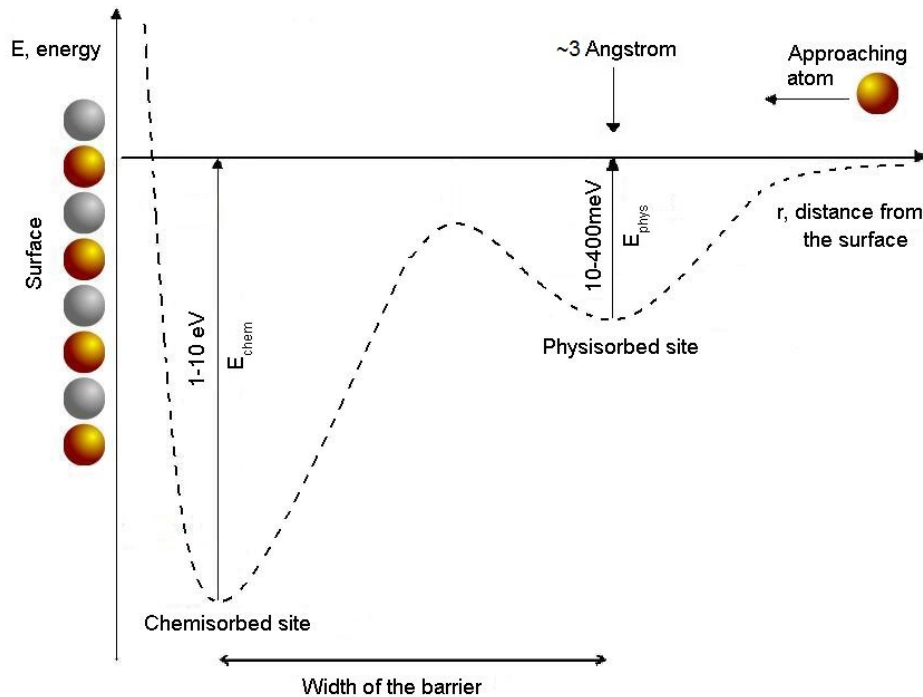
Figure 1.1: The interaction between an atom adsorbate and a surface as a function of the distance to the surface. In this picture, it can be recognized weak physisorbed sites (Van der Waals interaction, E_{phys}) with well depths in the range 10-400 meV at a distance of a few angstroms and chemisorbed sites (covalent bound, E_{chem}) with a strength of $\approx$ 1-10 eV close to the surface. The physisorption potential has been assumed to be a Lennard-Jones potential, whereas chemisorption is described in this diagram by a Morse potential.

We remark that all the physical-chemical processes described in this thesis occur with physisorbed adparticles in non-metallic surfaces. Inversely, we stress that the most part of existing scientific work concerning surface physical-chemistry considers chemisorbed adparticles in metallic surfaces. Physisorbed and chemisorbed adparticles (on non-metallic and metallic surfaces, respectively) span two different energetic ranges. Roughly speaking, physisorption imply smaller energy for the gas and quicker energy transfer (leading from a gas-particle-surface system to a adparticle-surface system), and viceversa for chemisorption. As consequence some processes are facilitated under certain conditions rather than others.

1.1.2.2 Sticking

The probability that an atom remains on the grain surface upon collision with it is estimated by the sticking coefficient.

The sticking coefficient has been introduced by Langmuir at the beginning of the last century, and the theory of sticking has been developed by Kisliuk in the mid-nineteenth century. Here we want to stress just a few key points concerning the sticking coefficient. The sticking coefficient could be considered a measure of how fast energy of gas phase atoms is transferred to the surface. Plenty of scientific works (experimental and theoretical) deal with parameters influencing sticking coefficients. The coefficient is a function of surface temperature, surface coverage and structural details as well as the kinetic energy and mass of the impinging particles. *Wang&Gomer* (1979) and *Kneitz et al.* (1999) (and references therein) show sticking coefficient changes as function of temperature of gas and surface; in particular the higher the temperature of gas and surface temperature, the smaller the sticking coefficient. We want to pinpoint here that the sticking coefficient shows a temperature (both of gas and of surface) dependence only in a big range of temperature (i.e, $\approx$ 600 K from 30 to 650 K, *Wang&Gomer* 1979). This means that the sticking coefficient is constant in our experiments, since we work with a surface temperature variation of 50 K (form 10 to 60 K) and a gas temperature variation < 150 K. We can use the following simple law to evaluate the sticking coefficient

$$s \propto \frac{E_s}{E_s + E_k} \tag{1.3}$$

where E_s is the "sticking energy" (determined by the physisorption binding energy E_b, see *Krügel* 2003) and E_k is the energy of gas particles. If

$$\text{If } E_s >> E_k \rightarrow s \approx 1.$$

In our experiments, for an O_2 molecule, $E_s > E_b \approx 0.1$ eV and $E_k \approx 0.025$ eV so $s > 0.8$. Inversely, for an H_2 molecule, E_s and $E_b < 0.04$ eV and $E_k \approx 0.025$ eV so $s < 0.6$. In this evaluation we have not considered that the sticking coefficient increases as a function of mass ratio of gas-to-surface atom (it would increase s for O_2 and decrease it for H_2). In summary, we realize that under our experimental conditions we have a sticking coefficient constant near to unity for all the species used (O_2, CO, N_2, H_2O and so on), except H_2 and D_2; this result has been already shown experimentally by *Bisschop et al.* (2006), *Matar et al.* (2008), and *Chaabouni et al.* (2012a).

1.1.3   Desorption

Once molecules are accommodated on the grain surface, they may remain almost indefinitely in that state. Due to thermal or non-thermal processes, the adsorbed species can acquire sufficient energy to overcome the activation barrier for desorption and return into the gas phase. Moreover we stress here that the energy acquired by adsorbed species can lead to other processes as: (1) decomposition of a molecular species to yield either gas phase products or other surface species; (2) diffusion of an adsorbate on the surface or into the bulk of the underlying solid. These two processes will be discussed in the following.

The way in which the adsorbed species acquires the energy produces essentially two types of desorption: thermal and non-thermal. The main difference between the two desorptions is the thermodynamic state. In the first case, the system is at any given time in thermal equilibrium and chemical equilibrium. More precisely the system changes linearly and continuously over the time, and it is in a metastable equilibrium. In the second case the system is in a non-equilibrium state and discontinuously undergoes a flux of matter and energy to and from other systems and/or to chemical reactions.

1.1.3.1   Thermal desorption

In the thermal desorption, we define the "residence time" as

$$\tau_{des} = \nu_0^{-1} \, exp(E_b/k_b T_s) \tag{1.4}$$

where E_b is binding energy of the adsorbate and T_s the surface temperature. It is, essentially, the characteristic time scale for a species to acquire sufficient energy, through thermal fluctuations, to desorb. $\tau_0 = 1/\nu_0$ corresponds to the period of vibration of the bond between

the adsorbed molecule and substrate. Thus ν_0 is the vibrational frequency of the adsorbed species on the surface and it can be evaluated by this equation

$$\nu_0 = \sqrt{\frac{2\,n_s\,E_b}{\pi^2\,m}} \tag{1.5}$$

where n_s indicates the surface density of sites, m is the mass of the adatom. For ν_0, one may use the frequency of lattice vibration of the grain, typically a few times $10^{12} - 10^{13} s^{-1}$.

Thermal desorption is usually analyzed through the *Polanyi-Wigner* equation. The desorption rate is expressed by a rate law of nth order

$$r_{des} = -\frac{d\theta}{dt} = k_n \cdot \theta^n \tag{1.6}$$

where n is the so-called "order" of the desorption and θ is the surface coverage. If the rate constant k_n is described by an *Arrhenius* equation (see Eq. 1.17 in Sec.1.2.1) then the rate law is usually referred to as the *Polanyi-Wigner* equation

$$r_{des} = -\frac{d\theta}{dt} = \nu_n \cdot exp(-\frac{E_b}{k_b\,T}) \cdot \theta^n \tag{1.7}$$

The factor ν_n can also be considered to be the "attempt frequency" at overcoming the barrier to desorption. Thus the pre-exponential/frequency factor (ν_n) may also be equated with the frequency of vibration of the bond between the molecule and substrate; this is because every time this bond is stretched during the course of a vibrational cycle can be considered an attempt to break the bond and hence an attempt to desorption (See *Nix*, 1997 for more details).

We postpone to subSec. 2.2.2.4 the discussion about experimental study of thermal desorption, and to Chapter 4 the evaluation of binding energies for different species.

1.1.3.2   Non-thermal desorption

Non-thermal desorption is the release in the gas phase of adsorbed species when the system is not at the thermodynamic equilibrium. Different types of non-thermal desorption can be considered. In the following we present a summary list.

1. *Photodesorption*: the absorption of a UV photon by a molecule condensed on a surface can result in its desorption (direct photodesorption) or in the kick-out of a nearby molecule (indirect photodesorption) (i.e. *DeSimone et al.* 2013; *Bertin et al.* 2013; *Fillion et al.* 2014; *Yuan&Yates* 2013).

2. *Sputtering*: an atom is ejected from a solid target material (i.e. ice) due to bombardment of the target by energetic particles, i.e. ions or electrons (i.e. *Behrisch* 1981; *Johnson et al.* 2013; *Cassidy et al.* 2013). The condition to observe sputtering is that the kinetic energy of the energetic particles is much higher than conventional thermal energies ($\gg$ 1 eV). Sputtering can lead to significant erosion of bombarded materials or ice.

3. *Chemical desorption*: the energy excess of an exothermic reaction is not dissipated on the surface and provokes the ejection of the newly formed species in the gas phase (*Astarita&Savage* 1980; *Dulieu et al.* 2013).

1.1.4   Surface migration: Thermal hopping and tunneling

Another important process for the description of surface physics is the migration of adsorbed atoms on the surface. Atoms and molecules physically adsorbed on a surface find themself in a potential minimum, and they cannot travel freely along the surface. Nevertheless, depending on the surface temperature, adsorbed species could be mobile in their physisorbed (or even chemisorbed) precursor states. The motion of an adatom on a periodic and regular

surface can be thought as a random site-to-site hopping process, namely a random-walk motion. The diffusing atom will have a mean square displacement in the time t given by

$$\langle \Delta r^2 \rangle = \nu \, a^n \, t \tag{1.8}$$

where ν is the frequency of hops, a is the jump distance, and n is the number of dimensions. Clearly in the case of surface diffusion, $n=2$. It is possible to define the diffusion coefficient D as the ratio of the mean square displacement over time weighted on the number z of neighboring sites where the adatom can hop:

$$D = \frac{\langle \Delta r^2 \rangle}{z \, t} = \nu \, a^n \tag{1.9}$$

The adsorbed atom vibrates and thereby swaps its kinetic and potential energy with a characteristic frequency ν_0. For two states separated by an energy difference E_{diff} (see Figure 1.2b), we can define the hopping frequency as

$$\nu_{hop} = \nu_0 \, exp(\frac{-E_{diff}}{k_b \, T}) \tag{1.10}$$

where T is the surface temperature. Diffusion occurs when $E_{diff} \approx k_b T$. E_{diff} is smaller than E_{des} (the desorption energy) and typically E_{diff}/E_{des} ranges between 0.05 and 0.5 (see Figure 1.2c). In general, the lower the desorption energy, the higher the mobility. Diffusion
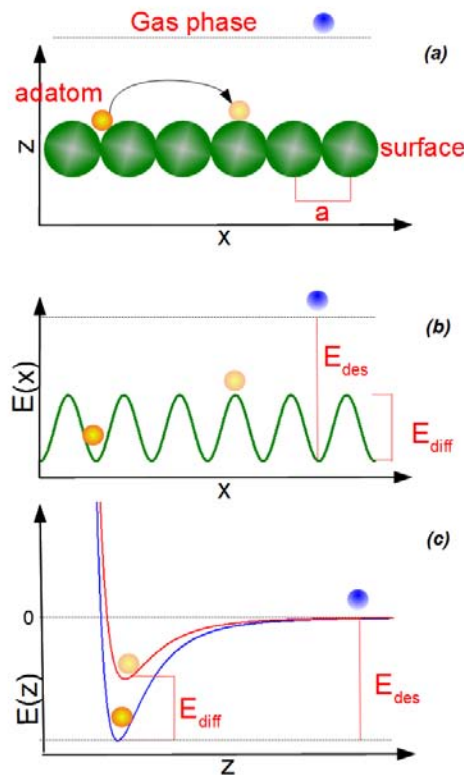
Figure 1.2: *(a)*: schematic diagram of a substrate (green circles) and adatom (orange circle) in an adsorption site and in a transition state (transparent orange circle). *(b)*: schematic potential energy diagram for adatom motion on a surface in the x direction. *(c)*: schematic potential energy diagram for adatom motion on a surface in the z direction.

can take place under different conditions, depending on the level of adsorbate coverage at the

surface or on the nature of the diffusion environment. Typically, four schemes are considered (*Oura et al.* 2003).

- *Tracer diffusion.* Individual adparticles motion. This condition is present at very low coverages where the interaction between adspecies is negligible. Tracer diffusion is a good approximation even for an ensemble of particle in which each adparticles can be considered to move independently of the others.

- *Chemical diffusion.* Ensemble adparticles motion. This condition is present at high coverages where interactions between adspecies become important. These interactions alter diffusion properties of individual adatoms and so surface diffusion coefficient may depend strongly on coverage (*Ehrlich* 1977).

- *Intrinsic diffusion.* It is the diffusion occurring on a uniform surface such as a single terrace, where no adatom traps or sources are present. Typically intrinsic diffusion can be measured in a small area compared to the inter-defect separation; in this case the activation barrier of a single terrace surface diffusion is measured (*Gomer* 1983).

- *Mass transfer diffusion.* It is the diffusion occurring on a irregular surface where adatom traps or sources are present. As in the case of chemical diffusion, these defects alter diffusion properties of individual adatoms. Inversely to intrinsic diffusion, mass transfer diffusion is measured over a distance that is large compared to the defect site size; in this case, the activation energy includes contributions due to transient binding to these sites.

Surface diffusion can occur through different mechanisms. These mechanisms influence different parameters as for example the temperature dependence and the kinetics of movement. Below, a list of the most important of these mechanisms.

1. *Hopping mechanism.* The adatoms reside on adsorption sites on the surface lattice (see Figure 1.3a). Motion occurs through successive jumps to adjacent sites, the number of which depends on the nature of the surface lattice. It has been observed experimentally for many species on different surfaces, i.e. nitrogen on Fe(100) (*Pedersen* 2000).

2. *Tunneling mechanism.* The adatoms tunnel across diffusion barriers (see Figure 1.3a). It can occur for low diffusing particle mass and low E_{diff}, and has been observed experimentally in the case of hydrogen diffusion on tungsten and copper surfaces (*Lauhon&Ho* 2000; *Manicò* et al. 2001). Diffusion via tunneling mechanism presents a nearly temperature-independent behavior.

3. *Atom Exchange mechanism.* The adatom exchanges place with an adjacent atom within the surface lattice (see Figure 1.3b). The surface atom becomes a new adatom (*Oura et al.* 2000; *Antczak&Ehrlich* 2007)

4. *Vacancy mechanism.* An atom jumps on a vacancy, so the vacancy will disappear in the place where it was, and appears in the place where the atom was. Another atom could jump on the newly formed vacancy, and another vacancy will originate, and so on the vacancy will move in random directions (see Figure 1.3c). It is a predominant mechanism of surface diffusion at high coverage. This process is similar to the so called "sliding puzzle". It has been observed experimentally by *Ural et al.* (1998) or through the Kirkendall effect (*Aloke* 2004).

Many experimental techniques exist to measure surface diffusion coefficients: some techniques are used to determine macroscopic mobility (distances of *nm* or more), others to study local diffusion (on the scale of nm). Both the different techniques used and the possibility that several surface diffusion mechanisms may be operative can influence the quantitative parameters describing the surface diffusion rate.

Here we focus our attention on two mechanisms: thermal hopping and tunneling. We can define, here, the hopping time τ_{hop}, as the inverse of Eq. 1.10

$$\tau_{hop} = \nu_0^{-1} exp(\frac{E_{diff}}{k_b\,T_s}) \qquad (1.11)$$
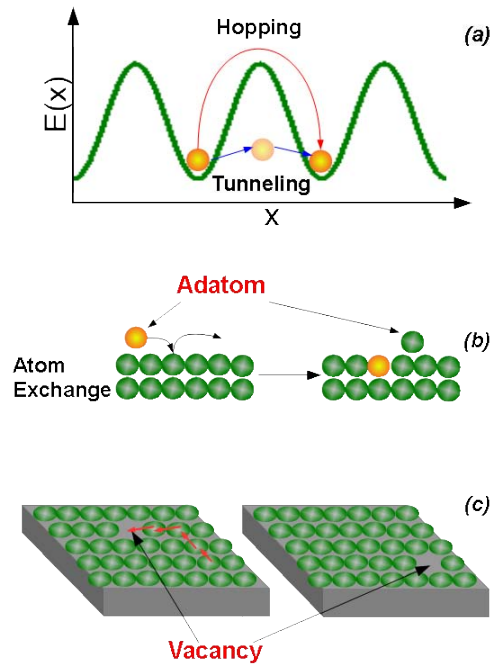
Figure 1.3: *(a)*: an atom can migrate in the adsorption sites via thermal hopping (in red) or tunnelling (in blue). *(b)*: an adatom exchanges place with an adjacent atom within the surface lattice. *(c)*: an atom jumps on a vacancy, another atom jumps on the newly formed vacancy, and so on. The vacancy moves in random directions.

where T_s is the surface temperature. It is evident from Eq. 1.11 that the hopping is dependent on temperature, and the higher the temperature, the smaller is τ_{hop}. Naturally if the temperature becomes too high the atoms or molecules can also evaporate; in fact, when the temperature increases the ratio of τ_{des} to τ_{hop} quickly decreases to unity. In other words, the particle can hop many times at low temperature, while at high temperature the probabilities of hopping and evaporate have similar values. Similarly to Eq. 1.11, the tunneling time through a rectangular barrier with height E_{diff}, and width a, is equal to

$$\tau_{tun} = \nu_0^{-1} exp(\frac{2a}{\hbar}(2ME_{diff})^{1/2}), \tag{1.12}$$

where M is the mass of the adsorbate. Figure 1.4 shows a sketch of particles adsorbed with a zero point energy in a surface potential. They have to overcome (or pass through) a barrier of dimension E_{diff} and a to diffuse. Tunneling diffusion is a low-temperature phenomenon. It should be the dominant process below the crossover temperature T_{tn-th}. Above T_{tn-th}, surface diffusion follows thermally-activated Arrhenius behavior, namely the thermal hopping. Due to the term $(2ME_{diff})^{1/2}$ in Eq. 1.12, the larger the mass of the adsorbate, the smaller should be the probability of tunneling. This statement would suggest that, experimentally, observing H tunneling is easier with respect to the one of other molecules. In truth, the mass of the adsorbate affects the hopping diffusion too. This means that the crossover temperature T_{tn-th} is placed at low temperatures, from which comes the difficulty to observe the tunneling behavior of diffusion. For the same reason a quantitative description of isotopic effect for the tunneling diffusion of atomic hydrogen is quite complicated. Some old works found diffusion slightly faster for heavy hydrogen isotopes, suggesting an anomalous inverse isotope effect (*DiFoggio&Gomer* 1982; *Wang&Gomer* 1985). More recent reports suggest that the isotope effect is negligible (*Daniel&Gomer* 1995; *Wong et al.* 1995). In any case, the theoretical issue remains unsettled, in part because of difficulties in describing phonon-adsorbate interactions (*Auerbach et al.* 1987; *Lee et al.* 1993).
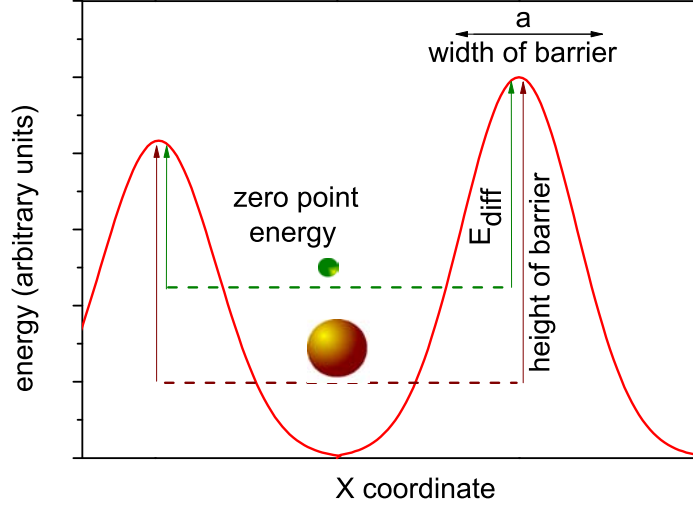
Figure 1.4: Scheme of surface potential in which two particles of different mass are trapped. Diffusion coefficients depend on the height E_{diff} and width a of the barrier, as well as on the mass of diffusing particles.

1.1.4.1 An evaluation of the crossover temperature T_{tn-th}.

We use two different theoretical models to evaluate how the two processes (thermal hopping and tunneling) affect diffusion as a function of surface temperature. The first one has been proposed by *Messiah* (1961), and recently used by *Cazaux&Tielens* (2004) in the case of H and D diffusion. In this model, the transmission coefficient (TC) from site i to site j by tunneling is given by

$$TC_{tunn} = 4\sqrt{\frac{E - E_{diff}(ij)}{E}} \left[\left(1 + \sqrt{\frac{E - E_{diff}(ij)}{E}}\right)^2 + \right.$$

$$\left. + \frac{E_{diff}(i)\,E_{diff}(j)\left[sinh\left(a\,\sqrt{\frac{2\,m\,(E_{diff}(i) - E)}{\hbar^2}}\right)\right]^2}{(E_{diff}(i) - E)\,E} \right]^{-1} \text{ , if } E < E_{diff}(i) \qquad (1.13)$$

where $E_{diff}(i)$ and $E_{diff}(j)$ are the energy of the two sites and

$$E_{diff}(i) - E_{diff}(j) = E_{diff}(ij), \qquad (1.14)$$

is the energy of the barrier between two neighbour sites. Similarly the transmission coefficient from site i to site j by thermal diffusion is

$$TC_{thermal} = 4\sqrt{\frac{E - E_{diff}(ij)}{E}} \left[\left(1 + \sqrt{\frac{E - E_{diff}(ij)}{E}}\right)^2 + \right.$$

$$\left. - \frac{E_{diff}(i)\,E_{diff}(j)\left[sin\left(a\,\sqrt{\frac{2\,m\,(E - E_{diff}(i))}{\hbar^2}}\right)\right]^2}{(E_{diff}(i) - E)\,E} \right]^{-1} \text{ , if } E < E_{diff}(i) \qquad (1.15)$$

The transmission coefficients have to be integrated over the range of energies available to the adatom and multiplied by the frequency factor to have the diffusion coefficients. Once again, in these equations we see that there are three parameters affecting the diffusion coefficients: height E_{diff} and width a of the barrier, and the mass of diffusing particles. Figure 1.5 shows the influence of each parameters for the diffusion coefficients as function of surface temperature. The choice of parameters values is arbitrary for all the simulations shown in Figure 1.5 and it is not driven by any physical intuition. Each parameter has a different effect both on the absolute value of diffusion coefficients and in the crossover temperature T_{tn-th}. Panel α of Figure 1.5 shows the sum of tunneling and thermal diffusion coefficients
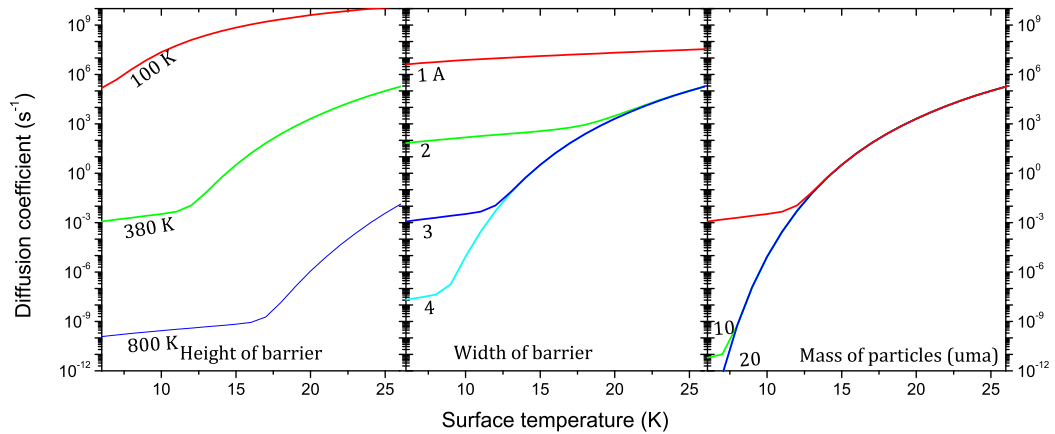
Figure 1.5: Panel (α): sum of thermal hopping and tunnelling diffusion coefficients as a function of surface temperature for three different values of E_{diff} (100, 380, and 800 K). The width a is fixed to 3 while mass is 2 amu. Panel (β): sum of thermal hopping and tunnelling diffusion coefficients as function of surface temperature for four different values of a (1, 2, 3, and 4 Å). The height E_{diff} is fixed at 380 K while mass is 2 a.m.u.. Panel (γ): sum of thermal hopping and tunnelling diffusion coefficients as a function of surface temperature for three different values of mass particle (2, 10, and 20 amu). The height E_{diff} is fixed at 380 K while the width is 2 Å.

as a function of surface temperature for three different values of E_{diff} (100, 380, and 800 K[2]). The width a is fixed to 3 while the mass is 2 a.m.u. (atomic mass unit). The increase in height E_{diff} shifts the crossover temperature T_{tn-th} to a higher temperature, and it has a drastic effect on the absolute value of diffusion coefficients along all the considered range of surface temperature. For example at 10 K, there is a difference of sixteen orders of magnitude between red and blue curves. Panel β shows the sum of thermal hopping and tunnelling diffusion coefficients as a function of surface temperature for four different values of a (1, 2, 3, and 4 Å). The height E_{diff} is fixed at 380 K while the mass is 2 amu. Here, the width a has a big influence only at low temperature. On the contrary, the crossover temperature T_{tn-th} is shifted brutally to high temperature as the width decreases. Finally panel γ shows the sum of thermal hopping and tunnelling diffusion coefficients as a function of surface temperature for three different values of mass particle (2, 10, and 20 amu). The height E_{diff} is fixed at 380 K while the width is 2 Å. Here the increase in the particle mass shifts the crossover temperature T_{tn-th} to low temperature and in general it should hinder diffusion (both by hopping or by tunneling). A practical application of this model is shown in Chapter 4, where the diffusion of oxygen atoms is treated.

The evaluation of the crossover temperature T_{tn-th} can be performed using another model. *Mott* (1969), *Pollak* (1972) and *Mott&Davis* (1979) show that the temperature dependence of tunneling can be expressed as follows

$$\tau_{tun} = \nu_0^{-1} exp(\frac{2a}{\hbar}(2mE_{diff})^{1/2} + \frac{E_1 - E_2}{3k_bT}) \qquad (1.16)$$

---

[2]We express energy in K rather than eV by using the relation eV=k_bK where k_b is the Boltzmann constant.

where E_1 and E_2 are the energy of two different adsorption sites. By inverting Eq. 1.11 and Eq. 1.16, we can move from the diffusion time to the diffusion coefficients and compare thermal hopping and tunneling terms. We obtain results similar to the Messiah's model. Panel α of Figure 1.6 shows the comparison of thermal hopping and tunneling terms for the two models. For both models the height E_{diff} of the barrier is 380 K, the width a is to 3 and the particle mass is 2 amu. Thermal hopping diffusion terms present a similar behavior for both the models, while an important difference is present in relation to tunneling terms, especially at high temperature. In any case, this does not affect the total diffusion coefficients since at high temperature thermal hopping is dominant. The total diffusion coefficients of the two models differ at maximum by a factor eight (at low temperature) and the crossover temperature T_{tn-th} arrives almost at the same time: 11 K for Mott model and 12 K for Messiah model. In conclusion, we can remark that tunneling should have a temperature
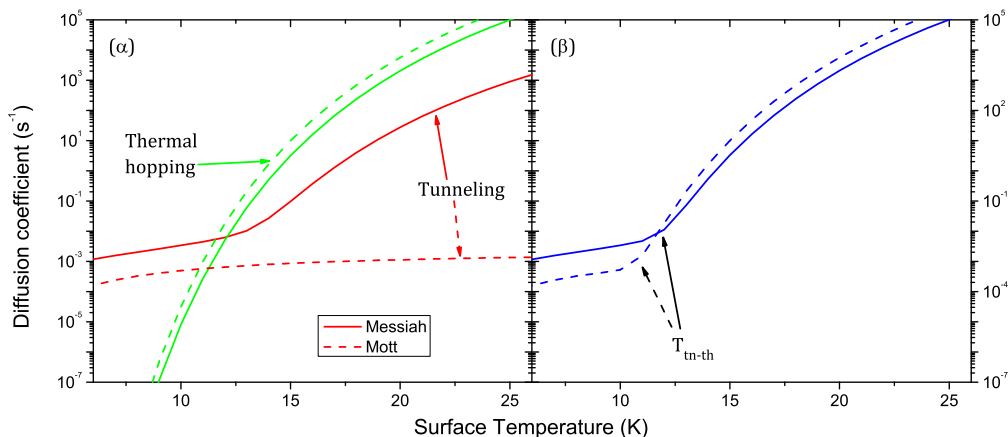
Figure 1.6: Panel (α): comparison of thermal hopping (green curves) and tunnelling (red curves) diffusion coefficients as function of surface temperature for Messiah (solid curves) and Mott (dashed curves) models. The height E_{diff} of barrier is 380 K, the width a is to 3 Åwhile mass is 2 uma. Panel (β): sum of diffusion coefficients shown in panel (α) for Messiah (solid curves) and Mott (dashed curves) models.

dependence and in particular it becomes more probable with temperature increase. The evaluation of the crossover temperature T_{tn-th} and therefore of the ratio between thermal hopping and tunneling is not trivial, since it depends on three parameters (E_{diff}, a and mass of particle) and also on the model used. Moreover a further complication comes from the percolation theory according to which only a small fraction of sites are accessible. This last concept will be treated in detail in Sec. 4.1.3

1.2   Gas Phase Chemistry

In this section we will present a smattering of chemical notions used both in gas phase chemistry and surface chemistry.

1.2.1   Chemistry in the gas phase

A chemical reaction is a process that leads to the transformation of one set of chemical substances to another. The rates of most reactions in gas phase are temperature sensitive, and an understanding of the molecular basis of this dependence is an essential goal in theoretical investigations of the kinetics. In 1889, Svante Arrhenius defined the activation energy as the minimum energy that has to be input to a chemical system with potential reactants to cause a chemical reaction. Experimentally, it has been found that the rate constant k of reactions is related to the temperature according to the following

$$k = A\, exp(-E_a/k_b\, T) \qquad (1.17)$$

which is called the *Arrhenius equation*, where k_b is the Boltzmann constant and T is the system temperature. This law can be modified to make the temperature dependence of the pre-exponential factor explicit (IUPAC 2006). The modified equation is usually of the form

$$k = A \ (T/T_0)^n \ exp(-E_a/k_b \ T) \tag{1.18}$$

where T_0 is a reference temperature and n is a value ranging between -1 and 1. In the case of classical Arrhenius equation n is 0. The equation contains two parameters:

- A is called the pre-exponential factor and has the units of the rate constant. A is correlated with the steric factor ρ through this equation $A \propto < \sigma v > \rho$, where $< \sigma v >$ is the collision frequency (σ is the cross section, v the velocity). The steric factor ρ is semi-empirically related to the orientation of the colliding molecules and can be regarded as the ratio of the cross section for reactive collisions to the total collision cross section.

- E_a is the activation energy. At an absolute temperature T, the fraction of molecules that have a kinetic energy greater than E_a can be calculated from the Maxwell-Boltzmann distribution, and turns out to be proportional to $e^{-E_a/k_b \ T}$.

1.2.2 Exothermic and endothermic reactions: enthalpy and activation barrier

Two different types of chemical reaction can be distinguished in nature, as shown in Figure 1.7, depending on how enthalpy changes (ΔH) from the initial to the final system:
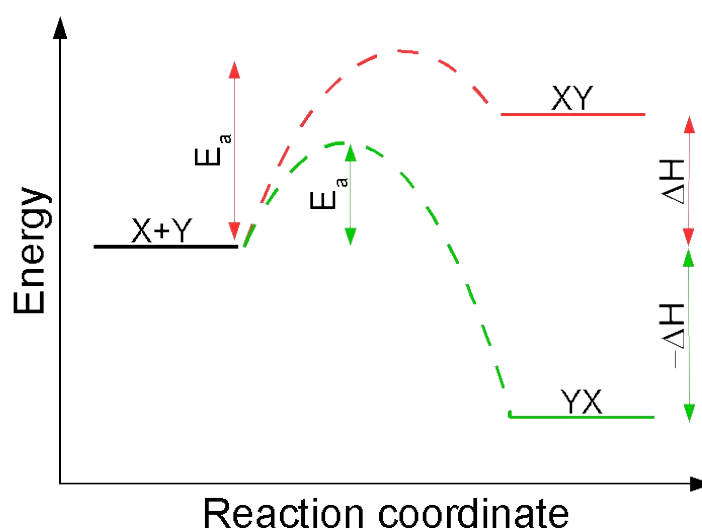
Figure 1.7: Enthalpy of exothermic (green curve) and endothermic (red curve) reactions.

1. *Endothermic reaction*, ΔH is positive. The system absorbs energy from its surroundings in the form of heat. The term derives from the union of the prefix "endon" (from the greek $\varepsilon\nu\delta o\nu$) meaning "within" and the root "therm" (from the greek $\theta\epsilon\rho\mu$-) meaning "hot".

2. *Exothermic reaction*, ΔH is negative. The system releases energy to the surroundings in the form of heat (or light, sound and so on). The term derives from the union of the prefix "exo" (from the greek $\varepsilon\chi o$) meaning "outside" and the root "therm" (from the greek $\theta\epsilon\rho\mu$-) meaning "hot".

Endothermic reactions are not likely to occur in our experiments due to the low energy that the surroundings (the cold surface) can provide to the system (the adsorbed molecules).

Figure 1.7 shows that the initial system has to overcome an energy barrier (namely activation energy), it does not matter the type of reaction. The initial (reactants) and final (products) systems can be thought as two minima for the potential energy separated by an energy barrier. The height of this barrier (E_a) indicates how fast a reaction can proceed. The activation barrier is a property of a reaction (reactants-products system), but it can change due to the presence of a third inert body, namely a catalyst or an inhibitor. A catalyst (or an inhibitor) can speed up (or slow down) a chemical reaction by providing a different route, with lower (or higher) E_a. A surface could be a catalyst. Particularly, interstellar dust grains act as a catalyst for the chemistry of ISM. Surface reactions can occur mainly via three mechanisms: Eley-Rideal, Langmuir-Hinshelwood and Harris-Kasemo. In the following sections we present, one by one, each mechanism.

1.3   Surface Chemistry

Surface chemistry can be roughly defined as the study of chemical reactions at interfaces. The presence of a surface can deeply change the rate of a reaction. For example the chemistry at the surface of dust grains plays a very important role in the formation and destruction of interstellar molecules. Interstellar grains in fact provide a surface on which accreted atoms and molecules from the gas can gather and react (through surface diffusion). In short, grains behave as catalysts.

Although most of the molecules detected in the interstellar clouds appear to be formed via sequences of gas-phase reactions (*Smith et al.* 2004; *Herbst* 2001), this is not true for all species in all types of sources. The most important exception remains the formation of molecular hydrogen from precursor hydrogen atoms, a process that must be very efficient to form copious amounts of H_2 even in diffuse clouds (*Pirronello et al.* 1997; *Vidali et al.* 2009; *Matar et al.* 2008). The formation of H_2 is certainly not the only example of reactions that occur more efficiently on surfaces in interstellar clouds. Today the formation of several other molecules by surface reactions has been studied. Among them there are carbon dioxide, water, formaldehyde, methanol and carbonic acid (i.e. see works of: Dulieu's group of Cergy-Pontoise University, Linnartz's group of Leiden Observatory, Watanabe's group of Sapporo University, and Vidali's group of Siracuse University).

1.3.1   Eley-Rideal mechanism

In this mechanism, proposed in 1938 by D. D. Eley and E. K. Rideal, only one of the molecules is adsorbed and the other one reacts with it directly coming from the gas phase, without being adsorbed on the surface of the catalyst (see Figure 1.8):

$$A(gas) + Surface \longrightarrow A(S) \tag{1.19}$$

$$A(S) + B(gas) \longrightarrow Products \tag{1.20}$$

ER reactions are somehow similar to gas phase reactions. The impinging particles either collide and react with one adsorbate or have enough energy to hop on the surface before thermalizing and accommodating in an empty adsorption site. In other words, ER mechanism is a nonthermal surface mechanism because it leads to a reaction between a thermally adsorbed surface species and a reactant which has not yet thermally accommodated to the surface. This point is of crucial importance to evaluate the activation barrier of a reaction, as we will discuss in Sec. 3.2.
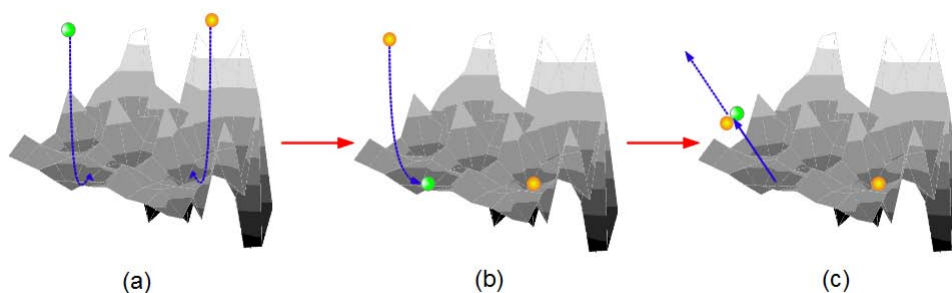
Figure 1.8: A schematic representation of the Eley-Rideal mechanism.

1.3.2 Langmuir-Hinshelwood mechanism

This mechanism describes the formation of molecules on a surface when two reaction partners are already adsorbed on then surface S, if at least one of them is mobile (see Figure 1.9):

$$A(gas) + Surface \longrightarrow A(S) \tag{1.21}$$
$$B(gas) + Surface \longrightarrow B(S) \tag{1.22}$$
$$A(S) + B(S) \longrightarrow Products \tag{1.23}$$

The LH mechanism is a thermal surface mechanism because both reactants are thermalized
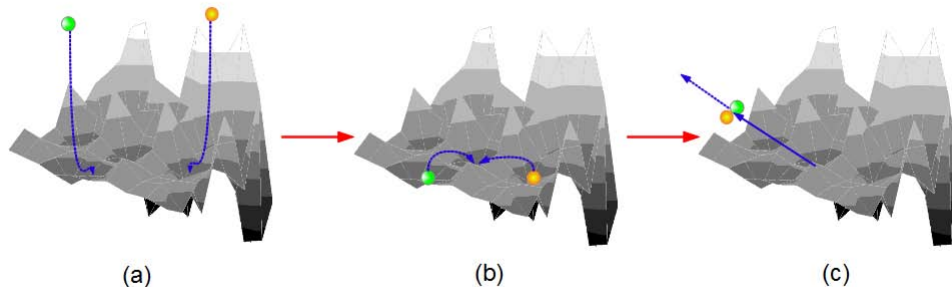
Figure 1.9: A schematic representation of the Langmuir-Hinshelwood mechanism.

to the surface temperature. Two possible rate limiting steps can be envisaged: either mobility of the reaction partners or the reaction itself. These two points will be discussed in Sec. 3.2.

1.3.3 Hot atom mechanism

Generally, only the ER and LH mechanisms are considered when the formation of molecules via surface chemistry is concerned. However, a molecule arriving at the surface may not be chemisorbed (or physisorbed) upon the first impact due to the inefficient energy transfer between the impinging particle and the surface. Before the complete dissipation of its incident energy, the adsorbed particle is not in thermal equilibrium with the surface. Hence, impinging particles could be able to hop on the surface and react with already adsorbed molecules lying several Angstroms away from the impact site. In the literature, this process is called "Hot Atom" (HA) or Harris-Kasemo (*Harris&Kasemo* 1981) mechanism (see Figure 1.10). The cross section of this mechanism is about one order of magnitude higher than that of the so-called Eley-Rideal mechanism.

To date, HA has been studied mainly from a theoretical point of view (*Martinazzo et al.*
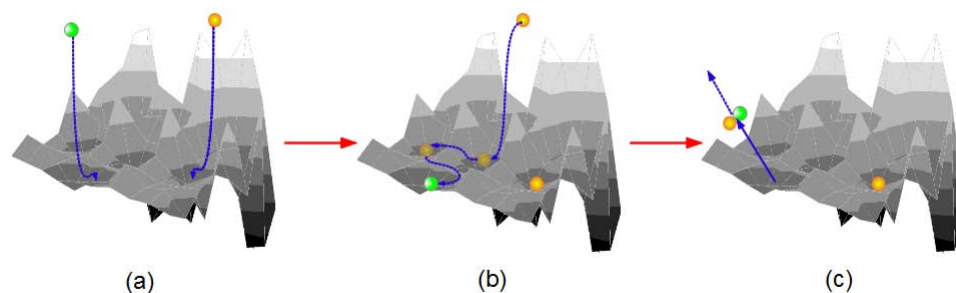
Figure 1.10: A schematic representation of the Harris-Kasemo mechanism.

2004, and *Molinari&Tomellini* 2002, and references therein), although some experimental studies exist (*Wei& Haller* 1996, and *Dinger et al.* 2001, and references therein). Previous works considered metallic surfaces only, and atoms with an energy greater than 0.5 eV or light atoms (H or D); under these conditions, the energy transfer between the particles and the surface is slow, so there is a high probability that the HA mechanism occurs. In our experiments, we worked under very different conditions. We performed the experiments on non-metallic surfaces (silicate, graphite, and water ice), atoms have an energy <0.01 eV and are heavier than H (i.e. O atoms, mass(O)/mass(H) = 16). These considerations lead us to assume that the HA mechanism should not be important under our experimental conditions, especially at low coverages.

Bibliography

1.01 Aloke, P., *The Kirkendall effect in solid state diffusion*, PhD Thesis, Eindhoven, Technische Universiteit Eindhoven (2004)

1.02 Antczak, G., and Ehrlich., G. *Surface Science Reports*, Volume 62, pp. 39-61 (2007)

1.03 Astarita, G., and Savage, D. W., *Theory of chemical desorption*, Chemical Engineering Science, Volume 35, Issue 3, pp. 649-656 (1980)

1.04 Auerbach, A., Freed, K. F., and Gomer, R., *Anomalous isotope dependence of hydrogen diffusion rates on tungsten (110) surfaces: Implications for lattice-hydrogen interactions*, The Journal of Chemical Physics, Volume 86, Issue 4, pp. 2356-2361 (1987)

1.05 Bacmann, A., Taquet, V., Faure, A., Kahane, C., and Ceccarelli, C., *Detection of complex organic molecules in a prestellar core: a new challenge for astrochemical models*, Astronomy and Astrophysics, Volume 541, id.L12, 5 pp (2012)

1.06 Behrisch, R., *Sputtering by Particle bombardment*, Springer, Berlin (1981)

1.07 Benderskii, A.V., and Wight, C. A., *Diffusion-limited geminate recombination of $O+O_2$ in solid xenon*, The Journal of Chemical, Physics, Volume 104, Issue 1, pp. 85-94 (1996)

1.08 Bertin, M., Fayolle, E. C.. Romanzin, C., Poderoso, H. A. M.; Michaut, X., Philippe, L., Jeseck, P., Öberg, K. I., Linnartz, H., and Fillion, J.-H. *Indirect Ultraviolet Photodesorption from $CO:N_2$ Binary Ices - an Efficient Grain-gas Process*, The Astrophysical Journal, Volume 779, Issue 2, article id. 120, 8 pp. (2013)

1.09 Bisschop, S. E., Fraser, H. J., Öberg, K. I., van Dishoeck, E. F., and Schlemmer, S., *Desorption rates and sticking coefficients for CO and N_2 interstellar ices*, Astronomy and Astrophysics, Volume 449, Issue 3, April III 2006, pp. 1297-1309 (2006)

1.10 Caselli, P., and Ceccarelli, C., *Our astrochemical heritage*, Astronomy and Astrophysics Review, Volume 20, article id.56 (2012)

1.11 Cassidy, T. A., Paranicas, C. P., Shirley, J. H., Dalton, J. B., Teolis, B. D., Johnson, R. E., Kamp, L., and Hendrix, A. R., *Magnetospheric ion sputtering and water ice grain size at Europa*, Planetary and Space Science, Volume 77, pp. 64-73 (2013)

1.12 Cazaux, S., and Tielens, A.G.G.M., *H_2 formation on Grain Surface*, Astrophysical Journal, Volume 604, Issue 1, pp. 222-237 (2004)

1.13 Chaabouni, H., Minissale, M., Manicó, G., Congiu, E., Noble, J. A., Baouche, S., Accolla, M., Lemaire, J. L., Pirronello, V., and Dulieu, F., *Water formation through O_2 + D pathway on cold silicate and amorphous water ice surfaces of interstellar interest*, The Journal of Chemical Physics, Volume 137, Issue 23, pp. 234706-20 (2012a)

1.14 Congiu, E., Minissale, M., Baouche, S., Chaabouni, H., Moudens, A., Cazaux, S., Manicò, G., Pirronello, V., and Dulieu F., *Efficient diffusive mechanisms of O atoms at very low temperatures on surfaces of astrophysical interest*, Faraday Discussion, Volume 168 (2014)

1.15 Daniel, E. A., and Gomer, R., *Diffusion of ^1H and ^2H on W(001)*, Surface Science, Volume 336, Issue 3, pp. 245-261 (1995)

1.16 De Simone, A., Crowell, V. D., Sherill, C. D., and Orlando, T. M., *Mechanisms of H_2O desorption from amorphous solid water by 157-nm irradiation: An experimental and theoretical study*, The Journal of Chemical Physics, Volume 139, Issue 16, pp. 164702-164702-10 (2013)

1.17 Difoggio, R., and Gomer, R., *Diffusion of hydrogen and deuterium on the (110) plane of tungsten*, Physics Review B (Condensed Matter), Volume 25, Issue 6, pp. 3490-3511 (1982)

1.18 Dinger,A., Lutterloh, C., and Küppers, J., *Interaction of hydrogen atoms with Si(111) surfaces: Adsorption, abstraction, and etching*, The Journal of Chemical Physics, Volume 114, Issue 12, pp. 5338-5350 (2001)

1.19 Dulieu, F., Congiu, E., Noble, J., Baouche, S., Chaabouni, H.,Moudens, A., Minissale, M., and Cazaux, S., *How micron-sized dust particles determine the chemistry of our Universe*, Nature Scientific Reports, Volume 3, id. 1338 (2013)

1.20 Ehrlich, G., *Direct observation of individual atoms on metals*, Surface Science, Volume 63, pp. 422-447 (1977)

1.21 Evans, J. W., Thiel, P. A., and Li, M. *Kinetic Monte Carlo Simulation of Epitaxial Thin Film Growth: Formation of Submonolayer Islands and Multilayer Mounds*, AIP Conference Proceedings, Volume, 916, p. 191 (2007)

1.22 Fillion, J.-H., Fayolle, E. C., Michaut, X., Doronin, M., Philippe, L., Rakovsky, J., Romanzin, C., Champion, N., Öberg, K. I., Linnartz, H., and Bertin, M., *Wavelength resolved UV photodesorption and photochemistry of CO_2 ice*, Faraday Discussion, Volume 168 (2014)

1.23 Gomer, R., *Surface Mobilities on Solid Materials*, in NATO ASI Series B., Vol. 86, New York: Plenum Press, (1983)

1.24 Harris, J., and Kasemo, B., *On precursor mechanisms for surface reactions*, Vacuum, Volume 31, p. 511 (1981)

1.25 Herbst, E., *The chemistry of interstellar space* Chemical Society Reviews, Volume 30, pp. 168-176 (2001)

1.26 Hörnström, S. E., Johansson, L., Flodström, A., Nhyolm, R., and Schhmidt-May, J. *Cover image Surface and bulk core level binding energy shifts in PtAu alloys*, Surface Science, Volume 160, Issue 2, pp. 561-570 (1985)

1.27 *IUPAC. Compendium of Chemical Terminology*, 2nd ed. . Compiled by A. D. Mc-Naught and A. Wilkinson. Blackwell Scientific Publications, Oxford (1997). XML on-line corrected version: http://goldbook.iupac.org (2006-)

1.28 Kisliuk, P. *The sticking probabilities of gases chemisorbed on the surfaces of solids*, Journal of Physics and Chemistry of Solids, Volume 3, Issue 1-2, pp.95-101 (1957)

1.29 Kneitz, S., Gemeinhardt, J., and Steinrück, H.-P., *A molecular beam study of the adsorption dynamics of CO on Ru(0001), Cu(111) and a pseudomorphic Cu monolayer on Ru(0001)*, Surface Science, Volume 440, pp. 307-320 (1999)

1.30 Krüugel, E., *The Physics of Interstellar Dust*, Bristol and Philadelphia, IOP Publishing Ltd (2003)

1.31 Johnson, R. E., Carlson, R. W., Cassidy, T. A., and Fama, M., *Sputtering of Ices*, The Science of Solar System Ices, Astrophysics and Space Science Library, Volume 356. ISBN 978-1-4614-3075-9. Springer Science+Business Media New York, p. 551 (2013) created by M. Nic, J. Jirat, B. Kosata; updates compiled by A. Jenkins.

1.32 Lauhon, L. J., and Ho, W., *Direct Observation of the Quantum Tunneling of Single Hydrogen Atoms with a Scanning Tunneling Microscope*, Physical Review Letters, Volume 85, Issue 21, pp. 4566-4569 (2000)

1.33 Lee, A., Zhu, X. D., Wong, A., and Deng, L., *Observation of diffusion of H and D on Ni(111) from over-barrier hopping to nonactivated tunneling*, Physical Review B (Condensed Matter), Volume 48, Issue 15, pp. 11256-11259 (1993)

1.34 Manicò, G., Ragunì, G., Pirronello, V., Roser, J. E., and Vidali, G., *Laboratory Measurements of Molecular Hydrogen Formation on Amorphous Water Ice*, The Astrophysical Journal, Volume 548, Issue 2, pp. L253-L256 (2001)

1.35 Martinazzo, R., Assoni, S., Marinoni, G. and Tantardini, G. F., *Hot-atom versus Eley-Rideal dynamics in hydrogen recombination on Ni(100). I. The single-adsorbate case.*, The Journal of Chemical Physics, Volume 120, p. 8761 (2004)

1.36 Matar, E., Congiu, E., Dulieu, F., Momeni, A., and Lemaire, J. L., *Mobility of D atoms on porous amorphous water ice surfaces under interstellar conditions*, Astronomy and Astrophysics, Volume 492, Issue 1, pp. L17-L20 (2008)

1.37 Minissale, M., Congiu, E., Manicó, G., Pirronello, V., and Dulieu, F., *CO_2 formation on interstellar dust grains: a detailed study of the barrier of the CO+O channel*, Astronomy and Astrophysics, Volume 559, pp. A49-57 (2013)

1.38 Molinari, E., and Tomellini, M., *Vibrational non-equilibrium and 'hot atoms' in the oxidation of carbon monoxide on catalytic surfaces*, Chemical Physics, Volume 277, Issue 3, pp. 373-286 (2002)

1.39 Mott, N. F., *Conduction in non-crystalline materials*, Philosophical Magazine, Volume 19, Issue 160, pp. 835-852 (1969)

1.40 Mott, N. F., and Davis, E., *Electronic Processes in Non Crystalline Materials*, Clarendon press (1979)

1.41 Oura, K., Lifshits, V. G., Saranin, A. A., Zotov, A. V., and Katayama, M. *Surface Science: an introduction*, Springer, Berlin (2003)

1.42 Pagani, L. Bourgoin, A., and Lique, F., *A method to measure CO and N_2 depletion profiles inside prestellar cores*, Astronomy and Astrophysics, Volume 548, id.L4, 5 pp (2012)

1.43 Pedersen, M. Ø., Österlund, L., Mortensen, J. J., Mavrikakis, M., Hansen, L. B., Stensgaard, I., Lægsgaard, E., Nørskov, J. K., and Besenbacher, F, *Diffusion of N Adatoms on the Fe(100) Surface*, Physical Review Letters, Volume 84, Issue 21, pp. 4898-4901 (2000)

1.44 Pirronello, V., C. Liu, L. Shen, and G. Vidali *Laboratory Synthesis of Molecular Hydrogen on Surfaces of Astrophysical Interest*, The Astrophysical Journal, Volume 475, Issue 1, pp. L69-L72 (1997)

1.45 Pollak, M., *A percolation treatment of dc hopping conduction, Journal of Non-Crystalline Solids*, Volume 11, Issue 1, pp. 1-24 (1972)

1.46 Smith, I. W. M., E. Herbst, and Q. Chang, *Rapid neutral-neutral reactions at low temperatures: a new network and first results for TMC-1,*Monthly Notices of the Royal Astronomical Society, Volume 350, Issue 1, pp. 323-330 (2004)

1.47 Ural, A., Griffin, P. B., and Plummer, J. D., *Experimental evidence for a dual vacancy-interstitial mechanism of self-diffusion in silicon*, Applied Physics Letters, Volume 73, Issue 12, pp 1706-1708 (1998)

1.48 Vidali, G., Li, L., Roser, J. E., and Badman, R., *Catalytic activity of interstellar grains: Formation of molecular hydrogen on amorphous silicates*, Advances in Space Research, Volume 43, Issue 8, pp. 1291-1298 (2009)

1.49 Yuan, C., and Yates Jr, J. T., *Lyman-α photodesorption from CO_2(ice) at 75 K: Role of CO_2 vibrational relaxation on desorption rate*, The Journal of Chemical Physics, Volume 138, Issue 15, pp. 154303-154303-6 (2013)

1.50 Wang, S. C., and Gomer, R., *Sticking coefficients of CO, O_2 and Xe on the (110) and (100) planes of tungsten*, Surface Science, Volume 84, pp. 329-354 (1979)

1.51 Wang, S. C., and Gomer, R., *Diffusion of hydrogen, deuterium, and tritium on the (110) plane of tungsten*, The Journal of Chemical Physics, Volume 83, p. 4193 (1985)

1.52 Wei, C., and Haller, G. L., *A comparison of the dynamics of CO oxidation by oxygen atoms and molecules on Pt and Pd surfaces*, The Journal of Chemical Physics, Volume 105, Issue 2, pp. 810-824 (1996)

1.53 Wong, A., Lee, A., and Zhu, X. D., *Coverage dependence of quantum tunneling diffusion of hydrogen and deuterium on Ni(111)*, Physical Review B (Condensed Matter), Volume 51, Issue 7, pp. 4418-4425 (1995)

2

Experimental apparatus and methods

On n'échappe pas de la machine.

G. Deleuze

This chapter presents the experimental apparatus and methods used to perform the experiments described along this thesis. All experiments described in this thesis are performed at LERMA-Cergy (Laboratoire d'Etude du Rayonnement et de la Matiére en Astrophysique et Atmospheres) laboratory in Cergy-Pontoise University (France) through the so called FOR-MOLISM (FORmation of MOLecules in the ISM) set-up; it is dedicated to the investigation of physico-chemical processes occurring to atoms and molecules on cold surfaces, i.e., dust grains dwelling in the interstellar medium.

2.1   Experimental apparatus

Figure 2.1 shows a schematic drawing of the FORMOLISM set-up. FORMOLISM consists of different parts:

1. an ultra high vacuum (UHV) chamber, i.e., the main chamber;

2. two triply differentially pumped atomic/molecular beamlines;

3. two microwave cavities mounted in the first stage of each beam and used for dissociating molecular gases;

4. A sample holder connected to a cryostat;

5. A quadrupole mass spectrometer (QMS);

6. An infrared spectrometer (FT-RAIRs).

Each part will be described in detail in the next sections.
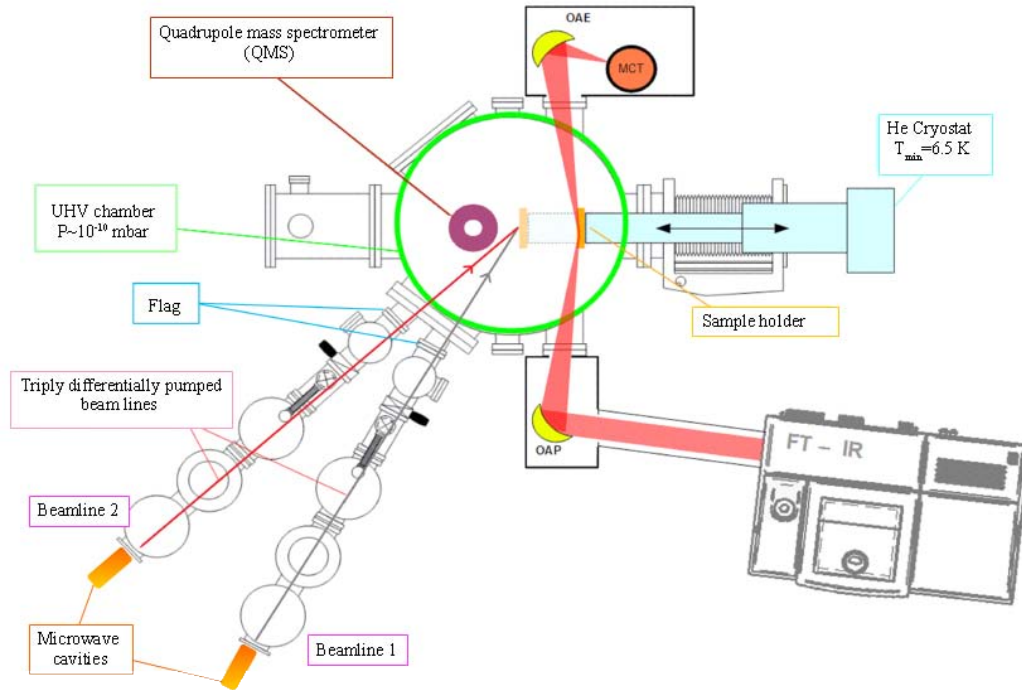
Figure 2.1: Schematic top-view of the FORMOLISM set-up and the FT-RAIRS facility.

2.1.1 The main chamber

The UHV main chamber consists of a stainless steel chamber, a cylinder of radius 15 cm and height 120 cm, that is evacuated by a cryopump, a titanium sublimation pump, a turbo molecular pump and an ion pump, so the residual pressure inside the chamber reaches values of 10^{-10}-10^{-11} $mbar$ corresponding to a molecular/atomic density of about $2 \times 10^6 cm^{-3}$. We are not able to perform experiments with pressure similar to those of interstellar medium, i.e. 10^{-13}-10^{-14} $mbar$, for two reasons:

- from a technical point of view, ultra high vacuum systems cannot reach this pressure;

- from a practical point of view, at these pressures, each single experiment would need weeks or months to be performed.

In any case, even if the pressure in the main chamber is higher than that encountered in interstellar medium, it is low enough to keep the amount of pollutants low on the surface of the sample; in fact, with a pressure of 10^{-10} $mbar$ and with a surface temperature of 10 K, the sample-holder is coated with ≈ 1 ML of water vapour[1] after only ≈ 5000 minutes (see *Accolla*, 2010). In the main chamber there is a leak valve equipped with a microchannel doser (Figure 2.2) that is used to make water ice films on the sample surface. When it is opened, water contained in a small vial, can diffuse into the chamber via a micro capillary array. The water diffuser can be moved and placed in front of or above the sample holder, depending on the kind of water ice to be grown on the surface of the sample, as described in Sec. 2.2.1.

2.1.2 The beamlines

The two beamlines form an angle of 18° and converge on an ideal point lying onto the central axis of the main chamber. This is the same design devised by *Pirronello et al.* (1997). Each beamline has three differentially pumped (atomic/molecular) stages, connected with

---

[1]The majority of the residual pressure is due to H_2, while H_2O, N_2, CH_4, and so on represent only 10 % of the total residual pressure ($\approx 10^{-11}$ mbar).
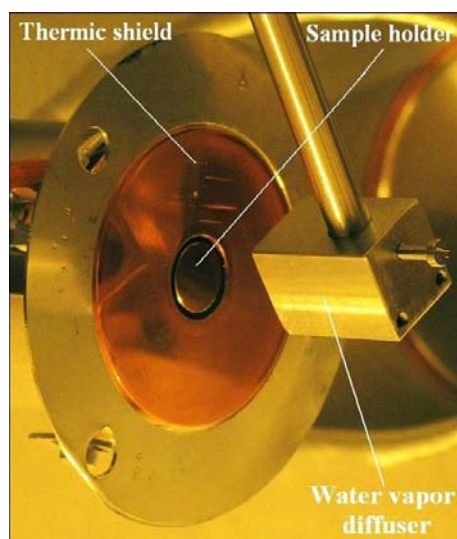
Figure 2.2: Photo of the water diffuser facing the sample holder surface, during water ice growth.

the main chamber and aimed at the surface of the sample holder. Through this design, a low and well-collimated flux of particles can be created. The gas coming from a bottle is introduced in the beamline via a quartz tube located in the first stage of the beamline, with a pressure of the order of 1 *mbar*. A small fraction of the gas passes into the second stage through a first tiny diaphragm (pressure of the order of 10^{-5} *mbar*), as shown in Figure 2.3. Here, a second tiny diaphragm leads to the third stage, where there is a residual pressure of 10^{-8} *mbar*, pumped down by turbo molecular pumps. Finally, after a third diaphragm, the gas arrives in the main chamber where there is a residual pressure of 10^{-10} *mbar*.

The two beamlines (that can be separated by the main chamber by two manually-operated valves) are always kept under vacuum. The three stages are continually pumped by turbo-molecular pumps, backed by mechanical rotary pumps, even when the beamlines are not in use.

A removable metallic plate (called "beam flag") is placed between the third stage and the main chamber. The flag is able to intercept the beam flux and the particles do not arrive directly to the icy sample, but they fill the main chamber: in this case, the particles will condense on the icy sample by "background" deposition with a flux 2 or 3 orders of magnitude less intense. When the flag is open the beam of particles reaches the sample surface directly. Figure 2.3 shows how the beam direction is adjusted and the gas is centered on the surface. A pointing laser, located in front of the quartz tube, passes through the diaphragms holes and arrives on the surface. The laser spots of the two beams are centered on the same area of the surface, through micro movement of the diaphragms and, also, of the whole beam stages.

2.1.3 The microwave cavities

Each beamline is equipped with a microwave cavity (a Surfatron cavity) and a microwave power supply delivering up to 300 W at 2.45 GHz. These two components are used for dissociating molecular gases such as hydrogen, deuterium, nitrogen or oxygen to produce atomic or molecular radicals. The molecular gases pass in a quartz pipe (diameter 4 mm, length 10-20 cm) traversing the microwave cavity with a pressure ranging from 0.3 to 4 mbar. Microwaves transfer energy to the gas by exciting and ionizing the species. They create a plasma in which electrons are accelerated. The dissociative electronic excitation of H_2, D_2, N_2, or O_2 produce atoms in the discharge zone. At the pressures used, the large number of collisions, especially on the walls of the pipe, favors the recombination of molecules after being dissociated. To minimize the spontaneous recombination of the atomic species and to reduce the discharge temperature the cavity is cooled by a flux of compressed air around the tube and by a water circuit cooling the metallic parts. We have estimated that the temperature
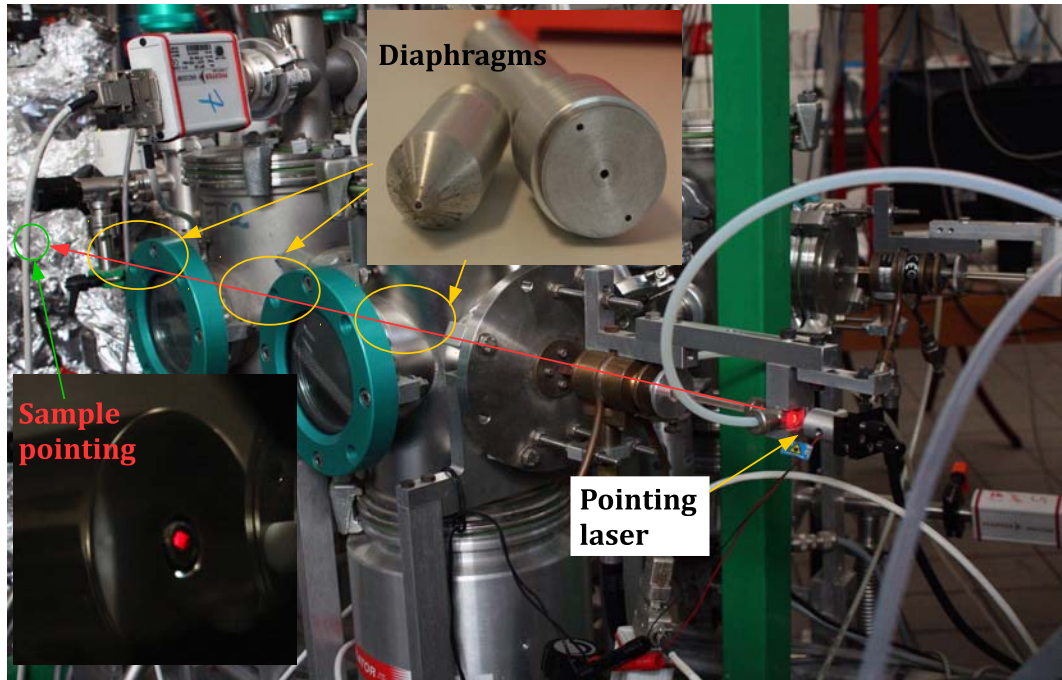
Figure 2.3: One of the two beamlines of FORMOLISM. Two of the three diaphragms (here disassembled) connect the three stages, and a system of laser pointing allows beam direction adjusting.

of the gas coming out from the pipe is lower than 450 K. Actually, due to multiple collisions the atoms generated in the discharge can thermalize upon impacts with the pipe internal surfaces. It is possible, however, that a gradient of temperature is present in the pipe. By considering the thickness of the pipe, the difference between the outer and the inner part should be lower than 100 K. Hence, an upper limit for the translational temperature is 450 K. SubSec. 2.3 presents the method used to know the excitation state of dissociated species. Figure 2.4 shows the discharge glows of H_2 (purple) and O_2 (off-white) gases.

2.1.4 The sample holder and the sample

The sample holder is an oxygen-free high thermal conductivity (OFHC) copper cylinder, with radius equal to 5 mm. The sample holder is placed in the center of the main chamber, at the same height of the beamlines, and an electric resistance is able to heat the sample holder up to 400 K. The sample holder is in contact with a closed-cycle He cryostat. By throttling the flow of liquid helium the sample can be cooled to 6.5 K. A buckler, made of a mixture of copper and nickel, protects and isolates the sample holder, the "400 K interface" and the second stage of the cryostat from IR radiation coming largely from the walls of the chamber (See Figure 2.5).

The sample holder is mounted on a translation plate, that allows us to move back and forth the sample holder with respect to the center of the chamber in order to allow a better positioning of the sample with respect to the QMS or the water vaporizer.

The "400 K interface" is connected to a controller (*Lakeshore 340*), that allows the reading of the different temperatures and, by varying the power of the heater, to regulate the sample temperature.

The sample is interchangeable by opening the main chamber. Two different sample were used to perform the experiments:

1. a non-porous amorphous olivine-type silicate

2. a HOPG (Highly Ordered Pyrolytic Graphite) slab
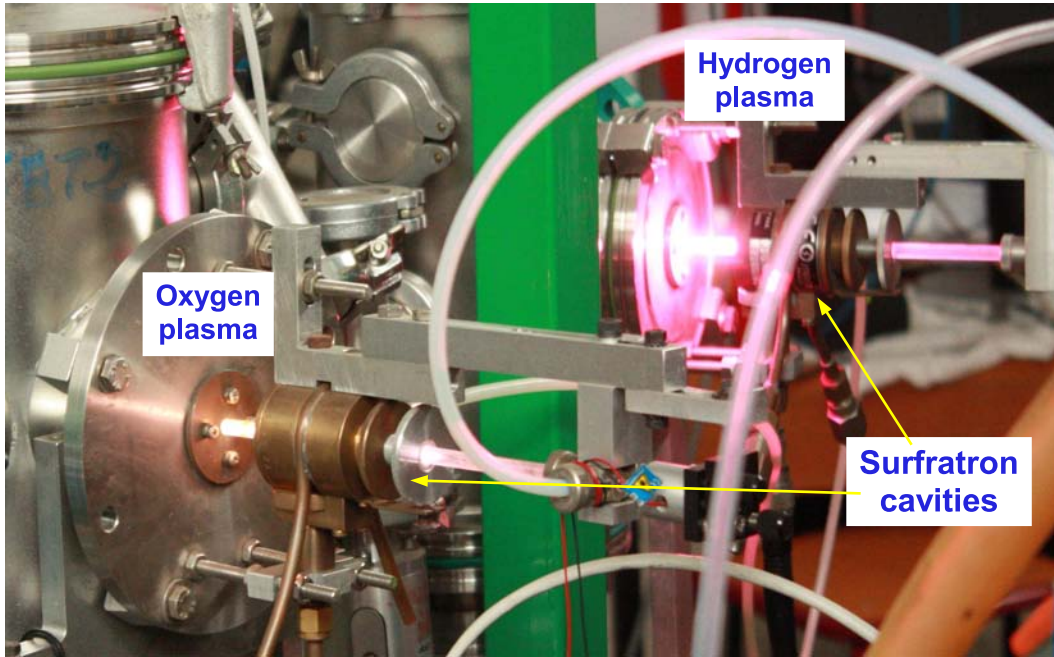
Figure 2.4: Picture of the dissociation of H_2 (purple) and O_2 (off-white) gases through Surfatron cavities in FORMOLISM setup.

The silicate sample was obtained by thermal evaporation of San Carlos olivine ($Mg_{1.8}Fe_{0.2}SiO_4$) onto a gold-coated substrate (1 cm in diameter), operating at temperatures between 6.5 K and 350 K. The surface density of adsorption sites is about the same of the one found on compact water ice samples. Sample preparation and surface analysis are described extensively in *Djouadi et al.* (2005).

The HOPG surface used in the experiments are a ZYA-grade HOPG samples, produced by MaTeck company; all HOPG samples had been previously exposed to an O-atom beam (oxidized) to avoid surface changes during the experimental sequences.

2.1.5   The Quadrupole Mass Spectrometer

Figure 2.6 shows a photo and a scheme of the Quadrupole Mass Spectrometer (QMS). In red the three main components, (i) an ionizer (bombardment by electrons from a hot filament), (ii) a mass filter (discrimination zone) consisting of four parallel metal rods, and (iii) the ion detector (electron multiplier). A gas (residual or desorbing form a surface) is ionized by electron impact. Free electrons are obtained by thermal emission from an electrically heated tungsten filament. Thermal electron emission can be described by Richardson-Dushman expression (*Richardson* 1929)

$$J = A_G T^2 \cdot exp(-\frac{\phi}{kT}) \tag{2.1}$$

with J the current density of emitted electrons, T is the thermodynamic temperature of the metal, ϕ the work function of the filament material and A_G is

$$A_G = \lambda_R A_0 \tag{2.2}$$

with

$$A_0 = \frac{4\pi m k^2 e}{h^3} \tag{2.3}$$

and λ_R is a material-specific correction factor that is typically of order 0.5 .

Ions are subsequently accelerated towards the quadrupole analyzer which consists of four cylindrical rods, arranged symmetrically at a distance $r_0(x,y)$ around the optical axis z of the system. Opposite rods are electrically connected. These four metallic rods represent the
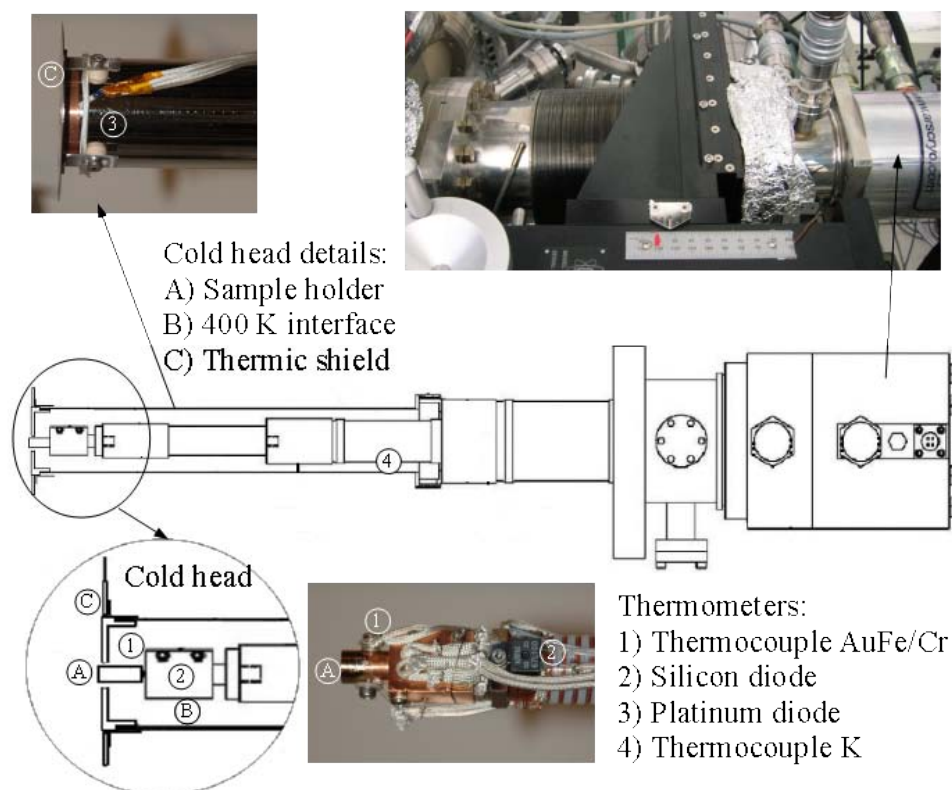
Figure 2.5: Scheme and photos of the cryostat, with longitudinal section of the sample holder.

ion mass filter able to select species according to their mass-to-charge ratio (m/z); in fact, a voltage combination of a direct and a radio frequency component is applied between adjacent and opposite rods. Varying the direct and the radio frequency component, the QMS is able to scan all the ions up to a choosen mass-to-charge ratio technically fixed (in our case 50 m/z. In the following, unless specified otherwise, z is equal to one and it will be omitted.).

The ion detector is a *Channeltron* (an electron multiplier). The output current generated in the *Channeltron* is converted into a digital signal. The digitized signal is then analyzed by the software provided by the QMS manufacturer *HIDEN*. It allows to monitor and record the acquired information, but also to adjust the electronic setting of the QMS and the dwelling time on each mass value. Moreover, it is possible to record simultaneously the sample temperature measured by a *Lakeshore* controller during TPD experiments.

The QMS is mounted in the upper part of the main chamber. It can be rotated by 190° around the sample and moved vertically. This detector is used in the lower position in order to measure the intensity of the incoming beams and the products of reaction occurring on the surface of the sample. In the upper position, the QMS is used to analyze the abundances of residual gases in the main chamber.

2.1.6   The Infrared Spectrometer

FORMOLISM is equipped with a Bruker Tensor 27 Fourier transform infrared spectrometer (FTIR) used to monitor the adsorbed/formed species *in situ*. Figure 2.7 shows a scheme of the spectrometer: a mid-IR source (Globar) is used as coherent thermal light source to produce a beam containing frequencies in the 4000-800 cm^{-1} (2.5-10 μm). The light passes though an aperture (typically of 2 mm) and arrives in a Michelson interferometer. The interferometer
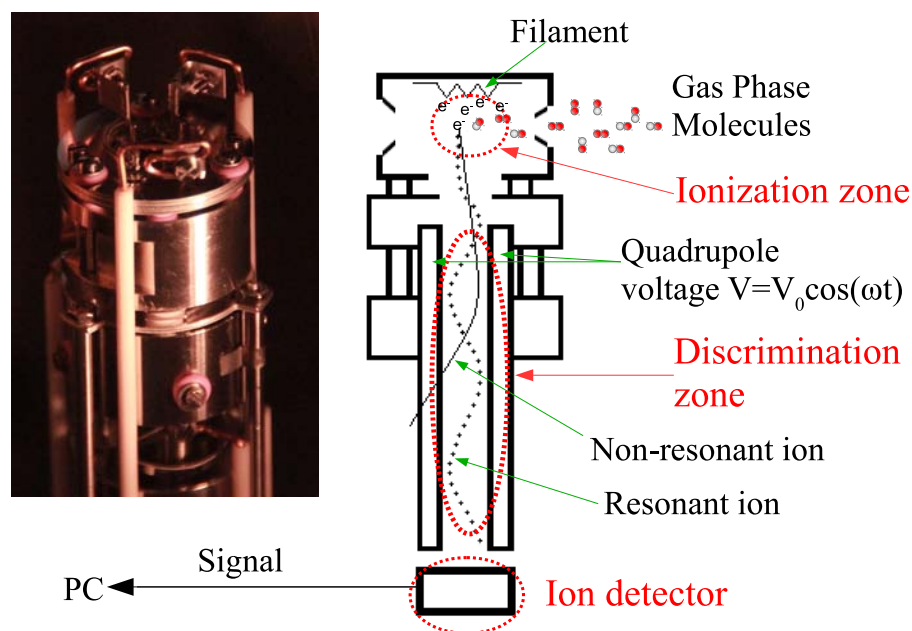
Figure 2.6: Photo and schematic view of the QMS head.

is composed of a beamsplitter (KBr) that splits the beam light in two parts, one is sent to a fixed mirror and the other to a moving mirror. The movement of this last mirror produces beams with different optical path length (namely different combination of frequencies in the recombined beam). The beamsplitter recombines the beams coming from the two mirrors. The resulting beam passes through an exit port and it is focused on the surface through an off-axis parabolic gold-plated mirror (effective focal length FL = 250 mm). The mirror is mounted within a differentially pumped housing adjacent to the UHV chamber and isolated from it with a differentially pumped potassium bromide (KBr) window. The FTIR is set up in a reflection-absorption infrared spectroscopy (RAIRS) configuration (see Figure 2.7) and the spectra are recorded at a grazing incident angle of $83 \pm 1°$. The parallel and unpolarized infrared beam is focused onto the sample using a $90°$ reflecting mirror (see Figure 2.7). Through a second pumped KBr window, the reflected infrared beam arrives in a second pumped housing using an off-axis ellipsoidal gold-plated mirror. This mirror has conjugate foci located at 250 mm and 40 mm, corresponding to distances to the surface sample and the MCT detector. The liquid-nitrogen-cooled mercury cadmium telluride (MCT) detector collects the raw data that are sent to the PC. Afterwards, OPUS software assembles all these data and turn the interferogram (the raw data, light absorption for each mirror position) into the typical IR spectrum (light absorption for each wavelength) through a Fourier transform. Each spectrum is usually acquired with a resolution of 4 cm^{-1} prior or subsequently to either deposition or TPD. The sample must be moved backward to allow for acquisition of a RAIR spectrum. One major problem of RAIR spectroscopy is the sensitivity. The signal is usually very weak owing to the small number of adsorbing molecules; in fact for an area of 1 cm^2 with less than 10^{15} adsorbed molecules, even for a IR active species, the signal is typically less than 0.01% of total absorption (or transmittance).

2.2   Experimental methods

In the next sections the experimental methods used are presented. We describe here how ices are grown (in particular water ice) on the sample, the techniques used to probe the products
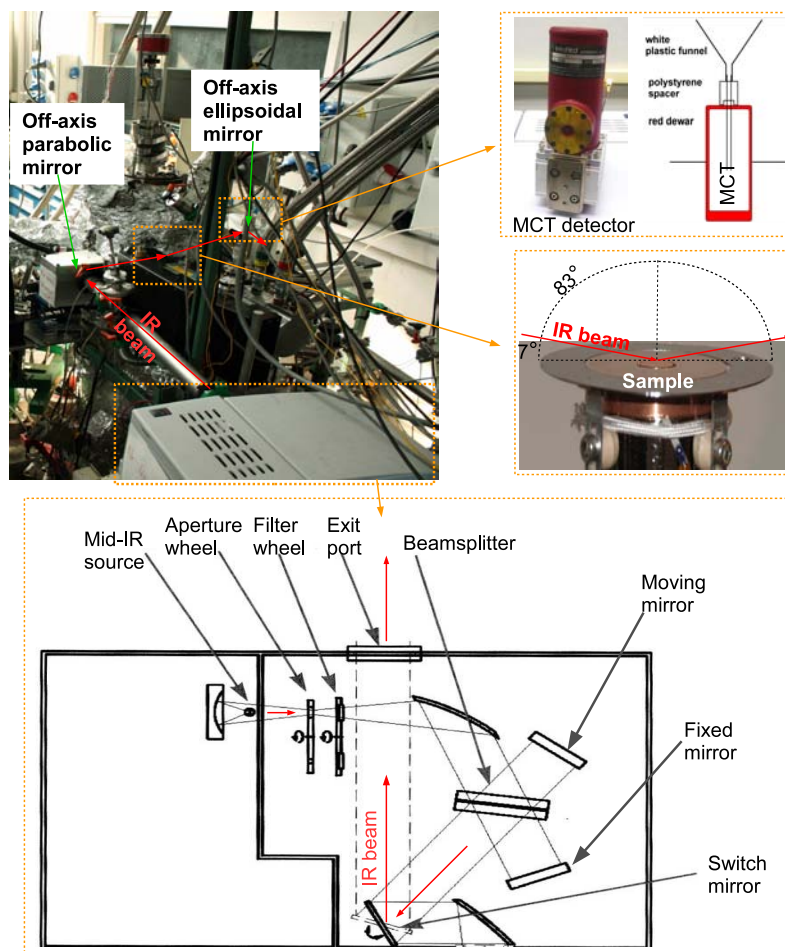
Figure 2.7: Photo and schematic view of the Infrared Spectrometer Bruker Tensor 27. Red arrows represent the path of IR beam from the Mid-IR source to the MCT detector in FORMOLISM.

and to monitor ices (mass spectroscopy and infrared spectroscopy), and finally how the beam fluxes and surface coverages are calibrated.

2.2.1 Water ice deposition on the sample holder

Two different techniques of water ice growth are used in the FORMOLISM set-up: either the "spray deposition" or the "background deposition". Both of them will be described in the following two sections.

The deposition by spraying is a direct way to grow the amorphous solid water (ASW) ice layer quickly and it is used to deposit large amount of water molecules. During the spray deposition, the microchannel array doser is placed at 2 cm in front of the sample holder surface maintained at 110 K, as shown in Figure 2.2.

As it is shown in Sec.2.1.1, a small glass vial containing purified liquid water is connected with the water diffuser located into UHV chamber via a leak valve. By opening this leak valve, the local pressure in the region between the diffuser and the copper substrate reaches about 10^{-6} $mbar$, while the residual pressure into the chamber is 10^{-9} $mbar$. It has been evaluated that the mean free path of H_2O molecules is about 1 m while the residual pressure is 10^{-6} $mbar$. Since the distance between the diffuser and the cold surface is smaller than the mean free path, the majority of the water molecules will hit the sample holder and the cryoshield and stick on them. For this reason, water molecules sent into the chamber during the direct deposition contribute marginally to the UHV pressure.

Spray deposition allows the growth of about a hundred monolayers of ASW within 5 minutes

(i.e. 0.33 ML/s).

The background deposition method is performed by filling uniformly the entire volume of the chamber with water vapor. Now the microchannel doser is kept high above the sample holder surface.

Knowing the pressure (P), the temperature in the chamber (T) and the mass of impinging molecules (m), the flux ϕ of molecules hitting the cold surface is

$$\phi = \frac{\bar{v}n}{4} = \frac{P}{4KT}\sqrt{\frac{8KT}{\pi m}} \tag{2.4}$$

where $\bar{v}$ is the molecular mean velocity and n is the molecular number density, while $1/4$ is a corrective factor due to the projection of a sphere on a disk.[2] The background method can be used only for the deposition of thin ice films due to the long time required. For a pressure of 1×10^{-8} $mbar$, a monolayer is grown in around 5 minutes. The recovery of the base pressure (10^{-10} $mbar$) takes about 30 minutes.

2.2.2 Mass spectroscopy: the different uses of the QMS

2.2.2.1 Cracking pattern

In subSec. 2.1.5, we have briefly described the QMS operation. We have claimed that gas species are detected after their ionization. This occurs in the so called ionization zone through electron impacts. Here we pinpoint that electron impacts could produce dissociation of species in addition to ionization. Actually it is necessary to pay attention to the fragment distribution of ionic species which results from dissociation and ionization of multi-atomic molecules of any given species in the ionizer, the so called cracking pattern. The probabilities of ionization and dissociation depend on molecular geometry (and intra-molecular bonds energy), angle of impact between molecules and ionizing electrons of the QMS, and the energy of ionizing electrons. For these reason, signals (and peaks) at different masses can derive from the same molecule, reflecting its partial fragmentation in the QMS head. Figure 2.8 shows the TPD curves of CH_3OH and six major signals are presented. Table 2.1 reports the cracking pattern of some molecules: NO_2, O_3, H_2CO, NH_2OH, $HCOOH$, and CH_3OH. The signals are normalized to the highest mass signal. Nitrogen dioxide is the simplest case listed in Table 2.1.

Table 2.1: List of the cracking pattern of the following molecules: NO_2, O_3, H_2CO, NH_2OH, ND_2OD, $HCOOH$, and CH_3OH. The signals are normalized to the highest mass signal. Mass and intensity are indicated in blue and in red respectively.

Molecule	Peak 1	Peak 2	Peak 3	Peak 4	Peak 5	Peak 6
–			Mass-%			
Nitrogen dioxide (NO_2)	30-100	46-14	–	–	–	–
Ozone (O_3)	32-100	48-67	16-4	–	–	–
Formaldehyde (H_2CO)	30-100	29-85	28-15	–	–	–
Hydroxilamine (NH_2OH)	17-100	33-86	16-86	30-66	32-14	–
(ND_2OD)	30-100	18-88	36-23	34-8	–	–
Formic Acid ($HCOOH$)	29-100	46-65	28-60	44-47	45-43	–
Methanol (CH_3OH)	31-100	32-67	15-50	29-45	30-16	28-7

This molecule is detected through mass 46 (NO_2^+) and mass 30 (NO^+) and the ratio between these masses is around 10-20 %, as shown in *Minissale et al.* (2013b). As already seen in *Mokrane et al.* (2009) and *Minissale et al.* (2014), the ozone signal is simultaneously detected at mass 48, 32, and 16. This is because the dissociation of O_3 is energetically more favorable than its ionisation (3.77 eV vs 12.53 eV). When O_3 enters the QMS head, it can undergo different processes:

- O_3 (+ e$^-$) $\rightarrow O_3^+$ (ΔH_f=12.97 eV)

---

[2]In this equation the sticking coefficient of H_2O should be taken into consideration, but it is neglected because it is close to unity in the range of temperature 10 - 120 K, thus every molecules hitting the surface will stick on it.
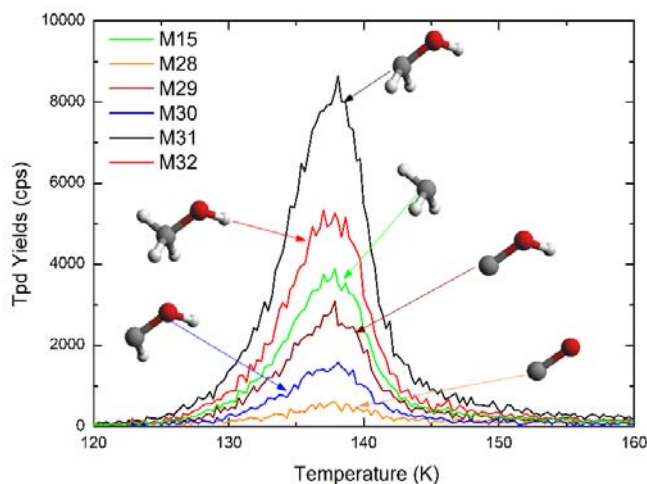
Figure 2.8: TPD curves of masses 32, 31, 30, 29, 28, and 15 after deposition of 1 ML of methanol. All the peaks at different masses derive from the same molecule, reflecting its partial fragmentation in the QMS head.

- O_3 $(+ e^-) \rightarrow O_2^+ + O$ $(\Delta H_f = 13.17 \text{ eV})$

- O_3 $(+ e^-) \rightarrow O^+ + O_2$ $(\Delta H_f = 14.72 \text{ eV})$

The third process is less probable than the first two, and in fact the peak at mass 16 is 4 % of the peak at mass 32. The difference between mass 32 and 48 could be explained by further electron impact. This last is more probable for O_3^+ rather than O_2^+. Actually due to its mass, O_3^+ has a lower speed and it spends more time in the ionization zone. We can draw on similar arguments (ionization versus dissociation, double electron impacts) to explain mass spectroscopy of H_2CO. In this case signals at masses 30 (H_2CO^+), 29 (HCO^+), and 28 (CO^+). As evident from the table, the larger the molecule, the higher the number of the mass signals. In particular, methanol (CH_3OH) cracking is very complex as evident from Figure 2.8. In conclusion, we claim here that, if on one hand the molecule fragmentation in the QMS complicates the mass spectroscopy analysis, on the other hand it is a powerful instrument to figure out some ambiguous cases. For example, molecules of the same masses, like CH_3OH and O_2 (mass 32) or CO and N_2 (mass 28), would be undistinguishable without the help of the cracking pattern.

2.2.2.2 Residual gas analyzer: knowing beam composition

In FORMOLISM set-up, the QMS can be rotated and put in front of the beams to know their gas composition. This method allows us to know if a molecular beam is polluted with other species. In particular, dissolved gases are contained (or present) in some species, that at standard temperature and pressure are in liquid or solid phase (i.e. CH_3OH, H_2O, or H_2CO). The degasification process can be checked and followed by verifying the gas composition as a function of time. Formaldehyde gas is obtained through depolymerization of paraformaldehyde (a white crystalline solid shown in Figure 2.9): depolymerization is achieved by immersing the phial containing paraformaldehyde on water constantly held at 62 °C. The resulting gas contains H_2CO, but also residual CO and H_2O. By placing paraformaldehyde under vacuum, we make the residual gas less soluble and its concentration decreases. Figure 2.9 shows all the steps of the H_2CO beam preparation from the depolymerization to the injection of the gas in the beam. When all the residual gas is pumped we have, at beginning of the beam (gauge
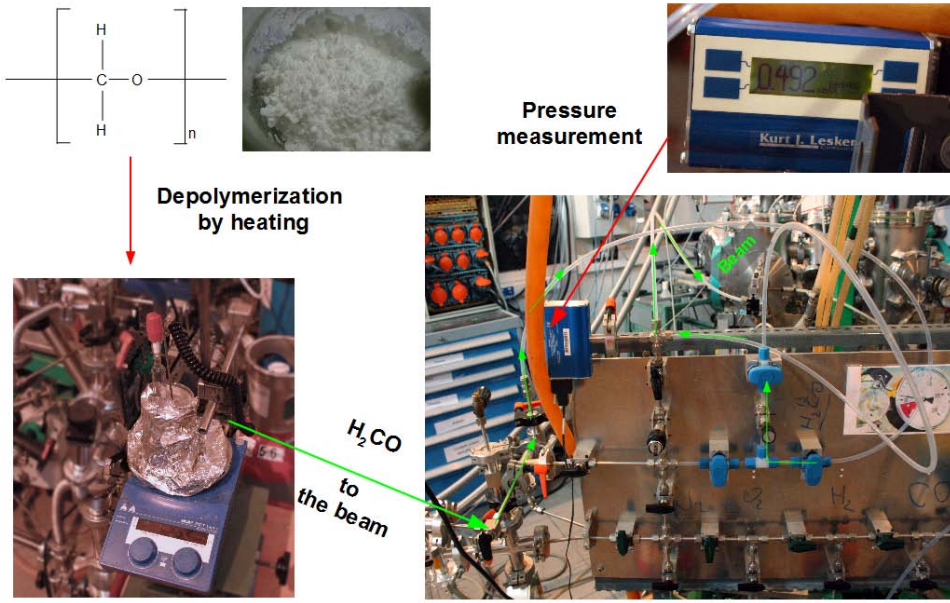
Figure 2.9: Photos of all the steps of the H$_2$CO beam preparation. From the top left, anticlock-wisely we have: paraformaldehyde powder, heating of paraformaldehyde by immersion in hot water, injection of H$_2$CO in the beam, and particular of the gauge used to measure the source pressure.

shown in Figure 2.9), a pressure of 0.42 mbar, corresponding to QMS signal of 810 and 690 cps for masses 30 and 29, respectively. Table 2.2 and top panel of Figure 2.10 show the ion count per second for four mass (30, 29, 28, and 18) during H$_2$CO beam preparation. These masses should correspond to three species: H$_2$CO for masses 30, 29, and 28; CO and/or N$_2$ for mass 28; H$_2$O for mass 18. The bottom panel of Figure 2.10 shows the evolution of the abundance ratio between these species. The ratio is calculated by considering that signal at mass 28 is composed of two parts, one is the residual gas (CO+N$_2$), the other is cracked H$_2$CO:

$$Mass28 = H_2CO + \text{Residual gas} \approx 0.15 \times Mass30 + \text{Residual gas}. \qquad (2.5)$$

At the beginning of the degasification process the ratio (CO+N$_2$)/H$_2$CO is

$$\frac{Mass28 - Mass30 \times 0.15}{Mass30 + Mass29 + Mass30 \times 0.15} = \frac{1300 - 90}{580 + 420 + 90} = 1.11, \qquad (2.6)$$

while after 150 minutes of pumping it becomes

$$\frac{Mass28 - Mass30 \times 0.15}{Mass30 + Mass29 + Mass30 \times 0.15} = \frac{10}{810 + 690 + 120} \approx 0. \qquad (2.7)$$

Similar trends are obtained for H$_2$O/H$_2$CO, starting from 0.84 and arriving at 0.

Up to now we have described how the QMS is used to know the beam composition of a molecular species, during the degasification process or generally speaking from a gas bottle. Clearly this method can be extended to determine the composition of a plasma. As already described in Sec. 2.1.3, each beamline of FORMOLISM houses a microwave cavity for dissociating molecular gases such as hydrogen, deuterium, nitrogen, or oxygen. The fraction of gas dissociated in the beamline can be measured comparing the molecular signal (D$_2$, H$_2$, N$_2$, or O$_2$) when the microwave discharge is switched on and off. The dissociation fraction is given by

$$\tau_{diss} = \frac{S_{off} - S_{on}}{S_{off}} \qquad (2.8)$$

where S is the signal for a species (for a specific mass) with either dissociation on or off. We obtained with this apparatus, a dissociation fraction of about 70-90% for D$_2$, 60-80% for H$_2$,
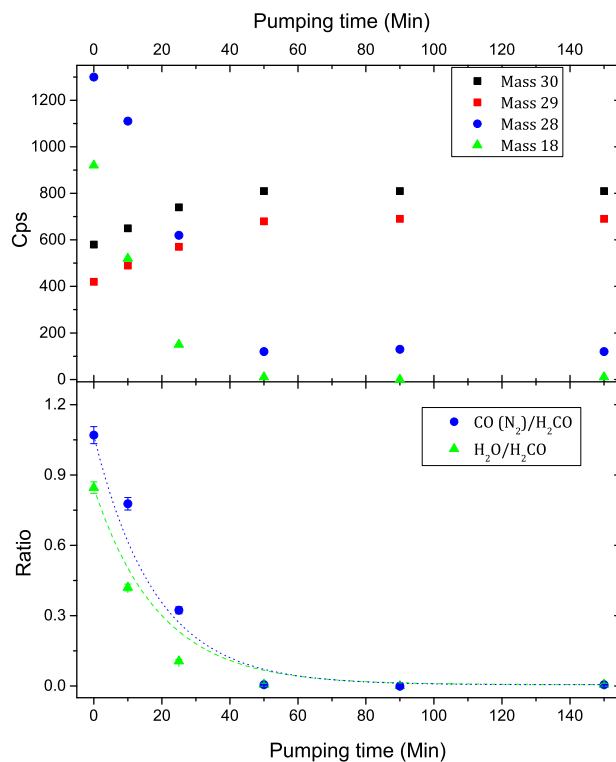
Figure 2.10: Top panel: ion count per second at mass 30, 29, 28, and 18 as a function of pumping time during H_2CO beam preparation. Bottom panel: ratio of CO/H_2CO and H_2O/H_2CO as a function of pumping time.

10-40% for N_2, and 40-80% O_2. Figure 2.11 shows the counts per second of mass 32 (O_2 molecules) and 16 (O atoms), respectively red and black curves, without and with discharge. When the discharge is off the signal at mass 32 is around 5000 cps and mass 16 is almost zero, except for a tiny signal coming from O_2 dissociation itself. On the contrary when the discharge is on mass 32 signal decreases to 1800 cps and mass 16 signal raises to 1200. By using Eq. 2.8, we find in this case a dissociation fraction for O_2 of around 65%.

2.2.2.3   Knowing electronic state of atoms and molecules

The QMS is also used to know the quantum state of the species sent on the substrate. Usually the energy of ionizing electrons is set to 30 eV to have a good ionization cross section and a reduced cracking pattern (which raises in complexity with electrons energy). Nevertheless the electrons energy can be tuned from 0 to 100 eV with a resolution of 0.2 eV. Each molecule has an ionization threshold which depends on the initial quantum state that has to be overcome to detect the species. By tuning the energy of the ionizing electrons of the QMS, we can selectively detect ground state or excited atoms and molecules, as described in *Congiu et al.* (2009). Here we stress that this method can only distinguish between electronic excited states, due to the 0.2 eV resolution; actually the energy difference between two vibrational (rotational) states is of 10^{-1}-10^{-2} (10^{-3}-10^{-4}) eV. Top and bottom panels of Figure 2.12 show, respectively, signals of O/O_2 (Mass16/Mass32) and N/N_2 (Mass14/Mass28) as function of electron energy when the discharge is ON (red curves) and OFF (green curves). In the O/O_2 case (top panels), we see that the Mass 16 signal drops off at around 13.5 eV (green curve is not present because no O atoms are present in the un-dissociated O_2 beam), while Mass 32 signals (red and green curves) fall to zero at 12.1 eV. We can explain these results by looking at the energy of the excited states of O and O_2. Atomic orbital theory predicts that O atoms in the ground state (^3P) are ionized by 13.6 eV electrons (*Moore* 1993) while in the first

Table 2.2: Count per second (Cps) of Masses 30, 29, 28, and 18 are reported as a function of pumping time. These masses correspond respectively to detection of H_2CO (Masses 30 and 29), CO (Mass 28), and H_2O (Mass 18).

	H_2CO		CO	H_2O
Time	Mass 30	Mass 29	Mass 28	Mass 18
(min)	Signal$_{(FlagOff-FlagOn)}$ (cps)			
0	580	420	1300	920
10	650	490	1110	520
25	740	570	620	150
50	810	680	120	10
90	810	690	130	0
150	810	690	120	0
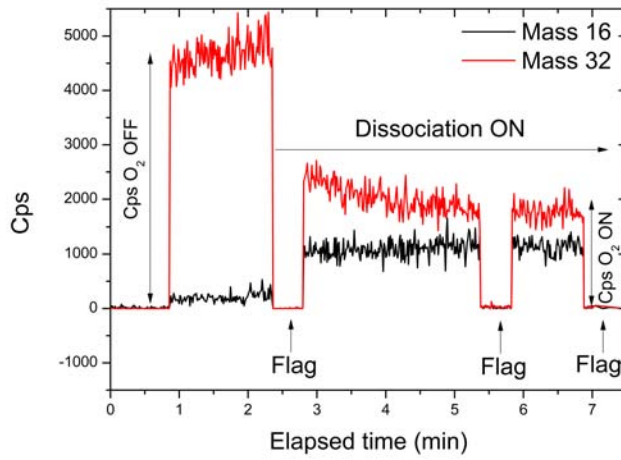
Figure 2.11: Counts per second of O and O_2 as a function of the energy of ionizing electron of the QMS with and without discharge.

excited state ^{1}D the minimum energy necessary for ionization is 11.7 eV (-1.9 eV). Hence, electrons less energetic than 13.6 eV can ionize excited (^{3}P ro-vibrational excited states or ^{1}D electronic excited state) O atoms only. The same argument can be applied to molecular oxygen. O_2 molecule has two low-lying excited singlet states, $O_2(a^1\Delta_g^-)$ and $O_2(b^1\Sigma_g^+)$, while the ground state is the triplet $O_2(X^3\Sigma_g^-)$ state[3]. The energy difference between the lowest energy of O_2 in the singlet state, and the lowest energy in the triplet state is about T_e ($a^1\Delta_g^-$ - $X^3\Sigma_g^-$) = 0.98 eV (Schweitzer&Schmidt 2003). The required energy to ionize an O_2 molecule in the ground state is 12.07 eV (*Tanaka&Tanaka* 1973). This means that electrons less energetic than this value cannot ionize O_2 in the ground state, while $O_2(a^1\Delta_g^-)$ molecules can be ionized by electrons with energy >11.09 eV. Finally electrons with energy below 11.09 eV can ionize $O_2(b^1\Sigma_g^+)$. By considering these argumentations we can go back to the top panels of Figure 2.12 and claim that the beam did not contain O or O_2 in an excited state. The O beam was thus composed of at least 99% ground-state O and O_2. In the case of nitrogen, theory predicts that N atoms in the ground state (^{4}S) are ionized by 14.53 eV electrons (*Moore* 1993) while in the first excited state ^{2}D the minimum energy necessary for ionization is 12.15 eV (-2.38 eV). Hence, electrons in the range 14.53-12.15 eV can ionize excited (^{4}S ro-vibrational excited states or ^{2}D electronic excited state) N atoms only. The ground state of N_2 molecule is the singlet $N_2(X^1\Sigma_g^+)$ state, while the first electronic excited state of N_2 molecule is the triplet states, $N_2(A^3\Sigma_u^+)$ (*Lofthus&Krupenie* 1977). The energy difference between the two states is about T_e ($A^3\Sigma_u^+$ - $X^1\Sigma_g^+$) $\approx$ 6 eV

---

[3]For the sake of completeness and clarity, in Appendix 6.2.2 we explain the meaning of the molecular spectroscopy symbols.
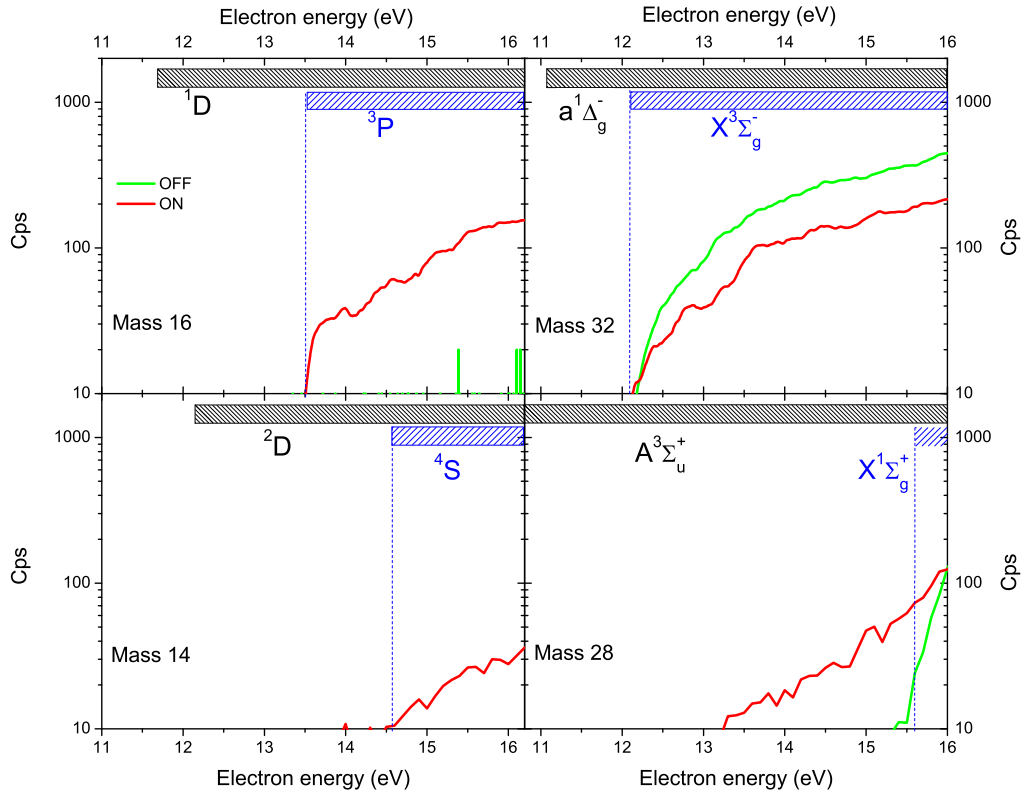
Figure 2.12: Signals at mass 16, 32 (O and O_2), 14, and 28 (N and N_2) when the discharge is ON and OFF (red and green curves respectively) as a function of the energy of ionizing electrons. The pinstriped bars indicate the required energy for ionizing the corresponding quantum state.

(*Friedl&Fantz* 2012). The required energy to ionize an N_2 molecule in the ground state is 15.6 *eV* (*Lofthus&Krupenie* 1977). This means that electrons less energetic than this value cannot ionize N_2 in the ground state, but can ionize $N_2(A^3\Sigma_u^+)$ molecules or ro-vibrational excited $N_2(X^1\Sigma_g^+)$. Bottom panels in Figure 2.12 show that the N_2 beam did not contain N atom in an excited state (green curve is not present because N atoms are not present in the un-dissociated N_2 beam). Similarly N_2 are not excited if the discharge is OFF (green curve), but excited N_2 are present when the discharge is ON.

2.2.2.4   TPD: Temperature Programmed Desorption

In subSec. 1.1.3 we have described the desorption process. We have claimed that two type of desorption can occur: thermal and non-thermal. In thermal desorption the adsorbed species acquires thermal energy to desorb. One of the most important methods to study thermal desorption is the *Temperature Programmed Desorption* (TPD). It consists in observing desorbed molecules from a surface when the surface temperature is increased. During the TPD the sample is heated linearly vs time with a rate β from its initial value T_0

$$T = T_0 + \beta t \tag{2.9}$$

where T is the temperature at time t, T_0 is the starting temperature value and

$$\beta = \frac{dT}{dt} \text{ in the units of K/sec} \tag{2.10}$$

Two examples of temperature ramps are shown in Figure 2.13. The intensity of the desorption signal, *I(T)*, is linked to the rate at which the surface concentration of adsorbed species
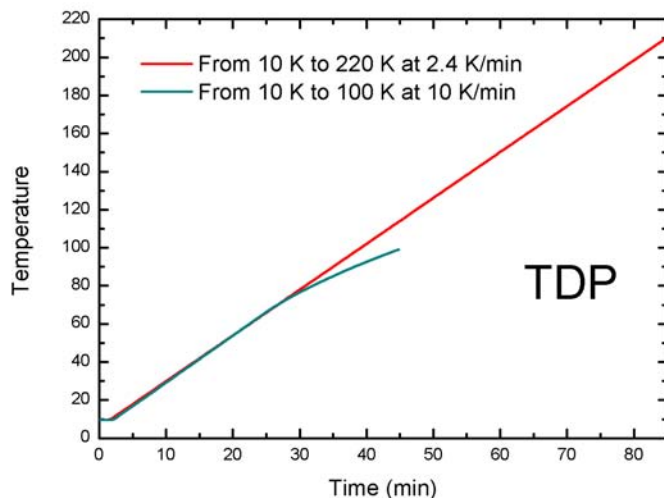
Figure 2.13: Sample temperature ramp as a function of elapsed time during two different TPD experiments; the red one from 10 K to 220 K with a rate of 2.4 K/min, the blue one from 10 K to 100 K with step of 10 K/min. If β is too large, the TPD loses its linearity because the heating capability of the system is not powerful enough.

decreases. This can be expressed as

$$I(T) \propto \frac{d\theta}{dt} = \nu_n \ \theta^n \cdot exp(-\frac{E_b}{k_b T})/\beta \tag{2.11}$$

where θ is the coverage. TPD methods can be understood with the help of the graphical representation shown in Figure 2.14. The expression of the signal intensity consists of three terms: one constant, ν, and two, the surface coverage and the exponential term, dependent on T. At low temperatures, the exponential term (blue curve in the top panel of Figure 2.14) is small; it increases with the temperature and the increase becomes significant when the value of $k_b T$ is equal to E_b. On the other hand, the coverage dependent term (red curve in top panel of Figure 2.14) is initially constant and decreases rapidly as the desorption becomes important and attains the value of zero at the end of the desorption. Bottom panel of Figure 2.14 shows the desorption trace. The description given is very simplistic but it suffices to understand the origin and shape of the desorption trace. Coming back to Eq.1.7, it can be seen that for $n = 0$, the desorption is independent from coverage, as in the case where the desorption comes from several layers of adsorbate. A typical signature of 0th order desorption is the presence of a common leading edge for different coverages and a rapid drop when all the molecules have desorbed. The case of $n = 1$ is called first order desorption, and corresponds to the thermal desorption of molecules already formed on the surface; a distinguishing trait is an asymmetrical desorption peak with the same peak position as a function of coverage. The case of $n = 2$ corresponds to second order desorption, in which the reaction rate is proportional to the product of the concentrations of the reactants. It is observed when the reaction occurs between two adsorbate species that become mobile on the surface during the heating and react with each other before desorbing. In this case, a symmetrical desorption peak shifts towards lower temperatures as the coverage increases. See Figure 2.15 for a comparison among the three cases. The TPD techniques allows the determination of kinetic and thermodynamic parameters of the desorption processes and of chemical reactions, if they occur.

Recently *Kimmel et al.* (2001) and *Amiaud et al.* (2006) used a different approach to explain TPD curves: they resorted to a binding energy distribution of adatoms-surface system. Newly adsorbed molecules are mobile enough to explore the surface and find the
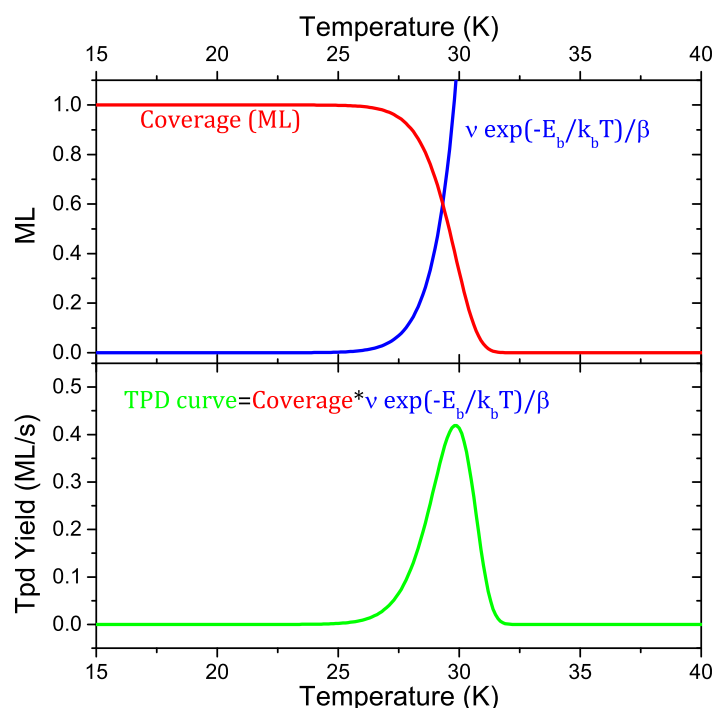
Figure 2.14: Simplified interpretation of a TPD peak. Top panel: variation of the pre-exponential term and exponential term as a function of temperature. Bottom panel: the shared area represents the desorption peak.

strongest bonding sites prior to desorption (*a* panel in Figure 2.16). With the increase in the doses deposited on the surface, the TPD curves gradually broaden towards lower temperatures (*b* and *c* panel in Figure 2.16). As the surface coverage increases, the molecules are adsorbed in less tightly bound adsorption sites, namely, the desorption temperature $T_{des} \propto$ desorption energy E_{des} (with peaks growing in height too). When the leading edge of the TPD curves (*d* panels in Figure 2.16) stops shifting towards lower temperatures, it means that all the adsorption sites on the surface are occupied, and any other incoming molecule is adsorbed on top of the first layer of molecules already adsorbed on the surface. This is when TPDs exhibit a 0th order desorption, the maxima of the desorption peaks increase and start shifting towards higher temperatures with increasing doses. The range of desorption temperatures is the signature of a distribution of binding energies available on the surface. The origin of such an energy distribution is linked to the disordered nature of the surface. As we have shown in this first example of TPDs, the partial pressure of atoms and molecules desorbing from the sample are measured by mass spectrometry. During TPDs, the QMS is placed in front of the sample to maximize the signal. In general, the data obtained from such experiments consist of intensity variations of each recorded mass fragment as a function of time/surface temperature. In the case of a simple reversible adsorption process it may only be necessary to record one signal - that is attributable to the molecular ion of the adsorbate concerned. A typical TPD trace for the desorption of NO from ASW ice at about 50 K is shown in Figure 2.17. To sum up, the following points are worth noting:

1. The area under a peak is proportional to the amount of molecules originally adsorbed, i.e. proportional to the surface coverage.

2. The kinetics of desorption (obtained from the peak profile and the coverage dependence of the desorption characteristics) gives information on the state of aggregation of the adsorbed species.

3. The position of the peak (the peak temperature) is related to the enthalpy of adsorption,
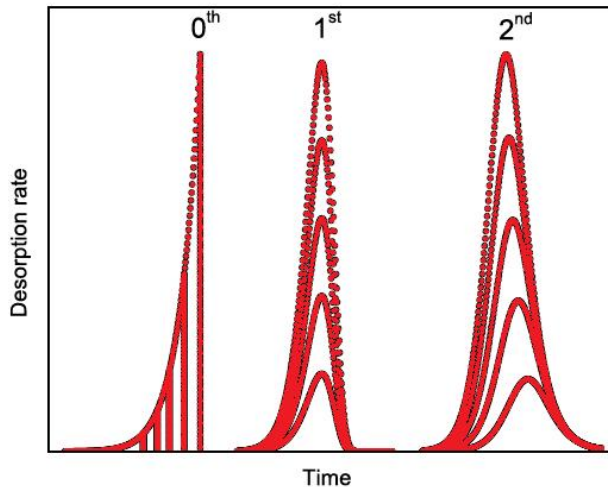
Figure 2.15: Representative thermal desorption curves with varying initial coverage and with parameters ν_n and E_{des}^{PW} held constant.

i.e. to the strength of the binding to the surface.

If there is more than one binding state for a molecule on a given surface (and if these have significantly different adsorption enthalpies) then one will be able to discriminate them by the presence of multiple peaks in the TPD spectrum.

2.2.2.5   DED: During-Exposure Desorption

As described in the previous section mass spectroscopy allows us to study the thermal desorption. In this case the QMS is placed in front of the sample to maximize the signal. We can also monitor the signal during the deposition phase: in this case the QMS is rotated to allow the beam to reach the sample, and at the same time to have a rather good detection. Thus we can study the sticking or one of the non-thermal desorption processes described in Sec. 1.1.3, the chemical desorption[4]. In analogy with acronym TPD, we called this method DED (*During-Exposure Desorption*). Actually, we probe desorption directly and we do not force the desorption as in the TPD's case. In general, DED is useful when the species, arriving from the gas phase or newly formed on the surface, are unable to thermalize on the surface, and they are released into the gas phase. The top panel of Figure 2.18 shows the QMS in the DED configuration; it is placed closed to the surface, with an angle of about 35°. The bottom panel of Figure 2.18 shows an example of measurements. We monitor the mass signal of D_2O (mass 20) during three distinct phases: before exposure, during exposure of D atoms on pre-adsorbed O_2 molecules, after exposure. We observe a direct D_2O signal far above the noise level in the exposure time (between 2 and 5 minutes), indicating that D_2O is chemically desorbed, during the D exposure.

2.2.3   Calibration of the H_2 and D_2 beams

To understand the physical-chemical processes occurring on the surface, it is mandatory to know how many molecules or atoms are aimed on the sample surface per second during exposure. Considering the so-called "fluence" (namely, the total number of particles sent per unit area), our experiments can simulate in a few minutes the chemical-physical reactions happening in thousands of years in an interstellar cloud[5]. To put it quantitative grounds it

---

[4]Chemical desorption will be described extensively in Sec. 4.3 of Chapter 4 (*Dulieu et al.* 2013).
[5]In fact the order of magnitude of the atomic hydrogen flux in a molecular cloud is $\approx 10^5 atoms\ s^{-1}\ cm^{-2}$ (*Li&Goldsmith* 2003) while the D-atoms flux in FORMOLISM set-up is $\approx 10^{13} atoms\ s^{-1}\ cm^{-2}$.
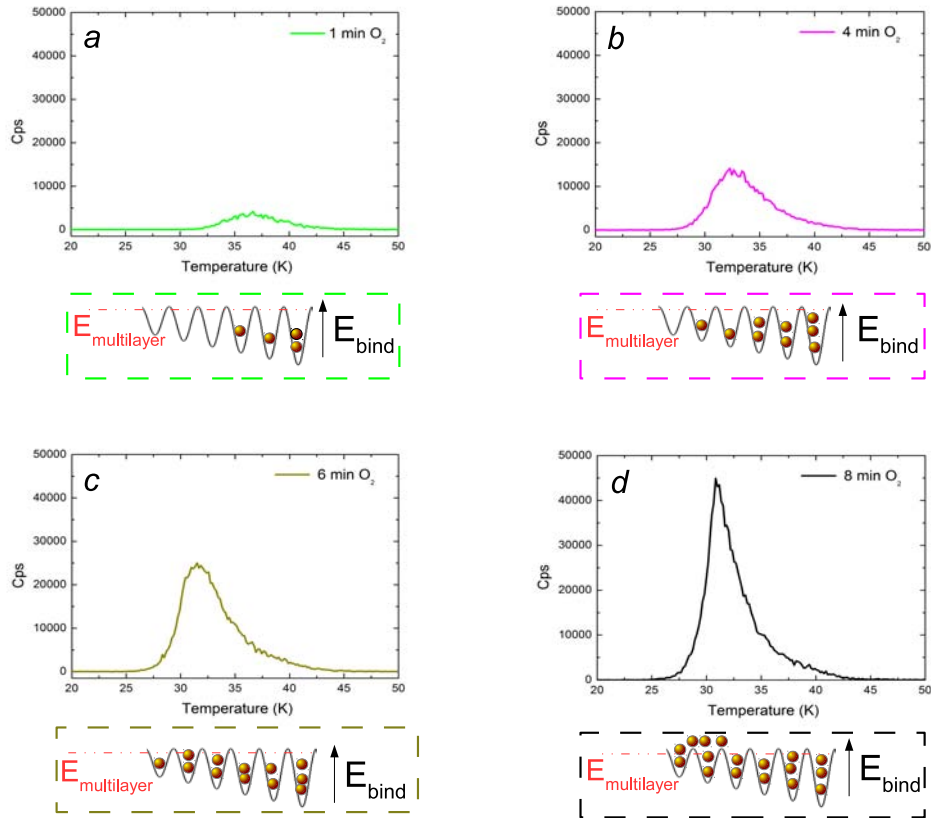
Figure 2.16: TDP curves of O_2 after deposition of different doses (1, 4, 6, and 8 minutes, respectively *a, b, c,* and *d* panels) on ASW ice. A schematic view of the occupied sites is shown for each TPD curve: the deeper the site, the higher its binding energy.

is very important to know as accurately as possible the flux of impinging particles during the irradiation.

In order to estimate the flux of D_2 molecules coming from the beam, the so-called *King and Wells method* has been used. This experimental method, accurately described by *Amiaud et al.* (2007), is generally used to evaluate the sticking coefficient of particles incident on a surface.

The experimental procedure is described hereunder. Initially, a non porous ASW[6] film ($\approx$ 100 ML thick) is grown at 110 K on the copper sample holder. Then, the icy sample is cooled down until 10 K, and irradiated with D_2. Simultaneously, the mass spectrometer detects the indirect D_2 signal in the vacuum chamber in real time (DED). The variation of the D_2 signal with time monitored by the QMS and shown in Figure 2.19, arises from the interaction between deuterium molecules and the icy surface. D_2 exposure begins when the beam is allowed into the main chamber at $t = 0$ s. During the first 125 s, an almost linear decrease of D_2 signal is observed due to the adsorption on the cold surface; then, there is a rising edge that reaches a plateau at $t = 220$ - 230 s: the plateau lasts as long as the surface is irradiated by the beam. Indeed, this region represents the steady state regime, because the number of molecules hitting the surface is equal to the number of molecules escaping from it. The initial decrease of the D_2 signal ($0s < t < 125s$) can be explained as an initial increase in the sticking coefficient of the icy sample. As a consequence of the gradual saturation of the surface after 125 s, the D_2 signal into the chamber begins to increase, thereby stressing that a lower number of molecules are sticking on the compact ice film.

---

[6]Some laboratory experiments (e.g. *Palumbo*, 2006; *Raut et al.*, 2007) seem to indicate the predominant non-porous nature of interstellar ices.
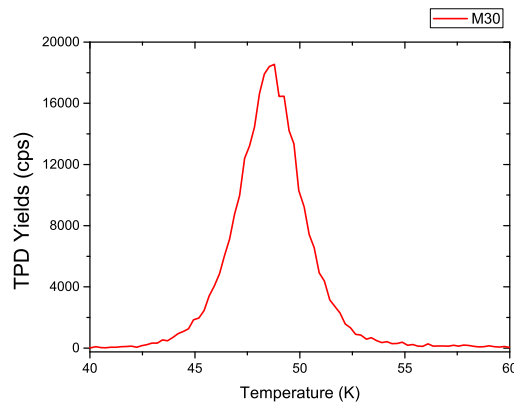
Figure 2.17: Typical TPD trace for the desorption of NO from ASW ice at 50 K

According to the estimation made by *Amiaud et al.* (2007), a compact ice layer begins to saturate after an exposure to 0.45 ML of D_2 (i.e. $0.45 \times 10^{15} mol/cm^2$). Hence, the flux of the D_2 beam is roughly given by

$$\phi_{D_2} = \frac{0.45 \times 10^{15}}{125} \approx 3.6 \times 10^{12} \, mol \, cm^{-2} \, s^{-1} \tag{2.12}$$

Usually rate of molecular dissociation is τ_{diss}=60-80 % are used, so it is possible to evaluate the atomic flux as follows:

$$4.3 \times 10^{12} \, mol \, cm^{-2} \, s^{-1} < \phi_D = 2 \times R_{diss} \times \phi_{D_2} < 5.7 \times 10^{12} \, mol \, cm^{-2} \, s^{-1} \tag{2.13}$$

where the factor 2 in the equation arises from the fact that the cracking of D_2 produces two atoms of D.

2.2.4 Calibration of the molecular beams

The calibration of molecular beams has been partially explained in Sec. 2.2.2.4. The technique used to determine the molecular flux was adapted from *Kimmel et al.* (2001). The molecular flux is calibrated by saturation of the first monolayer of molecules as shown in Figure 2.20 for the case of O_2. The method consists of depositing different amounts of O_2 (or another molecule) - under identical conditions of flux - on the surface maintained at the same temperature (typically T_s= 10 K). In the case of Figure 2.20 molecular oxygen is deposited on a non-porous ASW ice (in this case T_s=15 K). After each deposition the sample is heated up to 55 K and the thermal desorption of O_2 is monitored with the QMS. Afterwards, the temperature of the sample is cooled again to 15 K, and the same procedure is repeated by depositing different amounts of O_2. With the increase in the doses deposited on the surface, the TPD curves gradually broaden towards lower temperatures. In fact, as the surface coverage increases, the molecules are adsorbed in less tightly bound adsorption sites, namely the desorption temperature T_{des} shifts towards lower temperatures because the desorption energy E_{des} decreases (with peaks growing in height too). When the leading edge of the TPD curves stops shifting towards lower temperatures, it means that all the adsorption sites on the surface are occupied, and any other incoming molecule is adsorbed on top of the first layer of molecules already adsorbed on the surface. In this case TPDs exhibit a 0th order desorption, the maxima of the desorption peaks increase and start shifting towards higher temperatures with increasing doses. The unit of coverage we adopt − the monolayer (ML) − is defined as a single layer of atoms or molecules adsorbed on a surface. Similarly to Figure 2.15, Figure 2.20 shows different TPD spectra obtained by increasing the coverage of O_2. The shape of the TPD spectra changes with the coverage and multilayer peaks starts to show up when the coverage exceed 1 ML. In these experiments, the first monolayer was
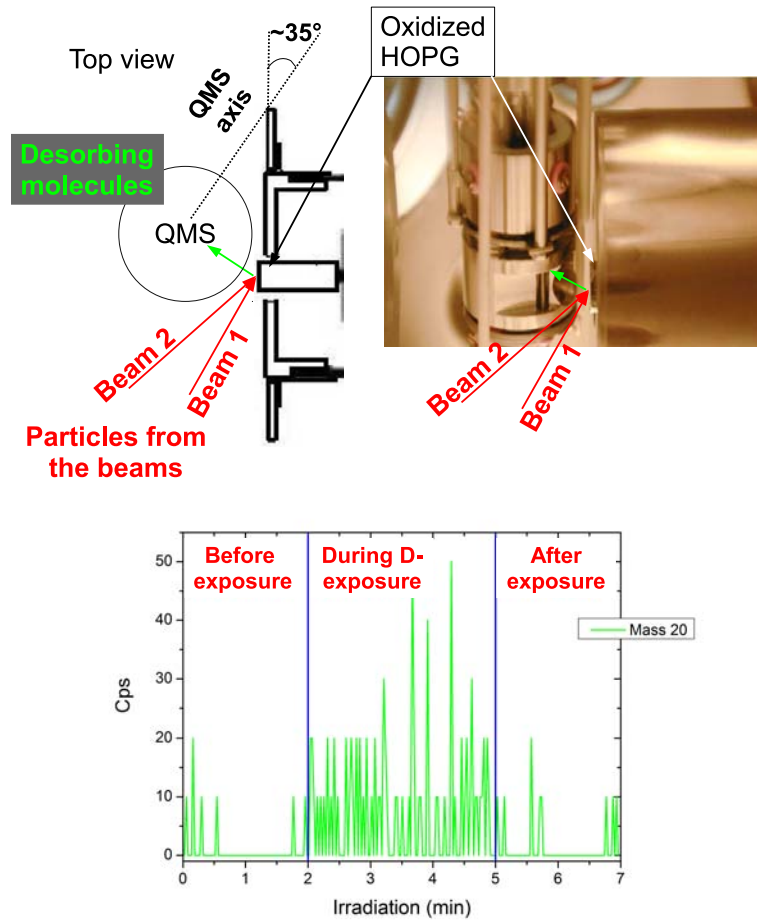
Figure 2.18: Top panel: schematic top-view and photo of DED method. Bottom panel: DED spectra during D-exposure on O_2.

obtained for an exposure time of about 6 minutes and therefore the O_2 flux is

$$\phi_{O_2} = \frac{10^{15}}{360} \approx 2.8 \times 10^{12} \, mol \, cm^{-2} \, s^{-1} \tag{2.14}$$

Here we have shown how O_2 monolayer and flux is determined on non-porous ASW ice; the calibration of other molecular species on other substrates follows substantially the same procedure. A particular case is represented by the O_3 molecule as described in the next section.

2.2.4.1 Determination of O_3 monolayer and detection efficiency

When a beam of O_2 is used, it is easy to calibrate the flux and understand when the saturation of one ML occurs. This is not the case for deposition of O_3. To calibrate one ML of O_3, it is necessary to study and evaluate the cracking pattern and the detection efficiency of ozone by the QMS, with respect to the well known O_2 detection, as described in Sec. 2.2.2.1. The left panel of Figure 2.21 displays the TPD spectra at mass 32 and 48 between 55 K and 90 K after a deposition of 5 minutes of oxygen atoms on silicate. The two traces exhibit the same shape, namely, the mass32/mass48 ratio remains constant (right panel of Fig. 2.21). The two curves are clearly due to the desorption of the same parent molecule (ozone) formed on the substrate. We determined that the mass-32 peak is due to ozone desorption and its fragmentation upon detection. The deposition of ozone from ex-situ synthesis confirms this fact: the amount of desorbing ozone can be monitored either via mass 32 or mass 48. By
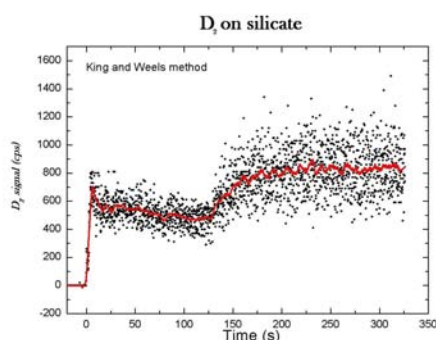
Figure 2.19: Background signal of molecular deuterium detected in the chamber by the mass spectrometer during the D_2-atoms exposure of compact water ice. The D_2 signal is used for the calibration of the molecular beam
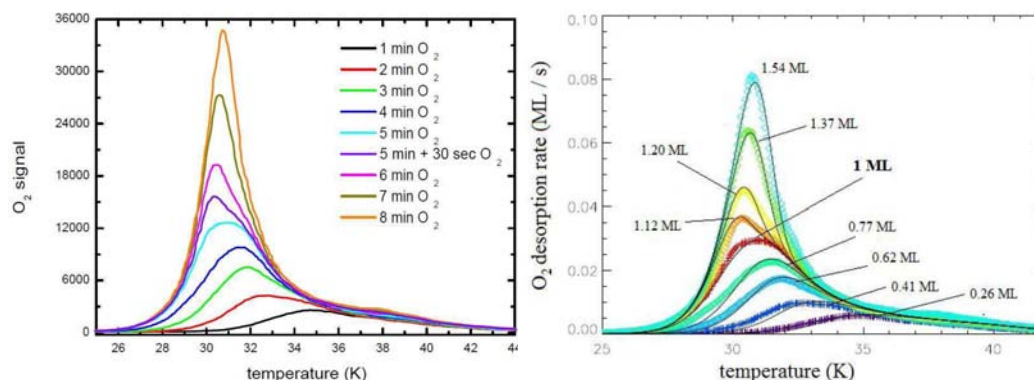
Figure 2.20: **(a)** Temperature programmed desorption spectra of O_2 from compact non porous ASW. The different O_2 exposures are displayed in the figure. **(b)** Simulated TPD spectra are over-plotted on the experimental curves.

computing the ratio between the two signals (mass32/mass48) after deposition of different doses, as shown in Figure 2.21 (right panel), a mean value of 1.5 was found. This fact led us to monitor ozone by the signal at mass 32, instead of that at mass 48, to have a better signal-to-noise ratio. We note here that this point explains the difference between conclusions of *Jing et al.* (2012) and *Minissale et al.* (2014).

Due to its important dissociative ionization, the ozone detection efficiency has to be determined for every single QMS. Actually, the results of the present work has been obtained during two periods of experiments, when two different QMSs were used. Even thought the settings of the two instruments were, at any time, exactly the same, the O_3/O_2 detection efficiencies found were different up to a factor of 30%. However, all the experimental values presented here were obtained with a constant O_3/O_2 detection efficiency. It should also be noted that, for this specific molecule (O_3), any other correction factor among those present in the literature would have be wrong in our case. To estimate the O_3/O_2 detection efficiency at mass 32, it is necessary to compare the area under the TPD curve of one ML of O_2 and that of one monolayer of O_3. Therefore, we also needed to determine for what O-exposure time we reached a complete monolayer of ozone. To calibrate the ozone monolayer, we adopted the same first layer-saturation method used for O_2. To do so, we gradually increased the amount of ozone formed on the surface (via $O+O_2$ reaction), until the second-layer desorption peak appeared. In fact, the second-layer desorption peak is a clear signature that the first monolayer has been completed and that a new layer is being grown. In Figure 2.22, we show four TPD curves of ozone obtained by increasing the exposure time of oxygen atoms (6, 8, 10, and 12 minutes). The saturation of the first layer corresponds to the red trace (squares),
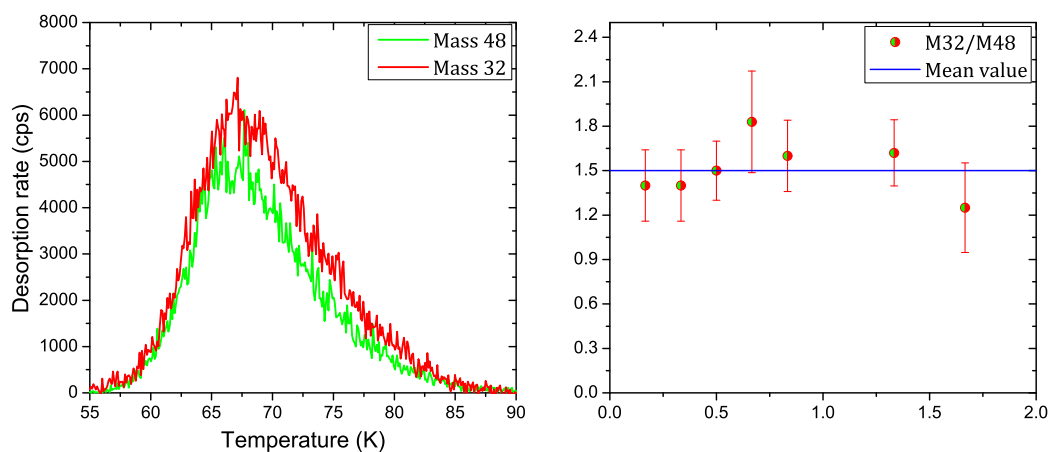
Figure 2.21: Adapted from *Minissale et al.* 2014a. *Left panel:* Ozone TPD curves at mass 32 and 48 between 55 and 90 K after deposition of 5 minutes of oxygen atoms on silicate held at 10 K. *Right panel:* Ratio of the integrated area of mass 32 and mass 48 TPD peaks (55-90 K) as a function of different doses of oxygen atoms.
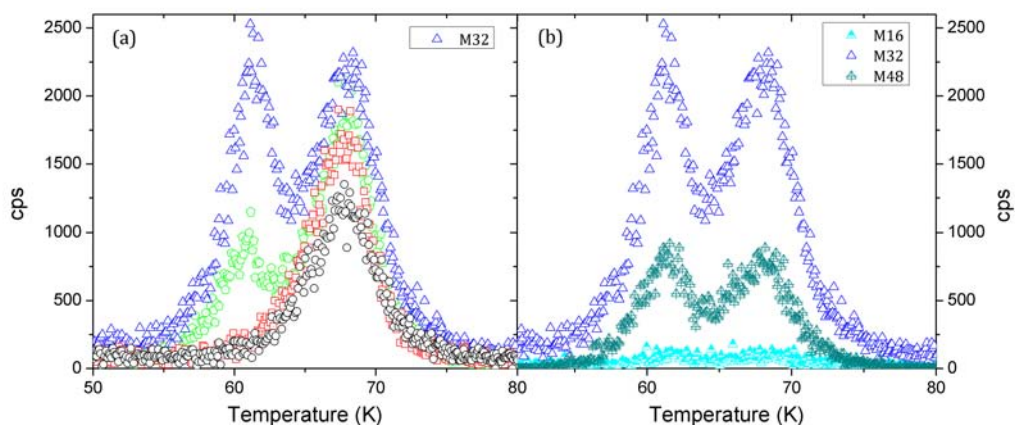
Figure 2.22: Adapted from *Minissale et al.* (2014a). Panel *a*: ozone TPD traces (at mass 32) between 50 and 90 K after four depositions of 6, 8, 10, and 12 minutes of oxygen atoms on silicate held at 10 K (Circles, squares, pentagons, and triangles respectively). Panel *b*: ozone TPD traces at mass 16, 32, and 48 between 50 and 90 K after deposition of 12 minutes of oxygen atoms on silicate held at 10 K.

and the appearance of the second peak is observed in green (pentagons). The apparent inconsistency between the TPD peak intensity in Figure 2.21 (left panel) and Figure 2.22 is due to different QMS settings. Still, we cannot be certain that the adsorption site densities for ozone and molecular oxygen are the same. If this hypothesis is true, we can finally derive the total detection efficiency (ef), by comparing the O_2 and O_3 monolayer. By applying the derived ef factor, we should find that the number of O atoms desorbed as O_2 and O_3 are equal to the number of O atoms exposed

$$O(sent) = O(TPDO_2) + ef \times O(TPDO_3).$$

In the case of efficient chemical desorption, the condition will be the following

$$O(sent) < O(TPDO_2) + ef \times O(TPDO_3).$$

This subject will be treated in Sec. 4.1.2 and 4.3.

2.2.5   Can reactions occur on gas phase?

In this section we show that all the reactions we study in our experiments are solid-state reaction and they cannot occur on the gas phase. *Minissale et al.* (2013b) shows that the order of deposition of the species changes the amount of reactants consumed and products formed. In this article we study the NO_2 formation via $NO+O_2$ reaction. Three cases are considered:

a NO deposited on pre-adsorbed O_2;

b NO and O_2 co-deposited;

c O_2 deposited on pre-adsorbed NO;

Without going into the details of the reaction (it will be treated extensively in Chapter 5), in all the cases we see NO_2 formation. In particular $NO_2(a)>NO_2(b)>NO_2(c)$. We should expect that $NO_2(b)>NO_2(a)\approx NO_2(c)$ if the reactions occur in the gas-phase. Moreover the relation $NO_2(a)>>NO_2(c)$ shows that the order of deposition of species and, as consequence, the surface chemistry play the main role in the consumption and formation of species.

Beyond this practical example, we know that in our experiments:

$$Flux_{mol} < 10^{13} \; \frac{mol}{cm^2 \, s}$$

and

$$v_{mol} = 5 \times 10^4 \; cm/s$$

so the density is

$$n_{mol} = \frac{Flux_{mol}}{v_{mol}} = 2 \times 10^8 \, mol/cm^3$$

The mean free path λ will be

$$\lambda_{mol} = \frac{k_b \, T}{\sqrt{2\pi} \, d^2 \, P} = \frac{1}{\sqrt{2\pi} \, d^2 \, n} \approx 10^5 \, cm = 1 \, km$$

where d is the diameter of molecules. The mean free path is 6 order of magnitude larger than the zone of beams interaction (few mm). Moreover interaction of beam molecules with residual gas of the main chambers can be neglected due to UHV conditions (pressure of 10^{-10} mbar). To sum up, we can exclude gas phase reactions in our experimental conditions.

Bibliography

2.01 Accolla, M. *Experimental Investigation on the Morphology of Interstellar Ice Analogues*, PhD thesis, University of Catania and University of Cergy-Pontoise (2010)

2.02 Amiaud, L., Fillion, J. H., Baouche, S., Dulieu, F., Momeni, A., and Lemaire, J. L., *Interaction of D_2 with H_2O amorphous ice studied by temperature-programed desorption experiments*, The Journal of Chemical Physics, Volume 124, Issue 9, pp. 094702-094702-9 (2006)

2.03 Amiaud, L., Dulieu, F., Fillion, J.-H., Momeni, A., and Lemaire, J. L., *Interaction of atomic and molecular deuterium with a nonporous amorphous water ice surface between 8 and 30 K*, The Journal of Chemical Physics, Volume 127, Issue 14, pp. 144709-144709-12 (2007)

2.04 Congiu, E., Matar, E., Kristensen, L. E., Dulieu, F., and Lemaire, J. L., *Laboratory evidence for the non-detection of excited nascent H_2 in dark clouds*, Monthly Notices of the Royal Astronomical Society: Letters, Volume 397, Issue 1, pp. L96-L100 (2009)

2.05 Djouadi, Z., D'Hendecourt, L., Leroux, H., Jones, A. P., Borg, J., Deboffle, D., and Chauvin, N., *First determination of the (re)crystallization activation energy of an irradiated olivine-type silicate* Astronomy and Astrophysics, Volume 440, Issue 1, pp. 179-184 (2005)

2.06 Dulieu, F., Congiu, E., Noble, J., Baouche, S., Chaabouni, H.,Moudens, A., Minissale, M., and Cazaux, S., *How micron-sized dust particles determine the chemistry of our Universe*, Nature Scientific Reports, Volume 3, id. 1338 (2013)

2.07 Friedl, R., and Fantz, U., *Spectral intensity of the N2 emission in argon low-pressure arc discharges for lighting purposes*, New Journal of Physics, Volume 14, pp. 043016-0430138 (2012)

2.08 Kimmel, J., Engelke, F., and Zare, R. N., *Novel method for the production of finely spaced Bradbury-Nielson gates* Review of Scientific Instruments, Volume 72, Issue 12, pp. 4354-4357 (2001)

2.09 Jing, D., He, J., Brucato, J. R., Vidali, G., Tozzetti, L., and De Sio, A., *Formation of Molecular Oxygen and Ozone on Amorphous Silicates*, The Astrophysical Journal, Volume 756, Issue 1, article id. 98, 7 pp. (2012)

2.10 Li, D., and Goldsmith, P. F. *H I Narrow Self-Absorption in Dark Clouds*, The Astrophysical Journal, Volume 585, Issue 2, pp. 823-839 (2003)

2.11 Lofthus, A., and Krupenie, P. H., *The spectrum of molecular nitrogen*, Journal of Physical and Chemical Reference Data, Volume 6, Issue 1, pp. 113-307 (1977)

2.12 Minissale, M., Congiu, E., Manicò, G., Pirronello, V., and Dulieu, F., *CO_2 formation on interstellar dust grains: a detailed study of the barrier of the CO+O channel*, Astronomy and Astrophysics, Volume 559, pp. A49-57 (2013a)

2.13 Minissale, M., Congiu, E., Baouche, S., Chaabouni, H., Moudens, A., Dulieu, F., Manicò, G., and Pirronello, V. *Formation of nitrogen oxides via NO + O_2 gas-solid reaction on cold surfaces*, Chemical Physics Letters, Volume 565, pp. 52-55 (2013b)

2.14 Minissale, M., Congiu, E., and Dulieu, F., *Oxygen diffusion and reactivity at low temperature on bare amorphous olivine-type silicate*, The Journal of Chemical Physics, Volume 140, p. 074705 (2014)

2.15 Mokrane, H., Chaabouni, H., Accolla, M., Congiu, E., Dulieu, F.,Chehrouri, M., and J. L. Lemaire, *Experimental Evidence for Water Formation Via Ozone Hydrogenation on Dust Grains at 10 K*, The Astrophysical Journal, Volume 705, pp. L195-199 (2009)

2.16 Moore, C. E., *Tables of Spectra of Hydrogen, Carbon, Nitrogen, Oxygen*, edited by J. W. Gallagher, CRC Press, Inc., Boca Raton (1993)

2.17 Palumbo, M. E., *Formation of compact solid water after ion irradiation at 15 K* Astronomy and Astrophysics, Volume 453, Issue 3, pp. 903-909 (2006)

2.18 Pirronello, V., Liu, C., Shen, L., Vidali, G., *Laboratory Synthesis of Molecular Hydrogen on Surfaces of Astrophysical Interest*, The Astrophysical Journal, Volume 475, Issue 1, pp. L69-L72 (1997)

2.19 Raut, U., Famá, M., Teolis, B. D., and Baragiola, R. A., *Characterization of porosity in vapor-deposited amorphous solid water from methane adsorption*, The Journal of Chemical Physics, Volume 127, Issue 20, pp. 204713-204713-6 (2007)

2.20 Richardson, E. G., *Two hot-wire viscometers*, Journal of Scientific Instruments, Volume 6, Issue 11, pp. 337-343 (1929)

2.21 Schweitzer, C., and Schmidt, R., *Physical mechanisms of generation and deactivation of singlet oxygen*, Chemical Review, Volume 103, p. 1685 (2003)

2.22 Tanaka, K. and Tanaka, I., *Photoelectron spectra from some autoionizing state of O_2 near the ionization threshold*, The Journal of Chemical Physiscs, Volume 59, p. 5042 (1973)

3

Model

This chapter presents the model used to explain and describe our experimental results. It is subdivided as follows:

1. Model

   1.1. Initial conditions

   1.2. Flux: ϕ_x

   1.3. Reaction probability: r

   1.4. Diffusion coefficient: k_{diff}

   1.5. Desorption coefficient: $\alpha_{N_x des}$

2. From model parameters to physical-chemical quantities

   2.1. Reactivity: reaction probability and activation barrier

   2.2. Mobility: k_{diff} and surface migration

   2.3. Desorption: desorption probability and binding energy

3.1 Model

In this section, we present the model used to simulate our experiments. The goal of the model is to understand which processes (physical or chemical) occur on the surface by fitting the experimental data.

This model was inspired by the one presented in *Katz et al.* (1999); we used rate equations (i.e., differential equations) to describe the temporal evolution of a system. The physical chemistry on cold surfaces is modeled by using a rate equation for each state of the system, namely the atomic or molecular species deposited on the surface and the ones formed. Among the processes described in Sec. 1.1 and 1.3, we are interested mainly in diffusion and reactivity (activation barrier for reaction) of the species. Other parameters, i.e., desorption energy of

molecules, are modeled independently as shown in *Amiaud et al.* (2007) and *Noble et al.* (2011), and they are not used as a free parameter in this model.

To describe the model, we consider a very simple case, hereafter called *model 1*. We suppose that a species, called N_1, is deposited on a surface; N_1 can diffuse on the surface and react with another N_1 to form N_2

$$N_1 + N_1 \rightarrow N_2. \tag{3.1}$$

We suppose that N_2 is fomed only on the surface, that is an inert species and it cannot react either with N_1 or another N_2. To simulate this condition we will use a set of two rate equations, one for N_1

$$\frac{dN_1}{dt} = \phi_1 - 2\,r_{ER}\,\phi_1\,N_1 - 4\,r_{LH}\,k_{diff}\,N_1^2 - \alpha_{N_1 des}\,N_1 \tag{3.2}$$

and, similarly, one equation for N_2

$$\frac{dN_2}{dt} = \phi_2 + r_{ER}\,\phi_1\,N_1 + 2\,r_{LH}\,k_{diff}\,N_1^2 - \alpha_{N_2 des}\,N_2 \tag{3.3}$$

On the left side of the equations we find the evolution over the time of the surface population of each species. Here, we stress that N_x is an dimensional less term, and it indicates the fraction of surface covered by the species x. Figure 3.1 shows four different cases: two in which the surface is covered with N_1 or N_2 and another two in which both the species are on the surface in different ratios. N_x can be multiplied by the surface density of adsorption sites of the considered surface to move from an dimensional less to a dimensional quantity; in example, if a surface contains 10^{15} sites per cm^2, a value for N_x of 0.5 means that 5×10^{14} molecules per cm^2 are present on the surface. The surface population of each species varies depending
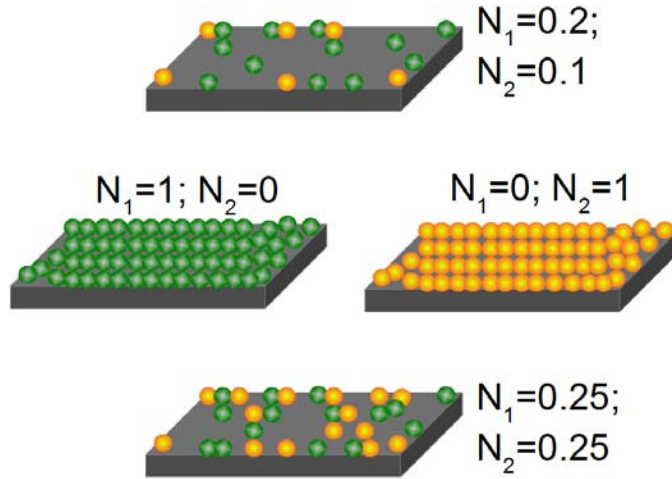
Figure 3.1

on the terms of the right side of Eq. 3.2 and 3.3, where we find positive terms, i.e., accretion from the gas phase (ϕ_x) or formation of new species ($r_{ER}\,\phi_1\,N_1 + r_{LH}\,k_{diff}\,N_1^2$), and negative terms, i.e., consumption of the reactive species ($-2\,r_{ER}\,\phi_1\,N_1 - 4\,r_{LH}\,k_{diff}\,N_1^2$), or desorption into the gas phase ($\alpha_{N_x des}\,N_x$). Clearly, each of these terms will depend in a different way on the surface density:

1. *Accretion from the gas phase*; this term is independent, or almost independent, on surface population. It is governed by ϕ_x (in s^{-1}) that represents the fraction of surface covered each second by the incoming species. It is obtained by normalizing the flux

(described in subSec.s 2.2.4 and 2.2.3) with respect to the site density of the surface. ϕ_x is an experimental parameter because can be tuned experimentally and it is a constant parameter in the model. ϕ_x fulfils the following conservation law

$$N_x(tf) = \int_0^{tf} \frac{dN_x}{dt} = \int_0^{tf} \phi_x = 1 \tag{3.4}$$

where N_x is a inert species and *tf* is the time to cover all the surface with N_x.

2. *Molecular formation (and consumption)*; this term depends strongly on the surface population of reactants. A reaction should consume more than one reactant, and the stoichiometric number accounts for this number, defined as positive for the products (molecular formation) and negative for the reactants (molecular consumption). Molecular formation (and consumption) is governed by the r_{ER} if the reaction occurs via ER mechanism and by $r_{LH} \, k_{diff}$ if the reaction occurs via the LH mechanism. r_{ER} and r_{LH} are the reaction probabilities ranging between 0 and 1; k_{diff} (in s^{-1}) is the diffusion coefficient and represents the fraction of surface scanned per second by a particle. By dividing by the density of the sites we can find the diffusion coefficient in the usual units, i.e., cm^{2}s^{-1}.

3. *Desorption into gas phase*; this term depends on the surface population of the reactants. The desorption into the gas phase is governed by $\alpha_{N_x des}$ that is the rate constant for desorption. It is called additional parameter because it is obtained by using different models (see Amiaud et al 2007 and Noble et al 2011) and it is a constant in the model.

By rewriting Eq.3.2

$$\frac{dN_1}{dt} = \underbrace{\phi_1}_{\substack{\text{experimental}\\\text{parameter}}} -2 \underbrace{r_{ER}}_{\substack{\text{model}\\\text{parameter}}} \phi_1 \, N_1 - 4\underbrace{r_{LH} \, k_{diff}}_{\substack{\text{model}\\\text{parameters}}} N_1^2 - \underbrace{\alpha_{N_1 des}}_{\substack{\text{additional}\\\text{parameter}}} N_1 \tag{3.5}$$

we note that the parameters of the model are essentially three: r_{ER}, r_{LH}, and k_{diff}. Through a fine-tuning of these parameters, the solution of Eq.3.2 has to converge to the following final condition

$$N_1(tf) = N_1 \text{ (amount measured in the experiments)}, \tag{3.6}$$

starting from the initial conditions of our experiments

$$N_1(0) = \text{experimental conditions at t=0.} \tag{3.7}$$

This point will be discussed in Sec. 3.1.2. Below we recap the key points of the model:

- dN$_1$/dt is the variation of the surface population of N$_1$; it depends on the terms on the right side as well as on its initial conditions (see Sec. 3.1.1).

- ϕ_x represents the flux of the particles accreting from the gas phase. It induces an increase of surface population (see Sec. 3.1.2).

- r$_{ER}$ and r$_{LH}$ represents the reaction probabilities of ER and LH, respectively; they are two of the free parameters. The role of the reaction probability is discussed in Sec. 3.1.3.

- k$_{diff}$ represents the diffusion coefficient. It is the third free parameter of the model and its role is discussed in Sec. 3.1.4.

- $\alpha_{N_x des}$ represents the desorption coefficient. It is an additional parameter and it is tuned using different models as discussed in Sec. 3.1.5.

3.1.1 Initial condition

To simulate the physical-chemical conditions present in our experiments, we can play with the initial conditions of the differential equations. Some experiments are performed by sending a species, i.e. N_1, on the top of another pre-adsorbed species, i.e. N_2. The experimental initial conditions, and as a consequence the model initial conditions, can lead to very different results, depending on the reactivity of the species. A practical application on this point is discussed in Sec. 5.2.1. The upper part of Figure 3.2 shows three different initial conditions:

a $N_1(0)=0$ and $N_2(0)=0$ (Nothing on the surface);

b $N_1(0)=1$ and $N_2(0)=0$ (Surface entirely covered with N_1);

c $N_1(0)=0$ and $N_2(0)=0.5$ (Half of the surface covered with N_2).
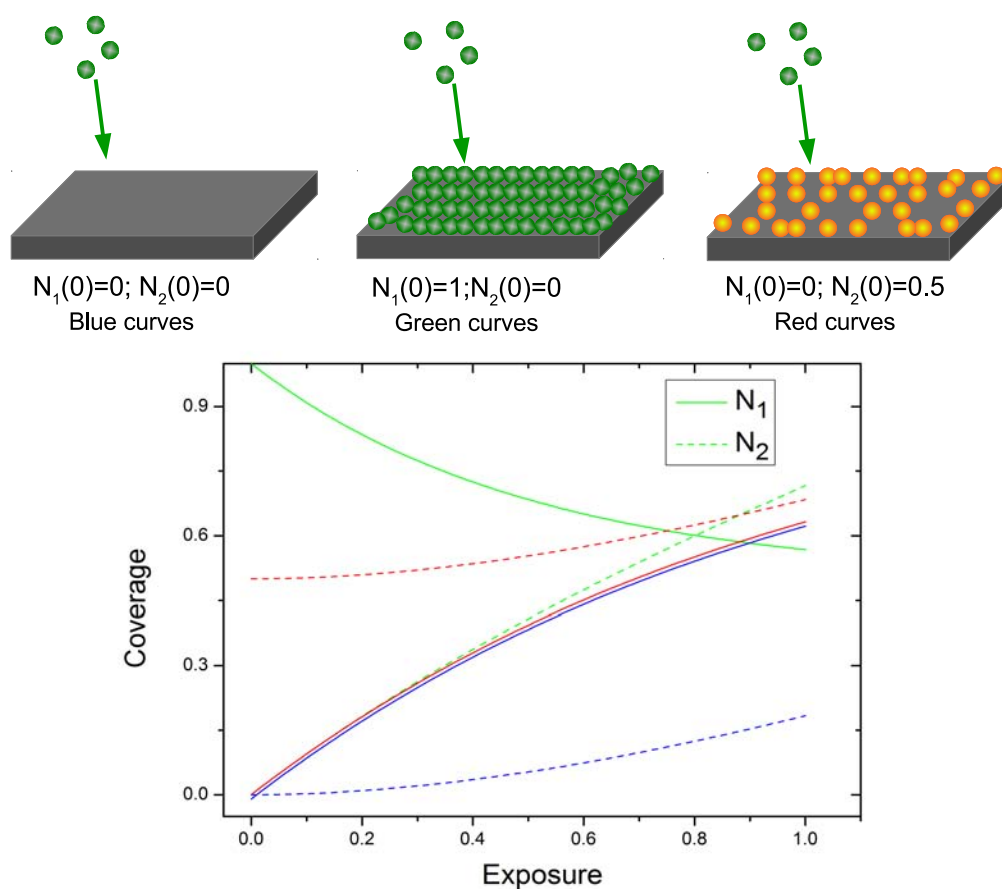
Figure 3.2: Schematic view of the initial coverages and results of *model 1* for three different initial conditions: blue curves, $N_1(0)=0$ and $N_2(0)=0$; green curves, $N_1(0)=1$ and $N_2(0)=0$; red curves, $N_1(0)=0$ and $N_2(0)=0.5$. The plot shows the surface populations of N_1 (solid lines) and N_2 (dashed lines) as a function of N_1 exposure. All other parameters are fixed, see text. The blue and red solid curves are identical and they have been offset in the figure for the sake of clarity.

The plot of Figure 3.2 shows the results obtained using *model 1* for three different initial conditions. The surface population (the coverage) evolution of the species is plotted as a function of N_1 exposure. Both exposure and coverage are dimensionless quantities, and they vary between 0 and 1. This value corresponds to the fraction of the surface covered with the species coming from the gas phase. In order to give a dimension (namely MonoLayer) to both exposure and coverage, the fraction of the surface covered has to be multiplied by the surface density of the sites. In the lower part of Figure 3.2, N_1 and N_2 coverages are

represented with solid and dashed lines respectively. In the model, all the parameters (fluxes, reaction probability, diffusion coefficients, and desorption rates) are fixed. In particular, N_1 flux is 1, N_2 flux is 0, the reaction probabilities are 0.5, the diffusion desorption coefficients are 0. In this case the reactions can occur only via ER; as discussed before, the non-mobility of reaction partners is a limiting factor for the LH mechanism.

The first set of initial conditions simulates an experiment in which species are sent onto a bare surface; the second and third ones simulate experiments in which species are sent on a surface entirely or partially covered with N_1 and N_2 layers, respectively. We note in Figure 3.2 that the N_1 curves for the first and the third set of initial conditions are identical (they have been offset in the figure for the sake of clarity). Actually, the difference of N_2 initial conditions does not affect the surface-population evolution of N_1. The N_2 initial conditions cause a shift for N_2 population (blue and red dashed lines). On the other hand, N_1 initial conditions strongly affect the evolution of N_1 and N_2 surface population. In fact the presence of a pre-deposited N_1, due to ER mechanism, favors a quick N_2 formation (dashed green line) and N_1 consumption (solid green line). In conclusion the initial conditions allow to simulate experiments in which

a species are sent onto a bare (or non-reactive) surface or

b species are sent on the top of a pre-adsorbed species.

3.1.2 Flux: ϕ_x

Similarly to the initial conditions of the differential equations, we can vary the incoming fluxes of the species, the so called experimental parameter. The upper part of Figure 3.3 shows three different examples of fluxes:

1. $\Phi(N_1(t))=1$ and $\Phi(N_2(t))=0$;

2. $\Phi(N_1(t))=0.5$ and $\Phi(N_2(t))=0.5$ (co-deposition experiment);

3. $\Phi(N_1(t))=0$ and $\Phi(N_2(t))=1$.

We stress here that the fluxes of the species are constant in our experiments and for this reason we keep Φ_x constant in the model. The first set of fluxes simulates an experiment in which only N_1 arrives from the gas phase and N_2 is only formed on the surface. The second set of fluxes simulates an experiment in which both N_1 and N_2 arrive from the gas phase, the species are co-deposited using the two beamlines (see Sec. 2.1.2). Finally, the third set of fluxes simulates an experiment in which only N_2 arrives from the gas phase. The lower part of Figure 3.3 shows the results obtained using *model 1* for the three cases. The surface-population evolution of the species is plotted as a function of the exposure of N_1 and/or of N_2 (sent on the surface). N_1 and N_2 are represented with solid and dashed lines respectively. In the model, all other parameters (initial conditions, reaction probability, diffusion and desorption coefficients) are fixed. In particular, $N_1(0) = 0, N_2(0) = 0$, the reaction probability is 0.5, the diffusion and desorption coefficients are 0. The flux change allows to simulate experiments in which

1. species are co-deposited on the surface or

2. species are subsequently deposited on the surface;

3. the flux changes in a set of experiments.

We remark that we keep the flux constant since in our experiments Φ_x does not vary except for a few %. There is nothing, of course, that prevents anyone from using a time dependent flux provided that the conservation law (Eq.3.4) is satisfied.
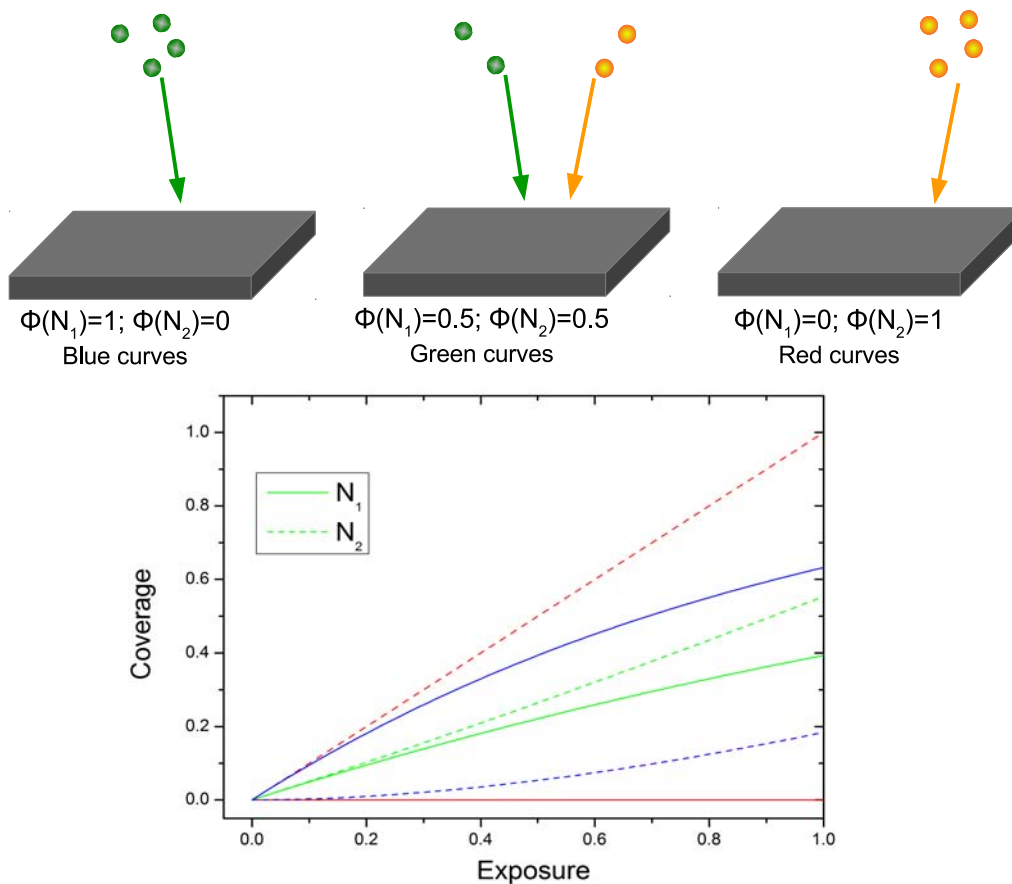
Figure 3.3: Schematic view of the incoming fluxes of species and results of *model 1* for three different types of fluxes: blue curves $\Phi(N_1(t))=1$ and $\Phi(N_2(t))=0$; green curves $\Phi(N_1(t))=0.5$ and $\Phi(N_2(t))=0.5$; red curves $\Phi(N_1(t))=0$ and $\Phi(N_2(t))=1$. The surface populations of N_1 (solid lines) and N_2 (dashed lines) are plotted as a function of the N_1+N_2 exposure. All other parameters are fixed, see text.

3.1.3 Reaction probability: r

The most important parameter describing the chemistry of a system in our model is the reaction probability. It indicates if a reaction can occur on the surface. It ranges between 0 and 1. In Sec. 3.2, we will explain how this parameter is linked to the energetic parameter, namely the activation energy to overcome the reaction barrier. In the model, we usually distinguish between ER and LH reaction probabilities. For the sake of simplicity, we set here $k_{diff}=0$ s^{-1}, and LH has not influence on model results. In this way, we can show how a change in the reaction probability (in this case r_{ER}) affects the model results.

Figure 3.4 shows the results obtained using *model 1* for five different values of r_{ER}: 0, 0.1, 0.2, 0.5, and 1. The surface population of N_1 and N_2 is plotted as a function of the N_1 exposure. N_1 and N_2 are represented with solid and dashed lines, respectively. In the model, all other parameters (initial conditions, fluxes, diffusion desorption coefficients) are fixed. In particular, $N_1(0) = 0, N_2(0) = 0$, $\Phi(N_1) = 1, \Phi(N_2) = 0$, the diffusion and desorption coefficients are 0 s^{-1}.

The case $r_{ER}=0$ is a trivial case: N_2 formation has a probability equal to zero and its surface population is zero at anytime; the only process that can occur is the adsorption of N_1 and its surface population increases linearly. On the contrary, a value of 1 for r_{ER} means that whenever a N_1 meets another N_1, a N_2 is formed. N_2 formation depends on the surface population of N_1; in fact, the probability for a N_1 to find another N_1 increases as a function of coverage. This means that N_1 (and N_2) is consumed (and formed) more rapidly at high
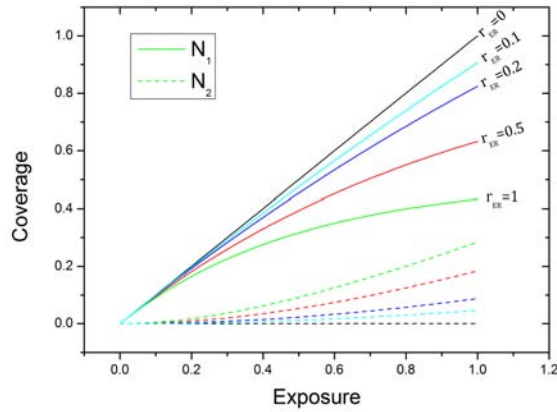
Figure 3.4: Results of *model 1* for five different values of r_{ER}: 0, 0.1, 0.2, 0.5, and 1. The surface populations of N_1 (solid lines) and N_2 (dashed lines) are plotted as a function of the N_1 exposure. All other parameters are fixed, see text.

coverage, i.e. green curves in Figure 3.4.

3.1.4 Diffusion coefficient: k_{diff}

k_{diff} is the parameter describing the mobility of the species on the surface. We remind that k_{diff} represents the fraction of surface scanned each second by a particle. We can find the diffusion coefficient into the usual units, $cm^2 s^{-1}$, by dividing for the density of sites. The mobility helps the meeting of species and, as a consequence, it increases the reaction rate. The mobility is strictly connected to the LH mechanism, and it is the main limiting step for this mechanism if $r_{LH} \neq 0$. For example, a $k_{diff}=0$ s^{-1} totally hinders LH. Figure 3.5
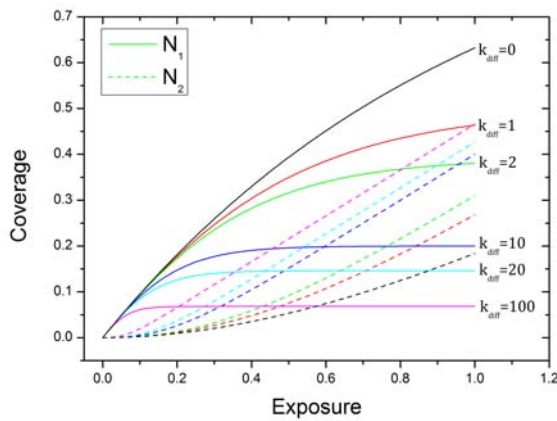
Figure 3.5: Results of *model 1* for six different values of k_{diff}: 0, 1, 2, 10, 20, and 100 s^{-1}. The surface populations of N_1 (solid lines) and N_2 (dashed lines) are plotted as a function of the N_1 exposure. All other parameters are fixed, see text.

shows the results obtained using *model 1* for six different values of k_{diff}: 0, 1, 2, 10, 20, and 100 s^{-1}. As usual, the surface populations of N_1 and N_2 is plotted as a function of the N_1 exposure. N_1 and N_2 are represented with solid and dashed lines respectively. In the model, all other parameters (initial conditions, fluxes, reaction probabilities, and desorption rates) are fixed. In particular, $N_1(0) = 0$, $N_2(0) = 0$, $\Phi(N_1) = 1$, $\Phi(N_2) = 0$, $r_{ER,LH} = 0.5$, and the desorption coefficients are 0.

We stress that only N_1 can be mobile, while k_{diff} is always zero for N_2. We note that $k_{diff} \neq 0 s^{-1}$ for N_2 would not produce any difference in the results, since N_2 is an inert species. The results of Figure 3.5 could be summarized with this statement: the higher the mobility, the easier N_1 is consumed and N_2 formed. N_2 formation does not only depend on the surface population of N_1 (i.e. the probability of a N_1 to knock another pre-adsorbed N_1), but also on diffusion properties of N_1:

$$P(reaction) = P_{ER}(\text{Surface population}) + P_{LH}(\text{Surface population, diffusion}). \quad (3.8)$$

Mobility opens another reaction route (LH mechanism) with respect to the case of $k_{diff}=0$ s^{-1}, especially at low coverages. In the model, we can distinguish between N_2 formed via the ER or the LH mechanism. Table 3.1 and Figure 3.6 show the individual contributions in percentage to N_2 formation by ER (solid lines) and LH (dashed lines) as a function of coverage. The results are obtained using four different values of k_{diff}: 0.01, 0.1, 1, and 10 s^{-1}. At left of Figure 3.6, we notice that the point in which LH becomes more efficient than ER shifts to low coverage as the k_{diff} increases. Actually, depending on k_{diff}, there will be a critical surface population ($N_{1-critic}$) for which LH is able to consume efficiently N_1. $N_{1-critic}$ can be roughly evaluated through the ER and LH ratio

$$\frac{2\,r_{ER}\,\phi_1\,N_1}{4\,r_{LH}\,k_{diff}\,N_1^2} \leq 1 \quad (3.9)$$

that, in the simplistic hypothesis that $r_{ER}=r_{LH}$, becomes,

$$\frac{1}{2\,k_{diff}\,N_1} \leq 1 \Rightarrow N_{1-critic} = \frac{1}{2\,k_{diff}} \quad (3.10)$$

For example, if $k_{diff}=1$ s^{-1}, a surface population higher than 0.5 will make LH more efficient than ER; if $k_{diff}=2$ s^{-1}, a surface population higher than 0.25 will make LH more efficient than ER, and so on. Moreover, we see that after this critic surface population the ratio ER over LH reaches a steady state, as shown by colored text in Table 3.1. Here again, the value of the ratio at the steady state depends on the value of k_{diff} (see right side of Figure 3.6).

Table 3.1: Amounts expressed in percentage of the species produced via ER and LH for four different values of k_{diff} (expressed in s^{-1}) as a function of exposure. In red the critic surface population for steady state of the ER-to-LH ratio.

	k_{diff}=0.01		k_{diff}=0.1		k_{diff}=1		k_{diff}=10	
	ER	LH	ER	LH	ER	LH	ER	LH
Exposure				%				
0	99.8	0.2	98.7	1.3	88.4	11.6	43.1	56.9
0.05	77	23	26.1	73.9	5.6	94.4	1.7	98.3
0.1	63.4	36.6	18.6	81.4	5.4	94.6	1.7	98.3
0.2	57.2	42.8	16.2	83.8	5.3	94.7	1.7	98.3
0.3	51.9	48.1	16.1	83.9	5.3	94.7	1.7	98.3
0.5	46.8	57.2	16.0	84.0	5.3	94.7	1.7	98.3
0.75	**44.2**	**55.8**	16.0	84.0	5.3	94.7	1.7	98.3
1	44.1	55.9	16.0	84.0	5.3	94.7	1.7	98.3

Up to now, we have shown how a different k_{diff} affects the results as a function of coverage. As discussed in Sec. 1.1.4, the mobility of species changes as a function of temperature. For this reason, in Figure 3.7 we show the individual contributions to N_2 formation by ER or LH mechanism for four different behaviors of $k_{diff}(T_s)$. The laws used for $k_{diff}(T_s)$ in Figure 3.7 are

1. $k_{diff}(T_s)=k_0 \times T_s/T_{ref}$ (black curves),

2. $k_{diff}(T_s)=k_0 \times T_s^3/T_{ref}^3$ (red curves),

3. $k_{diff}(T_s)=k_0 \times T_s^4/T_{ref}^4$ (blue curves),
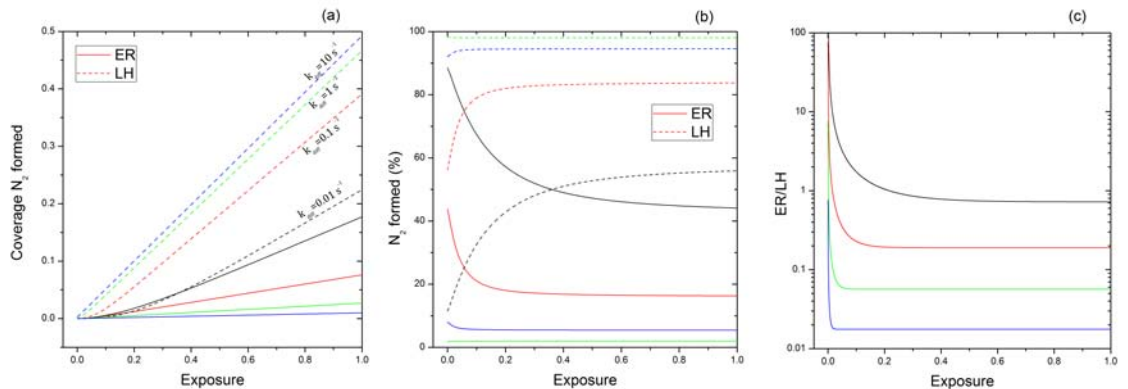
Figure 3.6: Individual contributions expressed in coverage *(a)* and percentage *(b)* to N_2 formation by ER (solid lines) and LH (dashed lines) as a function of exposure. Results of *model 1* are obtained for four different values of k_{diff}: 0.01, 0.1, 1, and 10 s^{-1}. *(v)*: ratio of ER-to-LH as a function of exposure for the four values of k_{diff}.

4. $k_{diff}(T_s) = k_0 \times \exp(-T_{ref}/T_s)$ (green curves),

where T_{ref} is a reference temperature (in this case 10 K) and k_0 the diffusion at T_{ref}. It must be noted that we have chosen the laws for $k_{diff}(T_s)$ without a particular physical reason. Table 3.2 shows the initial and final value of k_{diff} for the different laws used. From Figure 3.7

Table 3.2: k_{diff} values at T_s=6 and 38 K for four different temperature dependence.

$k_{diff}(T_s)$	$k_{diff}(6)$	$k_{diff}(38)$
$k_0 \times T_s/T_{ref}$	0.6	3.8
$k_0 \times T_s^3/T_{ref}^3$	0.22	54
$k_0 \times T_s^4/T_{ref}^4$	0.13	208
$k_0 \times \exp(-T_{ref}/T_s)$	0.36	5.9

we see that N_2 formation via LH mechanism increases between 6 and 40 K because of the increase of k_{diff}; after 30 K, the main part (> 95 %) of N_2 is formed via LH as visible in (c) panel in Figure 3.7. On the other hand, the ER contribution decreases as a function of temperature, and the ER contribution arrives at zero in the case of red and blue curves. Here we do not add the information about the desorption temperature, discussed in the following section. In principle, what we can expect is that at higher surface temperatures both ER and LH start to be inefficient because of the desorption of N_1 and the decrease of the residence time of species on the surface, thus the N_2 production efficiency by this mechanism drops off. We note here that the three potential laws have, at 10 K, the same value for k_{diff} and in fact the three lines (black, red, and blue) cross at 10 K. We postpone to Sec. 5.3.1 a practical application of this issue (*Minissale et al.* 2013).

3.1.5 Desorption coefficient: $\alpha_{N_x des}$

The last parameter that we can vary in our model is the desorption coefficient. Figure 3.8 shows the results obtained using *model 1* for five different values of $\alpha_{N_1 des}$ (in the (a) panel) and $\alpha_{N_2 des}$ (in the (b) panel): 0, 0.1, 1, 10, and 100 s^{-1}. The evolutions of surface population of N_1 and N_2 are plotted as a function of N_1 coverage. N_1 and N_2 are represented with solid and dashed lines respectively. In the model, all other parameters (initial conditions, fluxes, reaction probability, diffusion coefficients) are fixed. In particular, $N_1(0) = 0, N_2(0) = 0$, $\Phi(N_1) = 1, \Phi(N_2) = 0$, the diffusion coefficients are 0 s^{-1}. $\alpha_{N_1 des}$ and $\alpha_{N_2 des}$ are zero in the (b) and (a) panels, respectively.

The variation of $\alpha_{N_1 des}$ has influence on the surface population of both species; it induces N_1 desorption and the lack of N_1 prevents the formation of N_2. We see from left panel of
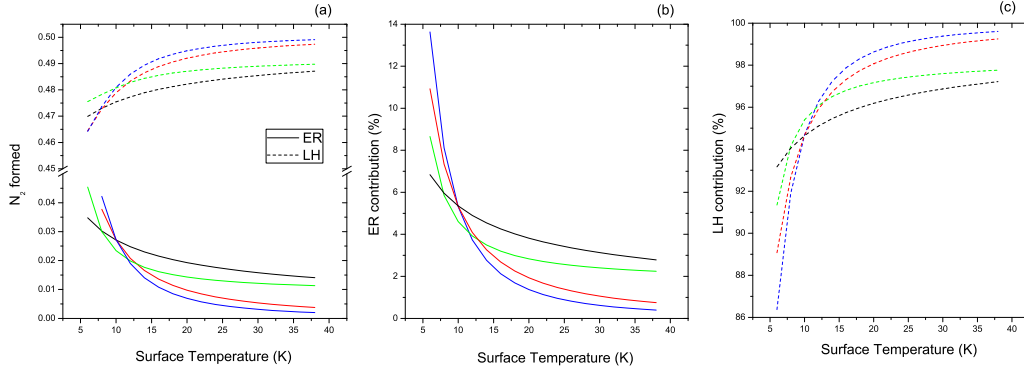
Figure 3.7: Model results showing the contribution to N_2 formation by either ER (solid lines) or LH (dashed lines) mechanism as a function of temperature for four different laws as described in the text. Contributions to N_2 formation are expressed as normalized coverage in the (a) panel, and as percentage in the (b) (ER contribution) and (c) panels (LH contribution).

Figure 3.8 that N_1 surface population reaches a steady state

$$\frac{dN_1}{d\theta} = 0 \Rightarrow \phi_1 = 2\,\phi_1\,r_{ER}\,N_1 + \alpha_{N_1 des}\,N_1 \qquad (3.11)$$

meaning that the amount of N_1 particles arriving from the gas phase is equal to the amount of particles consumed and desorbed. This condition will be satisfied at different coverages depending on the value of $\alpha_{N_x des}$: increasing the value of $\alpha_{N_x des}$, the steady state shifts toward low coverage. Moreover, we can evaluate the value of N_1(steady state) through the following equation

$$N_1(\text{steady state}) = \frac{\phi_1}{2\,\phi_1\,r_{ER} + \alpha_{N_1 des}}. \qquad (3.12)$$

So, the higher the $\alpha_{N_x des}$ value, the smaller is N_1(steady state). The variation of $\alpha_{N_2 des}$
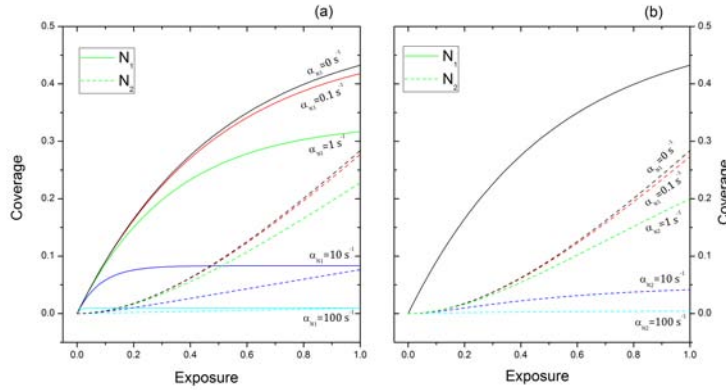
Figure 3.8: Results of *model 1* for five different values of $\alpha_{N_1 des}$ ((a) panel) and $\alpha_{N_2 des}$((b) panel): 0, 0.1, 1, 10, and 100 s^{-1}. The surface population evolutions of N_1 (solid lines) and N_2 (dashed lines) are plotted as a function of N_1 exposure. All other parameters are fixed, see text.

affects only the N_2 surface population. In the case $\alpha_{N_2 des}$=10 or 100 at high coverage this condition is satisfied

$$\frac{dN_2}{d\theta} \approx 0 \Rightarrow \phi_2 + 2\,\phi_1\,r_{ER}\,N_1 \approx \alpha_{N_2 des}\,N_2; \qquad (3.13)$$

we can evaluate the N_2 surface population at steady state through the following

$$N_2(\text{ss}) \approx \frac{\phi_2 + 2\,\phi_1\,r_{ER}\,N_1}{\alpha_{N_2 des}} \qquad (3.14)$$

and in the case of $\alpha_{N_1 des} \neq 0$, we can substitute N_1 by Eq. 3.12

$$N_2(\text{ss}) \approx \frac{\phi_2}{\alpha_{N_2 des}} + \frac{2 \ \phi_1^2 \ r_{ER}}{\alpha_{N_2 des}(2 \ \phi_1 \ r_{ER}) + \alpha_{N_1 des}}. \tag{3.15}$$

Here the first term depends on the ratio between flux and desorption of N_2, the second one depends mainly on the reaction probability. Clearly, N_2 does not reach the steady state and increases indefinitely if $\alpha_{N_2 des} = 0$. The evaluation of surface populations of N_1 and N_2 is more complex in the case $k_{diff} \neq 0$ for N_1. We will have, for N_1:

$$N_1(\text{ss}) = \frac{-(2 \ \phi_1 \ r_{ER} + \alpha_{N_1 des}) + \sqrt{(2 \ \phi_1 \ r_{ER} + \alpha_{N_1 des})^2 - 4\phi_1 \ k_{diff} \ r_{LH}}}{8 \ k_{diff} \ r_{LH}} \tag{3.16}$$

and, for N_2:

$$N_2(\text{ss}) = \frac{\phi_2 + \phi_1 \ r_{ER} \ N_1 + 2k_{diff} \ r_{LH} \ N_1^2}{\alpha_{N_2 des}} \tag{3.17}$$

We can notice from these two last equations that k_{diff} plays the main role in the steady state values of N_1: the higher k_{diff}, the lower N_1.

3.1.6 Conclusion

In this section we have presented the model used to simulate our experiments. The goal of the model is to describe the temporal evolution of the surface populations of the species adsorbed and formed on the cold surface. In the model a rate equation is used for each species. The solution of this rate equation converge to our experimental observable, namely the surface densities of the species deposited and/or formed at the end of each deposition. Each process (i.e. reactivity, diffusion, desorption) is described through a single parameter; an opportune variation of the full set of parameters is able to reproduce our data. In particular, we can vary the following parameters:

1. the initial conditions and the fluxes to describe different experimental procedures and methods;

2. $r_{ER,LH}$ to change the reactivity through the ER and LH mechanisms, these terms are surface temperature independent;

3. k_{diff} to change the diffusion coefficient, this term depends strongly on the surface temperature and it is able to increase the reactivity (through LH).

4. $\alpha_{N_x des}$ to change the desorption coefficient, this term depends strongly on the surface temperature and it is able to change considerably the surface population of a species.

In conclusion we have to remark that an important condition to find values of a good parameter is that the number of observables is greater than the number of parameters, namely the surface processes. In case this condition is not satisfied, we are not able to give a precise value of the parameter, but only a range of possible values; nonetheless, physical-chemical considerations can railroad, case by case, the parameters. Some practical cases are presented in Chapter 4 and Chapter 5.

3.2 From model parameters to physical-chemical quantities

In the previous section, we have discussed the different parameters that can be tuned to fit our experimental data. In this section, we explain how these parameters are linked to physical-chemical quantities.

3.2.1 Reactivity: reaction probability and activation barrier

The two reaction probabilities r_{ER} and r_{LH} give the probability that a reaction occurs, thus they have the same physical meaning and can be used to evaluate other physical quantities, namely the activation barrier, discussed in subSec. 1.2.2. By inverting a normalized Arrhenius equation the desorption energy E_a can be calculated as follows:

$$E_a = -k_b \, T_{eff} \, ln(r_{ER,LH}) \tag{3.18}$$

where $k_b T_{eff}$ is the energy of the considered system (hereafter, for the sake of simplicity, the k_b constant will be omitted). In collision theory, this law is derived by considering gas phase particles described through a Maxwell-Boltzmann energy distribution, and assuming that the interactions between the reactants can occur only via head-on collisions (see *Atkins&DePaula* 2006). For ER reactions, the use of Eq. 3.18 is plausible because the interactions occur between a particle coming from the gas phase ($MB(T_{gas})$) and a particle thermalized with the surface $MB(T_{solid})$. In this case, somehow similarly to gas phase reactions, the impinging particles either collide and react with one adsorbate or have enough energy to hop on the surface before thermalizing and accommodating in an empty adsorption site. Gas phase molecules coming from the beam are at around $T_{gas} = 300 \pm 20$ K while the target particles adsorbed on the substrate are thermalized with the surface at $T_{solid} = 10$-60 K. The temperature in Eq. 3.18 represents the average molecular (atomic) kinetic energy ($\overline{E}$) in a gas at thermodynamic equilibrium. $\overline{E}$ is proportional to the thermodynamic temperature. The problem is to know the exact temperature (T_{eff}) to insert in Eq. 3.18.

3.2.1.1 T_{eff} evaluation

The molecules in a gas at ordinary temperatures (i.e., at room temperature) can be considered to be in ceaseless, random motion at high speeds. The average translational kinetic energy for these molecules can be deduced from the Boltzmann distribution. In a gas at the temperature T_{gas}, it can be expressed for one molecule by the following equations,

$$\frac{1}{2}m_x\vec{v}_x^2 = \frac{1}{2}k_bT_{gas} \Rightarrow \vec{v}_x^2 = \frac{k_bT_{gas}}{m_x}, \tag{3.19}$$

where v_x and m_x are velocity and mass of the particle x, k_b is the Boltzmann constant.
The conditions present in our experiments are just a little bit more complex. In *model 1* the reactions can occur between two N_1 particles. We can consider the N_1+N_1 system as a two-body problem. We define the reduced mass - the effective inertial mass of the system - as follows

$$m \longrightarrow \mu = \frac{1}{\frac{1}{m_1} + \frac{1}{m_2}} = \frac{m_1 * m_2}{m_1 + m_2}, \tag{3.20}$$

and the relative velocity

$$\vec{v} = \vec{v}_1 - \vec{v}_2, \tag{3.21}$$

by taking the square of the relative velocity and by doing the average we obtain

$$< v^2 > = < v_1^2 > + < v_2^2 > - \underbrace{< 2\vec{v}_1 \cdot \vec{v}_2 >}_{=0} = < v_1^2 > + < v_2^2 >, \tag{3.22}$$

where $\langle 2\vec{v}_1 \cdot \vec{v}_2 \rangle = 0$ because of the isotropy of $\vec{v}_2$.
In the simplest case ($m_1=m_2$ and all the particles are at T_{gas}) through the equation below

$$\frac{1}{2}k_bT_{eff} = \frac{1}{2}\mu v^2 = \frac{1}{2}k_b\mu\left(\frac{T_{gas}}{m_1} + \frac{T_{gas}}{m_1}\right) =$$

$$= \frac{1}{2}k_b\mu\frac{2T_{eff}}{m_1} = \frac{1}{2}k_bT_{gas}, \tag{3.23}$$

it is possible to find the effective temperature of the molecules

$$T_{eff} = T_{gas}. \tag{3.24}$$

To generalize our evaluation of T_{eff} let us consider the following reaction

$$A + B \rightarrow C$$

where A and B are at different temperatures during the reaction

$$\begin{cases} B \text{ on adsorbed } A \Rightarrow T_A = T_{solid} \neq T_{gas} = T_B \\[2mm] A \text{ on adsorbed } B \Rightarrow T_B = T_{solid} \neq T_{gas} = T_A, \end{cases}$$

we will have a reduced mass of

$$\mu = \frac{m_A * m_B}{m_A + m_B},$$

then, in the case of A adsorbed and B arriving from the gas phase,

$$\begin{cases} \frac{1}{2} m_A\, v_A^2 = \frac{1}{2}\, k_b\, T_{solid} \Rightarrow v_A^2 = \frac{k_b\, T_{solid}}{m_A} \\[2mm] \frac{1}{2}\, m_B\, v_B^2 = \frac{1}{2}\, k_b\, T_{gas} \Rightarrow v_B^2 = \frac{k_b\, T_{gas}}{m_B}, \end{cases}$$

or, in the case of B adsorbed and A from gas phase,

$$\begin{cases} \frac{1}{2}\, m_A\, v_A^2 = \frac{1}{2}\, k_b\, T_{gas} \Rightarrow v_A^2 = \frac{k_b\, T_{gas}}{m_A} \\[2mm] \frac{1}{2}\, m_B\, v_B^2 = \frac{1}{2}\, k_b\, T_{solid} \Rightarrow v_B^2 = \frac{k_b\, T_{solid}}{m_B}, \end{cases}$$

and so

$$\frac{1}{2}\, k_b\, T_{1eff} = \frac{1}{2}\, \mu\, v^2 = \frac{1}{2}\, k_b\, \mu\, \left(\frac{T_{solid}}{m_A} + \frac{T_{gas}}{m_B}\right), \tag{3.25}$$

$$\frac{1}{2}\, k_b\, T_{2eff} = \frac{1}{2}\, \mu\, v^2 = \frac{1}{2}\, k_b\, \mu\, \left(\frac{T_{gas}}{m_A} + \frac{T_{solid}}{m_B}\right). \tag{3.26}$$

From these equations, by using T_{solid}=25 K, T_{gas}=300 K, m$_A$=10, and m$_B$=20 we obtain

$$T_{BonA} = \mu\, \left(\frac{T_{solid}}{m_A} + \frac{T_{gas}}{m_B}\right) = 208K,$$

$$T_{AonB} = \mu\, \left(\frac{T_{gas}}{m_A} + \frac{T_{solid}}{m_B}\right) = 116K.$$

These two T_{eff} can be used to find a lower and an upper limit for the activation barrier. Moreover, we note that the two reactions A$_{gas}$+B$_{solid}$ and B$_{gas}$+A$_{solid}$ could not have the same probability to occur at different temperatures due to a different residence time on the surface and diffusion coefficient of A and B or strong concurrence with other reactions, for example, A+A. These considerations lead us to give a range of values of the activation barrier, rather than an exact value (see *Minissale et al.* 2013 for a practical application).

3.2.2 Mobility: k$_{diff}$ and surface migration

Here we will focus on the diffusion coefficient k$_{diff}$ and its physical meaning. In our model, k$_{diff}$ is treated as a free numerical parameter that simulates the surface migration of the species on the surface. The resulting k$_{diff}$ values can be used to find the diffusion rate at given temperatures; as already said in subSec. 1.1.4 the different techniques used and the possibility that several surface diffusion mechanisms may be operative can influence the quantitative parameters (in this case k$_{diff}$) describing the surface diffusion rate. The main issue here is that no information can be inferred about the nature of the diffusive process. The problem can be inverted by using the temperature dependence of k$_{diff}$ to know what my be the type of the diffusive process. As we have shown in *Congiu et al.* (2014), diffusion coefficient k$_{diff}$ vs T$_s$ can be displayed in several ways according to the law used to describe them. For example k$_{diff}$ may follow

a an empirical law built for fitting the experimental values;

b an Arrhenius-law form, with an activation energy E_{diff} free to vary;

c a quantum-tunnelling form with a given width and height of the barrier;

A detailed analytical or numerical solution of the dependence of k_{diff} with T_s can help have some insight into the physical nature of the diffusive process at play. In Chapter 4 we will describe how these argumentations are used to infer the diffusive process of oxygen atoms.

Moreover, beyond the mechanism at play, we stress here that in our model k_{diff} has the s^{-1} dimension which can be converted into the usual unit $cm^2\ s^{-1}$ by dividing by the surface density of sites, i.e. 10^{15} molecules $cm^{-2} = 1$ ML.

3.2.3 Desorption: desorption probability and binding energy

$\alpha_{N_x des}$ are the desorption coefficients. In subSec. 1.1.3, we have already presented the theory of thermal desorption. The desorption coefficients are simply the inverse of the residence time. In particular, for N_x the desorption coefficient is

$$\alpha_{N_x des}(\theta) = \nu_0\ exp(-\frac{\int E_b(\theta)}{k_b\ T}) \qquad (3.27)$$

where the $\int E_b(\theta)$ represents the distribution of all the possible binding energies for N_x on a given surface. In fact, as we will see in the next chapter, with the increase in the doses deposited on the surface, the molecules are adsorbed in less tightly bound adsorption sites. In other words, E_b is not a unique value, but a distribution of energies depending on surface-adatom bonds. By multiplying the desorption coefficient by the coverage, we can obtain the desorption rate as follow

$$r_{des} = -\frac{dN_1}{dt} = \nu_0\ exp(-\frac{\int E_b(\theta)}{k_b\ T}) \cdot \theta^n \qquad (3.28)$$

We present a practical example of binding energies evaluation in Sec. 4.2

Bibliography

3.01 Amiaud, L., Dulieu, F., Fillion, J.-H., Momeni, A., and Lemaire, J. L., *Interaction of atomic and molecular deuterium with a nonporous amorphous water ice surface between 8 and 30 K*, Journal of Chemical Physics, Volume 127, Issue 14, pp. 144709-144709-12 (2007)

3.02 Atkins, J., and De Paula, P., *Physical Chemistry*, Oxford University Press, 8th Revised edition edition (2006)

3.03 Congiu, E., Minissale, M., Baouche, S., Chaabouni, H., Moudens, A., Cazaux, S., Manicò, G., Pirronello, V., and Dulieu F., *Efficient diffusive mechanisms of O atoms at very low temperatures on surfaces of astrophysical interest*, Faraday Discussion, Volume 168 (2014)

3.04 Katz, N., Furman, I., Biham, O., Pirronello, V., and Vidali, *Molecular Hydrogen Formation on Astrophysically Relevant Surfaces*, The Astrophysical Journal, Volume 522, Issue 1, pp. 305-312 (1999)

3.05 Minissale, M., Congiu, E., Manicò, G., Pirronello, V., and Dulieu, F., *CO_2 formation on interstellar dust grains: a detailed study of the barrier of the $CO+O$ channel*, Astronomy and Astrophysics, Volume 559, pp. A49-57 (2013)

3.06 Noble, J. A., Congiu, E., Dulieu, F. and Fraser, H. J., *Thermal desorption characteristics of CO, O_2 and CO_2 on non-porous water, crystalline water and silicate surfaces at submonolayer and multilayer coverages*, Monthly Notices of the Royal Astronomical Society, 2012, Volume 421, pp. 768-779 (2012)

Surface Physics

There is no quantum world.
There is only an abstract quantum physical description.
It is wrong to think that the task of physics is to find out how nature is.
Physics concerns what we can say about nature.

"The philosophy of Niels Bohr",
Niels Bohr

Fernanda, en cambio, lo buscó [el anillo] únicamente
en los trayectos de su itinerario cotidiano,
sin saber que la búsqueda de las cosas perdidas está
entorpecida por los hábitos rutinarios,
y es por eso que cuesta tanto trabajo encontrarlas.

"Cien años de soledad"
Gabriel García Márquez

4.1 Oxygen reactivity and diffusion

In this section, we describe the reactivity and diffusion of oxygen atoms on different surfaces. The reactivity is the study of how O atoms allotropize, or in other words how O_2 and O_3 are formed. In principle, oxygen reactivity should be described in Chapter 5 where we describe the surface chemistry. Nevertheless we treat the oxygen reactivity here because O-atom reactivity and diffusion of oxygen atoms are deeply related. Actually, from a physical point of view, the O-atom diffusion allows O atoms to meet with each other or with other species, and thus diffusion controls reactivity; in other words the allotropization is diffusion-limited. From a practical point of view, our detection instruments are not suitable to follow the evolution with time of fast processes like the diffusion, but they are able to measure the overall and macroscopic effect of these processes. We measure the amount of reactants consumed and products formed, which is a measure of the reactivity of the system. Since this last is determined by the chemical (activation barriers) and physical (diffusion) properties of the system, we can deduce the diffusion by measuring reactivity variation as a function of the experimental conditions used.

4.1.1 Experimental

Experiments were performed using the FORMOLISM set-up. The experimental procedure is very simple: oxygen atoms (and O_2 molecules) are aimed at a cold (6-25 K) sample and the products are probed using TPD and RAIRS. We have varied the following parameters:

- The substrate morphology (Amorphous water ice, porous (p) and compact (np), crystalline (c) ice, amorphous silicate, and graphite)

- The coverage of deposited O/O_2, from 0.1 to 1 ML

- The substrate temperature, from 6.5 to 25 K

- The dissociation rate of O_2 molecules (between 45% and 80%)

It was checked that no O_3 was present in the beam. This control was carried out by two different methods. The first control was performed by placing the quadrupole mass spectrometer (QMS) in front of the beam and by monitoring mass-48 signal of the direct beam, and the one of the beam when blocked by a metallic flag. The signal at mass 48 was always under the detection limit imposed by the electronic noise, and this is a first indication that no O_3 was present in the beam. A second check consisted of irradiating with $O+O_2$ the surface held at 55 K, then performing a TPD. At this temperature the residence time of O_2 is extremely short and prevents the formation of O_3 through the reaction $O+O_2$, while gas phase O_3 sticks and remains on the surface. A peak at mass 48 (and mass 32, see below) in the TPD would indicate that O_3 was actually present in the beam. With this second control experiment we could accurately determine that no ozone was present in the O beam.

The energetic state of atoms and molecules was checked before commencing the experiments as described in Sec. 2.2.2.3. We determined that the beam did not contain O or O_2 in an excited state, nor O_3 molecules. The O beam was thus composed of at least 99% ground-state O and O_2. We also recorded the mass 16 signal in all experiments, and did not detect any signal that could be interpreted as O-atom release in the gas phase. Actually, except for the direct beam, or for a very small fraction ($< 2\%$) due to cracking of O_2 and O_3 in the QMS, we never detected any signal at mass 16. This indicates that O atoms react and never desorb as such, but exclusively as O_2 and O_3 molecules.

The flux and the determination of O_2 and O_3 monolayer have been discussed in Sec. 2.2.4 and in *Minissale et al.* (2014a).

4.1.2 Oxygen reactivity

In the previous section, we have implicitly claimed that O_2 and O_3 molecules are formed by sending O atoms on a cold surface. Here, we discuss how the different parameters (substrate, coverage, surface temperature) change the reactivity and, as a consequence, experimental results. Figure 4.1 shows the results of experiments performed by varying the O/O_2 doses. Two desorption peaks are present: O_2 desorption occurs between 35 K and 50 K, and the ozone desorption is observed between 55 K and 75 K (directly, or via the O_2^+ fragments). We observe, at any coverage or temperature, ozone formation by depositing O and O_2 mixtures on ASW. O desorption is never observed. The shapes and positions of the O_3 peaks are the same as those of O_3 deposited from the gas phase, and are only coverage dependent. We can thus exclude any second order desorption effects, like it should be if O_3 were formed on the onset of or during desorption. By looking at the integrated area of TPD traces of Figure 4.1, we notice that the O_3/O_2 ratio increases with coverage, O_2 reaches rapidly an almost steady state while O_3 rises quite linearly. These experiments suggest that the reactivity of pure oxygen species is limited to two reactions:

$$O + O \rightarrow O_2 \quad R0.1$$
$$O + O_2 \rightarrow O_3 \quad R0.2$$
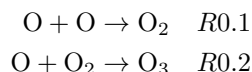
The $O + O_3 \rightarrow 2O_2$ reaction seems not to be competitive with the others, it would not be possible to obtain an almost pure O_3 sample with increasing coverage. About the two reactions R0.1 and R0.2, three questions arise:

1. when do these reactions occur?

2. which mechanism is at play?

3. what are the activation barriers?
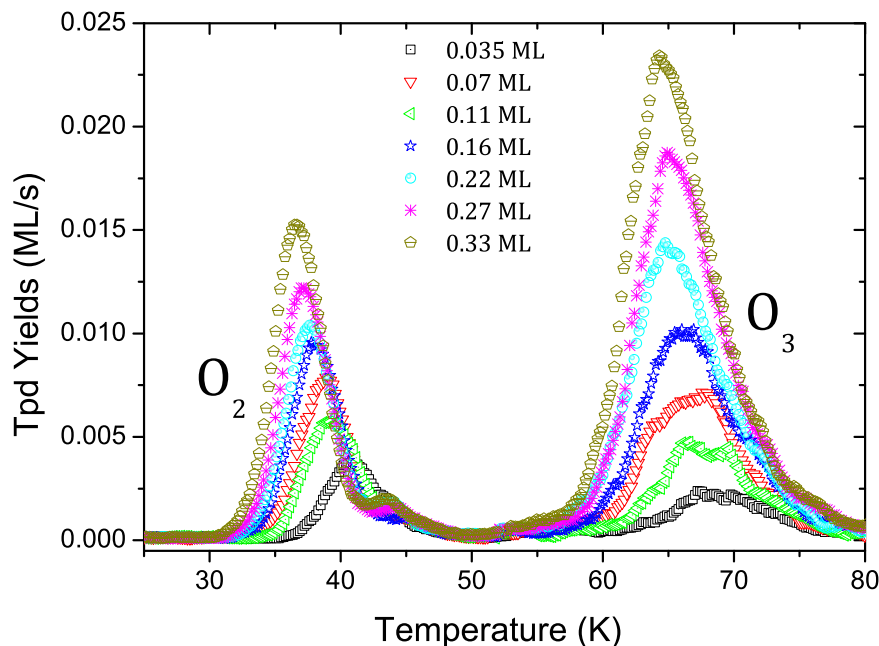
Figure 4.1: Adapted from *Minissale et al.* 2013b. TPD of O_2 and O_3 after deposition of various doses (0.04-0.4 ML) of an O-O_2 mixture on ASW ice held at 10 K.

As regards the first question, the formation of O_2 and O_3 can happen during the deposition or during the TPD when the temperature increases. To disentangle this issue, we have followed the evolution of the O_3 infrared absorption band intensity from 6.5 K to 35 K as shown in Figure 4.2. Because of a high detection limit (0.3 ML) this method could only be applied to the highest coverage experiment in Figure 4.1. Within experimental uncertainties the O_3 infrared band does not vary during the TPD in the high coverage experiment, except at the temperature above which ozone begins to come off the surface ($\sim$ 55K). However, due to the error bars, a small increase of the ozone band could have still been possible. We estimated that an upper limit for the fraction of extra ozone formed during the heating is 15%, a value that we will use below in the discussion. We can fairly say that the majority of O_3 is formed during deposition, and the results are consistent with the theory that thermally-induced diffusion during the TPD is a secondary effect compared to diffusion and reactions at the deposition temperature. Aware of this result, we can try to answer the second question (which mechanism is at play). In principle, the two reactions R0.1 and R0.2 may arise from direct reactions between an impinging atom and an adsorbed species (ER mechanism), or may occur by diffusion of the species on the surface (LH mechanism). Moreover, it is also possible that the Hot Atom Mechanism (HAM) has a role as we will discuss in the following. In other words, gaining knowledge about mechanisms at play means to understand what physical processes occur on the surface, i.e., O atoms diffusion. To figure out this matter is the subject of the next section. Finally, as already discussed in Chapter 3, the evaluation of the activation barriers (the third question) is strictly related to the evaluation of the diffusion coefficients of O atoms, presented in the next section. Nonetheless, we anticipate that R0.1 and R0.2 should be barrierless reactions, and in *Minissale et al.* (2014a) we provide an upper limit of 150 K for the activation energy barriers of both reactions.

4.1.3 Oxygen diffusion

To understand if diffusion plays an effective role in the O_3/O_2 formation, we have to play with the physical properties of the formation mechanisms. The ER mechanism happens
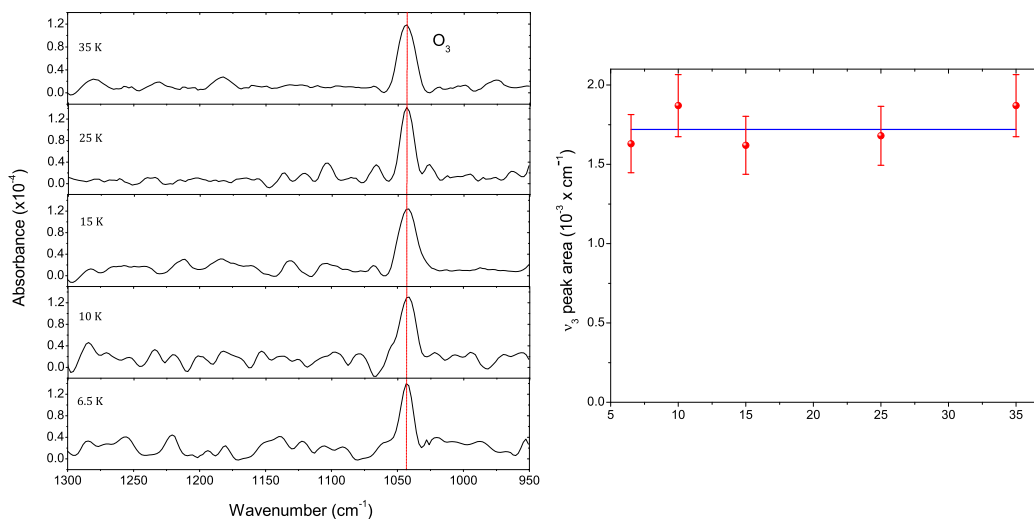
Figure 4.2: Adapted from *Minissale et al.* 2014a. Left panel: RAIR spectrum obtained at different Ts (bottom to top, 6.5, 10, 15, 25, and 35 K) after deposition of 0.3 ML of O atoms at 6.5 K; the absorption band is due to O_3. Right panel: integrated area of the ozone band as a function of surface temperature. The red solid line represents the mean value of the five integrated band areas.

between a gas phase reactant and a surface reactant; it is by construction not sensitive to the surface temperature and its efficiency depends solely on the coverage. On the contrary, the LH mechanism (as well as diffusion) depends on the temperature of the surface. For this reason, we have performed a second set of experiments in which we varied the deposition temperature of the substrate, but fixing the initial O/O_2 dose (coverage). The left panel in Figure 4.3 summarizes the outcome of six TPDs, in which the coverage was fixed (0.29 ± 0.03 ML) and the deposition temperature varied between 8 K and 30 K. We can observe, from curve to curve, a clear change in the O_3/O_2 ratio. This effect is due to the temperature of the substrate and is a sign of the role of diffusion in the formation of ozone. In fact, with increasing surface temperature, the mobility of O atoms is favored, ozone formation is more efficient, and the O_3/O_2 ratio increases. Each new adsorbed atom - if the diffusion is fast - is able to scan the surface to react with O_2 to form O_3, or with another absorbed O atom to form O_2 (that, in turn, will also be transformed into O_3 by the next incoming and mobile atom). In this scenario, almost all O atoms and O_2 molecules are transformed into O_3 molecules. On the contrary - if the diffusion is slow - an oxygen atom has not enough time to scan the surface and react with an adsorbed O_2. Another O atom then comes and more O_2 is formed via the O + O reaction. A reduced mobility leads to the accumulation of O atoms on the surface, the probability for an O atom to meet another O atom rises, and eventually O_2 formation is favored. By comparing RAIRS and TPD results, it is possible to see how the diffusion of O atoms changes the O_3/O_2 ratio. As stated above, we have assumed that an increase of 15 % of the ozone yield may have occurred during the heating from 6.5 to 35 K (see Figure 4.2). From TPD results, however, we obtain a variation of 47 % between the ozone yields after O deposition performed at 8 K and the one performed at 30 K. This indicates that, taking into account the possible 15 % contribution due to the heating, there is still 32 % (47 from TPD, -15 from RAIRS) difference between TPD experiments carried out at $T_s = 8$ and 30 K. The right panel of Figure 4.3 displays TPD (points) and RAIRS (gray shaded region) normalized peak areas (yields) of ozone and molecular oxygen. TPD variations (also considering the error bars) are greater than the ones in RAIRS data for ozone. This difference is clearly due to T_s, i.e., variations of O atom mobility on the silicate surface. As regards O_2 yield variations, at 30 K only 15% of the amount of O_2 formed at 8 K was observed.

In summary,
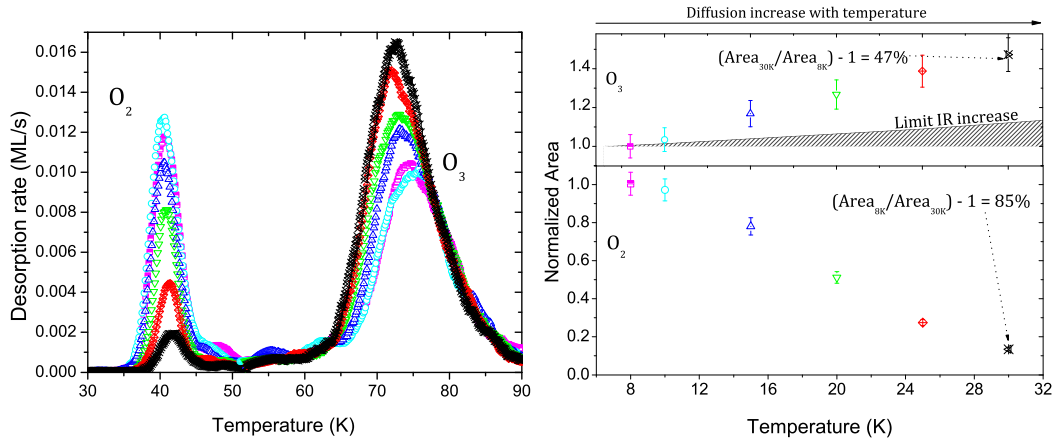
Figure 4.3: *Left Panel*: Series of 6 TPD curves after deposition of 0.3 ML of O atoms on silicate held at 8, 10, 15, 20, 25, and 30 K. *Right Panel*: Integrated peak areas of O_2 and O_3 TPD traces of left panel as function of deposition temperature. The peak areas were normalized with respect to the TPD yields after deposition at 8 K. Gray pinstriped region: range of values of the O_3 signal increases due to thermal diffusion derived from IR spectra.

1. in Sec. 4.1.2, we showed that an incoming O atom is more likely to find O_2 molecules as the coverage increases (Figure 4.1);

2. in Sec. 4.1.3, we showed the increase of the O_3/O_2 ratio with deposition temperature, which demonstrates the increase in diffusion with temperature (Figure 4.3)

In the next sections, we discuss the role of the substrate on the O_3/O_2 ratio variation and, through a model, we provide estimations of activation barriers for R0.1 and R0.2 and diffusion coefficients.

4.1.3.1 The role of substrate

The main conclusions of the previous section are that the O_3/O_2 ratio increases both as function of coverage and as function of surface temperature; but what is the influence of the substrate on the O_3/O_2 ratio? Figure 4.4 shows integrated areas (in ML) of the TPD peaks of O_2 (red squares), O_3 (green circles), and their sum (blue tringles) as a function of O-atom fluence for four substrates: non-porous ASW ice, crystalline ice, graphite, and silicate (*a,b,c,* and *d* panels, respectively). The dashed line corresponds to TPD yields after pure O_2 deposition carried out with the undissociated beam (the total amount of oxygen atoms deposited on the surface). The O_2 dissociation fraction is 71%±4 for all the experiments. We point out two main differences between the four panels:

1. The *crossing point* between O_2 and O_3 (namely the coverage for which $O_3 \geq O_2$) is at very low coverage, around 0.05 ML, for water ices (np-ASW and crystalline, respectively *a* and *b* panels), while it is at a higher coverage, 0.2-0.25 ML, for graphite and silicate (respectively, *c* and *d* panels).

2. The sum O_2+O_3 (blue triangles) follows the dashed line in the case of water ices, while it is beneath the dashed line for graphite and silicate.

The first difference can be explained by different O-atom diffusion coefficient on the different substrate; the higher the diffusion, the larger the probability of species encounter, and, as a consequence, the higher the reactivity. The crossing point is in some way a measure of the reactivity and, therefore, of the diffusion coefficients (k). In particular, $k_{water-ices} > k_{bare-substrates}$ in the plausible hypothesis that activation barriers for R0.1 and R0.2 are the same for all substrates. The second difference can be explained by the different chemical desorption probability of O_2 molecules on the various substrates(*Chaabouni et al.* 2012;
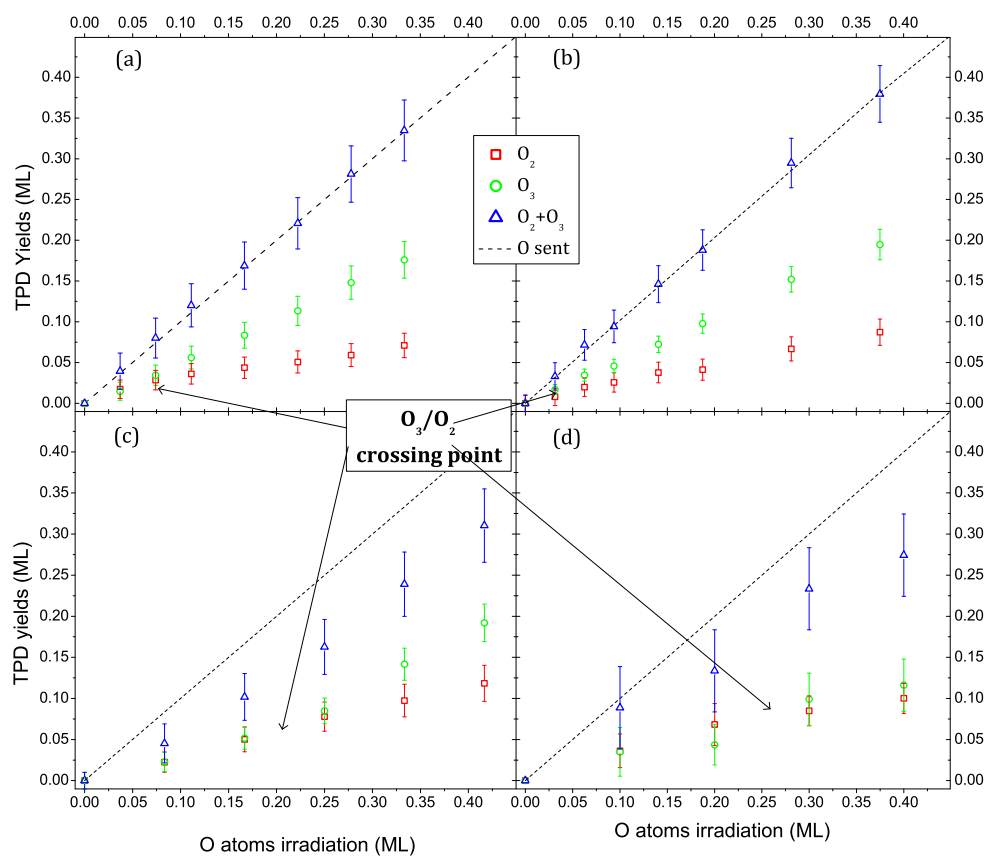
Figure 4.4: Integrated areas (in ML) of the TPD peaks of O_2 (red squares) and O_3 (green circles) vs O-atom fluency for four substrates: non-porous ASW ice, crystalline ice, graphite, and silicate (a, b, c, and d panels, respectively). Blue triangles: sum of O_2 and O_3. Dashed lines represent the total amount of oxygen atoms deposited on the surface.
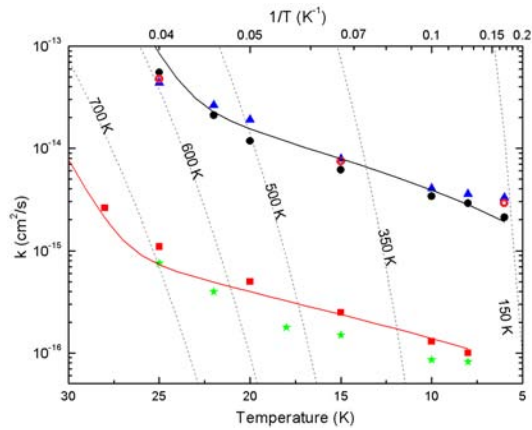
Figure 4.5: From *Congiu et al.* (2014). Diffusion constants k of O atoms obtained on np-ASW (open pink circles), on crystalline water ice (black circles), p-ASW (blue triangles), amorphous silicate (red squares), and oxidized HOPG (green stars), plotted as a function of surface temperature. Dashed lines represent a series of Arrhenius-type laws generated by using five values of E_{diff} (from 150 to 700 K). The two solid lines are best fits of the experimental values obtained through the quantum-tunneling diffusion law for O atoms on compact water ice (black solid line) and amorphous silicate (red solid line); see Table 4.1 for the best fit values of a (barrier width) and E_a (barrier height).

Dulieu et al. 2013). Actually, as discussed in *Minissale&Dulieu* (2014c), the missing atoms in the case of bare substrates is due to the prompt release of O_2 upon formation. This prompt release is apparently impeded on water ices.

4.1.3.2 Model

In this section, we provide an estimation of activation barriers for R0.1 and R0.2 and of the diffusion coefficients on the various substrates. Experimental data are inserted into a model composed by a series of rate equations used to simulate the O_2 and O_3 formation yields according to coverage and surface temperature. The model includes both LH and ER mechanisms, and it allows reactions to occur during the deposition phase, as well as during the heating phase (TPD). A complete account of our model is given in *Minissale et al.* (2014a) and in Chapter 3. Here we will focus on the diffusion rates k and the different methods by which they are calculated. In Figure 4.3, we have already demonstrated that reactions mostly occur during the exposure phase. The diffusion of atoms during the heating phase is negligible because not more than a few percent of the deposited O atoms remain available on the surface in the low coverage regime. The effect of any possible diffusion during the TPD lies within the error bars of the experimental data, and can be neglected. For this reason, in what follows, we will address only the diffusion coefficients at a fixed temperature for each one of the substrate investigated.

Other parameters are the dissociation fraction τ, and the chemical desorption rate, that was studied in *Dulieu et al.* (2013) and *Minissale&Dulieu* (2014c), it will be discussed in Sec. 4.3. The diffusion coefficents k include two components due to quantum tunnelling and thermal motion:

$$k = k_{qt} + k_{tm}. \tag{4.1}$$

In our model, k can be treated as a free numerical parameter during the deposition phase at constant temperature, owing to the fact that the evolution of the coverage with time is known and provides a strong constraint. Therefore, resulting k values are a set of constants giving the diffusion rate at given temperatures, although no information can be inferred about the nature of the diffusive process. In Figure 4.5. the diffusion constants k that we obtained for various substrate compositions are plotted as a function of temperature. An important finding of this comparative study is that diffusion coefficients on water ices (regardless of its morphology) are about one order of magnitude greater than those on silicate and graphite.
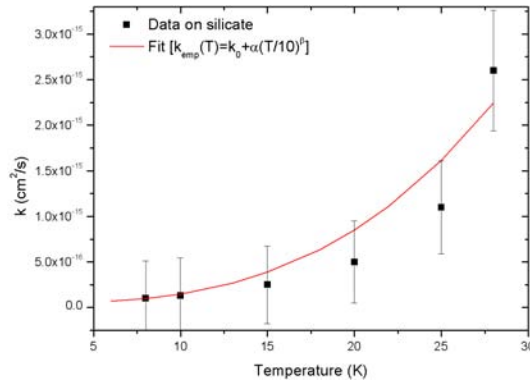
Figure 4.6: From *Congiu et al.* (2014). Black squares represent diffusion constants of O atoms on amorphous silicate as a function of temperature. The red solid line is a best fit of diffusion constants vs temperature obtained by using the empirical law given in Eq.4.2; see Table 4.1 for best fit values of k_0, α, and β.

Diffusion constants k vs T_s can be displayed in several ways according to the law used to describe them, namely, k may have (a) an empirical law built for fitting the experimental values, (b) an Arrhenius-law form, with an activation energy E_{diff} free to vary, or (c) a quantum-tunnelling form with a width and height of the barrier. A detailed analytical or numerical solution of the dependence of k with T_s can help have some insight into the physical nature of the diffusive process at play. Case (a), the empirical law we used for fitting the diffusion constant as a function of surface temperature, has the form

$$k_{emp}(T) = k_0 + \alpha (T/10)^\beta. \qquad (4.2)$$

Figure 4.6 displays a fit of the experimental values obtained on amorphous silicate according to the empirical law given in Eq. 4.2. k_0 can be considered the minimum value of k, or the value k must tend to near T = 0 K. α is a free parameter with values between 0 ad 1, and it accounts for diffusion efficiency differences between the various substrates. α=1 for water ice while it is about 0.1 for graphite and silicate. The dependency on the surface temperature is governed by the factor $(T/10)^\beta$, the exponent β can have a value between 3 and 4, with variations due to the surface nature, although the best fits give typical values of 3.5. Case (b), the classical Arrhenius law used to model the diffusion coefficient k is

$$k_{arr}(T) = \nu_0 \, exp[-E_{diff}(T)/T] \qquad (4.3)$$

E_{diff} is the diffusion barrier expressed in kelvin (eV/k_b) and ν_0 (= 10^{12} s^{-1}), the pre-exponential factor, can be seen as a trial frequency for attempting a new event. In Figure 4.7 we present a fit of the diffusion coefficient k on non-porous ASW obtained by using the Arrhenius law. Figure 4.7 actually displays activation energies for diffusion (E_{diff}) as a function of temperature. In fact, according to Eq. 4.3, a suited set of E_{diff} can be used to derive one diffusion coefficient for each temperature. It is thus possible to link each of these diffusion coefficients to an Arrhenius behavior, and find one energy barrier at each temperature as shown in top panel of Figure 4.7 (see also dashed lines in Figure 4.5). However, a disordered surface has a complex distribution of adsorption and diffusion barrier energies, and for each surface there exists a unique distribution that can be quite different, even in substrates of the same composition and morphology. We have tried to implement this kind of complication to fit our results. In bottom panel of Figure 4.7 we present an attempt to model the distribution of diffusion energies on amorphous water as a function of surface temperature, calculated assuming an Arrhenius behaviour and according to the experimental values of diffusion coefficients k. The colour scale represents the fraction of adsorption sites with energy E_{diff}(T) populating 1 ML. From bottom panel of Figure 4.7 it is clear that the contour lines are not horizontal, as they should be in a fixed distribution of diffusion energies characterizing a given substrate. This implies that the distribution of diffusion energies cannot be constant in the narrow (6-25 K) temperature interval investigated, but its centre
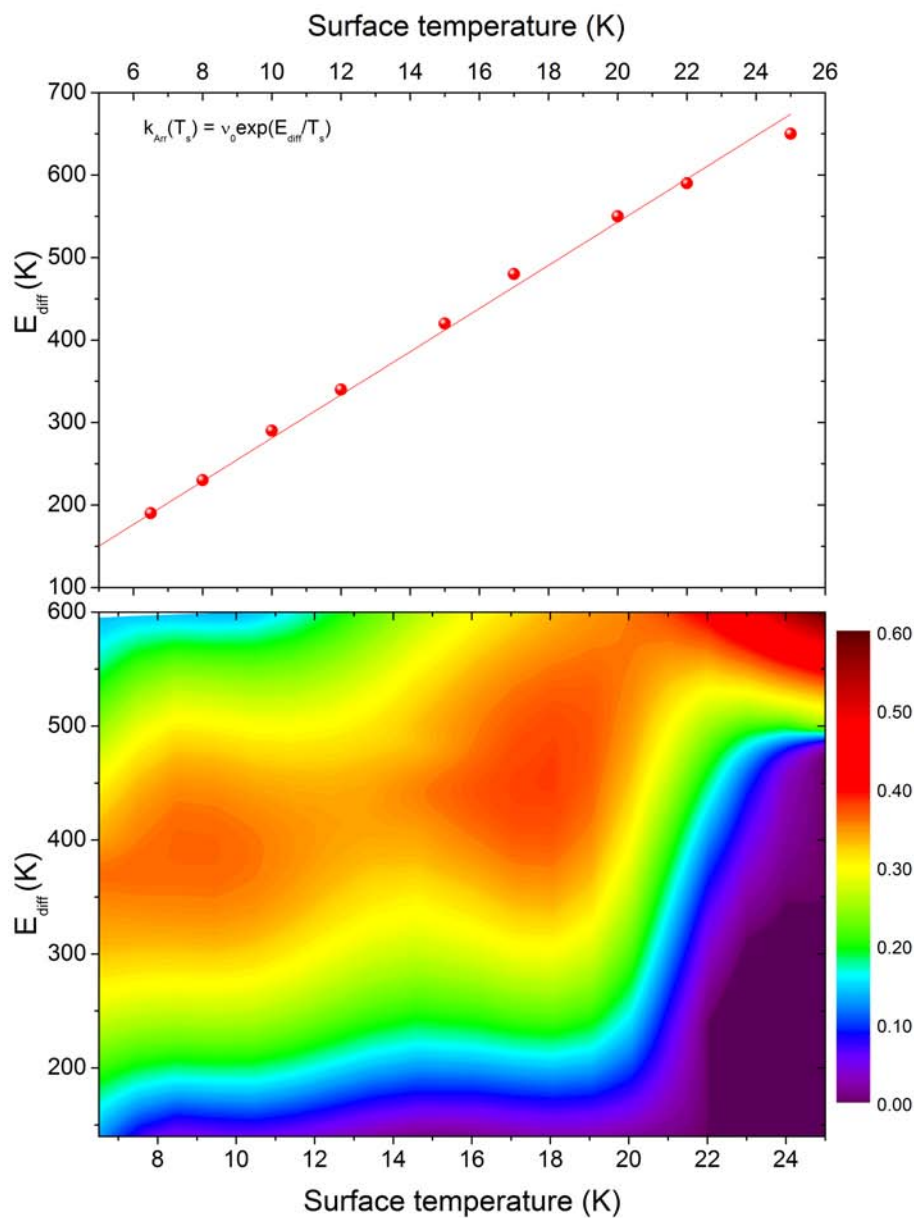
Figure 4.7: Top panel (from *Congiu et al.* (2014)): Energy barrier for diffusion on compact water ice as a function of surface temperature in the case of Arrhenius-type diffusion coefficient. The red solid line represents a linear fit of $E_{diff}(T)$; see Table 4.1 for the interval of E_{diff} values needed to obtain k_{Arr} between 6 and 25 K. Bottom panel: Distribution of O-atom diffusion energies on amorphous water ice as a function of surface temperature calculated according to the experimental values of the diffusion coefficients and assuming an Arrhenius (thermal) behaviour. The colour scale represents the fraction of adsorption sites ($1=10^{15}$ sites $cm^2=1$ ML) with $E_{diff}(T)$ at temperature T.

has to shift to higher energies with temperature to reproduce the observed trend in diffusion coefficients. We believe that a change in the distribution of barrier energies within such a narrow temperature range is not physically plausible, although not impossible, in the case of "stiff" surfaces such as silicate and graphite, nor in the case of the various morphologies of water ice at such low temperatures. To sum up:

1. an Arrhenius law form in which only one E_{diff} exists and is independent of the temperature is not able to fit the data;

2. an Arrhenius law form in which a fixed distribution of E_{diff} exists is not able to fit the data;

3. our data are fitted both through a $E_{diff}(T)$ or through a temperature dependent distribution of E_{diff}.

This is why we discarded the Arrhenius-type behavior of k as it made no physical sense to us. In fact, a systematic increase of the Arrhenius barrier with temperature seemed to us an ad hoc solution. Also, this implies that at low temperatures (6 K) diffusion occurs through low diffusion barriers (e.g., $E_{diff} = 170$ K). If such low barriers actually exist, they represent fast connections between adsorption sites. Why then would these low energy barriers vanish at higher temperatures? To put it in other terms, why and how atoms would diffuse through slow pathways (high diffusion barriers) at high temperatures (>20 K), if faster pathways exist? We consider this unlikely and not physically reasonable.

In Figure 4.8 we show a comparison between the classical behavior (described by an Arrhenius-type law) of the diffusion coefficient as reported by *Karssemeijer et al.* (2012) for CO molecules on hexagonal water ice, and the trend that we find experimentally for O atoms on amorphous silicate and crystalline water ice. It is clear that our experimental values do not follow an Arrhenius behavior, suggesting that a classical description is incomplete to explain the experimental data (squares and triangles in Figure 4.8). In fact, in a pure thermal diffusion the slope is very different, and if we fit the data by using a classical Arrhenius law, we find values of ν_0 and E_{diff} not physically acceptable. Therefore, a quantum mechanical approach ought to be used to account for the deviations from the classical trend. Our results on oxygen atoms are consistent with a tunnelling-dominated diffusion as found for H atoms on np-ASW by *Senevirathne et al.* (2014) in the 6 - 13 K temperature range (the slopes of H- and O-diffusion coefficient behaviors are similar). They also found that diffusion of H atoms is enhanced around 13 K, as occurs to O atoms around 22 K, just where classical thermal motion begins to predominate over quantum processes (*Senevirathne et al.* 2014; *Minissale et al.* 2013). *Hama et al.* (2012) found that this temperature border between quantum and classical diffusion of H atoms is likely to be at $T_s < 10$ K. We found that at very low temperatures the diffusion of O atoms is better simulated by quantum tunneling through a square barrier (*Messiah* 1973). The physical parameters we use to describe such a quantum jump are the width a and the height E_a of the barrier. The choice of a square barrier, the simplest shape of a potential, was made purposefully to show that the right trend is obtained if one uses quantum-tunneling diffusion, not because we believed that a square barrier was the right one. We believe that any other more realistic potential shape we could use, would not fundamentally change the results, and it would still be unrealistic given the complexity of the distribution of diffusion barriers. We did not try to obtain the best fit of our data, but tried to show that the right trend is obtained if one uses quantum-tunneling diffusion (see solid lines in Figure 4.5). Hence, we chose to model the quantum diffusion with two parameters which have a simple physical meaning, although they correspond to macroscopic values that come from the interplay of many microscopic different situations. The values of k and of all the parameters used to fit the diffusion coefficient on each substrate, using the three methods, are listed in Table 4.1. The diffusion coefficients of O atoms calculated on water ices are one order of magnitude greater than those found on amorphous silicate and oxidized HOPG, namely O diffusive mechanism is more efficient on icy grains. Also, as opposed to the case of H atoms, there is no difference between the efficiency of O mobility on the three types of water ices investigated (p-ASW, np-ASW, and c-SW). In the light of our experimental results, we can only observe and simply report this finding. In fact, to deal
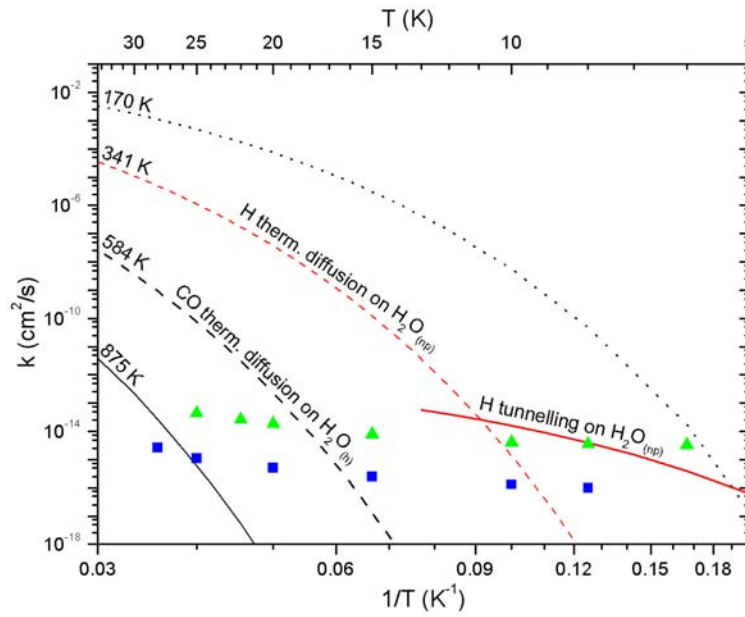
Figure 4.8: From *Congiu et al.* (2014). Comparison between diffusion behaviors of CO molecules, H atoms, and O atoms. Blue squares and green triangles represent O-atom diffusion coefficients as a function of surface temperature on amorphous silicate and crystalline water ice, respectively (this work). The black dashed line represent the thermal diffusion (Arrhenius behavior) of CO molecules on hexagonal water ice found in *Karssemeijer et al.* (2012). The red solid line and the red dashed line display the H-atom tunnelling (6 - 13 K) and the H thermal diffusion ($T_s > 13$ K), respectively, obtained by *Senevirathne et al.* (2014) on compact amorphous water ice.

with atoms makes it very difficult to derive key parameters such as the energy barrier for diffusion, or even the energy barrier for desorption, hence no pertinent assumption can be made to explain these findings from a physical chemical point of view. However, to give a physical explanation of our results is beyond the scope of this thesis, since we believe that quantum calculations and simulations will be necessary to thoroughly describe O diffusion mechanisms at low temperatures.

Table 4.1: Best fit parameters of the three methods used to model the diffusion coefficients for O diffusion on five different grain surface analogues

	Quantum tunneling		Arrhenius law	Empirical law		
	a (Å)	E_a	$E_{diff(6<T<25)}$(T)	k_0 (10^{-15})	α	β
Porous ASW	0.69±0.10	530±70	170<E_{diff} <600	1.30	1	3
Non-porous ASW	0.7±0.05	520±60	170<E_{diff} <600	1.21	1	3
Crystalline SW	0.69±0.05	500±50	170<E_{diff} <600	1.42	1	3
Amorphous silicate	0.67±0.10	720±70	290<E_{diff} <740	0.15	0.1	4
Oxidized HOPG	0.67±0.10	740±60	290<E_{diff} <740	0.1	0.1	4

4.1.3.3 The role of amorphicity and morphology in diffusion processes

The majority of theoretical models describing diffusion consider a potential of the type used in crystalline-like solids (see *Oura et al.* (2003) and references therein). In reality there is robust observational evidence that an amorphous nature is the most probable structure for grains in space (*Leger et al.* 1979). Taking this into account, the situation changes dramatically as it can be seen in *Smoluchowski* (1979, 1981). While in a crystalline solid the atoms are regularly arranged in a lattice, which means that the crystal can be built up by periodic repetition of identical cells, amorphous solid does not show any periodic structure. The number of nearest neighbors of atoms or molecules and the distances between them are

usually very similar in crystalline and amorphous solid, because of atoms (or molecules) have rather well-defined effective radii and the bonds between them are almost unaffected by the degree of crystallinity; in contrast the second, third, etc., neighbors of each site in general will be different in amorphous solids. This difference is described by the so called *pair correlation*

(a) Amorphous solid   (b) *pair correlation* function
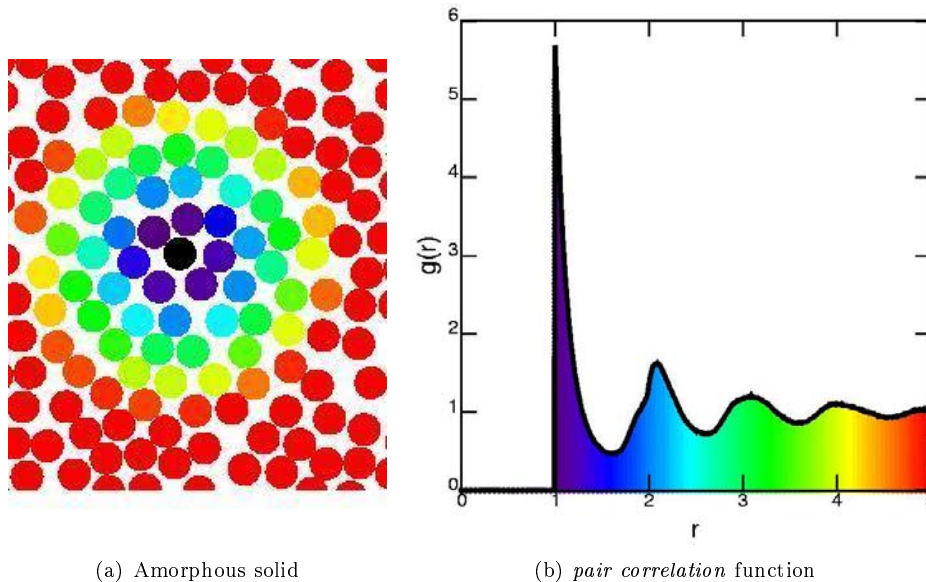
Figure 4.9: Left side: schematic representation of the *pair correlation* function $g(r)$ for an amorphous solid. Right side: *pair correlation* function $g(r)$ as a function of the distance between two atoms.

function $g(r)$ which indicates the probability of finding an atom at a particular distance r from another atom. It is given by the following expression

$$g(r) = \frac{V}{4\pi r^2 N^2} \langle \sum_i \sum_{j \neq i} \delta(r - r_{ij}) \rangle \tag{4.4}$$

where N is the total number of particles contained in a volume V. A schematic representation of the $g(r)$ is shown in Figure 4.9. $g(r)$ provides a measure of the local spatial ordering in a solid. Using this function one can calculate the spectrum of the binding energies of atoms adsorbed on various sites of the amorphous surface.

Figure 4.10 represents, in a certain sense, the $g(r)$ function with the contribution for high r suppressed by the rapid drop-off of the binding energy $E(r)$. The most important difference between crystalline and amorphous surfaces is that, on a periodic surface (as the crystalline one), the motion of atoms can be represented as a temporary spread of a quantum mechanical wave packet describing the adsorbed atom while on an amorphous surface, and so in a non-periodic sequence of potential wells, this is not possible. Thus, a diffusing atom (for instance of hydrogen) attains accessibility to the whole amorphous surface only at relatively high temperatures through thermal hopping. The most important implication of the breadth of the spectrum shown in Figure 4.10, is that the adsorbed atom will become rapidly localized by tunneling to a site of lowest energy in its proximity; it will diffuse only when the temperature is high enough and thermal hopping is possible.

In this scenario, why do we find similar diffusion coefficients for different morphologies of water ices? The answer can be found in the percolation theory. We know that an amorphous surface has a larger distribution of energy and width of barriers for diffusion with respect to a crystalline surface. If on one hand the amorphicity reduces the fraction of sites accessible (if energy and width of barriers are too large, the atom will be localized), on the other hand it makes other sites more accessible. In other words, on amorphous surfaces diffusion has less sites available with respect to crystalline ones, but between these sites the diffusion is very
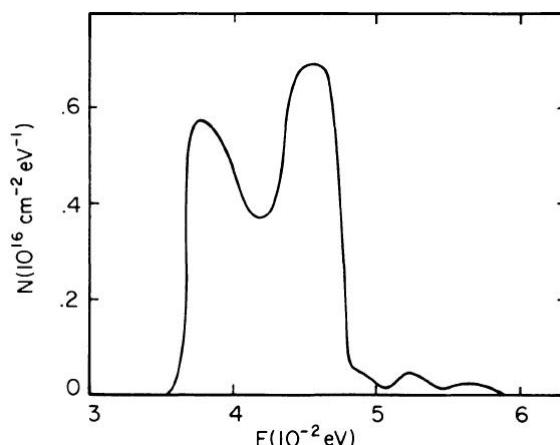
Figure 4.10: Number N of adsorption sites of hydrogen atoms on amorphous ice per unit area and unit energy as a function of the binding energy E. The area under curve corresponds to 10^{14}-10^{15} atoms per cm^2 of the surface. Taken from *Smoluchowski* (1979).

fast. The overall effect is that diffusion coefficients do not change as a function of amorphicity. We remark here that we measure average diffusion coefficients and we are not able to measure a specific diffusion coefficient from one to another site. To test this alternative scenario, we develop a very simple model somehow inspired by *Wolff et al.* (2010). Figure 4.11 displays a sample of the squared grid. We define three different connections between sites:

1. Thick lines correspond to fast connections with diffusion energy E_h-d;

2. Thin lines correspond to "average" connections with diffusion energy E_h;

3. No lines correspond to slow connections with diffusion energy E_h+d,

where d determines in a way the degree of amorphicity; if d=0 the grid represents a crystalline solid. We stress that this model is not intended to be complete. Actually, a distribution for the width of barriers has to be considered too. Nevertheless, we chose to overlook the distribution of width of barriers for a question of simplicity. In this manner, we can show what is the role of amorphicity in a simple way. The computational procedure is very simple: two atoms fall down randomly on the surface, they are free to migrate, and the code is stopped when they meet and react. We measure the time between the fall and the encounter. Colored points in Figure 4.11 correspond to three different starting conditions: (1) an islet of three connections in red; (2) a deep site in green; (3) a connected grid in blue. The results depends on the initial conditions and Figure 4.12 shows a typical encountering time distribution obtained for a random initial condition and a random degree of amorphicity d. Our free parameters are E_h and d. In order to understand the role of amorphicity, we have fixed E_h. We find generally that the presence of fast and slow connections (with d= 15% of E_h) decreases significantly reaction times with respect to the case d=0. Actually the presence of fast connections prevails over the presence of slow connections. This result is in opposition with the Smoluchowski theory, for which the amorphicity hinders the diffusion, no matter which type (tunneling or hopping). If we have a look at the probability density function of atoms on the grid built after a complete set of model runs ($\approx$ 50), we find that atoms are active and mobile only on well connected network (E_h-d), as shown Figure 4.13. This is very probably the reason for which when such degree of amorphicity is introduced, it does not fundamentally change the diffusion. We already claimed that a periodic surface (as the crystalline one) favors the spread of a quantum mechanical wave packet describing the adsorbed atom. On an amorphous surface, the loss of a global symmetry of site energies is compensated for by the presence of an enhanced diffusion on fast connections.
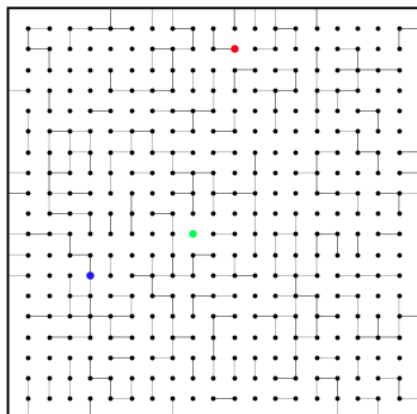
Figure 4.11: Squared grid with three different connections between sites: thick, thin, and no lines correspond to fast, "average", and slow connections, respectively. Colored points correspond to three different starting conditions.
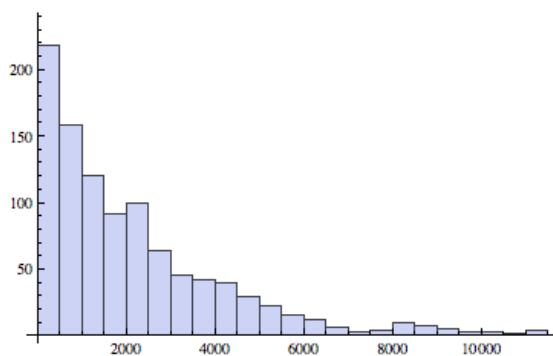
Figure 4.12: Typical encountering time distribution obtained for a random initial condition and a random distribution of sites for two atoms diffusion on the grid presented in Figure 4.11.
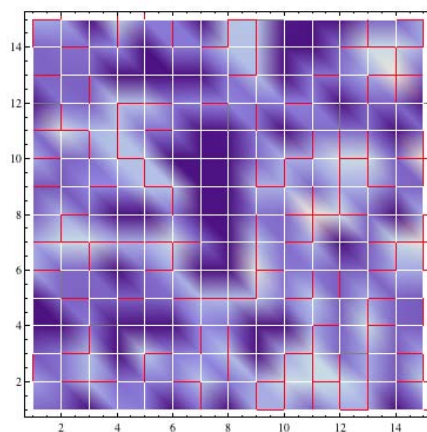
Figure 4.13: Probability density function of atoms on the grid. In white and in red well and poorly connected sites respectively.
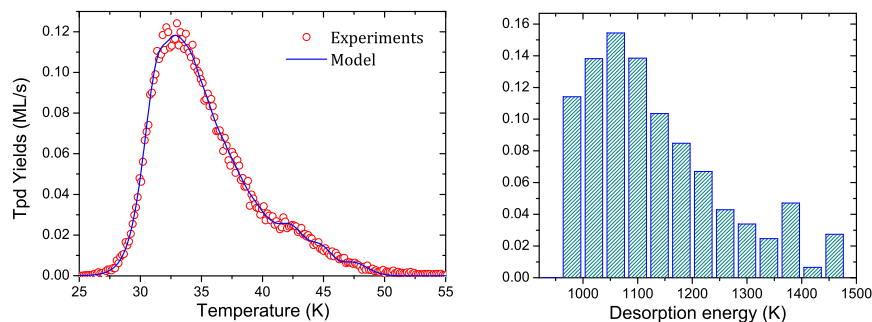
Figure 4.14: Left panel: TPD traces after irradiation of 1 ML of O_2 on silicate at 10 K. The blue line (model) was obtained by using an energy distribution for adsorption sites. Right panel: Fraction of adsorption sites as a function of energy corresponding to the O_2 TPD spectrum at left.

4.2   Evaluation of desorption energies

4.2.1   Desorption energy of non-reactive species: the case of O_2 and O_3 molecules

The analysis of TPD spectra is an excellent means to find the desorption energy for a lot of molecules. The shape of the TPD curves is linked to physisorption energies of adsorbate and surface and to the potential structure of the latter. We already stated in Sec. 2.2.2.4 that the disordered nature of a surface entails a wide range of binding energies available on the surface, and as a consequence also a range of desorption temperatures. To take this into account, thermal desorption is described in terms of an Arrhenius expression using a (discrete or continuous) range of desorption energy as

$$R(\theta) = -\frac{d\theta}{dt} = \sum_{i=0}^{15} \nu \, \alpha_i \, \theta^n \, e^{-(E_0 + i*\sigma)/T}/\beta \Rightarrow R(\theta) \quad = \int_{E_0}^{E_{max}} \nu \, \alpha_\theta \, \theta^n \, e^{-(E(\theta))/T}/\beta \quad (4.5)$$

where R is the desorption rate, θ the adsorbate coverage, t the time, ν the pre-exponential factor of desorption (the vibrational frequency of the molecules at the surface, 10^{12} s^{-1}), n the order of the desorption process, T the temperature, E the activation energy for desorption, α are normalization coefficients, and β is the heating ramp. The left panel of Figure 4.14 displays the case of desorption of 1 ML of O_2 from amorphous silicate. Red points represent the experimental TPD curve and the blue line is obtained by using a discrete distribution of adsorption sites. The right panel of Figure 4.14 shows the distribution of the occupied sites according to their energy. By integrating all columns, we obtain the amount of O_2 deposited, 1 ML in this case. Thanks to this figure, we can point out that the choice of only one desorption energy for a molecule is very simplistic. This matter will be discussed in Sec. 6.2. Nevertheless, to give an idea of the desorption energies as a function of coverage, we can choose the peak of the distribution shown in the right panel of Figure 4.14. α and β panels of Figure 4.15 show desorption energy distribution for different doses of O_2 and O_3 desorbing from np-ASW and amorphous silicate. The desorption energy decreases with the coverage, meaning that molecules populate less deep adsorption sites or that intermolecular interactions (i.e., repulsions) have the effect of lowering the binding energy. This behavior is more pronounced on amorphous silicate; for this surface, the difference between low coverage and multilayer desorption energy is larger with respect that present on np-ASW. This is shown in panel γ of Figure 4.15, where the normalized (with respect to the monolayer energy) desorption energies are plotted as a function of coverage. This approach can be used to estimate the desorption energy of different molecules. A list of desorption energy for different molecule and substrates determined with this method is shown in Table 4.2.
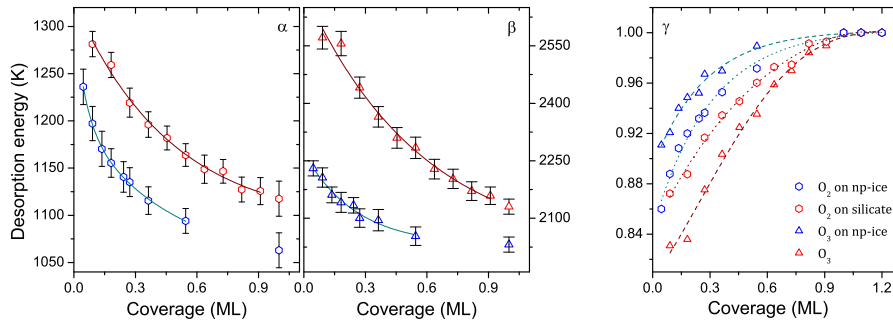
Figure 4.15: α and β panels: desorption energy of O_2 and O_3 as a function of deposited coverage on two substrates, np-ASW and amorphous silicate. γ panel: O_2 desorption energies of panels α and β normalized w.r.t the desorption energy at a coverage of 1 ML.
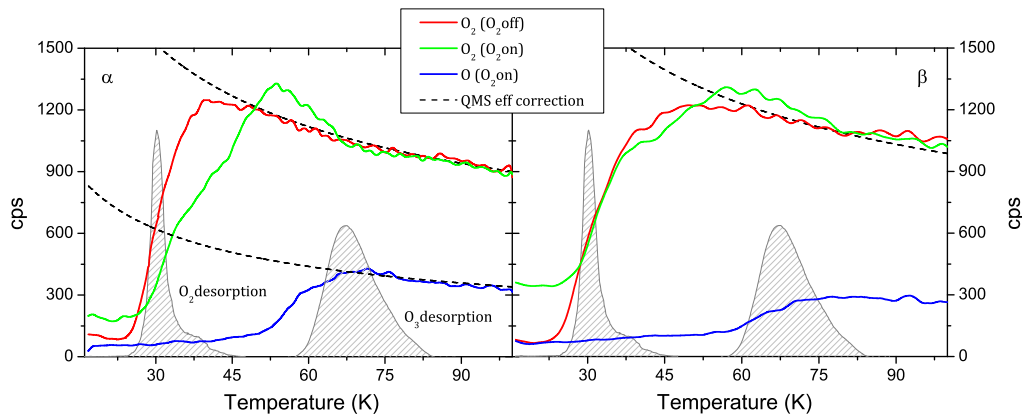
Figure 4.16: Temperature-programmed DED of masses 16 and 32 recorded during irradiation of O atoms on np-ASW (panel α) and oxidized HOPG (panel β). Initial temperature is 100 K and a ramp of -1 K/min has been used to reach 15 K.

4.2.2   Desorption energy of reactive species: the case of O atoms

The approach described above to the estimate desorption energy of O_2 and O_3 can be used only in the case of non-reactive species. This means that once a species has been deposited, it remains inert on the surface up to an increase in surface temperature, namely a TPD. If the species is reactive, a TPD of such species cannot be performed, hence this method cannot be used. This is the case of O and N atoms. They promptly allotropize on the surface and TPDs cannot be used to estimate their desorption energies. Nevertheless the desorption energy can be evaluated by performing a temperature programmed DED (TP-DED). The procedure consists of looking at the products formed as a function of surface temperature. In this way, we can have an idea of the residence time of this species at a given surface temperature. Figure 4.16 displays a particular experiment performed on np-ASW (panel α) and oxidized HOPG (panel β) to determine the O-atom desorption energy. O atoms are sent on the surface and we follow the signal at masses 16, 32, and 48 as a function of surface temperature. Initial surface temperature is 100 K and with a ramp of -1 K/min, the surface reaches 15 K. Figure 4.16 clearly shows three trends for mass 16: (1) a lower plateau (T < 45 K for np-ASW and T < 52 K for oxidized HOPG) where the majority of O atoms stick on the surface; (2) an upper plateau (T > 68 K for np-ASW and T > 75 K for oxidized HOPG) where all O atoms desorb from the surface; (3) a transition region (45 K < T < 68 K for np-ASW and 52 K < T < 75 K for oxidized HOPG) where mass 16 signal falls down from the upper to the lower plateau. Before delving into the details of the transition region, we have to explain the behavior that gives the upper plateau. We notice that between 100 K and 70-75 K the signals of both mass 16 and mass 32 increase. This increase is due to the
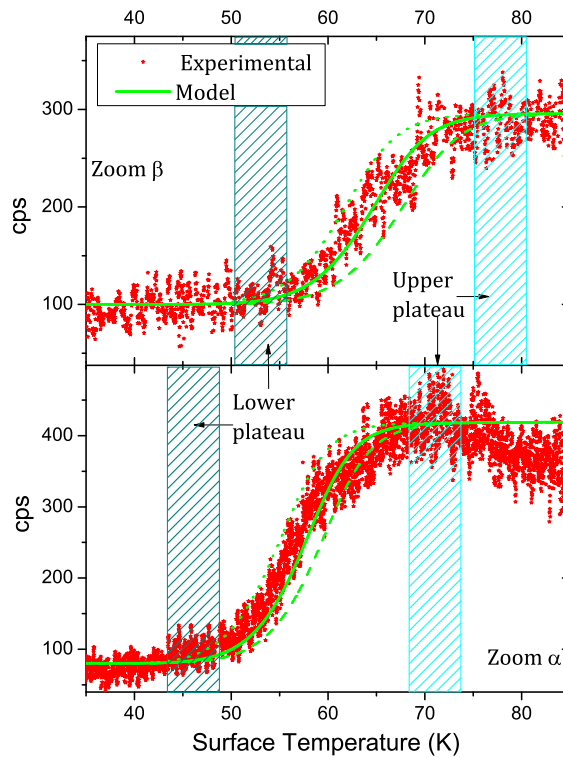
Figure 4.17: Comparison of experimental (red stars) and model results (green curves) of TP-DED of mass 16 in the 35-85 K region for oxidized HOPG (upper panel) and np-ASW (lower panel).

different temperature of the desorbing molecules. We know that the detection efficiency of the QMS depends on the particle speed: the higher the speed, the lower the efficiency. At a certain T_s, the main part of desorbing molecules have a $T_{desorbing}=T_s$. Hence, at $T_s=100$ K, DED signal is lower than the one at $T_s=70$ K. The QMS efficiency can be corrected through a factor proportional to

$$\sqrt{\frac{100}{T_s}}$$

through which we obtain the dashed curves in Figure 4.16. We can now focus on the transition region. In the case of a non-reactive species, transition region can be explained only through an increase of the residence time (i.e. O_2, red curves), and so it is not difficult to estimate the binding energy of such a species. In the case of a reactive species (i.e. O atoms) a signal decrease during the TP-DED could be due either to desorption or reactivity of the system. This complicates the evaluation of binding energy. By using the same rate equation model used for the diffusion-reactivity of the O_x system, we are able to fit the transition region as shown in Figure 4.17. We consider a thermal diffusion of O and we use the binding energy of O atoms as a free parameter. For instance the green curves on panel β of Figure 4.17 (oxidized HOPG) are obtained by using $E_{diff}=950$ K and $E_b=1580\pm70$, while for panel α (np-ASW) $E_{diff}=900$ K and $E_b=1420\pm50$. The choice of E_{diff} is not arbitrary but it comes from a previous evaluation by *Minissale et al.* (2014s). Nevertheless, it should be noted that this is only a preliminary evaluation of the O-atom binding energy and it has to be improved through further modeling.

4.2.3 Conclusion

In this section we discussed how desorption energies can be evaluated

1. from TPD spectra, following *Kimmel et al.* (2001) and *Amiaud et al.* (2006), for pure

non-reactive species (O_2, CO, NO, and so on)

2. from DED measurements of reactive species (O and N)

We present a list of desorption energies for different species adsorbed on np-ASW, amorphous silicate, and HOPG for low coverage and monolayer regime. All the experimental data were recorded during the present thesis work, even if not all the data have been presented.

Table 4.2: List of desorption energies of some atoms and molecules adsorbed on np-ASW, amorphous silicate, and HOPG for low coverage and monolayer regime. Experiments are performed with pure species beam. Where not specified the error bar is $\pm$ 40 K.

Species	E_{des} K					
	np-ASW		amorphous silicate		HOPG	
	0.1 ML	1 ML	0.1 ML	1 ML	0.1 ML	1 ML
N_2	–	–	–	1000	1230	1040
O	1420$\pm$50	–	–	–	1580$\pm$70	–
O_2	1192	1060	1278	1117	1250	1020
O_3	2200	2031	2500	2130	2230	2040
NO	1510	1560	1440	1490	1610	1650
NO_2	–	–	3630	3810	3610	3900
CO	1320	980	–	–	1380	1010
CO_2	2460	–	–	–	2530	2460
H_2CO	3290	3010	–	–	3420	3100
HCOOH	–	4330	–	–	–	4220
CH_3OH	–	–	–	–	3900	4110

[a] The desorption energy evaluation is similar to that discussed for O atoms.

4.3   Chemical desorption

The chemical desorption process starts from the energy excess usually present in radical-radical reactions. The chemical desorption efficiency will depend on how the newly formed molecule dissipates the energy excess. Actually, in order to desorb, the molecule has to convert a fraction of this excess formation energy into kinetic energy, and especially into motion perpendicular to the substrate. In other words, the problem lies on how the newly formed molecule manages the energy excess and interacts dynamically with the surface. The total budget of energy excess (enthalpy of reaction) is the most important parameter describing the chemical desorption. The larger the enthalpy of reaction, the more probable is chemical desorption. On the contrary, the binding energy of the newly formed species should be considered as a limiting factor. Among diverse parameters, the degrees of freedom of the newly formed molecules seem to play a important role: in fact more degrees of freedom lead to an easier distribution to internal modes and thus dissipation. The last parameter that we consider is the interaction with the substrate, namely the phonon propagation. The water ice substrate has larger capabilities to dissipate the excess energy than other substrates (silicate and oxidized graphite), and therefore the probability of chemical desorption is lower. Nevertheless, the "softness" of the water ice substrate is not sufficient to forbid chemical desorption, as shown in *Amiaud et al.* (2007) and *Govers et al.*, (1980) in the case of H_2. Further works stress - in the case of water - the role of the surface coverage in the inhibition of chemical desorption processes (*Congiu et al.* 2009).

   In this section we present experimental results proving the chemical desorption (CD) of different molecules. All the experiments described in this section are performed using the FORMOLISM set-up and follow a similar experimental procedure described in Sec. 2.2.2.5.
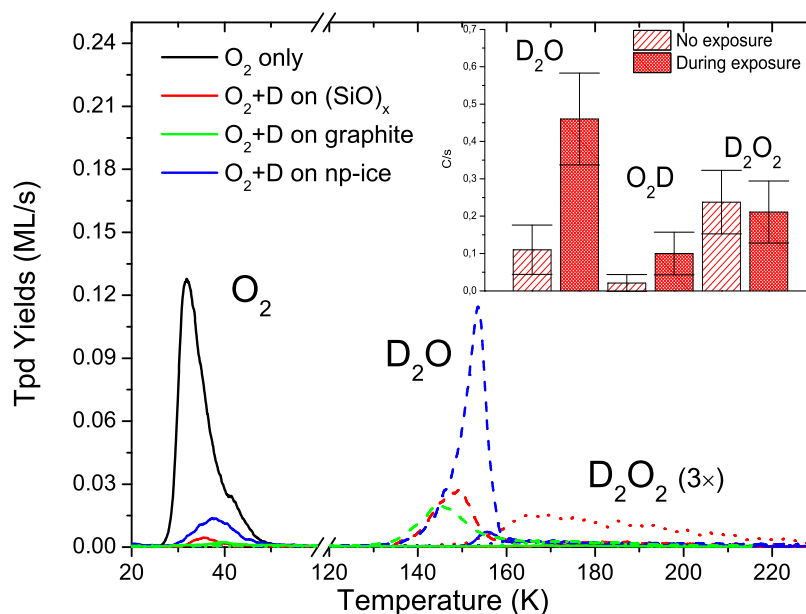
Figure 4.18: From *Dulieu et al.* (2013). TPD curves of O_2 (solid), D_2O(dashed), and D_2O_2 (dotted) species after irradiation of D atoms on 1 ML coverage of O_2 ice deposited on different substrates (amorphous silicates in red, graphite in green and np-ASW ice in blue) held at 10 K. Inset: D_2O, D_2O_2 and D_2O mass signals monitored with the QMS during the exposure of D atoms on 1 ML coverage of O_2 ice deposited on the silicate substrate at 10 K.

4.3.1   The chemical desorption of the O-H system

The study of CD for the O_x+H reaction network is quite a complicated case to study, since a plenty of reactions (> 20) are involved and several molecules can be formed. For this reason, firstly we have studied separately the case O_2+H and only then O+H.

4.3.1.1   Chemical desorption in O_2+H experiments

We have studied experimentally the CD for the reaction O_2+H and subsequent reaction on different surfaces. For the sake of clarity, here we focus our attention mainly on CD and we postpone to Sec. 5.1 the discussion about the chemical network of these experiments. Figure 4.18 shows the results after irradiation with D atoms of 1 ML of O_2 molecules. We use D atoms instead of H atoms to increase the signal to noise ratio and to easily distinguish ASW substrate and newly formed molecules. After the deposition at 10 K, the surface temperature is increased up to 200 K and molecules are measured in the gas with a mass spectrometer. Solid, dashed, and dotted lines represent thermal desorption spectra of O_2, D_2O (mass 20), and D_2O_2 (mass 36) respectively. Different colors represent the surface in which experiments are performed: red for amorphous silicate, green for graphite, and blue for np-ASW. The black line represents a TPD of 1 ML of O_2 deposited on silicate. O_2 desorbs as a single peak at around 35 K. When O_2 is irradiated with D atoms the desorption of O_2 is very weak compared to the deposition of O_2 only, meaning than most ($\geq 90\%$) of the initial O_2 molecules have been consumed. D_2O and D_2O_2 desorption features are observed at 150 K, and before 200 K, respectively. Previous studies showed that O_2 reacts quickly with D, forming O_2D, D_2O_2, and finally D_2O (*Miyauchi et al.* 2008; *Ioppolo et al.* 2009; *Dulieu et al.* 2010). The area of the desorbed peaks indicates that

1. on graphite only 15% of the oxygen has been included in D_2O, meaning that around 85% of the O_2 molecules are missing from the surface.

2. on silicate only 25%+5% of the oxygen has been included in D_2O and D_2O_2 formed and O_2 not consumed, meaning that around 70% of the O_2 molecules are missing from

the surface.

3. on water ice 45%+16% of the oxygen has been included in the D_2O and D_2O_2 molecules, meaning that around 40% of the O_2 molecules are missing from the surface.

The O_2 molecules missing in the desorption spectra are believed to be ejected into the gas phase during exposure with D atoms, following chemical reaction. In this sense, once new species are formed, and are unable to thermalize on the surface, they are released into the gas phase (the so called chemical desorption). To prove the existence of this process, we have performed several DED during D irradiation. The measurements are reported in the inset of Figure 4.18 (for the silicate surface) before and during D irradiation for D_2O (mass 20), DO_2 (mass 34), and D_2O_2 (mass 36). We observe a direct D_2O signal far above the noise level, indicating that D_2O is chemically desorbed. On the other hand, we detect a very small increase of the DO_2 signal (in the noise) and no increase of the D_2O_2 signal. OD (mass 18) and O_2 (mass 32) are also monitored, but the presence of H_2O (mass 18) and O_2 as minor contaminants in the vacuum decreases the signal to noise ratio, allowing only a one sigma detection of O_2. The DED measurements provide clear evidences of the CD of D_2O. We remark that quantitatively DED and TPD experiments cannot be directly compared since the QMS is not located at the same place during these experiments. The possible reactions routes leading to D_2O formation and consequent CD are the following

$$O_2 + D \rightarrow DO_2 + D \rightarrow \tag{4.6a}$$
$$D_2O_2 + D \rightarrow D_2O + OD \tag{4.6b}$$
$$OD + OD + 2D \rightarrow 2\,D_2O \tag{4.6c}$$

Both D_2O_2 + D (exothermicity $\approx$ 3.1 eV) and OD + D (exothermicity $\approx$ 5.2 eV) can contribute to D_2O CD but we can not differentiate which contribute is larger. The branching ratio between the two reaction routes can give an idea of contributions. Nonetheless the ambiguous signals of reaction routes marker (D_2O_2 for the first one, and OD for the second one) do not allow to give a precise evaluation. However, recently, *Oba et al.* (2013) have shown that H_2O_2 + H has a high barrier and it is therefore probable that OH+H is the main carrier of H_2O CD.

4.3.1.2 Chemical desorption in O_3+H experiments

We performed complementary TPD experiments to address the origin of the very important chemical desorption of D_2O. In particular we studied the reaction O_3 + H. Here we used hydrogen instead of deuterium. Figure 4.19 represents the desorption spectra of water after its formation via 1 ML of O_2 with 7 ML of H on silicate held at 10 K (blue); 1 ML of O_3 with 7 ML of H on silicates held at 10 K (red); 1 ML of O_3 with 7 ML of H on silicate held at 45 K (green). We can see that in the case of O_3, there is a higher production of H_2O, because the formation of water is made by two sub-routes

$$O_3 + H \rightarrow O_2 + OH \rightarrow \tag{4.7a}$$
$$OH + H \rightarrow H_2O \tag{4.7b}$$
$$O_2 + H \text{ see eq. 4.6a.} \tag{4.7c}$$

Performing experiments at 45 K, where O_2 is evaporating at a high rate, almost forbids the O_2 + H sub-route, so the O_3 + H at 45 K is almost like observing the OH + H reaction. Figure 4.19 clearly shows that almost no water seems to be produced in the experiments performed at 45 K, indicating a very strong chemical desorption during exposure through the reaction OH + H. To check that the disappearance of the water signal for O_3 + H at 45 K is not due to the fact that the reaction does not proceed, we measured the amount of O_3 present on the surface as O_3 was exposed to H atoms. We see that the peak of O_3, located at 67 K in the TPD, decreases as the exposure with H atoms increases. This shows that even if the residence time of H atoms on the surface is short at 45 K, it is long enough to activate radical-radical reactions, as observed here for the reaction O_3 + H and also observed
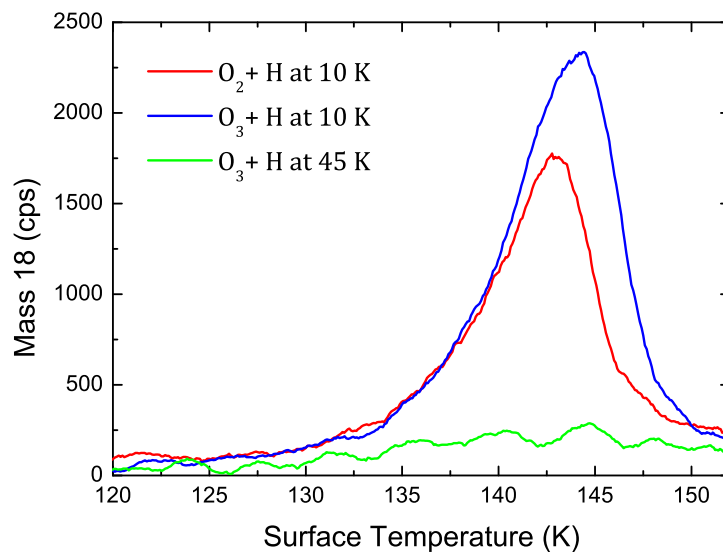
Figure 4.19: From *Dulieu et al.* (2013). Water TPD after irradiation of: 1 ML of O_2 with 7 ML of H on silicates held at 10 K (blue); 1 ML of O_3 with 7 ML of H on silicates held at 10 K (red); 1 ML of O_3 with 7 ML of H on silicates held at 45 K (green).

for NO +H (*Congiu et al.* 2012). To summarize, we show that the OH + H route is the one responsible for the important amount of water produced during exposure of O_2 with H or D. Since most of the water formed through this route is ejected in the gas phase, this allows us to bring further constraints on our first TPD experiment. The reaction O_2 + D leads to the formation of D_2O_2 and then D_2O + OD, or to the formation of 2 OD. Since OD on the surface reacts with a D to form D_2O and is ejected in the gas, D_2O and D_2O_2 observed in the TPD are the result of reactions 4.6b and 4.6c. This implies that the 35 % of D_2O found on the surface comes from reactions 4.6b and 4.6c, and that the branching ratio is k= 0.35. Further details about the branching ratio are present in *Chaabouni et al.* (2012) and *Dulieu et al.* (2013).

4.3.1.3   Chemical desorption in O+H experiments

The main conclusion of the previous sections is that H-irradiation of O_2:O_3 ices produces high CD of newly formed water molecules, mainly via the OH + H reaction. Aware of this statement, we have studied the case of O + H reaction. This reaction in theory includes all the possible reaction routes, since once O atoms adsorb on the surface, they can form O_2 and O_3. We know that

$$O + H \rightarrow OH + H \rightarrow \qquad H_2O \qquad (4.8a)$$
$$O + O \rightarrow O_2 + H \rightarrow \quad \text{see eq 4.6a}$$
$$O_2 + O \rightarrow O_3 + H \rightarrow \quad \text{see eq 4.7a}$$
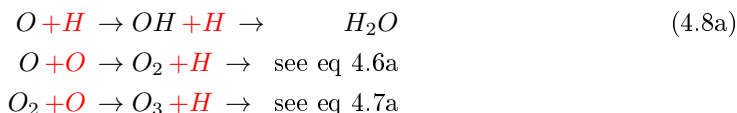
Figure 4.20 displays DED measurements of masses 17 and 18 during O + H irradiation on oxidized graphite held at 10 K. We note that during the exposure both signal at mass 18 and signal at mass 17 are higher than the background signal. This is evident on right panel of Figure 4.20 where we display signals of mass 17 and 18 normalized to their respective no-deposition signals. The DED measurements provide clear evidence of newly formed molecule CD (H_2O and OH). Actually neither mass 18 nor mass 17 are present in the beam and, as a consequence, molecules detected through these masses have to be formed on the surface and released in the gas phase. The allotropization of O atoms complicates the analysis of these results, or at least of mass 18. Actually we have shown that the signal at mass 18 is present
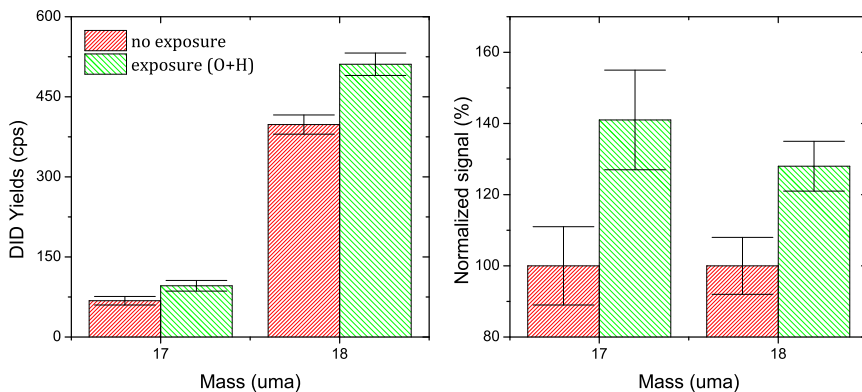
Figure 4.20: Left panel: DED measurements of mass 18 and mass 17 (H_2O and OH) during O + H deposition on oxidized graphite held at 10 K. Right panel: DED measurements of mass 18 and mass 17 (H_2O and OH) during O + H deposition normalized to background signal.

in O_2:O_3+H experiments. This means that signals at mass 18 can be due to H_2O CD via Eq.s 4.6c, 4.7b, and 4.8a.

Conversely, signals at mass 17 are not present in O_2:O_3+H experiments, and thus what we measure is necessarily due to the first step of Eq. 4.6c. We stress here that, H_2O is detected both via masses 17 and 18, due to cracking in the QMS head (see Sec. 2.2.2.1). Their ratio is around 17% in the case of water. Figure 4.21 shows that during no irradiation the M17/M18 ratio is 17%. These signals come from the residual water present in the main chamber. On the contrary, the ratio can reach 40% during irradiation. This indicates that the signal at mass 17 is due to OH CD in the first step of Eq. 4.6c

4.3.2 The influence of the substrate: CD of O_2

4.3.2.1 Experimental results

The aim of this section is to describe the role and the contribution of the different parameters influencing the chemical desorption. We have chosen to present the case of O atoms reactivity on oxidized graphite for two reasons. First, O atoms reactivity is a well known system (*Ward&Price* 2011; *Minissale et al.* 2013; *Minissale et al.* 2014a; *Congiu et al.* 2014) and, since only 2 reactions are involved:

$$O + O \longrightarrow O_2 \qquad (R0.1)$$

$$O + O_2 \longrightarrow O_3 \qquad (R0.2),$$
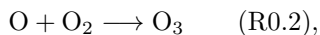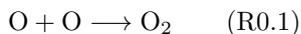
we can immediately realize how the different parameters affect the two reactions. Second, among substrates already studied, the oxidized graphite exhibits the highest chemical desorption efficiency. Some of the experimental results that we analyze here are shown in panel *c* of Figure 4.4. For the sake of clarity, we replot it in panel *a* of Figure 4.22. The dashed line corresponds to the conservation of the total number of O atoms: as if all the atoms (in the form of O, O_2, and O_3) desorb during the TPD, therefore the triangles (formed O_2+formed O_3) should overlie this line. This line was determined experimentally using the undissociated beam (pure O_2 beam). We did not detect any signal that could be interpreted as O-atom desorption in the gas phase during the TPD, and the sum O_2+O_3 does not fit the dashed line, as opposed to what observed on a water substrate (see Figure 4.23 and *Minissale et al.* 2013). The large deficit in O atoms (namely the sum of O_x) is due to the CD. The excess of chemical energy of the newly formed molecule is partly transferred to kinetic energy (by bouncing on the substrate), and the desorption may occur. We can also remark that in panel *a* of Figure 4.22 the O_2/O_3 ratio depends on the coverage, or more precisely, that the number of missing O is decreased with the coverage.
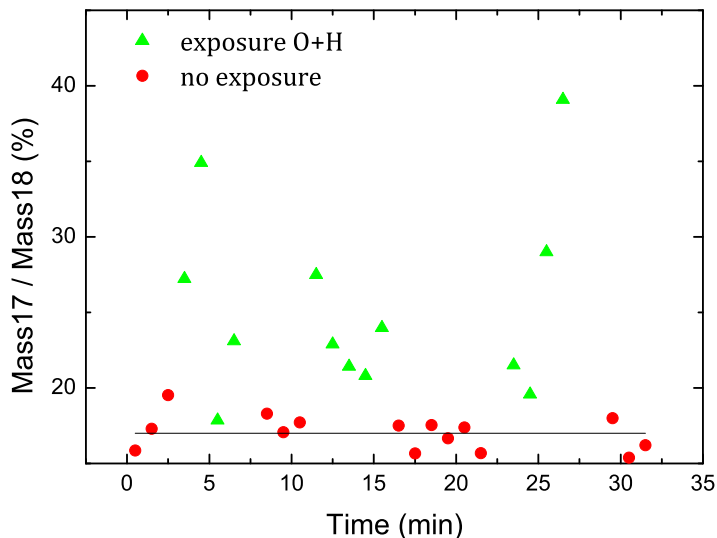
Figure 4.21: Variation of M17/M18 ratio in DED measurements of O+H on graphite held at 10 K.

To get a better proof of the change in chemical desorption efficiency, we re-plot the results of panel a in panel b of Figure 4.22. We use as x-axis the fraction of O_2 (fO_2) and as y-axis the fraction of O_3 (fO_3). fO_2 is obtained by dividing the yield of O_2 (YO_2) by the dose D_f (defined as the flux Φ multiplied by the exposure time t_f), and the fraction of O_3 is calculated the same way ($fO_3 = \frac{YO_3}{D_f}$). We can define the efficiency of chemical desorption as f_{CD} =1 - fO_3-fO_2. The equality fO_3+fO_2=1 means that all atoms have remained on the surface before the TPD and so the chemical desorption is fully inefficient. We have represented this case using a broad black line on Figure 4.22. On the contrary, if there is no O_2 or O_3 desorption during TPD, all the atoms should have gone in gas phase during the reaction, f_{CD} =1, and the chemical desorption is fully efficient. Panel b of Figure 4.22 shows that f_{CD} changes for experiments where the dose has been changed (red stars, same data as in panel a). The lowest coverage case lies just above the dotted line which corresponds to 50 % of chemical desorption, while the highest coverage lies above the 18 % chemical desorption line. With the increase of the coverage, there is a rather vertical shift upward. This shift illustrates two facts: (i) the O_2 production saturates because O_2 molecules are transformed in O_3 molecules by new incoming O atoms; (ii) the larger the coverage, the lower the chemical desorption efficiency. We want to stress that for increasing doses we need to increase exposure times, keeping the flux of the atomic beam constant. The measurement is made at the end of the exposure, but the coverage evolves during the exposure phase. Any experimental point does not represent a constant coverage, but the evolution from zero to the final coverage. Actually, our experiments represent an integration over the time of events. From stars in panel b of Figure 4.22, it is clear that chemical desorption efficiency is reduced with the coverage, but the experimental method partly conceals the correlation between the coverage and the chemical desorption, because the coverage is not the parameter directly varied. For this reason we performed a second set of experiments. This time, while keeping constant the dose (0.5 ML) - using the same evolution of the coverage (at first approximation) - we incremented the surface temperature for different experiments from 8 to 25 K (above 25 K O_2 starts to desorb). A change of the surface temperature varies the diffusion properties, and as a consequence, changes the balance of the two reactions (R0.1) and (R0.2) and the final products. These experiments are represented with blue circles in panel b of Figure 4.22. All these points are located around the 18% dashed line. The O_2/O_3 balance changes: the higher the surface temperature, the larger is the fO_3, as expected. More surprisingly, the
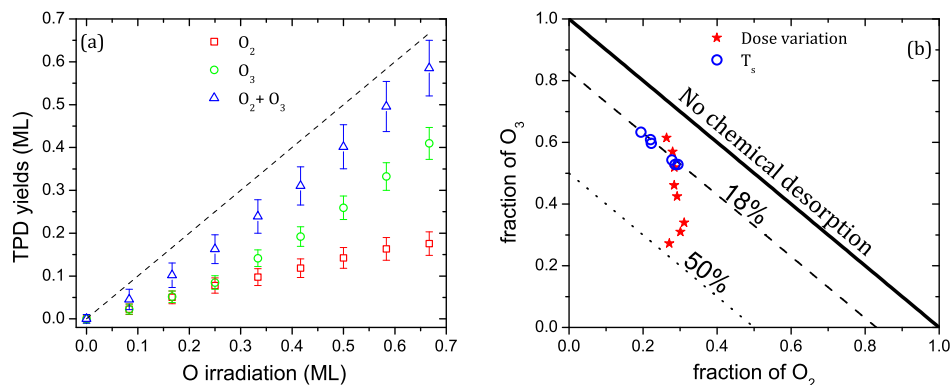
Figure 4.22: Adapted from *Minissale&Dulieu* (2014b). Panel *a*: integrated TPD spectra yields of O_2 (squares) and O_3 (circles) obtained after exposition of different doses of O (75 %) and O_2 (25 %) on oxidized HOPG. The straight dashed line corresponds to a full conservation of the O atoms on the form of O_2 and O_3. Panel *b*: fraction of O_3 vs O_2. Red stars correspond to experiments shown in panel *a* (variation of the dose at fixed surface temperature, 10 K), and blue circles correspond to different depositions of fixed dose (0.5 ML) at different surface temperatures (8, 10, 15, 20, 22, and 25 K). Solid, dashed and dotted lines are obtained using f_{CD}=0, 18, and 50 %, respectively.
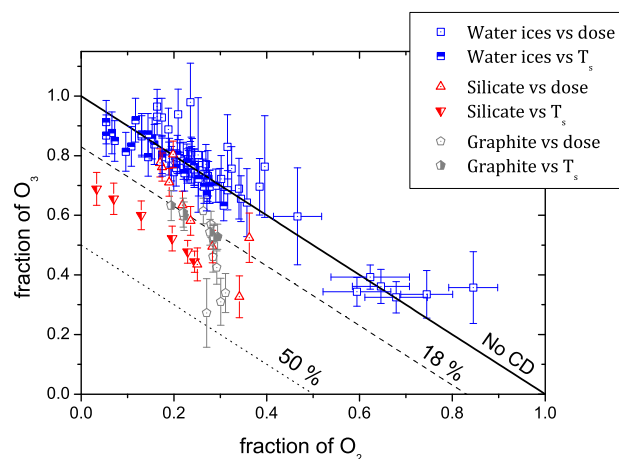
Figure 4.23: Fraction of O_3 vs O_2 for different experiments on different surfaces. See legend and caption of Figure 4.22, panel *b*

chemical desorption seems to be rather insensitive to the final-product ratio. In the same way we re-plot data obtained on other surfaces (amorphous silicate and different morphology of water ices), as shown in Figure 4.23. We notice that on water ices all data (vs T_s and vs coverage) are on the no-CD line. Data on silicate show a behavior similar to the ones of graphite: the chemical desorption seems to be rather insensitive to the final product ratio for data vs T_s, while it decreases for data vs coverage. It should be noted that on silicate this decrease is less important that on graphite.

4.3.2.2   Model and discussion

To analyze our experimental results, we can consider how the populations adsorbed on the substrate evolve with time (or coverage). In particular, there are three populations evolving with the deposited dose: O(t), O_2(t), and O_3(t). However, we are only able to measure O_2(t_f) and O_3(t_f) final populations, represented through grey circles on Figure. 4.24. The evolution of the two populations has two origins: external incoming fluxes of O and O_2 molecules (represented by broad arrows), and chemical evolution of the populations. O
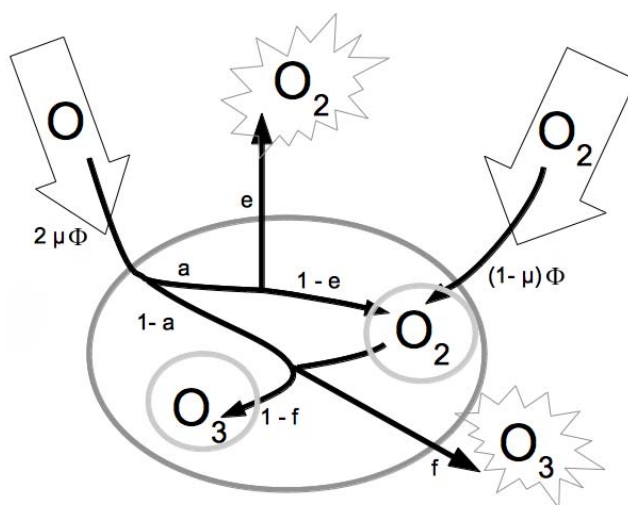
Figure 4.24: Adapted from *Minissale&Dulieu* (2014b). Schematic view of the processes occurring on the surface. *e* and *f* are the chemical desorption probability of (R0.1) and (R0.2) respectively.
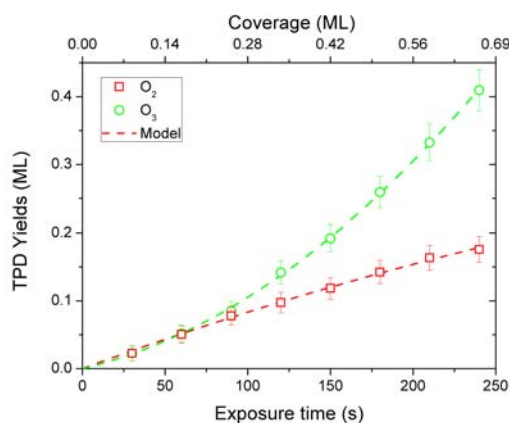
Figure 4.25: Adapted from *Minissale&Dulieu* (2014b). Red squares and green circles: O_2 and O_3 experimental yields (in ML) obtained after different exposure times (in *seconds* in the lower x-axis, in *ML* in the upper x-axis). Lines: best fit and computation of O_2 and O_3 populations, assuming a linear decrease of chemical desorption with the coverage of (R0.1), and no chemical desorption from (R0.2).

atoms undertake the two reactions (R0.1) and (0.R2). The branching ratio between (R0.1) and (R0.2) is expressed by the parameter *a*. If *a*=1, only (R0.1) takes place, if *a*=0, only (R0.2) takes place. Clearly the balance between the two reactions is dependent on the populations, so from one experiment to another, and even during each experiment, *a* varies ranging always between 0 and 1. The parameter *e* describes the chemical desorption of (R0.1), and the parameter *f* describes the chemical desorption of (R0.2). If *e*=1, all the O_2 formed via O+O reactions promptly desorb. Parameters *e* and *f* actually describe the chemical desorption process.

The details of equations are presented in *Minissale&Dulieu* (2014b); Figure 4.25 shows the comparison of model results (red and green lines, respectively O_2 and O_3) with experimental points (squares and circles, respectively O_2 and O_3). The match is excellent, and the deviation can be attributed to experimental uncertainties rather than to the poor level of the simulations. We note that an excellent match can as well be obtained with a *f* parameter frozen to few %; however, the linear dependence cannot be straightforwardly demonstrated. In fact, the accuracy of the experimental data is not sufficient to analize the case of *e* and *f* with values of only a few %. Model results can be summarized as follows:

a the chemical desorption is mostly carried by the O+O reaction with an efficiency close to 80 % (78 ±5 %) on a bare oxidized graphite. The other reaction, O+O_2, has a more limited reactive desorption efficiency, set to 5 ± 5%.

b The chemical desorption is highly dependent on the presence of other molecules adsorbed on the substrate and decreases linearly with the surface coverage.

To understand these statements, we have to make clear that the two involved reactions are different in many aspects: the masses and the degrees of freedom of products, the binding energy of reactants, and the enthalpy of reaction. Table 4.3 regroups the different properties of the reactions and their products. From Table 4.3, we can infer why chemical desorption

Table 4.3: List of different physical properties of reactions (R0.1) and (R0.2): mass of reaction products expressed in *g/mol*; degrees of freedom of reaction products; enthalpy of formation of each reaction expressed in *kJ/mol*; binding energy of (R0.1) and (R0.2) products (O_2 and O_3, respectively) expressed in *kJ/mol*.

Reaction	Mass (g/mol)	Degrees of freedom	Δ_f	$E_{binding}$ (kJ/mol)	CD %
R0.1 O+O →O_2	32	6	498	10	79
R0.2 O+O_2 →O_3	48	9	106	17.5	5

of (R0.1) is larger than that of (R0.2) , by looking at each of the following parameters:

1. *Enthalpy of formation.* As already stated, the chemical desorption process requires some energy excess: the source of the energy is certainly the enthalpy of formation, and we can see that (R0.1) has a larger available energy with respect to (R0.2).

2. *Degrees of freedom.* The initial energy shall be spread among more degrees of freedom in the case of O_3 than in the case of O_2. The share of energy available for the motion perpendicular to the surface (required for desorption) is more limited in the case of O_3. So the energy available for desorption favors chemical desorption of O_2.

3. *Binding energy.* It is a limiting factor, since molecules have to overcome a binding energy barrier to desorb. Here again, (R0.1) is favored thanks to a lower binding energy.

4. *Mass of newly formed molecule.* It may have an indirect impact on the chemical desorption. Actually, phonon propagation is dependent on the mass of the colliding molecule with the surface. It is known that light molecules such as H_2 have a rather weak sticking coefficient (about 0.3 at room temperature) with surfaces indicating a poor energy transfer (*Chaabouni et al.* 2012b). On the contrary heavier ones, like CO or O_2, have large (> 0.9) sticking coefficients (*Bisschop et al.* 2006). Of course, it depends on the type of surface, and, in some cases, collisions can be treated classically and an effective mass of the surface can be found. The analysis of measurements of hyperthermal O_2 scattered from a graphite surface shows that the effective mass of 1.8 graphite carbon ring ($\simeq$ 130 a.m.u.) can be adopted (Hayes et al. 2012). In our case, we cannot directly use this value since we use oxidized graphite, although treating the graphitic surface as in its entirety can be a good approximation. The collision is not done with a unique carbon atom, or eventually a pair, or even a ring, it is a collective response of the surface. We can use then an effective mass quite larger than the mass of O_2 and O_3. To estimate the energy transfer for each molecule, we use a classic elastic collision as zero order approximation, and check the kinetic energy transfer. If the impactor has a mass m and the immobile target has mass M, thus the kinetic energy retained after collision for m can be written as follows:

$$\epsilon = \left(\frac{m-M}{M+m}\right)^2 \tag{4.9}$$
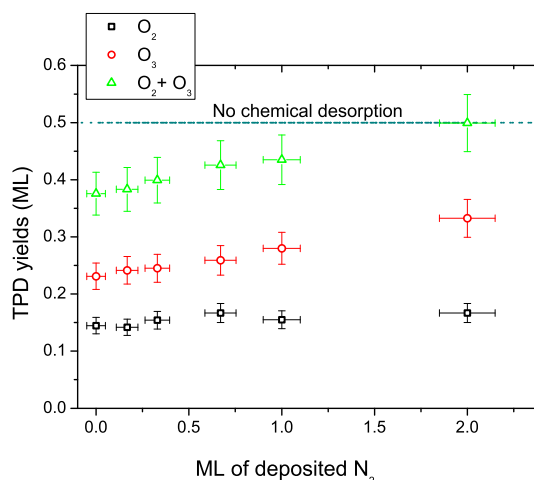
Figure 4.26: Adapted from *Minissale&Dulieu* (2014b). O_2 (black squares), O_3 (red circles) and their sum (green triangles) obtained after 0.5 ML of beam exposure as a function of the dose of N_2 molecules previously deposited on the oxidized graphite sample. The dark cyan dashed line corresponds to no chemical desorption.

Using m=32 or 48 a.m.u., and M=130 a.m.u., we find $\epsilon_{O_2} = 37\%$ and $\epsilon_{O_3} = 21\%$. Once again, the mass parameter favors the chemical desorption of O_2 molecules, because they keep more kinetic energy after the collision with the surface ($\epsilon_{O_2} > \epsilon_{O_3}$).

All the four parameters are in favor of (R0.1) and therefore our first experimental statement (statement a) is fully explained. The second one (statement b) that deals with the coverage may be explained through the fourth parameter. The energy transfer has higher values if the molecule collides with another adsorbed species: all the energy is transferred in case of equivalent mass molecules, and 0.96 in case of O_3-O_2 collisions. In other words, all the kinetic energy of the newly formed molecules is transferred to another adsorbed molecule upon collision. *Minissale&Dulieu* (2014b) have tested successfully this scenario by adding a non reactive molecule (N_2) on the substrate. Figure 4.26 shows the influence on CD of a variable amount of pre-deposited N_2. Total yields increase with the dose of N_2 pre-adsorbed on the surface. The CD process vanishes progressively and disappears between 1 and 2 pre-adsorbed layers of N_2. These experiments show the importance of the coverage from a different point of view, that is an efficient energy transfer between newly formed molecules and the molecules adsorbed in the vicinity of the formation site.

4.3.3 Conclusion

In this section, we have described some aspects of the chemical desorption process. We have presented some relevant experiments and we have shown the importance of different parameters for the CD efficiency (substrates, enthalphy, coverage, and so on). Here we report a list of CD efficiencies for different reactions on three different surfaces (np-ASW, amorphous silicate, and oxidized graphite). Some of the reactions used to evaluate CD are presented in the next chapter. Other reactions have been discussed shortly in this thesis and we need further experiments to give a quantitative and precise evaluation of their CD efficiency.

We clearly claim in Sec. 4.3.2 that CD efficiency can be explained by looking essentially at 4 physical parameters of the reaction: (1) exothermicity of reaction (ΔH), (2) mass, (3) degrees of freedom (DF), and (4) binding energy of products. Here we show that using the following law

$$CD = e^{-\frac{E_{binding} \times DF}{\epsilon \times \Delta H}} \tag{4.10}$$

we are able to calculate the CD efficiency. A comparison of model and experimental results for some reactions is shown in Figure 4.27. Model results (red hexagons and green squares)

Table 4.4: List of experimental CD efficiencies for different reactions on three different surfaces (np-ASW, amorphous silicate, and oxidized graphite). For the cases in which we were not able to measure quantitatively the CD efficiency, we provide upper or lower limits. We list theoretical CD efficiencies calculated for an a oxidized graphite.

Experiments	Method		Reaction	Desorbing product	Experimental CD efficiency			Theoretical CD efficiency
	DED	TPD			np-ASW	Amorphous Silicate	Oxidized HOPG	Oxidized HOPG
				(eV)			(%)	
O+H	√	√	O+H	OH	25 ± 15*	–	50 ± 25*	41
			OH+H	H_2O	30 ± 15*	–	50 ± 25*	28
O$_2$+H	√	√	OH+H	H_2O	$<40\pm20$⊛	$<70\pm20$⊛	$<80\pm20$⊛	
			O_2+H	O_2H	<8*	10 ± 10⊛	–	1.7
			O_2H+H	H_2O_2	<8*	<5⊛	–	
			O_2H+H	2 OH	<8*	<5⊛	–	
			H_2O_2+H	H_2O+OH	<5*	<5⊛	–	
O$_3$+H	√	√	O_3+H	O_2+OH	–	<10⊛	<8*	
			OH+H	H_2O	–	80 ± 20⊛	–	
O+O	√	√	O+O	O_2	<5ℵ	40 ± 10^{a}♀	80 ± 10^{a}♂	71
			O_2+O	O_3	<5ℵ	<5♀	<5♂	0.9
N+N	√	√	N+N	N_2	$>50^{b}$*	$>70^{b}$*	$>70^{b}$*	85
CO+H	√	√	CO+H	HCO	–	–	10 ± 8*	0.5
			HCO+H	CO	–	–	40 ± 20*	43
			HCO+H	H_2CO	–	–	<8*	8
H$_2$CO+H	√	√	H_2CO+H	CH_3O	–	–	<8*	
			H_2CO+H	HCO	–	–	10 ± 5*	
			HCO+H	CO	–	–	40 ± 20*	
			HCO+H	H_2CO	–	–	10 ± 5*	
			CH_3O+H	CH_3OH	<8*	–	<8*	
Ar+H	√	√	Ar+H	Ar	–	<5*	–	
NO+H/O/N	X	√	many	many	<8*	<8*	<8*	
CO+O	√	√	HCO+H	H_2CO	<5*	–	<5*	
H$_2$CO+O	X	√	H_2CO+O	CO_2	<10*	–	<10*	
CH$_3$OH+H	√	√	CH_3OH+H	CH_3OH	<8*	–	<8*	5.3
CH$_3$OH+O	√	√	CH_3OH+O	CH_3OH	<8*	–	<8*	

√ and X are used to indicate if the experimental procedure (DED or TPD) have been used or not, respectively; [a] CD decreases as a function of coverage; [b] experiments performed with excited particles (see Sec. 2.2.2.3); ⚥ *Chaabouni et al.* 2012; ⊛ *Dulieu et al.* 2013; ℵ *Minissale et al.* 2013; ♀ *Minissale et al.* 2014a; ♂ *Minissale&Dulieu* 2014b; * This work.

have been obtained by using two different values of ϵ: for red hexagons $\epsilon = 0.4$ while for green squares it is given by Eq. 4.9. We remark that this second choice of the ϵ value gives a better fit with respect to $\epsilon = 0.4$. Nevertheless, some improvements have to be made both from an experimental (to reduce error bars) and a theoretical point of view.

Bibliography

4.01 Amiaud, L., Fillion, J. H., Baouche, S., Dulieu, F., Momeni, A., and Lemaire, J. L., *Interaction of D_2 with H_2O amorphous ice studied by temperature-programed desorption experiments*, The Journal of Chemical Physics, Volume 124, Issue 9, pp. 094702-094702-9 (2006)

4.02 Amiaud, L., Dulieu, F., Fillion, J.-H., Momeni, A., and Lemaire, J. L., *Interaction of atomic and molecular deuterium with a nonporous amorphous water ice surface between 8 and 30 K*, The Journal of Chemical Physics, Volume 127, Issue 14, pp. 144709-144709-12 (2007)

4.03 Bisschop, S. E., Fraser, H. J., Öberg, K. I., van Dishoeck, E. F., and Schlemmer, S., *Desorption rates and sticking coefficients for CO and N_2 interstellar ices*, Astronomy and Astrophysics, Volume 449, Issue 3, pp. 1297-1309 (2006)

4.04 Bulanin, K. M., Alexeev, A. V., Bystrov, D. S., Lavalley, J. C., and Tsyganenko, A. A., *IR Study of Ozone Adsorption on SiO_2*, The Journal of Chemical Physics, Volume 98, pp. 5100-5103 (1994)
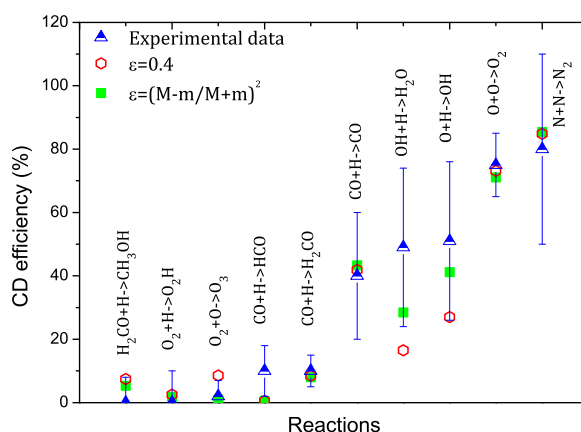
Figure 4.27: Comparison between calculated and experimental CD efficiency for the set of reactions investigated in this work.

4.05 Chaabouni, H., Minissale, M., Manicò, G., Congiu, E., Noble, J. A., Baouche, S., Accolla, M., Lemaire, J. L., Pirronello, V., and Dulieu, F., *Water formation through O_2 + D pathway on cold silicate and amorphous water ice surfaces of interstellar interest*, The Journal of Chemical Physics, Volume 137, Issue 23, pp. 234706-20 (2012)

4.06 Chaabouni, H., Bergeron, H., Baouche, S., Dulieu, F., Matar, E., Congiu, E., Gavilan, L., and Lemaire, J. L. *Sticking coefficient of hydrogen and deuterium on silicates under interstellar conditions*, Astronomy and Astrophysics, Volume 538, id. A128, 6 pp. (2012b)

4.07 Clough, S. A., and Kneizys, F. X., *Coriolis Interaction in the ν_1 and ν_3 Fundamentals of Ozone*, The Journal of Chemical Physics, Volume 44, pp. 1855-1861 (1966)

4.08 Congiu, E., Matar, E., Kristensen, L. E., Dulieu, F., and Lemaire, J. L., *Laboratory evidence for the non-detection of excited nascent H_2 in dark clouds*, Monthly Notices of the Royal Astronomical Society: Letters, Volume 397, Issue 1, pp. L96-L100 (2009)

4.09 Congiu, E., Chaabouni, H., Laffon, C., Parent, P., Baouche, S. and Dulieu, F., *Efficient surface formation route of interstellar hydroxylamine through NO hydrogenation. I. The submonolayer regime on interstellar relevant substrates*, The Journal of Chemical Physics, Volume 137, p. 054713 (2012)

4.10 Congiu, E., Minissale, M., Baouche, S., Chaabouni, H., Moudens, A., Cazaux, S., Manicò, G., Pirronello, V., and Dulieu F., *Efficient diffusive mechanisms of O atoms at very low temperatures on surfaces of astrophysical interest*, Faraday Discussion 168 (2014)

4.11 Dulieu, F., Amiaud, L., Congiu, E., Fillion, J.-H., Matar, E., Momeni, A., Pirronello, V. and Lemaire, J. L., *Experimental evidence for water formation on interstellar dust grains by hydrogen and oxygen atoms*, Astronomy and Astrophysics, Volume 512, p. A30 (2010)

4.12 Dulieu, F., Congiu, E., Noble, J., Baouche, S., Chaabouni, H.,Moudens, A., Minissale, M., and Cazaux, S., *How micron-sized dust particles determine the chemistry of our Universe*, Nature Scientific Reports, Volume 3, id. 1338 (2013)

4.13 Govers, T. R., Mattera, L., Scoles, M., *Molecular beam experiments on the sticking and accommodation of molecular hydrogen on a low-temperature substrate*, The Journal of Chemical Physics, Volume 72, pp. 5446-5455 (1980)

4.14 Hama, T., Kuwahata, K., Watanabe, N., Kouchi, A., Kimura, Y., Chigai, T., and Pirronello, V., *The Mechanism of Surface Diffusion of H and D Atoms on Amorphous Solid Water: Existence of Various Potential Sites*, The Astrophysical Journal, Volume 757, p. 185 (2012)

4.15 Hayes, W. W., Oh, J., Kondo, T., Arakawa, K., Saito, Y., Nakamura, J., Manson, J. R., *Scattering of O_2 from a graphite surface*, Journal of Physics: Condensed Matter, Volume 24, Issue 10, article id. 104010, 9 pp. (2012)

4.16 Ioppolo, S., Cuppen, H. M., Romanzin, C., van Dishoeck, E. F., and Linnartz, H., *Laboratory Evidence for Efficient Water Formation in Interstellar Ices*, The Astrophysical Journal, Volume 686, p. 1474 (2008)

4.17 Jing, D., He, J., Brucato, J. R., Vidali, G., Tozzetti, L., and De Sio, A., *Formation of Molecular Oxygen and Ozone on Amorphous Silicates*, The Astrophysical Journal, Volume 756, Issue 1, article id. 98, pp. 7 (2012)

4.18 Karssemeijer, L. J., Pedersen, A., Jónsson, H., and Cuppen, H. M., *Long-timescale simulations of diffusion in molecular solids*, Physical Chemistry Chemical Physics, Volume 14, Issue 31, p. 10844 (2012)

4.19 Kimmel, J., Engelke, F., and Zare, R. N., *Novel method for the production of finely spaced Bradbury-Nielson gates*, Review of Scientific Instruments, Volume 72, Issue 12, pp. 4354-4357 (2001)

4.20 Leger, A., J. Klein, S. de Cheveigne, C. Guinet, D. Defourneau, and M. Belin, *The 3.1 micron absorption in molecular clouds is probably due to amorphous H_2O ice*, Astronomy and Astrophysics, Volume 79, pp. 256-259 (1979)

4.21 Messiah, A., *Quantum Mechanics*, Wiley, Amsterdam (1973)

4.22 Minissale, M., Congiu, E., Baouche, S., Chaabouni, H., Moudens, A., Dulieu, F., Cazaux, S., Accolla, M., Manicò, G., and Pirronello, V., *Quantum Tunneling of Oxygen Atoms on Very Cold Surfaces*, Physical Review Letter, Volume 111, pp. 053201-5 (2013)

4.23 Minissale, M., Congiu, E., and Dulieu, F., *Oxygen diffusion and reactivity at low temperature on bare amorphous olivine-type silicate*, The Journal of Chemical Physics, Volume 140, pp. 074705 (2014a)

4.24 Minissale, M. and Dulieu, F., *Influence of surface coverage on the chemical desorption process*, The Journal of Chemical Physics, Volume 141, Issue 1, p. 014304 (2014b)

4.25 Minissale, M., Baouche, S., Chaabouni, H., Congiu, E., Moudens, A., and Dulieu, F., *Solid-state formation of CO_2 via the $H_2CO + O$ reaction*, submitted to Astronomy and Astrophysics (2014s)

4.26 Miyauchi, N., Hidaka, H., Chigai, T., Nagaoka, A., Watanabe, N., and Kouchi, A. *Formation of hydrogen peroxide and water from the reaction of cold hydrogen atoms with solid oxygen at 10 K*, Chemical Physics Letters, Volume 456, p. 27 (2008)

4.27 Mokrane, H., Chaabouni, H., Accolla, M., Congiu, E., Dulieu, F.,Chehrouri, M., and J. L. Lemaire, *Experimental Evidence for Water Formation Via Ozone Hydrogenation on Dust Grains at 10 K*, The Astrophysical Journal, Volume 705, p. L195 (2009)

4.28 Mott, N. F., and Davis, E., *Electronic Processes in Non Crystalline Materials*, Clarendon press (1979)

4.29 Mott, N. F., *Conduction in non-crystalline materials*, Philosophical Magazine, Volume 19, Issue 160, pp. 835-852 (1969)

4.30 Oura, K., Lifshits, V. G., Saranin, A. A., Zotov, A. V., and Katayama, M. *Surface Science: an introduction*, Springer, Berlin (2003)

4.31 Pollak, M., *A percolation treatment of dc hopping conduction*, Journal of Non-Crystalline Solids, Volume 11, Issue 1, pp. 1-24 (1972)

4.32 Senevirathne, B., Andersson, S., Dulieu, F., and Nyman, G., *Hydrogen atom mobility on crystalline and amorphous ice*, Physical Chemisty Chemical Physics, submitted manuscript (available at: https://dl.dropboxusercontent.com/u/9601281/Senevirathne_-etal2014.pdf)

4.33 Smoluchowski, R., *Rate of H_2 formation on amorphous grains*, Astrophysics and Space Science, Volume 75, Issue 2, pp. 353-363 (1981)

4.34 Smoluchowski, R., *Formation of H_2 on amorphous ice grains and their importance for planetary atmospheres*, Astrophysics and Space Science, Volume 65, Issue 1, pp. 29-38 (1979)

4.35 Ward, M. D., and Price, S., *Thermal Reactions of Oxygen Atoms with Alkenes at Low Temperatures on Interstellar Dust*, The Astrophysical Journal, Volume 741, pp. 121-130 (2011)

4.36 Wolff, A., Lohmar, I., Krug, J., Frank, Y., and Biham, O. *Diffusion-limited reactions on a two-dimensional lattice with binary disorder*, Physical Review E, Volume 81, Issue 6, id. 061109 (2010)

Surface Chemistry

5.1 Water formation via O$_2$+H(D): the effect of the substrate

Oxygen is the third most abundant element in the Universe (Suess&Campbell 1956) after Hydrogen and Helium, and is present in the solid phase of icy grain mantles in the interstellar medium. For this reason, over the last decade a number of independent laboratory experiments involving oxygen has been performed. In particular, in many experimental works (*Ioppolo et al.* 2008; *Dulieu et al.* 2010; *Mokrane et al.* 2009; *Cuppen et al.* 2010; *Jing et al.* 2011; *Oba et al.* 2012; *Chaabouni et al.* 2012) all the possible chemical pathways involving O and H (molecules and/or atoms, i.e., O, O$_2$, O$_3$, OH, H and H$_2$) in solid phase were investigated. Three different hydrogenation routes for water formation have been identified: O + H, O$_2$ + H, and O$_3$ + H. These studies demonstrated that water is the principal product of such reactions. We will not discuss exhaustively the solid state formation of water ice through these routes. The goal of this section is to show the effect of the substrate on water formation efficiency in the submonolayer and monolayer regimes, and the reaction used to achieve this purpose is the O$_2$+D reaction.

5.1.1 Experimental

Experiments on water formation from O$_2$ and D atoms have been performed at 10 K on different surface samples: (i) silicate (as described above), (ii) non-porous amorphous solid water (np-ASW) ice, and (iii) porous amorphous solid water (p-ASW) ice. The np-ASW ice film with a thickness of about 50 layers is grown at 110 K. The p-ASW ice film with 10 layers of thickness is grown by background vapor deposition on top of the compact water ice substrate kept at 10 K using the same microchannel array doser placed in the remote position. The exposure of O$_2$ molecules and D atoms is always done at 10 K. Under our experimental conditions, 1 ML of D-atoms corresponds to 7 min of D deposition time, while 1 ML of O$_2$ ice is obtained after 6 min of O$_2$ exposure time.
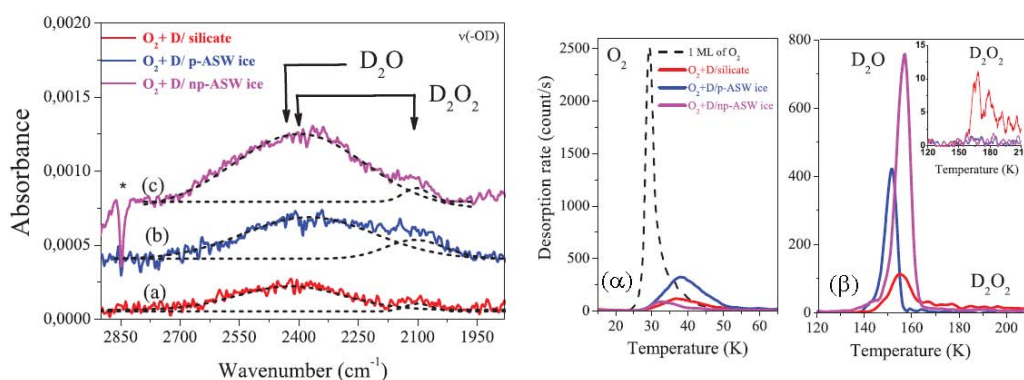
Figure 5.1: Adapted from *Chaabouni et al.* (2012). RAIRS spectra of D_2O and D_2O_2 (left panel) and desorption peaks of O_2, D_2O, and D_2O_2 (right panel) after the exposure of 1 ML of solid O_2 and 2.0 ML of D atoms on different substrates held at 10 K: (a) amorphous silicate, (b) p-ASW ice, and (c) np-ASW ice. The dashed curves at left are gaussian fits. (The adsorption band at 2850 cm^{-1} is due to an impurity.)

5.1.2 Results and discussion

Left panel and right panel of Figure 5.1 show respectively the RAIR spectra and TPD curves after the exposure of 1 ML of solid O_2 and 2.0 ML of D atoms on different substrates held at 10 K: (a) amorphous silicate, (b) p-ASW ice, and (c) np-ASW ice. In the RAIR spectra, we assign the broad absorption peak at around 2404 cm^{-1} to the overlapping of D_2O and D_2O_2 -OD stretching vibrations modes. The small peak at around 2107 cm^{-1} is attributed to the ν_6 vibration mode of D_2O_2 (*Jing et al.* 2011). In addition, a small peak at around 1215 cm^{-1} is attributed to OD-bending mode of D_2O and a second small peak at around 1050 cm^{-1} is attributed to the OD-bending of D_2O_2. (*Miyauchi et al.* 2008 ; *Jing et al.* 2011) Right panel of Figure 5.1 shows three sets of TPD: between 10 K and 60 K where the O_2 desorption occurs, 120 K and 180 K for D_2O, and 140 K and 220 K for D_2O_2. All these results clearly show a difference in the amount of reactants consumed (O_2) and products formed (D_2O and D_2O_2). By using RAIRs results (see *Chaabouni et al.* 2012 for details), we estimated the amount of D_2O water molecules formed on each substrate held at 10 K to be ≈ 0.37ML on the silicate surface, ≈ 0.89ML on the p-ASW ice, and ≈ 1.25ML on np-ASW ice surfaces. These results give a lower limit of the O_2 consumed (we only have to multiply by a factor of 2). It appears that $\geq 19\%$ of the initial coverage of O_2 has to be consumed on the silicate surface, $\geq 45\%$ on the p-ASW ice, and $\geq 63\%$ on the np-ASW ice surfaces. From the TPD results we can independently check the amount of O_2, too. We obtained that, on the silicate substrate, most of O_2 molecules (96%) are consumed by D-atoms and only 18% of O_2 molecules are used to form D_2O and 24% to form of D_2O_2[1]. While in the case of the np-ASW ice substrate, the yield of D_2O molecules reaches its maximum of about 55% and that of D_2O_2 5% when 85% of O_2 molecules are destroyed by D atoms. This difference between consumed reactants and products formed can be explained through the chemical desorption process. Actually RAIRS and TPD experiments showed that the efficiency of D_2O water formation depends strongly on the substrate, like the case of O_2 formation, discussed before (*Minissale&Dulieu* 2014c). The fraction of D_2O water ice formed on the surface of the silicate at 10 K was found to be $\approx 20\%$, two and three times lower than the fractions of D_2O water molecules formed on the porous amorphous water ice ($\approx 45\%$) and the nonporous amorphous water ice ($\approx 55\%$-60%) surfaces, respectively. We can fit our data through the model described in Chapter 3 by using two parameters, the branching ratio (α) of O_2D+D reaction and the chemical desorption probability of D_2O (see Figure 5.2 and *Chaabouni et al.* (2012)). The catalytic effect of the water ice substrate enhances the reaction rates between D and O_2. An enhanced diffusion increases the O_2+D reaction efficiency by reducing D+D reaction.

---

[1]This means that each 100 O_2 molecules, 96 are consumed, 2×18 and 24 molecules of D_2O and D_2O_2 are formed, respectively; hereafter percentages refer to the total amount of O_2.
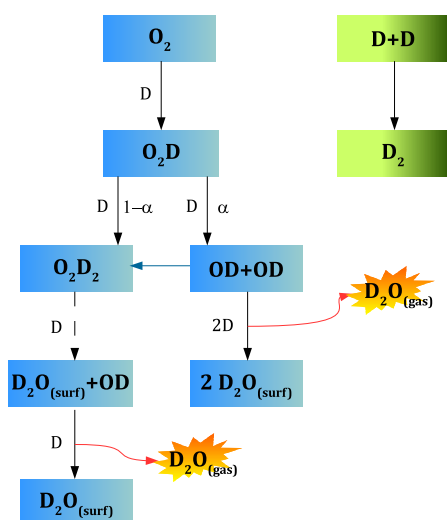
Figure 5.2: Adapted from *Chaabouni et al.* (2012). Schematic illustration showing the possible reaction routes for the formation of D_2O involving O_2 and D atoms. The solid and the broken black arrows indicate the reactions without and with activation barriers, respectively. The blue arrow indicates the reaction which is less probable on the bare silicate substrate than on amorphous water ice. Red arrows indicate when the D_2O chemical desorption can occur.

The D+OD reaction, due to its high exothermicity and low degree of freedom, is responsible for a high chemical desorption probability for water molecules. The difference between the chemical desorption rate of water molecules on silicate (80%) and on water ices (40%) can be explained in two ways:

1. O_2D+D allows ($\alpha \approx 0.7$) the formation of two OD intermediates (that do not recombine) on the silicate surface rather than water ices. On water, more OD recombines to form D_2O_2. As a consequence more D_2O molecules undergo chemical desorption on silicate.

2. If α is constant, the chemical desorption probability changes between the silicate surface and water ices, as proposed in *Minissale&Dulieu* (2014)

Very probably both mechanisms are at play. In summary the surface (and its morphology) affects surface physics (especially D diffusion and CD efficiency) that in turn modifies surface chemistry favoring some reactions and so formation of some molecules. For example H_2O_2 formation is favored on multilayer regimes, then on water surfaces, on silicate and finally on graphite. See Sec. 4.3 for a detailed discussion of the chemical desorption of the O-H system.

5.2   Nitrogen oxides chemistry

Inversely to the O/H chemistry, the O/N chemistry is a poorly studied domain. Recently a number of studies involving N/H chemistry have been reported (*Hidaoka et al.* 1995). The solid state formation of NH_3 has been discussed (*Hidaka et al.* 2011) and NO ice was shown to be a good starting point in the formation of large molecules such as NH_4NO_3 or Hydroxylamine, NH_2OH (*Congiu et al.* 2012a, 2012b; *Fedoseev et al.* 2012), one of the potential precursors of complex pre-biotic species in space (*Blagojevic et al.* 2003). Both nitric oxide and ammonia are considered important precursor species in the formation of N-containing organics. NO, specifically, is a seed for N- and O-bearing species (*Joshi et al.* 2012) such as NO_2, N_2O, HNO, HONO, HNO_3, and NH_2OH. In this section, we deal with the O/N chemistry on the solid phase and we present experimental results for NO+O, NO+O_2,

and $NO+O_3$ reactions in the solid state that mainly lead to the formation of NO_2. These results could be useful to explain the O/N chemistry in different environments:

- in Earth's atmosphere (*Atkinson* 2000), as well as in Venus' (*Watson et al.* 1979). Nitrogen oxides play a critical role in the tropospheric and stratospheric chemistry of very important compounds such as ozone (O_3) (*Toon&Tolbert* 1995), the hydroxyl radical (OH), and nitric acid (HNO_3). NO_2, in particular, can deplete ozone in two different ways, as explained in *Toon& Turco* (1991). NO and especially NO_2 are therefore considered to be very important in the formation and loss of tropospheric ozone and probably bring about climate change and global warming (*Hartmann et al.* 2000).
Oxydised nitrogen chemistry at high latitudes is very complex (*Jones et al.* 2001), and it is necessary to study both the background chemistry determining NO_x concentrations in the polar troposphere and to understand any exchange processes between snow and air.
NO_x concentrations were studied in many works (*Jones et al.* 2001; *Honrath et al.* 1999; *Ridley et al.* 2000) proposing that NO_x is produced within the snow pack, Arctic and Antarctic, and in particular upon ice particles. The present work was hence intended to study all the surface reactions involving oxide nitrogen species (NO, NO_2, N_2O etc) and affecting NO_x concentrations. We will also show that water ice is a good catalyst for these reactions.

- In the interstellar medium. O/N chemistry still remains not fully understood although molecules containing a N-O bond, like NO, N_2O and HNO have been detected in the ISM (*Listz&Turner* 1978; *Ziurys et al.* 1991, 1994; *Martin et al.* 2003). Astrochemical models predict typical NO abundances in the gas-phase, with respect to molecular hydrogen, of $f(NO/H_2) \approx 10^{-7}$-$10^{-6}$. The actual observed abundance (*Millar et al.* 1997) is about a factor 10 lower: $f(NO/H_2) \approx 10^{-8}$. This difference may be due to lacking destruction (*i.e.*, consumption) routes that have not taken correctly into account; actually large amounts of NO (up to 10 % of the gas-phase abundance) are likely to accrete on the cold (10 K) dust grains, and therefore to react with H, O, and N atoms arriving from the gas-phase.

In Sec. 4.1.2 we pointed out that the use of a O-atom beam is associated with the presence on the surface of O_2 and O_3 molecules (arriving from the gas phase or formed on the surface). For this reason, any time that we want to study a reaction involving O atoms and a species X, we need to know in advance what is the reactivity of oxygen allotropes with the X species. Therefore, in this section we present firstly $NO+O_2$ and $NO+O_3$ reactions and then the $NO+O$ reaction.

5.2.1 $NO+O_2$

In this section, we present the experimental results of NO oxidation by O_2: this reaction leads to NO_2 formation (concurrently to other nitrogen oxides) and it occurs in solid phase via the ER mechanism. The LH mechanism proved to be not efficient under our experimental conditions. This reaction has been discussed in more detail in *Minissale et al.* (2013a).

5.2.1.1 Experimental

The experiments were perfomed on four different surfaces: amorphous silicate sample, amorphous or crystalline water ice (see Sec. 2.2.1 for methodology of ice preparation), and oxidized graphite substrate. Experiments were performed through three different procedures:

1. NO deposited on top of pre-adsorbed O_2 (*a* method in Figure 5.3);

2. O_2 deposited on top of pre-adsorbed NO (*b* method in Figure 5.3);

3. NO and O_2 co-deposited on the cold sample (*c* method in Figure 5.3);
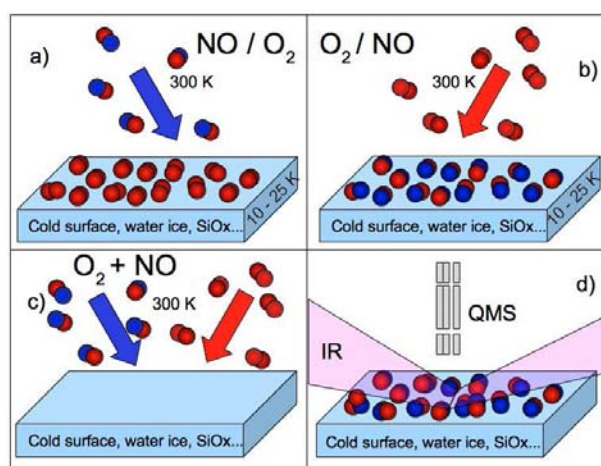
Figure 5.3: Schematic representation of our experiments. (a) NO is deposited in a layer of O_2 previously deposited on the cold sample. (b) O_2 is deposited on a layer of NO. (c) NO and O_2 are co-deposited on the cold sample. (d) The products are probed using Temperature Programmed Desorption and Reflection Absorption Infrared Spectroscopy.
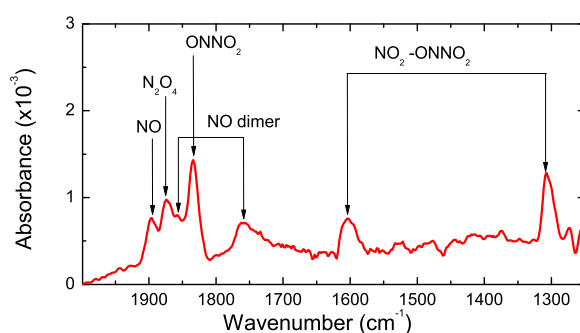
Figure 5.4: Adapted from *Minissale et al.* (2013a). The red trace shows the RAIR spectrum of 5 ML of O_2 and 2.5 ML of NO after co-deposition at 10 K. Seven spectral features due to NO, $(NO)_2$, NO_2, N_2O_3 and N_2O_4 are marked.

All the species are calibrated by saturation of the first layer (*Noble et al.* 2012). Doses are expressed in monolayers (ML) units, 1 ML corresponding to the surface fully covered with one layer of adsorbate. After deposition of the two reactants, the sample is probed using FTIR, and finally with TPD as shown in Figure 5.3d.

5.2.1.2 Result and discussion

Figure 5.4 shows the RAIRS spectrum obtained after co-deposition of 5 ML of O_2 and 2.5 ML of NO on silicate held at 10 K. We recorded infrared spectra for other doses, deposition methods, and substrates. We decided to show this spectrum because the co-deposition method prevents obvious multilayer screening effects, even though a rather "large" dose is required to detect without ambiguity the infrared bands already present at sub-monolayer coverage. We assign the band at 1897-1902 cm^{-1} to NO monomer (*Fatelay et al.* 1959), while bands at 1863 and 1776 cm^{-1} are signatures of NO dimer (*Congiu et al.* 2012a; *Fateley et al.* 1959). N_2O_4 is present at 1875 cm^{-1} (*Fulvio et al.* 2009). We have attributed the broad band at 1311 cm^{-1} to ν(N-O) symmetric s-stretching NO_2 and the one at 1605 cm^{-1} to ν(N-O) asymmetric stretching of NO_2 (*Bartram&Koel* 1989; *Schwalke et al.* 1986). Finally, the peak at 1832 cm^{-1} is attributed to the asymmetric stretch of $ONNO_2$ (*Stirling et al.* 1984) that very probably contributes to the bands at 1311 cm^{-1} and 1605 cm^{-1}. We explain the
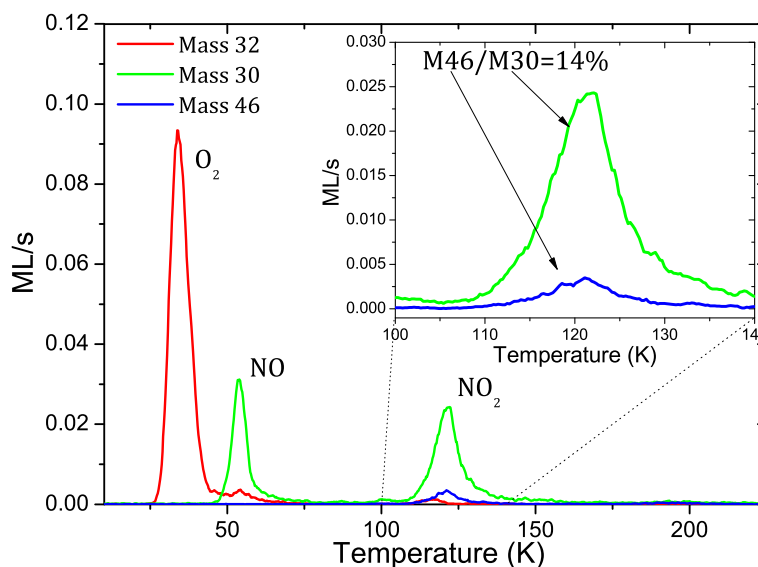
Figure 5.5: TPD curves after irradiation of 1 ML of O_2 and then of 0.5 ML of NO on silicate at 10 K. In the inset, we show a zoom of the TPD trace between 100 and 140 K of mass 46 and 30.

presence of these species through the reaction scheme shown below

$$NO + O_2 \rightarrow NO_3 \quad R2.1a$$
$$NO + NO_3 \rightarrow 2NO_2 \quad R2.1b$$
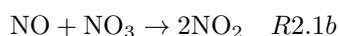
together with the following reactions

$$NO + NO \rightarrow (NO)_2 \quad R2.2$$
$$NO_2 + NO_2 \rightarrow (NO_2)_2 \quad R2.3$$
$$NO + NO_2 \rightarrow ONNO_2 \quad R2.4$$
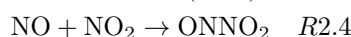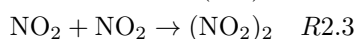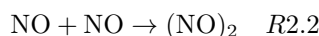
Through the spectrum in Figure 5.4 we can point out a few experimental facts:

i The presence of NO suggests the incompleteness of the reaction NO+O_2

ii all listed reactions take place at 10 K

iii NO_3 is an intermediate species with short solid-state lifetime; it is continuously formed by R2.1a and destroyed by R2.1b and its amount on the surface never increases, so we cannot distinguish its infra-red bands (*Jacox&Thompson* 2008) from the noise.

(i) and (ii) suggest that the diffusive phase is inefficient for consuming NO and probably the reactivity of R2.1 is mostly happening during the deposition phase via Eley-Rideal mechanism.
We have performed a set of TPD experiments to test the R2.1-R2.4 chemical network. We have studied the NO, O_2 and NO_2 species because we can calibrate separately the doses of these three species as for each we can obtain a pure beam. All the above statements and the R2.1-R2.4 chemical network are confirmed also by results of TPD experiments. Figure 5.5 shows TPD curves of mass 30 u.m.a., 32 u.m.a. and 46 u.m.a. after deposition of 1.0 mono-layer (ML) of O_2 and 0.5 ML of NO (O_2 first, then NO) on the silicate sample maintained at 10 K. Three peaks are evident: the first one between 25 and 45 K is due to the O_2 desorption (mass 32), the second one to the desorption of NO (mass 30) (46-65 K) and the last one is due to the NO_2 desorption. This peak is visible at mass 46 (uma), as well as at mass 30 (uma) owing to fragmentation of NO_2 within the QMS. Because of substantial cracking of nitrogen
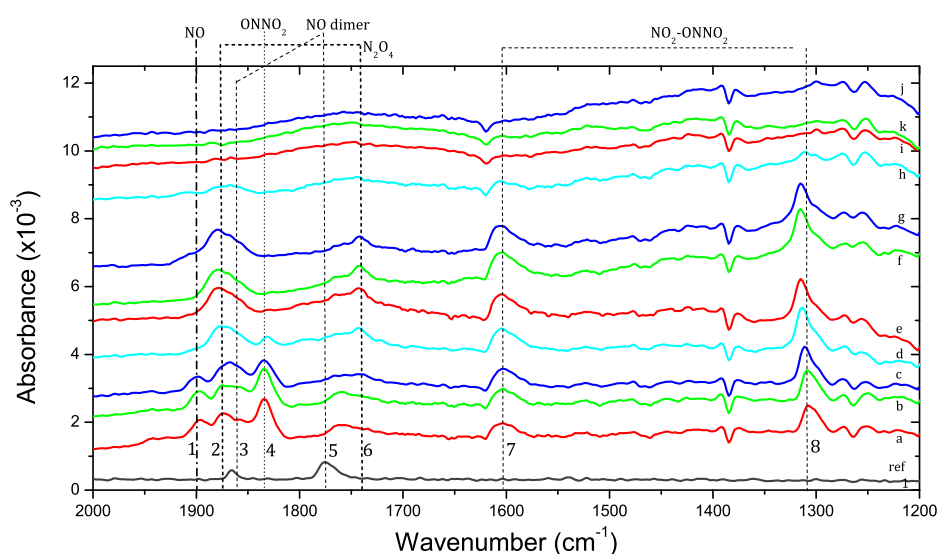
Figure 5.6: RAIR spectrum *ref* is obtained after deposition of 2.5 ML of NO at 10 K. Curves from *a* to *j* shows RAIR spectra recorded, respectively, at 10, 24, 44, 64, 84, 104, 114, 124, 134, 144, and 164 K after deposition of 5 ML of O_2 and 2.5 ML of NO on silicate held at 10 K. Eight features due to NO, $(NO)_2$, NO_2, $ONNO_2$ and N_2O_4 are marked.

dioxide in the QMS ionization head (see Sec. 2.2.2.1), only 14% of NO_2 is detected via mass 46. In the figure we have added a zoom-in window of the TPD between 100 and 140 K to appreciate the signals of mass 46 and 30, identically shaped and both peaking at 122 K. This is clearly a signature of NO_2 molecules as checked with control experiments carried out using a beam of NO_2 molecules. A further control has been carried out by studying the temperature evolution of infrared peaks. Figure 5.6 shows a reference spectrum of 2.5 ML of pure NO (in gray) and the temperature evolution of peaks after deposition of 5 ML of O_2 and 2.5 ML of NO. RAIR spectra are recorded at 10, 24, 44, 64, 84, 104, 114, 124, 134, 144, and 164 K, from *a* to *j* spectrum, respectively. With respect to the signatures shown in Figure 5.4 there is no difference, except for the presence of an additional N_2O_4 band at 1732 cm^{-1}. Figure 5.7 shows the temperature evolution of the integrated area of each peak. We used the "Peak Analyzer" function of ORIGIN software for analyzing overlapped multi-peaks, as shown in Figure 5.8 in the case of overpopulated region between 1810-1920 cm^{-1}. In Figure 5.7, we can distinguish three different region:

a before NO desorption ($T_{surface}$ <60 K);

b between NO and NO_2 desorption (60<$T_{surface}$ <120 K);

c after NO_2 desorption ($T_{surface}$ >120 K).

In region *a* all the features are already present. The NO-bond features (NO dimer and monomer, $ONNO_2$ at 1832 cm^{-1}) decrease as a function of surface temperature and they go to zero above 64 K, namely the NO desorption temperature. The increase in the NO_2-bond features (NO_2 and N_2O_4) corresponds to the decrease in NO-bond in this region. These variations are probably originated from LH process. Surface temperature increase favors surface diffusion of NO and O_2 (not yet desorbed) and, as a consequences, R2.1-R2.4 chemical network can occur via LH mechanism. When both NO and O_2 have desorbed, no reactions can occur any more, except for R2.4. This corresponds to region *b*. Finally region *c* is at temperatures higher than 110-120 K; here both the remaining IR bands start to decrease due to NO_2 and N_2O_4 desorption. In this discussion, the role of $ONNO_2$ is unclear. This molecule is ambiguous because we are not able to measure directly $ONNO_2$ through mass spectroscopy and only an infrared feature (at 1832 cm^{-1}) distinguishes $ONNO_2$ from NO_2. This feature disappears at 64 K, together with NO features, suggesting that desorption energy of $ONNO_2$
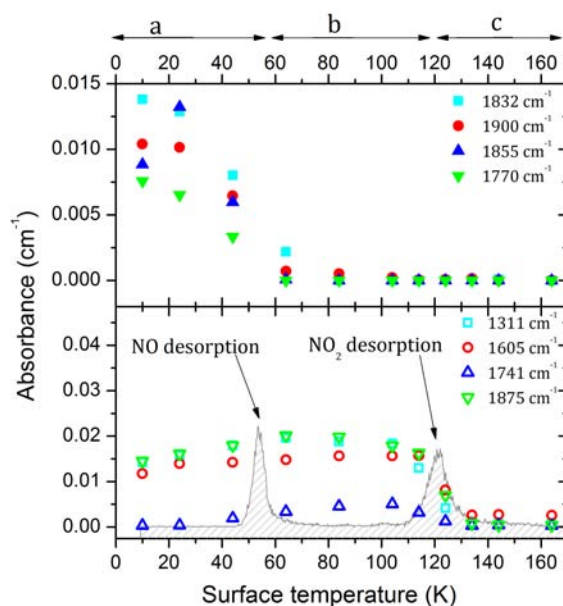
Figure 5.7: Integrated area as a function of surface temperature of the features shown in Figure 5.6. The TPD peaks added in the figure show NO and NO_2 desorption.
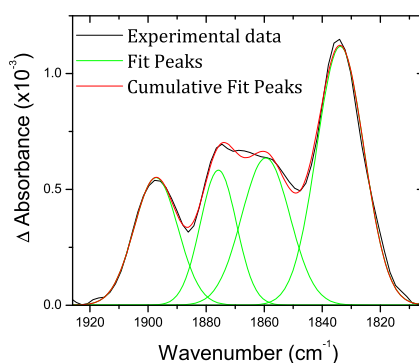
Figure 5.8: Example of overlapped multi-peaks analysis in the spectral region 1810-1920 cm^{-1}.

is similar to the NO one. *Bartram&Koel* (1989) explain this low desorption energy in two possible ways

1. from a chemical point of view, the most probable configuration of dinitrogen trioxide is ON-NO_2 (NO and NO_2 are bound through nitrogen atoms). From a physical point of view, the physisorption occurs probably through the NO part. Hence, ON-NO_2 has the same desorption energy of NO which dimerizes anyway on the surface.

2. The increase in temperature induces a dissociation of ON-NO_2. The newly formed NO molecule desorbs, while NO_2 remains on the surface (forming N_2O_4 too).

5.2.1.2.a   Initial conditions and model

Up to now, we have described only co-deposition experiments, but we have shown in Figure 5.3 that other experimental procedures have been used. In particular, we checked if a different order of deposition of the species changed the final products. The points in Figure 5.9 represent the TPD area under NO, O_2, and NO_2 curves for three different order of deposition of NO and NO_2
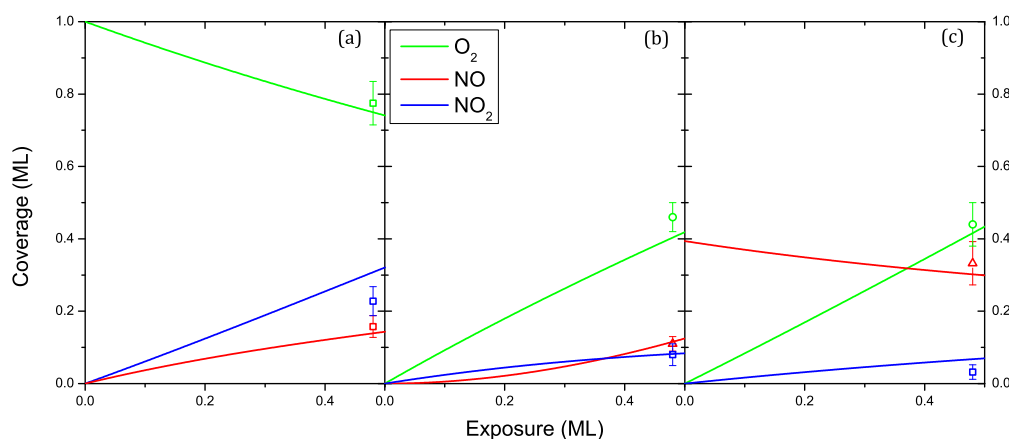
Figure 5.9: O_2, NO and NO_2 yields obtained after 1 ML of O_2 and 0.5 of NO by changing sequential order of species deposition on the surface: (a) O_2 deposited first, (b) co-deposition, (c) NO deposited first; solid curves are obtained by fitting experimental data through a rate-equation model.
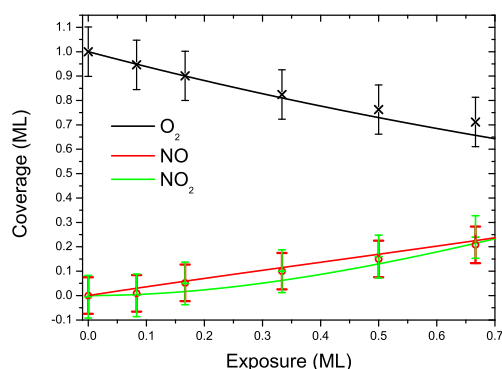
Figure 5.10: O_2, NO and NO_2 yields vs NO dose obtained after irradiation of 1 ML of O_2 with various NO exposures; solid curves are obtained by fitting the experimental data with a rate-equation model.

- panel a: 0.5 ML of NO deposited on 1 ML of O_2;

- panel b: 0.5 ML of NO + 0.5 ML of O_2 codeposited;

- panel c: 0.5 ML of O_2 deposited on 0.4 ML of NO;

The reactivity is larger when O_2 is deposited first, the lowest when NO is the first species deposited. The results displayed in Figure 5.9 demonstrate that (i) the non completeness of the reaction NO+O_2 and (ii) the reactivity occurs at 10 K, since these results confirm that not all NO is consumed and that reactions have occurred during the deposition phase. The low reaction yield of O_2-on-NO experiments can be explained by the dimerisation of NO (reaction R2.2) and the non-reactivity of the dimer with O_2. R2.1 and R2.3 are actually in competition and the dimerisation prevents from completing the reaction. Solid lines in Figure 5.9 are obtained by using a rate-equation model (see Chapter 3), in which we consider seven different species. Two are deposited on the surface, NO and O_2, and the others, NO_3, NO_2, $(NO)_2$, $(NO_2)_2$ and N_2O_3 are formed via surface reactions. Results from the model reproduce the experimental data indicating that all reactions happen via ER mechanism and NO_3 is the first intermediate as its concentration never increases. In addition, they also reproduce the non completeness of NO+O_2 reaction. In fact, R2.1 occurs with a probability of 60±10 %, indicating that the reacting cross section is about 6 Å^2, close to the geometrical
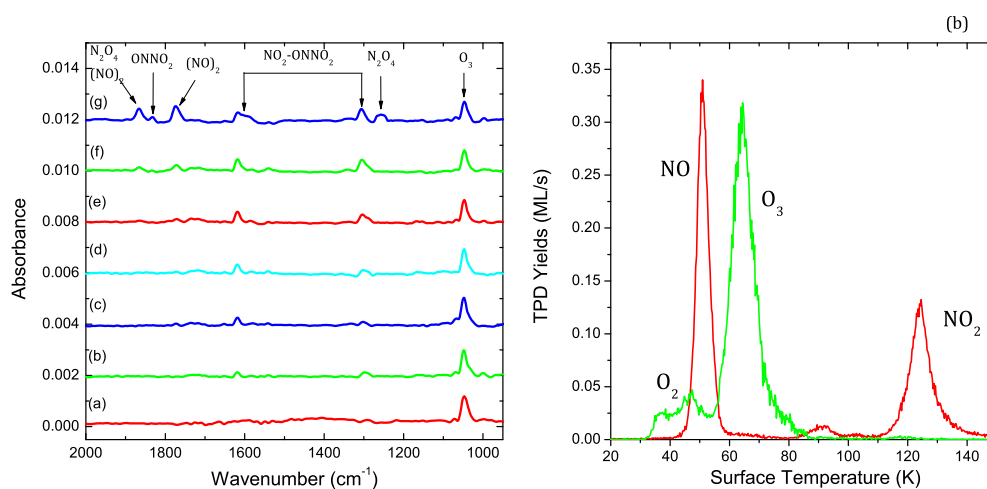
Figure 5.11: Left panel: RAIR spectra after deposition on oxidized HOPG at 10 K of 1.5 ML O_3 with increasing doses of NO from (a) to (g): 0, 0.2, 0.4, 0.6, 0.9, 1.8, and 3.5 ML of NO. Right panel: TPD curves of NO, O_2, O_3, and NO_3 after deposition at 10 K of 1.5 ML O_3+ 3.5 ML of NO on oxidized HOPG.

size of the molecules. The ER mechanism is the limiting factor for the formation of NO_3, and hence of NO_2 and other nitrogen oxides. If NO is not directly reacting with species coming from the gas phase, it accumulates and may form dimers, hindering thus NO_3 and NO_2 production. We have also performed experiments similar to that in Figure 5.5 but with varying NO doses. By measuring the area under the curve for each species and experiments, we can derive the amount of O_2 and NO consumed, and NO_2 formed. This is shown in Figure 5.10. We see that when the NO dose increases, the O_2 signal decreases. NO is still present and obviously has not fully reacted, as we already said before, while NO_2 raises quite linearly.

Finally Figure 5.10 shows the comparison of model and experiments as a function of NO coverage (same experiments shown in panel *a* of Figure 5.9). As we can see, all experimental points are well fitted by simulated curves, which confirms that the model is able to reproduce our experimental results and to describe the physics and the chemistry happening on the surface.

5.2.2   NO+O_3

5.2.2.1   Experimental

The reaction NO+O_3 has been studied using only one procedure: NO has been deposited upon pre-accreted O_3, since we do not have a pure beam of O_3. Ozone is accreted by sending O+O_2 on the surface (*Minissale et al.* 2014a). This procedure does not allow us to work with high coverages (more than 2 ML) because of layering effects, i.e., for a high NO coverage, the top NO layers will not react with O_3 molecules since ozone will be shielded by the underlying NO molecules. Furthermore this procedure maximizes the effect of ER mechanism.

5.2.2.2   Results and discussion

The left panel of Figure 5.11 shows RAIR spectra recorded after irradiation of 1.5 ML predeposited O_3 with increasing doses of NO at 10 K on oxidized HOPG. The spectrum of curve (a) is obtained after deposition of 1.5 ML O_3 (1043 cm^{-1}). The NO coverage increases from 0.2 ML (curve b) to 3.5 ML (curve g), while the intensity of the O_3 band slowly decreases, and that of the nitrogen oxide bands (NO_2, $ONNO_2$, N_2O_4 and $(NO)_2$) increases. In line with the spectra recorded for NO+O_2 we assign the bands at 1874 and 1773 cm^{-1} to the NO dimer

NO deposited (ML)
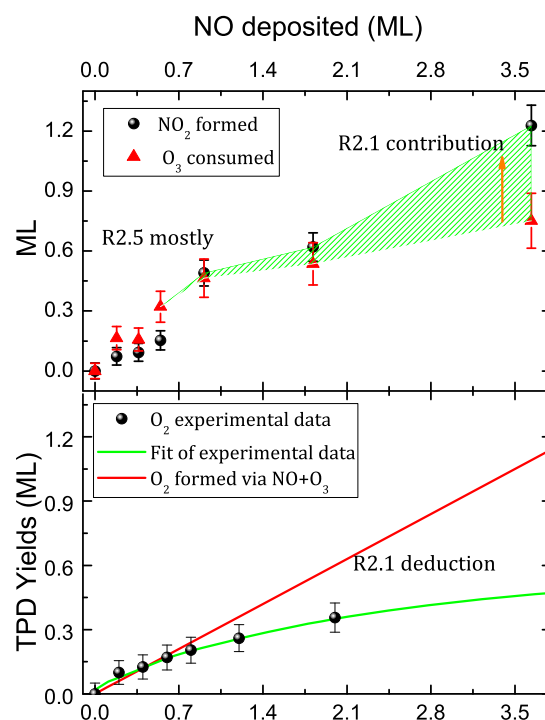
Figure 5.12: Adapted from *Minissale et al.* (2014b). Top panel: integrated area of NO_2 (black circles) and consumed O_3 (red triangles) peaks. Red triangles are obtained by subtracting the integrated area of $O_3(NO = x)$ from $O_3(NO = 0)$. The green pinstriped zone indicates the zone where reaction R2.1 starts to be efficient. Bottom panel: integrated area of O_3 TPD curves (black circles) as a function of deposited NO, and corresponding fit (green solid line); the red solid line shows the theoretical amount of O_2 formed via the $NO+O_3$ reaction as if R2.1 was completely inefficient.

(*Fateley et al.* 1959). N_2O_4 is found at 1874 cm^{-1} (*Fulvio et al.* 2009). The broad band at 1307 cm^{-1} is attributed to the n(N-O) symmetric stretch of NO_2 (or $ONNO_2$) and the band at 1612 cm^{-1} to the n(N-O) asymmetric stretch of NO_2 (or $ONNO_2$) (*Bartram&Koel* 1989; *Schwalke et al.* 1986). The band at 1838 cm^{-1} is due to the asymmetric stretch of $ONNO_2$ (*Stirling et al.* 1994). The right panel of Figure 5.11 shows TPD curves after deposition of 1.5 ML pre-deposited O_3 with 3.5 ML of NO at 10 K on oxidized HOPG. Similar experiments have been conducted on a surface of nonporous (compact) amorphous solid water ice and no evident differences - except for small band shifts - have been found.

These results can be explained through the following reactions:

$$NO + O_3 \rightarrow NO_2 + O_2 \quad R2.5$$

together with the R2.1-R2.4 chemical networks described in the previous section. It is evident that the reaction $NO+O_3$ is strongly connected to reaction $NO+O_2$. In fact, when NO and O_3 form NO_2 and O_2 via reaction R2.5, solid O_2 contributes to NO_2 formation via the R2.1 reactions. Two different phases can be distinguished. Initially when the NO coverage is low ($\ll 1$ ML), O_3 adsorbed on the surface is consumed in Eley-Rideal-like reactions by NO depletion from the gas phase. When NO_2 and O_2 surface densities start to increase, the NO + O_3 reaction probability decreases, and instead, reactions R2.1 and R2.4 become more efficient. At that stage it is unlikely that NO_2 forms via reaction R2.5. The top panel of Figure 5.12 shows the integrated area of the NO_2 and O_3 features as shown in Figure 5.11. The lower panel of Figure 5.12 shows the integrated area of the TPD curves of the infrared inactive O_2 as obtained through a similar set of experiments that are not shown in Figure 5.11. For a coverage lower than 1 ML of NO, the consumption of O_3 and the formation of NO_2 behave linearly. The formation of O_2 follows a similar trend. Gradually (for NO coverages thicker than 1 ML), the formed O_2 (experimental points) starts to separate from the linear regime.
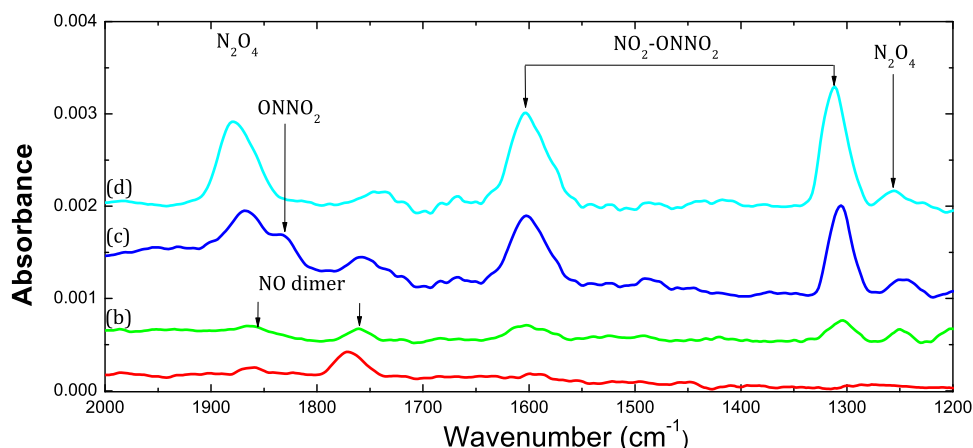
Figure 5.13: Adapted from *Minissale et al.* (2014b). RAIR spectra obtained after deposition on a silicate sample held at 10 K of: (a) 1.5 ML of NO ; (b) co-deposition of 1.5 ML NO+O; (c) co-deposition of 3.5 ML of NO+O; (d) co-deposition of 3.5 ML of NO+O, TPD until 86 K, then cooling to 50 K again.

This is expected as the O_2 reacts with NO through R2.1 and O_2 cannot grow anymore, since the NO molecules cannot react efficiently with the underlying O_3. Both effects decrease the O_2 abundance. At this point O_3 is only partially consumed. This is shown in Figure 5.12 by the saturation of O_3 (red triangles, top panel). After this effect of saturation, (between ≈ 0.8 and 1.8 ML) NO_2 concentration continues increasing (NO coverage >2 ML) through R2.1 as shown by the green pinstriped zone of Figure 5.12.

5.2.3   NO+O

5.2.3.1   Experimental

The NO+O reaction was studied by co-depositing reactants on different substrates (silicate and gold), and in different ice environments (pure NO+O, NO:H_2O+O, and NO:CO+O). In addition, we performed every single experiment under different coverage conditions. The submonolayer regimes cover from 0.1 to 1 ML and the multilayer regimes are in the range of 1 to 10 ML. The experiments were performed by using two different setups: FORMOLISM in LERMA lab at the Cergy-Pontoise University and SURFRESIDE[2] in Sackler Laboratory at the Leiden Observatory. Different physical conditions have been used to constrain the reaction mechanisms. *Minissale et al.* (2014b) have shown that surface temperature and coverage induce no pronounced changes on products. In the case of the submonolayer and multilayer regimes, some reactions change slightly their efficiencies. Furthermore different substrates do not affect strongly the results, but only cause small spectral shifts. For these reasons in the next section we will present only some prime examples of the performed experiments and the results obtained. We will focus on the results obtained on silicate in the submonolayer regime. We refer to *Minissale et al.* (2014b) for details and further works about NO+O reaction.

In the experiments presented in the next section oxygen atoms were produced through O_2 dissociation. Typical values of dissociation are the 70%, meaning that every ten O_2, seven are dissociated (14 O) and 3 remain undissociated and reach the surface. Moreover, O_3 can be formed on the surface. In other words, the presence of O_2 and O_3 in the beam and on the surface force us to consider NO+O_2 and NO+O_3 reactions for the study of NO+O reaction.

5.2.3.2   Results and discussion

Figure 5.13 shows four RAIR spectra recorded after NO+O deposition on a silicate sample held at 10 K. In particular, curve (a) shows the unprocessed spectrum for 1.5 ML of NO;
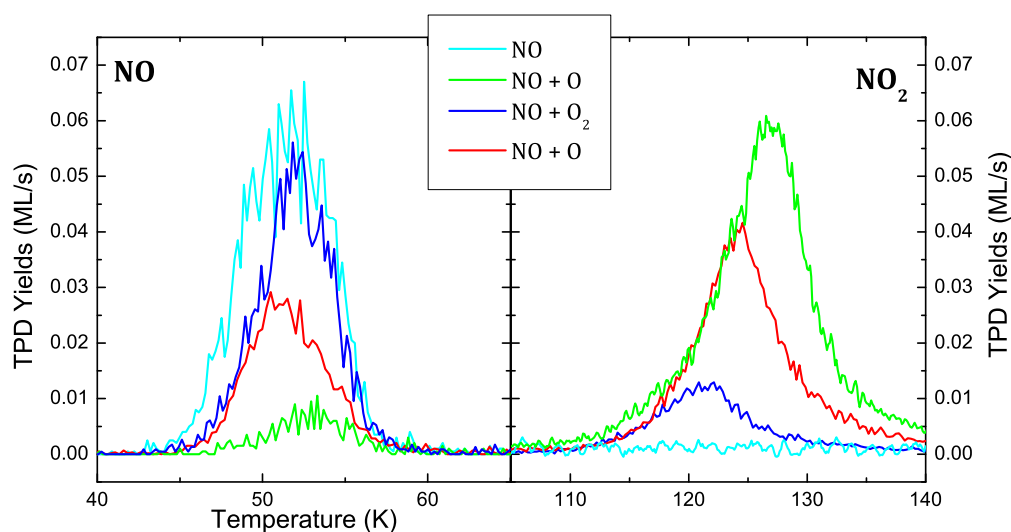
Figure 5.14: Adapted from *Minissale et al.* (2014b). TPD curves of NO (mass 30, left panel) and NO$_2$ (mass 46, right panel) for four different (co)deposition experiments: 0.4 ML of NO (cyan line), 0.4 ML NO + 1.5 ML of O (green line), 0.4 ML NO + 1.5 ML of O$_2$ (blue line) and 0.4 ML NO + 1.5 ML of O$_3$ (red line). A silicate sample held at 10 K was used as substrate.

curves (b) and (c) show the results of a co-deposition resulting in 1.5 and 3.5 ML thick ice of NO + O (+ O$_2$), respectively; finally curve (d) shows the spectrum after the same deposition sequence used in curve (c), but with also annealing to 86 K and cooling to 50 K. In line with spectral assignments of subSec. 5.2.1 and 5.2.2, in curve (a) the NO (dimer) symmetric and asymmetric N-O stretch modes can be seen at around 1861 and 1770 cm^{-1}. The other three curves are clearly different with a number of new spectral features. Peaks at 1304-1311 and 1602 cm^{-1} are due to both NO$_2$ and ONNO$_2$ (i.e., N$_2$O$_3$). Peaks at 1878, 1741 and 1256 cm^{-1} are due to N$_2$O$_4$. The peak at 1834 cm^{-1} is also due to ONNO$_2$ (N=O stretch). This latter peak does not show up in curve (d) indicating that ONNO$_2$ is not present at high temperature (>80 K). For this reason, in curve (d), we think that the peaks at 1304-1311 and 1602 cm^{-1} are due to NO$_2$ ice. Here the annealing offers an additional tool for bands assignments. For instance, both NO dimer and N$_2$O$_4$ can contribute to the bands shown in curve (c) between 1890-1850 and 1755-1730 cm^{-1}. However, since the spectrum in curve (d) is obtained after annealing to 86 K - at this temperature all NO molecules have desorbed - the peaks at 1878 and 1741 cm^{-1} can only be due to N$_2$O$_4$. This facilitates the overall assignment of all IR bands. We explain the presence of these species by adding the following reaction to the R2.1-R2.5 chemical network:

$$NO + O \rightarrow NO_2 \quad R2.6$$
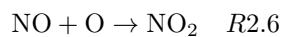
The reaction NO+O is evidently connected to NO+O$_2$ and NO+O$_3$ reactions, due to oxygen allotropes present in the beam and on the surface. Similarly to the case of NO+O$_2$ and NO+O$_3$, we have performed TPD experiments to study the NO+O reaction and to compare the O$_x$ reactivity with NO. Figure 5.14 shows TPD curves of NO and NO$_2$ for different (co)deposition experiments: 0.4 ML of NO (cyan line), 0.4 ML NO + 1.5 ML of O (green line), 0.4 ML NO + 1.5 ML of O$_2$ (blue line) and 0.4 ML NO + 1.5 ML of O$_3$ (red line). In NO+O experiments almost all NO molecules are consumed. Clearly when O-atoms are produced through O$_2$ dissociation, O$_2$ molecules can still reach the surface. This also means that O$_2$ can react with oxygen atoms to form O$_3$, specifically when the species are co-deposited. So the formation of NO$_2$ can occur via reactions R2.1-R2.5-R2.6. In the case where the O/O$_2$ beam impacts on already accreted NO molecules, R2.5 is less probable and the possible pathways are limited to reactions R2.1 and R2.6. This is the case in Figure 5.14 (green line) where almost all the NO is converted into NO$_2$ (right panel) and only a small number (about
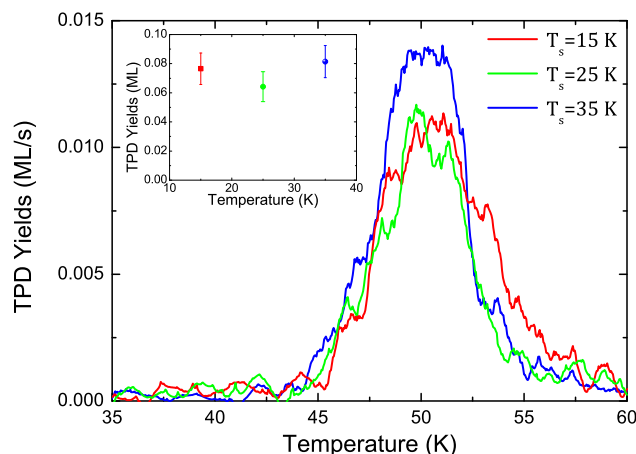
Figure 5.15: Adapted from *Minissale et al.* (2014b). Three TPD (mass 30) plots of NO after deposition of 0.5 ML NO + 1 ML O at different temperatures: 15 K (in red), 25 K (in green), and 35 K (in blue). In the inset the integrated areas under the TPD curves are shown.

8%) of NO molecules do not react. The incomplete conversion of NO into NO_2 is not likely to be due to the activation barrier of R2.1. It could be explained by a low penetration depth of O atoms into the NO ice, but it is more probably due to a small mismatch between the areas covered by the two beams (NO and O) in FORMOLISM. Moreover, the blue line in Figure 5.14 shows that O_2 is less reactive than O in reactions with NO, and this can further slow down the destruction of NO and concurrent formation of NO_2 in NO+O experiments.

These experiments confirm from one side the fast formation of NO_2 at low temperature via the NO+O reaction and from the other side, they suggest that the NO-formation reaction

$$NO_2 + O \rightarrow NO + O_2 \quad R2.7$$

is very slow with respect to NO-consumption reactions (mainly R2.6). In other words $k(NO+O) \gg k(NO_2+O)$. For this reason we neglect R2.7 in the present discussion and refer to *Ioppolo et al.* (2014b) for more details.

5.2.3.2.a   Dependence on surface temperature

In *Minissale et al.* (2014b), we have shown that the different substrates (silicate, compact ASW ice, and gold) and the ice composition used do not visibly affect the final products. They are, however, responsible for small shifts of the IR features. Surface coverage only slightly changes the final products of our experiments. In particular, multilayer regimes facilitate dimerization reactions. In order to investigate any temperature dependence of the NO+O reaction, experiments were performed in which the deposition temperature was varied. Figure 5.15 shows three NO TPD curves after deposition of 0.5 ML NO + 1 ML O on a silicate sample held at 15 K (red curve), 25 K (green curve), and 35 K (blue curve), respectively. The amount of NO left as a function of substrate temperature (calculated by integrating the area of each NO peak) is plotted in the inset of Figure 5.15. Within the experimental error bars, this does not show any substantial temperature dependence. The reaction is already efficient at low temperatures and seems to be essentially barrier free.

5.2.4 NO_2 reactivity

The experiments on NO_2 reactivity with H, N, and O atoms were carried out with FOR-MOLISM and the SURFRESIDE (based in Leiden) setups within a collaboration between
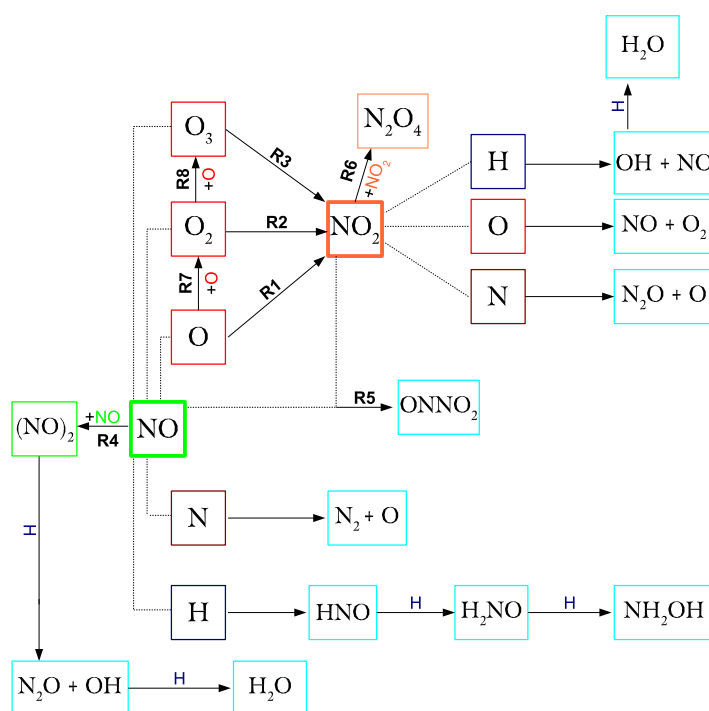
Figure 5.16: Scheme involving reactions of NO and NO_2 with H, N, and O_x particles.

the LERMA-Cergy and the Astrochemistry group at the Leiden Observatory. The NO_2 reactivity has been discussed in *Ioppolo et al.* (2014b) and the main conclusion are here listed very briefly for the sake of clarity:

1. The final products of NO_2 hydrogenation are NH_2OH and H_2O. Hydroxylamine is found to be formed through a series of barrierless surface reactions.

2. N_2O is formed through the nitrogenation of NO_2. N_2O is not destroyed in reactions with H-, O-, and N-atoms. We point out that no experiments of N_2O irradiations have been performed, and this statement comes rather from indirect verifications.

3. Several nitrogen oxides, such as $(NO)_2$, N_2O_3, and N_2O_4, are formed through surface NO_2 + H/O/N reactions.

5.2.5 Conclusion

We can sum up the results presented in this section and in *Congiu et al.* (2012a, 2012b), *Fedoseev et al.* (2012), *Minissale et al.* (2013a), *Minissale et al.* (2014b), and *Ioppolo et al.* (2014b) through the reaction network shown in Figure 5.16 and in Table 5.1 Once we have drawn the different reactions identified experimentally, we can remark that the most stable species (N_2, N_2O, NH_2OH, and H_2O) seem to be the end of the chemical journey in the O and N world.

5.3 O/C/H chemistry

5.3.1 Carbon dioxide formation on cold surfaces

Carbon dioxide has already been detected in the interstellar medium (ISM) by *d'Hendecourt & Jourdain de Muizon* already few decades ago (1989). It represents one of the most common and abundant types of ices, and many astronomical observations (by the Infrared Space

Table 5.1: List of reactions (their final products and their efficiency) studied in the frame of nitrogen oxides chemistry.

Experiment	Final products			Barrier
NO+H	NH_2OH	H_2O	N_2O	No
NO+N	N_2	NO_2	O_3	No
NO+O	NO_2	$ONNO_2$	N_2O_4	No
NO+O_2	NO_2	$ONNO_2$	N_2O_4	Small
NO+O_3	NO_2	$ONNO_2$	N_2O_4	Small
NO_2+H	NH_2OH	H_2O	–	No
NO_2+N	N_2O	O_3	–	Small
NO_2+O	NO	O_3	$ONNO_2$	Small

Observatory and the Spitzer Space Telescope) confirm the presence of CO_2 in different environments, such as Galactic-centre sources (*de Graauw et al.* 1996), massive protostars (*Gerakines et al.* 1999; *Gibb et al.* 2004), low-mass young stellar objects (*Nummelin et al.* 2001; *Aikawa et al.* 2012), brown dwarfs (*Tsuji et al.* 2011) background stars (*Knez et al.* 2005), in other galaxies (*Shimonishi et al.* 2010; *Oliveira et al.* 2011), and in comets (*Ootsubo et al.* 2010). CO_2 is predicted to have a low abundance in the gas phase (N_{CO_2}/N_{H_2}=6.3×10^{-11}; *Herbst & Leung* 1986), and this is confirmed by observations (*van Dishoeck et al.* 1996). Low abundances in gas phase, together with its observed high abundances in the solid phase, cannot be explained exclusively by formation via gas-phase schemes (*Hasegawa et al.* 1992), therefore surface reactions are invoked to justify the high abundance of carbon dioxide ices. Extensive experimental studies have been carried out to study formation routes of CO_2 formation in solid-phase: on the one hand, irradiation of CO ices (pure or mixed with H_2O) with photons, charged particles or electrons, leads to efficient formation of CO_2 (*Ioppolo et al.* 2009; *Laffon et al.* 2010); on the other hand, *Whittet et al.* (1998) evoke chemical pathways occurring without the addition of energy to explain CO_2 detection in those interstellar environments where a lack of UV photons forbids ice processing (i.e., the molecular cloud Taurus). In this section, we deal with CO_2 formation on solid phase through two (non energetic) pathways:

1. CO+O

2. H_2CO+O

5.3.1.1   CO+O

The first successful laboratory investigation of the formation of CO_2 by non-energetic processes was performed by *Roser et al.* (2001), who studied the surface reaction of CO and O atoms. In a first set of experiments they co-deposited the two species at 5 K and performed a TPD. Probably due to the low sensitivity of the quadrupole mass spectrometer they were using at that time, they did not detect any CO_2 formation. To prove the formation of carbon dioxide through such a pathway and to give a first estimate of the barrier for such a reaction they subsequently devised an experiment in which the co-deposited layer of CO and O atoms was covered by a layer of porous water ice. The TPD performed under such conditions allowed to detect the formation of CO_2 thanks to the reaction of CO and O migrating in the interconnected pores of the amorphous ice. Under the hypothesis that the mobility of species stemmed from thermally activated processes, a reaction barrier of 290 K was obtained that explained the formation of carbon dioxide even in quiescent clouds. *Raut&Baragiola* (2011) confirmed the formation mechanism of CO_2 investigated by *Roser et al.* (2011). They performed experiments showing the formation of small amounts of CO_2 during co-deposition of CO and cooled O and O_2 at 20 K, although they did not provide any activation barrier. Here we present further experimental studies for CO+O reaction and we also determined an activation energy of the CO+O reaction and the physical chemical mechanisms occurring on the surface by developing a kinetic model.

5.3.1.1.a Experimental

CO_2 production on cold surfaces (10 - 40 K) was investigated by concurrent exposures of CO molecules and O atoms. The CO + O reaction is studied in a submonolayer regime on two different substrates: amorphous solid water (ASW) ice and oxidized graphite. The ^{13}CO molecules and O atoms are sent simultaneously (co-deposition) on the surface via two triply differentially pumped beam lines. We used ^{13}CO instead of ^{12}CO to increase the signal-to-noise ratio of the mass signal of the ^{13}CO reactant and the final $^{13}CO_2$ product. Hereafter we refer to ^{13}CO as CO. The O atoms are produced by dissociation of O_2 molecules. The dissociation efficiency of O_2 was $\tau = 73\pm5\%$ at the time of the experiments performed on ASW and $61\pm7\%$ when we perfomed the experiments on graphite. Atoms and undissociated molecules are cooled and instantaneously thermalized upon surface impact with the walls of the quartz tube.

We have calibrated the molecular beam as described in Sec. 2.2.4 and found that the first monolayer (1 ML=10^{15} molecules cm^{-2}) of both ^{13}CO and O_2 was reached after an exposure time of about six minutes, which therefore gives a flux $\phi_{O_2off,CO}$=(3.0$\pm$0.3)$\times10^{12}$ molecules cm^{-2}s^{-1}. Once the O_2 discharge is turned on, the O-atom flux is ϕ_O=2τ ϕ_{O_2off} =5.4$\times10^{12}$ atoms cm^{-2}s^{-1} and the O_2 flux ϕ_{O_2on}=(1-τ) ϕ_{O_2off}=10^{12} molecules cm^{-2}s^{-1} . In addition, we determined that the beam did not contain O or O_2 in an excited state by tuning the ionizing electron energy inside the QMS head as described in Sec. 2.2.2.3.

5.3.1.1.b Results and discussion

As previously claimed (i.e. in Sec. 5.2) to study CO+O reaction, we need to know what is the reactivity of CO with the other oxygen allotropes (O_2 and O_3). From an energetic point of view, oxidation of CO to form carbon dioxide may proceed by the following reactions:

$$CO + O \rightarrow CO_2 \quad R3.1$$
$$CO + O_2 \rightarrow CO_2 + O \quad R3.2$$
$$CO + O_3 \rightarrow CO_2 + O_2 \quad R3.3$$
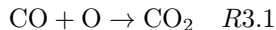
for which enthalpies of formation are ΔH=-532, -33, and -425 kJ/mol, respectively (NIST Chemistry WebBook). *Roser et al.* (2001) and *Raut&Baragiola* (2011) have already studied reaction R3.1, showing that this reaction can produce carbon dioxide without the intervention of energetic processes. As for reaction R3.2, *Mallard et al.* (1994) suggested a very high activation energy barrier ($\sim$ 24000 K), while reaction R3.3, to the best of our knowledge, has not been studied yet. Panel *a* of Figure 5.17 shows three TPD spectra of mass 45 for $^{13}CO_2$ after deposition on oxidized graphite held at 10 K of 1 ML CO (black squares), co-deposition of 1 ML CO+O_2 (red circles), and 1 ML CO+O_3 (green triangles). The three TPD curves and integrated areas of the curves are very similar and this suggests that the CO+O_2 reaction does not occur or that at least it is very inefficient at producing CO_2 in accord with *Mallard et al.* (1994). We have another indication of the CO+O_2 inefficiency by comparing the area of the CO peak with and without O_2. In the two cases we do not detect any measurable variations of the CO yield. We get to the same conclusion as far as the CO+O_3 reaction is concerned. No difference can be appreciated in the comparison between the peak area of CO, of background CO_2 and of O_3. This indicates that CO+O_3 is not a fast reaction to produce CO_2 either. Another control experiment consist into verify that CO_2 is really formed on the surface and that it is not present as an impurity in the CO bottle. To check this possibility, we have performed the experiments shown in panel *b* of Figure 5.17. The TPD spectra of mass 45 shown are recorded after exposure on a graphite surface - held at 10 K - of 4 ML of CO (black squares) and after 4 ML of CO+O (blue stars). The difference between the two TPDs is evident, and comparing the two CO_2 signals we find CO_2(CO dep)/CO_2(CO+O dep)$\sim$8%, which confirms that the majority of the CO_2 detected is formed through surface reactions. Figure 5.18 shows the TPD traces resulting from irradiating ASW ice held at 20 K with 0.5 ML of CO+O (i.e., 0.5 ML CO, 0.15 ML O_2, 0.7 ML O). Four main peaks appear at masses 29, 32, and 45. The mass-29 peak is clearly due to the CO desorption, which
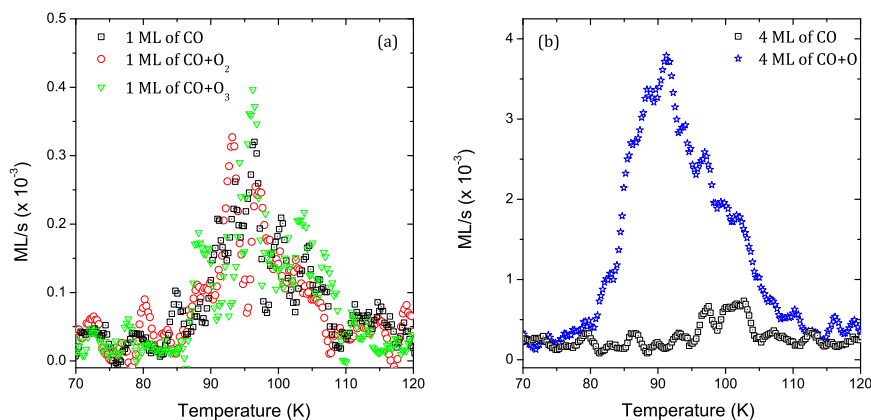
Figure 5.17: Adapted from *Minissale et al.* (2013c). Panel *a*: TPD curves of mass 45 ($^{13}CO_2$) between 65 and 125 K after deposition of 1 ML of ^{13}CO (black squares), $^{13}CO+O_2$ (red circles) and $^{13}CO+O_3$ (green triangles) on graphite held at 10 K. Panel *b*: TPD curves of mass 45 ($^{13}CO_2$) between 60 and 120 K after 4 ML of ^{13}CO exposure (black squares), and after 4 ML of $^{13}CO+O$ (blue stars) on graphite held at 10 K.

occurs between 32 K and 55 K and peaks at 41 K. Mass 32 presents two peaks, the first one between 28 and 42 K - peaked at 34 K - is due to O_2 desorption while the second one peaking at around 65 K included between 55 K and 75 K is due to the desorption of O_3 detected in the form of O_2^+ fragments, as a result of the O_3 cracking in the head of the QMS (see Sec. 2.2.2.1). Finally, the tiny high-temperature peak also shown in the insert comes from the CO_2 desorption occurring between 75 and 95 K and peaking at 83 K.

The experiments performed at different surface temperatures give results similar to the ones just described. In fact, we observe always four peaks (except for the 50 K experiment, where O_2 has already desorbed before starting the TPD), but their intensities change with temperature as shown below. Figure 5.18 indicates that two molecules are actually formed on the surface, O_3 and CO_2. Moreover, O_2 can also be either formed on the surface via the O+O reaction or come from the beam because of the non-total dissociation of O_2 molecules. Considering all reactants and products and remembering that reactions R3.2 and R3.3 can be disregarded, R3.1 is in competition with the two barrierless reaction (Minissale et al. 2013b, 2014a):

$$O + O \rightarrow O_2 \quad R3.4$$
$$O + O_2 \rightarrow O_3 \quad R3.5$$
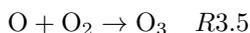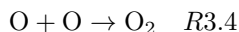
To understand how efficiently the CO+O reaction proceeds and to derive its activation barrier, we performed several experiments at a fixed coverage and by varying the surface temperature. Temperature, in fact, affects both oxygen atom diffusion and the desorption of species and these two processes give us the key to understand our results (Figure 5.18) and consequently the way CO_2 is formed.

As we can see in Figure 5.19, the CO_2 signal is already present at 10 K, and it reaches a maximum when the surface temperature during exposure is 35 K. Subsequently, for higher temperatures the CO_2 signal decreases and becomes zero at 60 K. This behavior can be explained by considering three different "temperature zones":

1. before O_2 desorption (below 30 K);

2. between O_2 and CO desorption (30-35 K);

3. after CO desorption (35 K).

Top panel of Figure 5.19 shows that in the range between 10 K and 30 K, the majority of oxygen atoms are used to produce ozone via reaction R3.4 and R3.5, and its production
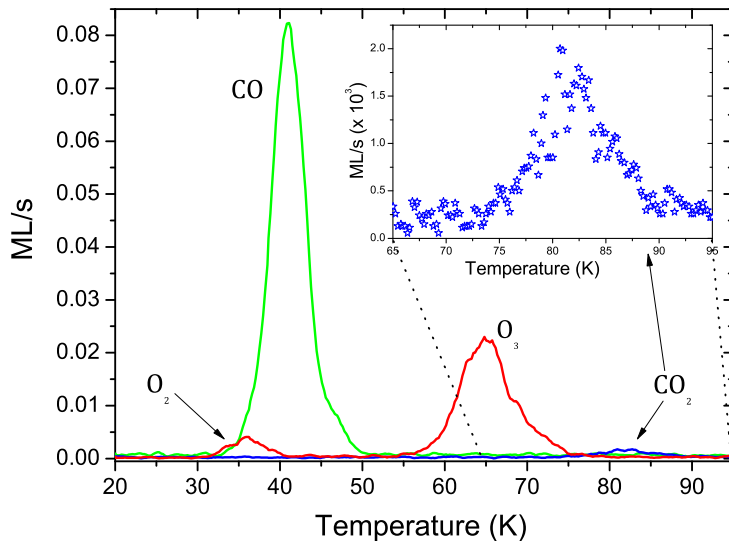
Figure 5.18: Adapted from *Minissale et al.* (2013c). TPD curves at mass 29, 32, and 45 after irradiation of 0.5 ML of ^{13}CO + O on ASW ice held at 20 K. Four peaks are visible. The first peak between 28K and 42K is due to O_2 desorption, the second one between 32 and 55K is due to ^{13}CO desorption. The third peak between 55K and 75 K represents O_3 desorption, while the high-temperature peak is the desorption of $^{13}CO_2$ (75-95 K).

rises with temperature owing to the increase in O diffusion. In this first temperature zone, only a small amount of oxygen atoms are used to produce CO_2, probably via the Eley-Rideal mechanism. When O_2 starts to desorb (second temperature zone), O atoms have a lower probability of meeting O_2 molecules to form O_3. In fact, we see a decrease in the amount of O_3 desorbed, while in this range of temperature the probability that an oxygen atom encounters a CO molecule increases (as a consequence of the reduced coverage of O_2). Finally at temperatures higher than 35 K, CO desorption begins and the CO_2 signal begins to drop with same pattern observed for ozone, as shown in the bottom panel of Figure 5.19. This suggests that also at high temperatures (45 - 50 K) molecules and atoms coming from the beam still have a residence time on the surface long enough to react and form appreciable amounts of ozone and CO_2. The shapes of the CO_2 and O_3 yields suggest that CO_2 formation is limited by O_2 molecules or, in other words, that reaction R3.1 is in competition with reactions R3.4 and R3.5. In fact, only when the O_3 signal decreases (and O_2 desorbs) CO_2 formation rises. However, presence of O_2 apart, CO_2 always forms in small amounts, and this very probably indicates the existence of an activation barrier (hereafter E_a) for the reaction CO+O. To evaluate E_a and to understand what surface mechanisms are responsible for CO_2 formation we used the model described in Chapter 3.

5.3.1.1.c   Model: evaluation of the CO+O barrier

In this section we present the model used to fit our experimental data. We consider five species: two are coming exclusively from the beam, O atoms and CO molecules, two are formed only on the surface, O_3 and CO_2, and one, O_2, is coming both from the beam and formed on the surface. The free parameters of the model are r_{ER} and r_{LH} probabilities for the reaction CO+O via ER and LH. The additional parameters that we used are:

- ϵ, the chemical desorption probability for O+O reaction. It is equal to zero in the case of a water ice surface while it is 0.5 if the experiments are carried out on graphite.

- k, the diffusion coefficient for O atoms. We used the law

$$k = k_0(1 + T^3/T_0^3), \tag{5.1}$$
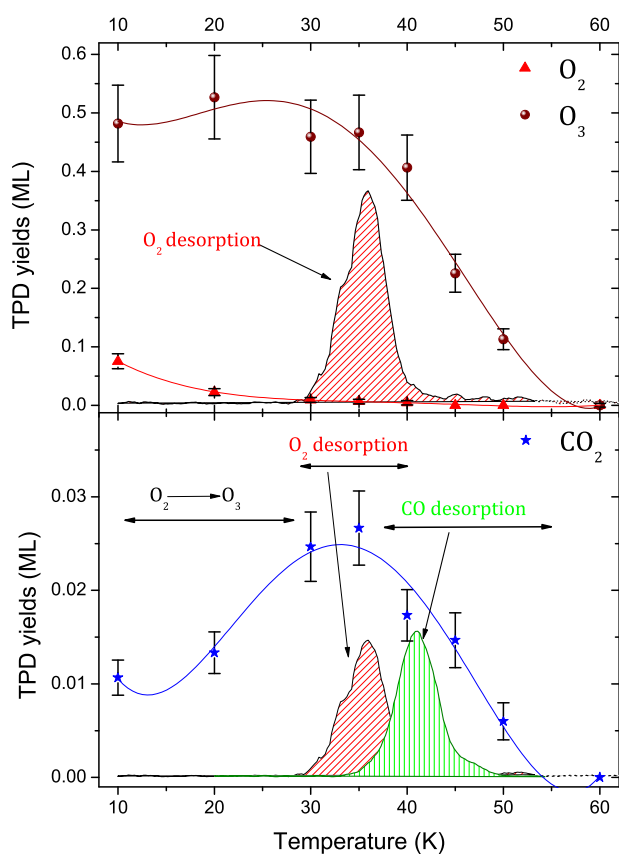
Figure 5.19: Adapted from *Minissale et al.* (2013c). Integrated area under the TPD curves of O_2 and O_3 (triangles and circles on top panel, respectively), and of $^{13}CO_2$ (stars on bottom panel) as a function of surface temperature. The points are obtained through deposition of 0.5 ML of $^{13}CO+O$ on ASW ice held at different temperatures (10 K, 20 K, 30 K, 35 K, 40 K, 45 K, 50 K, 60 K). The solid line is a fit of the area behavior. The TPD peaks (obtained at $T_{surface}=20K$) added in the figure show when O_2 and ^{13}CO desorb, and this helps interpret the O_3 and $^{13}CO_2$ yield behaviors with temperature.
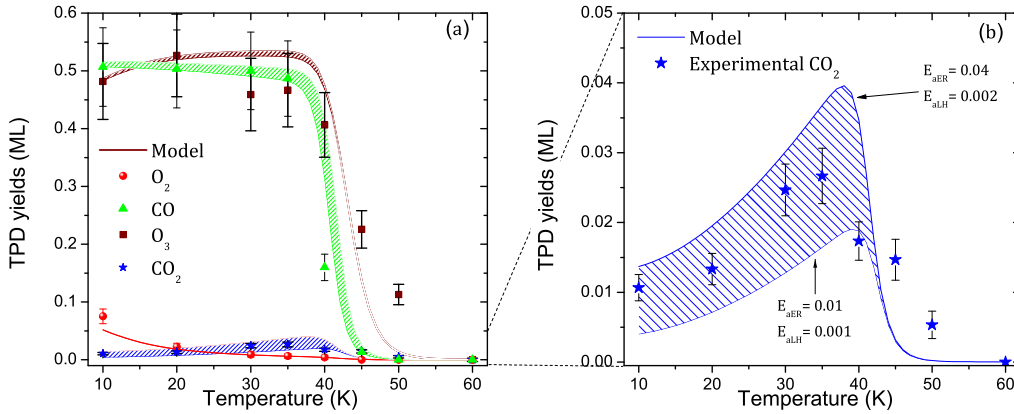
Figure 5.20: Adapted from *Minissale et al.* (2013c). Panel *a*: model results for all species on ASW. The curves were obtained by using $r_{aLH}=0.0019\pm0.0005$ and $r_{aER}=0.021\pm0.007$. The circles, stars, triangles and squares represent O_2, CO_2, CO, and O_3 experimental results respectively. Panel *b* displays a magnified view of the CO_2 yield around its maximum for clarity.

where k_0 is 0.9 and T_0 is 10 K.

- E_{O_2} and E_{CO}, desorption barriers for O_2 and CO. We used two energies 1310 K/k_b and 1430 K/k_b, even if a distribution of energy could be used.

In our model, we could have added another couple of parameters, $k_{O_2,CO}$, representing the O_2 and CO diffusion. However, O diffusion should be dominant with respect to O_2 or CO diffusion. The addition of O_2 and CO diffusion would cause a quicker consumption of O atoms, without significant changes of the final amount of species. Introducing two more free parameters would then be of secondary importance for the purpose of this work and it would add more complexity. For these reasons we have chosen to neglect the diffusion of O_2 and CO, and also because their mobility is likely to be almost zero at T< 20 K. Panel *a* of Figure 5.20 shows the comparison of experimental (points) and model (curves) results. We chose to fit CO_2 experimental yields, since they are the most important constraints for our free parameters, namely the reaction probabilities of CO+O reaction (panel *b* of Figure 5.20). We find that the best couple of reaction probabilities is $r_{aER}= 0.021$ and $r_{aLH}= 0.0019$. As described extensively in *Minissale et al.* (2013c), the model allows us to distinguish and quantify the contribution to CO_2 formation by either ER or LH mechanism. CO_2 formation via ER mechanism appears to be constant with temperature between 10 and 40 K also because, in theory, this mechanism is temperature independent. At higher surface temperatures, however, ER starts to be inefficient because of the desorption and the decrease of the residence time of species on the surface, thus the CO_2 production efficiency by this mechanism drops off. On the contrary, the LH mechanism depends on the surface temperature and its efficiency increases going from 10 to 40 K owing to the favored diffusion of atoms. Beyond 40 K, as occurs for the ER case, the probability that O atoms and CO molecules leave the surface is high and the CO_2 yield decreases fast with temperature. The ER and LH contribution to CO_2 formation is approximately equal at low temperatures (below 20 K), while at high temperatures most CO_2 is formed via the LH mechanism. This is not surprising considering the power law dependence on the temperature of the diffusion parameter (Eq. 5.1).

As already claimed in Sec. 3.2, the reaction probabilities r_{aER} and r_{aLH} give the probability that a reaction occurs, in this case CO+O. By inverting a normalized Arrhenius equation, the activation barrier energy E_a can be calculated as follows:

$$E_a = -k_b\,T_{eff}\,log(r_a). \qquad (5.2)$$

Two alternative strategies can be used to evaluate the activation barrier of the reaction; we can derive the reaction barrier E_a either from r_{aER} or r_{aLH}. The problem is to know the

effective temperature (T_{eff}) to insert in Eq. 5.2.

ER case In Sec. 3.2, we described how T_{eff} can be evaluated. We remember that

$$T_{eff} = \mu(\frac{T_{solid}}{m_x} + \frac{T_{gas}}{m_y})$$ (5.3)

So in the case of ER, for T_{gas}=300 K and T_{solid}=25 K, we can consider three different cases for T_{eff}:

- T_{eff}'=T_{gas}= 300 K

- T_{eff}"= 202 $\pm$ 5 K

- T_{eff}"'= 123 $\pm$ 10 K

where μ is the effective mass of the CO and O system. These temperatures correspond to the velocity of the center of mass of the system. Evidently, we do not take into account the case T_{eff}=T_{solid}, because that means to consider molecules already thermalized with the surface, as in a pure LH process.
In the first case (T=T_{gas}=300 K) we obtain a barrier of 1200 K. Clearly, in our experiments we cannot consider CO and O as two gases at the same thermodynamic equilibrium so the temperature is likely to be lower than 300 K. This means that E_a=1200 K is only an upper limit of the activation barrier.
The second and third cases give a CO+O reaction barrier E_{aER} in the range 780-475 K/k_b.

LH case The Eq. 5.2 has to be used with care in the case of LH, since the temperature dependence of r_{LH} is not as simple as in the Arrhenius case. Moreover, the temperature dependence cannot be derived from the experimental values because they do not provide enough constraints, hence we give a mean value $\overline{r_{LH}(T)} = 0.0019$ across the whole temperature range investigated (10 - 60 K). We then try to estimate the reaction barrier by taking into account the two following considerations:

i although O-atoms diffusion is predominant with respect to that of O_2 and CO, at high temperatures O_2 and CO diffusions have to be taken into account if a proper evaluation of r_{LH}(T) is required.

ii Non-exponential behaviour of the CO_2 formation rate due to occurrence of tunneling at very low temperatures (*Goumans&Andersson* 2010)

Figure 5.21 displays a comparison between experimental and theoretical values of r_{LH}, by considering tunneling for CO+O reaction and O_2-CO diffusion. These considerations suggest that r_{LH}(T), for T<25K, is better described by this law:

$$r_{LH}(T) = exp(-E_a/k_b\,T_{eff}) + r_{tunn}(E_a, T),$$ (5.4)

where r_{tunn}(E_a,T) ($\geq$0) represents the rate of tunneling of the CO+O reaction, and it is able to increase the reaction probability value at low temperature. By inverting Eq. 5.4 we have

$$E_a = -k_b\,T_{eff}\,log(r_{LH}(T) - r_{tunn}(E_a, T)) > -k_b\,T_{eff}\,log(r_{LH})$$ (5.5)

By putting T_{eff}=25 K in Eq. 5.5, r_{LH}(25K)=0.0019 and r_{tunn}(E_a,T)=0, thus we obtain a lower limit for E_a of 160 K/k_b. This value is underestimated for two reasons:

- At 25 K the tunneling term could become dominant with respect to the classical term (Arrhenius law), and clearly is not zero.

- $\overline{r_{LH}(T)}$ is a mean value, and very probably r_{LH}(T) presents a minimum around 25 K

This means that r_{LH}(25K)<<0.0019 and E_a >>160 K/k_b are consistent with the values obtained for r_{ER}.
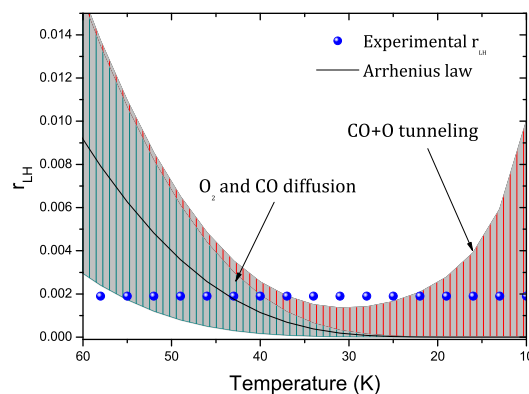
Figure 5.21: Adapted from *Minissale et al.* (2013c). Temperature dependence of $r_{LH}(T)$ between 10 and 60 K. The two pinstriped regions indicate how a different parametrization of tunneling for CO+O reaction (red zone) and of O_2 and CO diffusion (green zone) can change our estimation of $r_{LH}(T)$. Blue circles represent our experimental data. Solid line is an example of a pure Arrhenius behavior.

5.3.1.1.d   Conclusions

We have described above how we evaluated the activation barrier of the CO+O reaction. Our model allows us to distinguish which mechanisms (Eley Rideal or Langmuir-Hinshelwood) is at play in different temperature regimes and we are able to give a range of values of the activation barrier of reaction CO+O of 780-475 K/k_b. We have to make clear that these values make sense only in the range of validity of Eq. 5.5. Finally, it should be noted that the range of activation energy barriers given in this work are only apparently inconsistent with the 290 K/k_b value of *Roser et al.* 2001. In fact, they provide an estimation (not a measure) of the barrier by using only the classical LH mechanism (very low T_{eff}), but on the other hand the ER mechanism (high T_{eff}) with the same barrier would produce more CO_2 than that they observed. Their estimate can thus be considered a lower limit of the barrier which is included in our study of the LH case.

5.3.1.2 H_2CO+O

Formaldehyde (H_2CO) was the first polyatomic organic molecule detected in the interstellar medium (*Zuckerman et al.* 1970). It can be detected through 1_{11} - 1_{10} ground-state rotational transition at 4830 MHz (*Snyder et al.* 1969), and its distribution is found similar to that of HII and CO in different environments, i.e our Galaxy (*Davies& Few* 1979; *Tang et al.* 2013, and references therein), and in Galactic radio sources (*Downes et al.* 1980).

H$_2$CO has been observed both in some comets (*Crovisier&Bockeleé-Morvan* 1999; *Mumma et al.* 2005), and in interstellar ices (*Keane et al.* 2001). Its abundance with respect to water ice varies from 1% to 6% in high- (*Keane et al.* 2001; *Dartois* 2005) or low- (*Boogert et al.* 2008) mass protostars, or hot corinos (*Maret et al.* 2004). Gas-phase reactions (*Shalabiea&Greenberg* 1994), and UV photolysis of H_2O-CO ice (*Allamandola et al.* 1988; *Schutte et al.* 1996; *Watanabe et al.* 2007) can produce efficiently formaldehyde, but surface reactions, as hydrogenation of CO ice (*Hiraoka et al.* 1994; *Watanabe&Kouchi* 2002; *Watanabe et al.* 2004;*Madzunkov et al.* 2009) are needed to explain the observed abundances in the solid phase.

Formaldehyde is a key species in the grain-surface chemistry in interstellar clouds (*Schutte et al.* 1993, 1993b). *Hidaka et al.* (2004) and *Fuchs et al.* (2009) show that formaldehyde can form methanol (CH_3OH) through H-atom additions, and we show that it can produce CO via H-atom abstraction. Moreover H_2CO is involved in the formation of large molecules

containing C-H, C-O, O-H, and C-N bonds (*Schutte et al.* 1993b): during the warm-up of the ice on grains, formaldehyde can react with NH_3, H_2O, and itself (H_2CO) to form respectively amine, diols or $[-CH_2-O-]_n$ groups (*Noble et al.* 2012b; *Theulé et al.* 2013; *Mispelaer et al.* 2013); for this reason, it could be considered a primary precursor of some complex organic materials (*Schutte et al.* 1993b). In this section, we show experimentally that formaldehyde is also reactive with ground-state $O(^3P)$ atoms to form CO_2, one of the most abundant species in interstellar ices. Formaldehyde seems to play a crucial role in the chemistry of interstellar ice, and in particular in the balance between CO_2, CH_3OH, and CO.

5.3.1.2.a   Experimental

All the experiments were performed by sending O atoms on formaldehyde ices previously grown on the cold sample. The two species are deposited by using, at different times, the same triply differentially pumped beam line. As described in Sec. 2.2.2.2, formaldehyde gas is obtained by depolymerization of paraformaldehyde. The resulting gas contains a little part of CO. To avoid CO adsorption we deposit formaldehyde at 60 K. Moreover, we used different isotopes of formaldehyde to better constrain our findings: $H_2^{12}CO$, $D_2^{12}CO$, and $H_2^{13}CO$. In the case of $D_2^{12}CO$ the purity is of about 98 %, while for $H_2^{13}CO$ is of 99 %. Hereafter we refer to ^{12}C simply as C. Oxygen atoms are generated (in the ^3P ground state) by dissociating O_2 molecules and typical values of 70±5 % are used for the dissociation efficiency. From calibrations we have found that, the first monolayer (1 ML=10^{15} molecules cm^{-2}) of formaldehyde was reached after an exposure time of about 12 minutes while for O_2 the same dose was reached after six minutes, which gives respectively a flux of ϕ_{H_2CO}=(1.3±0.4)×10^{12} and ϕ_{O_2off}=(3.0±0.3)×10^{12} molecules $cm^{-2}s^{-1}$. Once the O_2 discharge is turned on, the O-atom flux is ϕ_O=2τ ϕ_{O_2off} =5.4×10^{12} atoms $cm^{-2}s^{-1}$ and the O_2 flux ϕ_{O_2on}=(1-τ) ϕ_{O_2off}=10^{12} molecules $cm^{-2}s^{-1}$.

   CO_2 formation was investigated on two different surfaces, ASW and an oxidized slab of HOPG. During each phase (ices growth or O-atom deposition) the surface is held at a given constant temperature. After each O-atom deposition, the products are probed through RAIRS technique. When about 5 ML of oxygen atoms were deposited on the surface, the surface was heated with a linear temperature ramp of 10 K/min until the adsorbate had fully desorbed from the surface (around 200 K). For both substrates (ASW ice and graphite), we used two surface temperatures (10 and 60 K). We also performed an experiment to check the H_2CO reactivity with O_2 and O_3 to form CO_2. For this purpose, we performed two sets of TPD experiments. First, the H_2CO+O_2 reaction was checked by depositing 2 ML of O_2 on top of H_2CO ices. The H_2CO+O_3 reaction was studied through a similar experiment except that we had previously produced ozone via the $O+O_2$ reaction occurring on the surface, subsequently we eliminated the residual O_2 by heating to 50 K, and only then, deposited H_2CO at 60 K.

5.3.1.2.b   Results and discussion

The main aim of the experiments (and their results) described in this section is to know if H_2CO is able to react with O_x (O, O_2, and O_3).

   As said in the previous section, O_2 is present in the O beam and therefore O_3 can be formed on the surface at temperatures lower than < 55 K (*Minissale et al.* 2014a). For this reason, at first, we have studied separately the reactions H_2CO+O_2/O_3 and only then the reaction H_2CO+O.

   Figure 5.22 shows TPD curves of mass 30 a.m.u. (H_2CO) in panel *b* and of mass 44 a.m.u. (CO_2) in panel *a* after deposition, on oxidized HOPG held at 10 K, of:

1. 2 ML of H_2CO (black squares),

2. 5 ML of O (cyan circles),

3. 2 ML of H_2CO + 5 ML of O atoms (blue stars),

4. 2 ML of H_2CO+O_2 (red triangles),
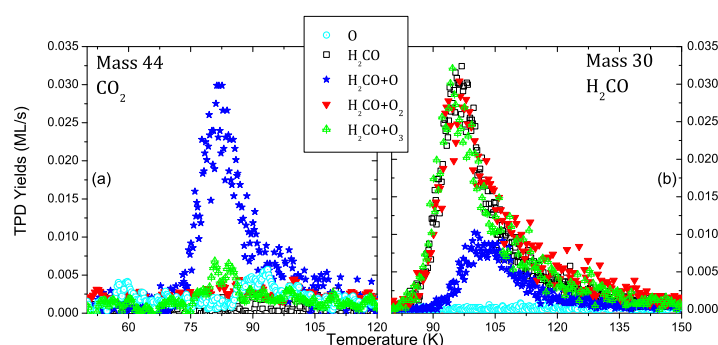
Figure 5.22: Adapted from *Minissale et al.* (2014s). CO_2 (panel *a*) and H_2CO (panel *b*) TPD traces obtained after deposition on oxidized HOPG held at 10 K of: 2 ML of H_2CO (black squares), 5 ML of O (cyan circles), 2 ML of H_2CO+O_2 (red triangles), 2 ML of H_2CO+O_3 (green tringles), and 2 ML of H_2CO + 5 ML of O atoms (blue stars).

5. 2 ML of H_2CO+O_3 (green tringles).

The TPD curves shown in panel **b** and their integrated areas suggest that H_2CO is not consumed by O_2 or O_3. Actually this is not a surprising result since reactions

$$H_2CO + O_2 \rightarrow HCO + HO_2 \ (\Delta H = +160 \text{ kJ/mol}) \ R3.6 \quad\quad (5.6)$$

$$H_2CO + O_3 \rightarrow HO_2 + HCO_2 \ (\Delta H > 200 \text{ kJ/mol}) \ R3.7. \quad\quad (5.7)$$
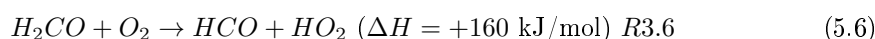
are endothermic (*NIST Chemistry WebBook*) and present high (> 1600 K/k_b) activation barriers (*Michael et al.* 1999; *Braslavsky&Heicklen* 1976). Moreover, the inefficiency of R3.6-7 is confirmed by the absence of newly formed species.

On the other hand, we argue that H_2CO ice is consumed after the oxygen irradiation (blue stars in Figure 5.22) to form CO_2. The experiments in which only O atoms are deposited has been carried out to make sure that CO_2 is not present in the O beam, and it is truly formed on the surface, following H_2CO oxygenation. Actually, a signal at mass 44 (CO_2) is visible in panel *a* of Figure 5.22 (cyan circles), and could come either from O beam or be formed via oxygenation of residual CO. In any case, it is ten times smaller than mass-44 signal coming from H_2CO oxygenation experiment (blue stars).

Further evidence of H_2CO consumption and CO_2 formation are provided by RAIR spectra. Figure 5.23 shows RAIR spectra recorded after deposition at 10 K (top panel) and 55 K (bottom panel) on ASW ices of 2 ± 0.5 ML of H_2CO with increasing doses of oxygen atoms (0, 0.5, 0.8, 1.2, 2, 3.8 ML, respectively, from spectrum *a* to *f*). We assign the band at 1732 cm^{-1} to the CO stretch of H_2CO. The peak between 2349-2345 cm^{-1} is assigned to anti symmetrical stretch of CO_2. The band peaking at 1047 cm^{-1} is due to the ν_3 asymmetric stretching mode of O_3. Moreover we assign the weak and broad band at 1502 cm^{-1} to the CH_2 scissoring of H_2CO. *Minissale et al.* (2013b ,2014a) show that solid-state formation of O_3 is efficient at temperatures lower than 55 K. Actually, temperatures higher than 55 K prevent O_2 adsorption on the surface and, as a consequence, O_3 is no longer formed. These differences become evident by comparing top and bottom panels of Figure 5.23. The two sets of spectra differ for two main differences: O_3 band is not present and the feature at 2347 cm^{-1} increases steadily with O-exposure. These two pieces of evidence, as discussed in detail in the model section, make the evaluation of H_2CO+O activation barrier easier.

Similar results are obtained when the experiments are performed on graphite. The different substrates (HOPG or compact ASW ice) are responsible for small shifts of the IR features, as well as for a change in the band intensities; actually, under the same conditions (equal amount of O sent on H_2CO), HOPG facilitates CO_2 formation with respect to the formation of O_3 and vice versa on ASW. This is a consequence of two effects:

- different diffusion constants of O atoms for oxidized HOPG and ASW ice, $k_{diff-HOPG} < k_{diff-ASW}$ (*Congiu et al.* 2014);
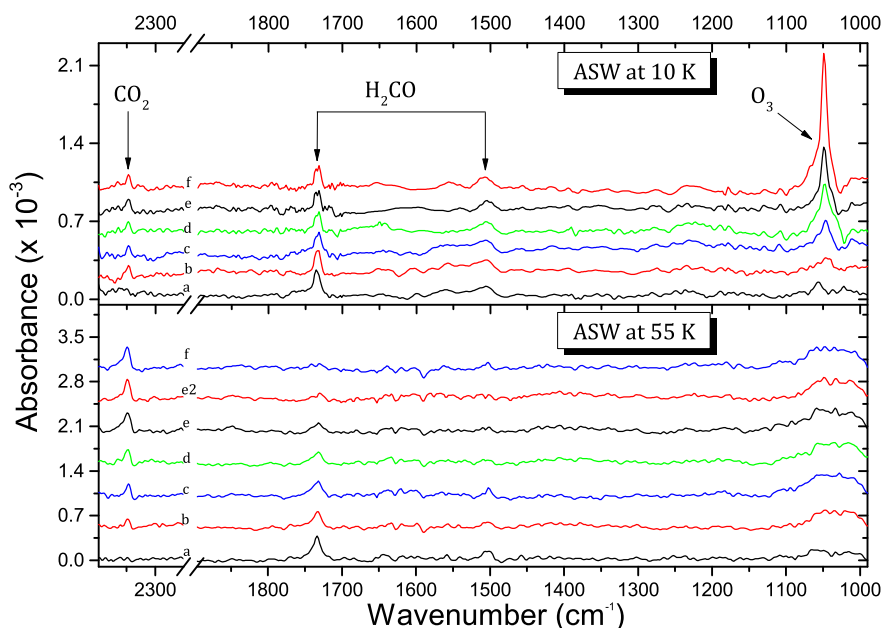
Figure 5.23: Adapted from *Minissale et al.* (2014s). Six RAIR spectra obtained after deposition on a ASW ice held at 10 K (top panel) and 55 K (bottom panel) (H_2CO was always deposited at 60 K) of: (a) 2±0.5 ML of H_2CO; (b) 2±0.5 ML of H_2CO + 0.5±0.1 ML of O atoms; (c) 2±0.5 ML of H_2CO + 0.8±0.1 ML of O atoms; (d) 2±0.5 ML of H_2CO + 1.2±0.2 ML of O atoms; (e) 2±0.5 ML of H_2CO + 2.0±0.3 ML of O atoms; (f) 2±0.5 ML of H_2CO + 3.8±0.3 ML of O atoms. In bottom panel one more spectrum is present: (e2) 2±0.5 ML of H_2CO + 2.8±0.3 ML of O atoms.

- different probabilities of chemical desorption for O_2, $\epsilon_{diff-HOPG} > \epsilon_{diff-ASW}$ (*Dulieu et al.* 2013; *Minissale&Dulieu* 2014c).

On the one hand, fast diffusion of O atoms and low probability of chemical desorption of O_2 on ASW allow O atoms to allotropize into O_2 and then into O_3 ($O_3 \gg CO_2$). On the other hand, on HOPG, surface density of O_2 decreases due to chemical desorption. O atoms stay longer on the surface, and thus have a higher probability to react with H_2CO and form CO_2 ($O_3 \approx CO_2$), due to the lack of O_2 and the slower diffusion constant.

All the experiments presented up to now show the consumption of H_2CO and the formation of CO_2.

These results are very similar to those obtained experimentally by *Chang&Barker* (1979) at high temperature (> 300 K) in gas phase and theoretically by *Dupuis&Lester* (1984). The simplest explanation for CO_2 formation is the O-atom addition to the doubly-bonded carbon atom in H_2CO and the following formation of a vibrationally excited triplet of methylenebis(oxy),

$$H_2CO + O(^3P) \longrightarrow H_2CO_2(^3B_3 -^3 B_2) \quad R3.8a$$

that, following the decomposition process

$$H_2CO_2 \longrightarrow CO_2 + H_2 \quad R3.8b,$$

leads to CO_2 formation (for details on the solid-state network see *Minissale et al.* (2014s)).

5.3.1.2.c   Model: evaluation of the H_2CO+O barrier

In this section we present the model used to fit our experimental data and in particular to evaluate the activation barrier of H_2CO+O reaction. In the model (see Chapter 3 for details), we have considered only the most abundant species present on the surface (O, H_2CO, O_2,

O_3, and CO_2), and the reactions R3.4, R3.5, and R3.8. H_2 is not considered in our model, since our experiments are performed at high temperature and H_2 desorbs very quickly from the surface. In any case, H_2 is inert at low temperature and it cannot change the surface density of the other species. The above-mentioned surface reactions can occur through two mechanisms: the Eley-Rideal (ER) and the Langmuir-Hinshelwood (LH) mechanisms. In the ER mechanism one molecule is already adsorbed on the surface and the other comes from the gas phase (i.e., the beam line); it becomes more efficient as the surface coverage increases. In the LH mechanism, both molecules are bound to the surface and by diffusion they can meet each other and react. LH is highly dependent on the surface temperature. Aware of these facts, we have chosen to fit the data of Figure 5.23 (bottom panel) to give a more precise evaluation of the H_2CO+O barrier. Actually, physical-chemical conditions in these experiments allow us to simplify our model and reduce the errors:

- O-atom diffusion is very fast, and the main part of adsorbed O atoms are consumed through R3.4;

- R3.5 can be neglected, since it is prevented by O_2 desorption;[2]

- R3.8 is most likely to occur via ER, since O atoms are deposited on the H_2CO ice.

Clearly the last point does not exclude that R3.8 could occur via the LH mechanism and, in fact, it is the main source of error in the barrier determination. The LH mechanism depends strongly on O-atom diffusion barrier (E_{Odiff}), one of the free parameters of the model. E_{Odiff} is a thermal diffusion and quantum effects are negligible at this temperature (*Minissale et al.* 2013). It has an upper limit of 900 K/k_b (*Cazaux et al.* 2010), and a lower limit given by ozone formation in our experiments (< 0.05 ML). A value lower than 600 K/k_b for E_{Odiff} increases the efficiency of R3.4, and produces more than > 0.05 ML of ozone. These two limits change the amount of CO_2 formed via LH by 20 % of the total if E_{Odiff}=900 K/k_b, and by 5 % if E_{Odiff}=600 K/k_b. This indetermination, as we will see below, complicates the evaluation of the activation barrier of reaction R3.8 (E_a), the second free parameter of the model. A priori, E_a is a positive real number and becomes equal to zero in the case of a barrierless reaction. Figure 5.24 shows the results of the model (lines) compared with experimental data (symbols). We have used four values for E_a: 550 K/k_b (panel α), 390 K/k_b (panel β), 280 K/k_b (panel γ), and 200 K/k_b (panel δ). We have varied E_{Odiff} in the 600-900 K/k_b range, and Figure 5.24 shows four cases: 600 (dash-dotted line), 700 (dashed line), 800 (dotted line), and 900 K/k_b (solid line). Panel α shows that a too high value (> 550 K/k_b) for E_a is not able to fit our data for any value of E_{Odiff}; actually small amounts of CO_2 and H_2CO are respectively formed and consumed. Moreover, a big amount of ozone is formed. On the other hand, a value too small (< 200 K/k_b) for E_a has an opposite effect, CO_2 is formed too rapidly and H_2CO too quickly consumed by O atoms (panel δ). Couples of values of E_a and E_{Odiff} ranging in 390-280 K/k_b and 600-900 K/k_b respectively (panels β and γ) give excellent fits of the experimental data. Since the fit depends on two parameters, we are not able to give a precise value of the activation barrier of R3.8. Anyway, we have to stress that a determined value for E_{Odiff}, automatically railroads the value of E_a: by using E_{Odiff}=700±150 K/k_b, we find E_a=335±55 K/k_b.

5.3.1.3   Conclusion

In this section we have shown that carbon dioxide can be formed efficiently through CO+O and H_2CO+O reactions on cold surfaces, such as amorphous water or oxidized graphite. We have estimated, through a model, values of 630±100 K and 335±55 K for their activation barrier. These reactions are relevant to astrochemistry to explain CO_2 abundances, as well as the CH_3OH ones, in interstellar ices as we will explain in the last chapter. As shown in Table 5.2, another non-energetic route competes in the CO_2 formation, namely the CO+OH reaction (some experimental works have already been conducted by *Oba et al.* (2011), *Noble et al.* (2011), *Ioppolo et al.* (2013)). The CO+OH pathway seems to be facilitated by the low

---

[2]Actually, through preliminary experiments, we know that atomic oxygen has a large residence time even at 55 K.
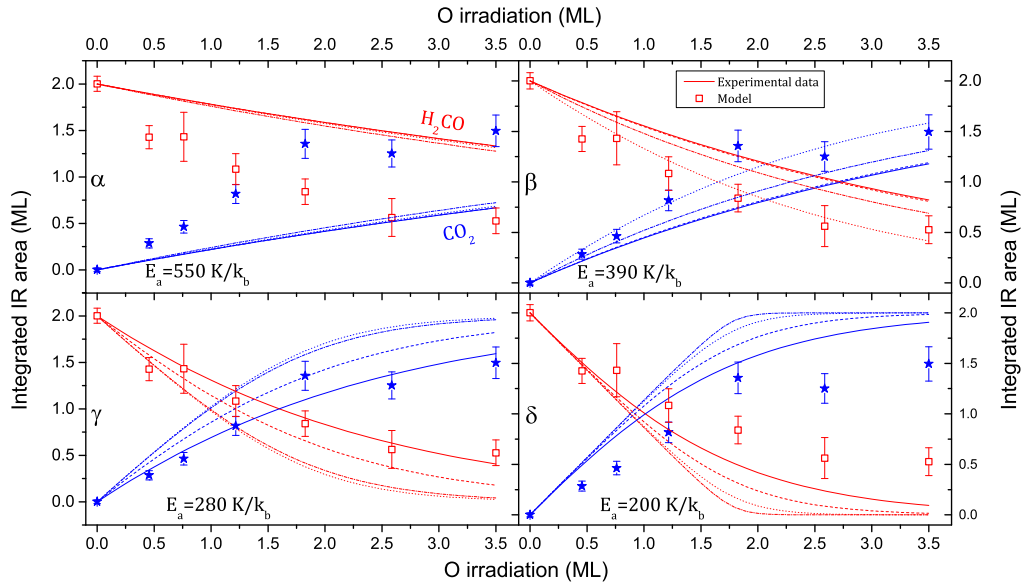
Figure 5.24: Comparison between model (curves) and experimental data (points); IR yields of H_2CO (red) and CO_2 (blue) are shown as a function of O-atom coverage. Four values of E_{Odiff} are used: 900 K/k_b (solid line), 800 K/k_b (dashed line), 700 K/k_b (dotted line), 600 K/k_b (dashed-dotted line). From panel α to δ, E_a is 550 K/k_b, 390 K/k_b, 280 K/k_b, and 200 K/k_b respectively.

Table 5.2: List of solid state reactions and their activation barriers to form CO_2.

Molecule	Enthalpy (kJ/mol)	Reaction	Activation barrier (kJ/mol)	(K)
CO_2	-393[a]	$CO+O$	5.1[b]	630[b]
		$CO+OH$	≤ 3.3[c]	≤ 400[c]
		H_2CO+O	2.8[d]	335[d]

[a] NIST Chemistry WebBook; [b] *Minissale et al.* 2013c; [c] *Oba et al.* 2011, *Noble et al.* 2011; [d] *Minissale et al.* (2014s).

barrier of the reaction, but it has an other type of hindrance. In fact, it requires OH formation first (see *Chaabouni et al.* 2012; *Cuppen et al.* 2010, and references therein for details on OH formation in space). In H-rich environments, OH can be formed easily, although it can be very quickly destroyed to form water. These facts suggest that the efficiency of the three reaction strongly depends on three parameters:

- the O/H ratio, very probably the most important parameter;

- the grain temperature: the higher the temperature, the shorter the H residence time on the grain and thus the probability of OH formation;

- H and O diffusion on the surface: since only H diffusion is usually considered in models (e.g., *Garrod&Pauly* 2011), the CO+O contribution is, in our opinion, underestimated.

5.3.2   The cycle of the CO-H chemistry

CO hydrogenation has been the subject of study by many experimental groups (*Hiraoka et al.* (1994, 2002), *Watanabe&Kouchi* (2002), *Watanabe et al.* (2004), and *Fuchs et al.* (2009)). Nevertheless experimental results of these works seem to lead to different conclusions. Briefly *Watanabe et al.* (2002, 2004) and *Fuchs et al.* (2009) found that the CO+H reaction leads to formaldehyde and methanol formation, while formaldehyde is the only species formed in *Hiraoka et al.* (1994, 2002). To disentangle this problem and due to the fundamental importance of the CO-H chemistry in astrochemistry, we have decided to restudy the problem, with the awareness that we can use different experimental conditions. Table 5.3 lists the
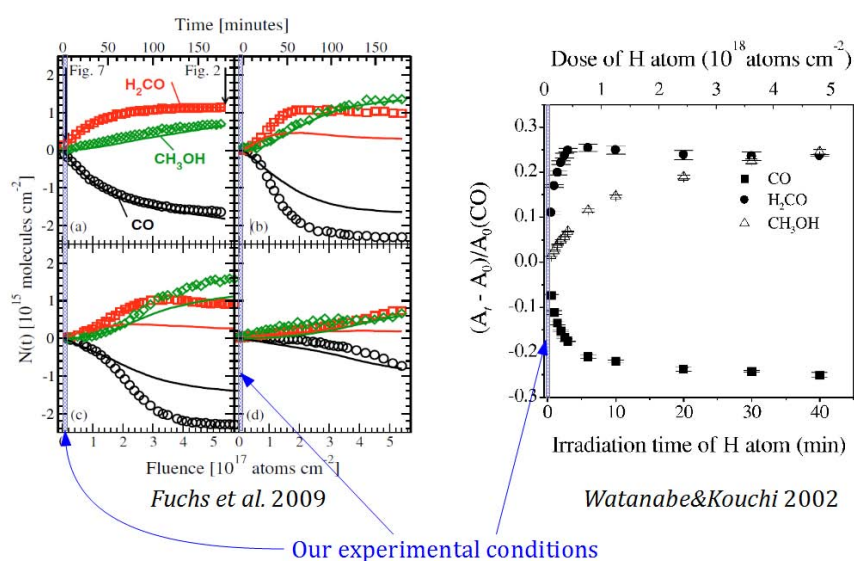
Figure 5.25: Comparison of our experimental fluence regimes (blue bands) with the ones of *Watanabe&Kouchi* (2002) and *Fuchs et al.* (2009).

experimental conditions and results of each works carried out so far. We remark that the

Table 5.3: List of publications about the solid state reaction CO+H with experimental conditions and products.

Article	Flux	Fluence		CO initial thickness	Major products of CO+H
	atoms$\times$cm^{-2}s^{-1}	atoms$\times$cm^{-2}	ML	ML	
Hiraoka et al.	10^{13}	3.6×10^{16}	36	$\approx$10	H_2CO
Watanabe et al.	2×10^{15}	$>10^{17}$	< 100	10	H_2CO and CH_3OH
Fuchs et al.	5×10^{13}	$>10^{17}$	< 100	1-9	H_2CO and CH_3OH
This work	5×10^{12}	6×10^{15}	6	<2.5	CO

probability of H-atom recombination increases as a function of H-atom flux; hence H atoms have larger time of residence in our experiments. On the other hand, the total amount of H atoms sent on CO ices is two order of magnitude smaller with respect to *Watanabe et al.* (2004) and *Fuchs et al.* (2009), as shown in Figure 5.25. Our experimental conditions are somewhat similar to those of *Hiraoka et al.* (1994, 2002).

5.3.2.1 CO+H

Figure 5.26 shows the TPD curves of mass 28, 29, 30, 31, and 32 u.m.a. after deposition of 2.5 ML of CO (red curves), and 2.5 ML of CO + 6 ML of H (green curves) on graphite maintained at 10 K. For both depositions it is present a peak at mass 28 between 25 and 60 K due to CO desorption; it is shown in logarithmic scale in the zoom-in inset. Similar peaks are present at mass 29 and mass 30. These two peaks are very probably due to the desorption of isotopes of carbon monoxide (^{13}CO and $C^{18}O$ respectively): we find that the ratio (the area under the peaks) of ^{13}CO/CO=1.3% is not far from 1.1 % found in IUPAC 1998. Similarly, the ratio $C^{18}O$/CO=0.3% fit exactly with that found by *Cook&Lauer* (1968). The comparison between the two depositions (pure CO vs CO+H) suggests that only a small part of CO ice reacts with H atoms. Actually, the initial ice layer thickness is 2.5 ML and at the end of irradiation with 6 ML of H, 0.4 ML of CO is consumed (around 16% of the initial ice coverage). *Hiraoka et al.* (2002), *Watanabe et al.* (2004) and *Fuchs et al.* (2009) have found a slower reactivity of CO with H atoms. For example *Fuchs et al.* (2009) found that a fluence of H atoms of $\approx2\times10^{16}$ cm^{-2}s^{-1} is needed to consume 15% of initial CO ice
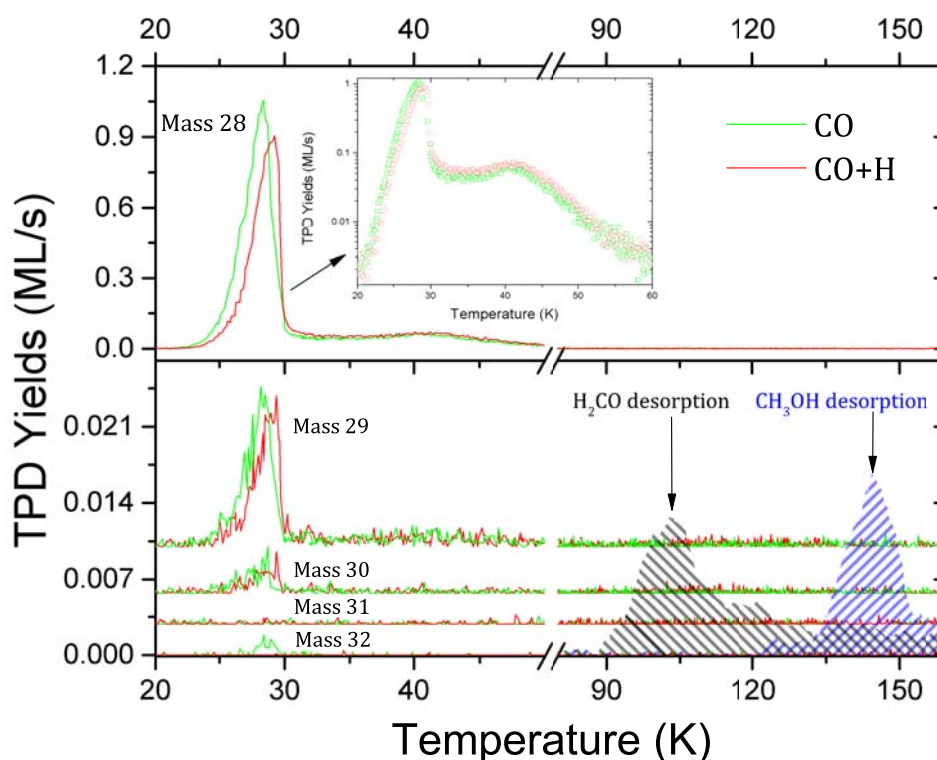
Figure 5.26: TPD traces for mass 28, 29, 30, 31, and 32 obtained after deposition on oxidized HOPG held at 10 K of: 2.5 ML of CO (red curves), and 2.5 ML of CO + 6 ML of H (green curves). The pinstriped TPD curves added in the figure show when H_2CO and CH_3OH desorb. The TPD spectra diplayed in the bottom panel are offset for clarity.

compared to 2×10^{16} cm^{-2}s^{-1} to consume 16% in our experiments. CO hydrogenation can lead to formaldehyde and methanol formation through the following hydrogenation scheme:

$$CO \xrightarrow{+H} HCO \xrightarrow{+H} H_2CO \quad R3.9a$$

$$H_2CO \xrightarrow{+H} CH_3O \xrightarrow{+H} CH_3OH \quad R3.10$$
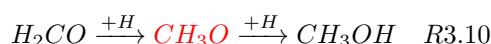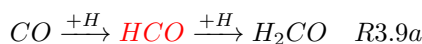
where in red we indicate undetected species. Reactivity of CO+H is limited to R3.9a in *Hiraoka et al.* (2002), and continues to R3.10 in *Watanabe et al.* (2004) and *Fuchs et al.* (2009). In our experiments, only R3.9a takes place on the surface. Figure 5.26 shows two pinstriped TPD curves of H_2CO and CH_3OH obtained after deposition of 1 ML of H_2CO and CH_3OH respectively. H_2CO can be detected via mass 30 and 29, and CH_3OH via mass 32, 31, 30, and 29. None of these masses present a peak at desorption temperatures of H_2CO and CH_3OH for CO+H experiment. We can sum up our experimental results through the following statements:

a the reactivity of CO with H atoms seems to be higher (more CO consumed, with the fluence being equal) with respect to that found in *Watanabe et al.* (2004) and *Fuchs et al.* (2009);

b the two products found by *Watanabe et al.* (2004) and *Fuchs et al.* (2009), namely formaldehyde and methanol, have not been detected;

c Initial reactants> unreacted reactants + final products, something is lost.

How can we explain these differences? To give an answer to this question we decided to study separately the hydrogenation of H_2CO and CH_3OH. The H_2CO+H experiments are treated in the next section while we determined that experimentally

d methanol hydrogenation does not occur.

5.3.2.2 H₂CO+H

Figure 5.27 shows the TPD curves of mass 28, 29, 30, 31, and 32 u.m.a. after deposition 1.8 ML of H_2CO (red curves), 1.8 ML of H_2CO + 3.6 ML of H (blue curves), and 3.6 ML of H (green curves) on graphite maintained at 10 K. Three main peaks are visible in the figure: between 25 and 60 K due to CO desorption; between 85 and 130 K due to H_2CO desorption; between 130 and 160 K due to CH_3OH desorption; each one of these peaks is detected via different masses depending on the cracking pattern of each molecule (see Sec. 2.2.2.1). We notice by comparing the TPD curves after 1.8 ML of H_2CO and 1.8 ML of H_2CO + 3.6 ML of H that a large part of formaldehyde is consumed: after H-atom irradiation, 1.4±0.3 ML of initial formaldehyde ice is consumed and only 0.4±0.2 ML remains unreacted. By looking at the CO and CH_3OH peaks, we estimated that 0.25±0.2 ML of CO and 0.3±0.1 ML of CH_3OH are formed. We can explain these products through the following hydrogenation scheme,

$$H_2CO \xrightarrow{+H} HCO + H_2 \xrightarrow{+H} CO + 2\,H_2 \quad R3.9b$$

$$H_2CO \xrightarrow{+H} CH_3O \xrightarrow{+H} CH_3OH \quad R3.10$$
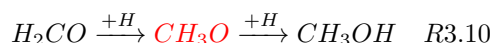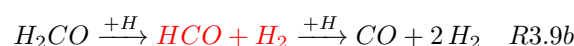
although we cannot explain the lack of CO (under the form of CO, H_2CO, and CH_3OH molecules) at the end of the irradiation, like in the case of CO+H experiment. We can sum up our experimental results through the following statements:

e the reactivity of H_2CO with H atoms seems to be quicker than CO+H;

f H_2CO+H has two products: CO and methanol;

g initial reactants>unreacted reactants + final products, something is lost.

Coming back to the question of the previous section, we can affirm that the total hydrogenation of CO leading to CH_3OH is not necessarily the only process occurring on the surface. Actually, in these experiments, we have shown that a dehydrogenation of H_2CO can lead to CO formation. The difference between our results and the results of *Watanabe et al.* (2004) and *Fuchs et al.* (2009) can be explained by looking at the different physical-chemical conditions used, namely H-atom fluxes and fluences and CO ice thickness. As we already claimed, the higher the flux, the smaller the residence time of H atoms, thus the smaller the probability of the CO+H reaction. This is consistent with the comparison of ours and *Fuchs et al.*'s results if we consider equal fluences. If H-atom flux explains CO consumption, fluence and CO ice thickness explain the reactivity and the final products. Roughly the higher the fluence, the higher the probability for R3.9a and R3.10 to occur. Also this point is coherent with all experimental results; in fact we know that

$$Fluence_{Thiswork} < Fluence_{Hiraoka} < Fluence_{Fuchs\ and\ Watanabe}$$

and the products are, respectively, CO (*this work*), H_2CO (*Hiraoka et al.* 2002), H_2CO and CH_3OH (*Watanabe et al.* 2004; *Fuchs et al.* 2009). Finally the "apparent" no-conservation of matter (initial reactants> unreacted reactants + final products) can be explained through the third physical-chemical parameter, CO ice thickness. *Watanabe et al.* (2004) have performed their experiments for large CO ice thickness (120 Å> 10 ML), while *Fuchs et al.* (2009) have used variable CO ice thickness (from 1 to 10 ML) showing that the efficiency of H_2CO and CH_3OH formation increases as a function of CO ice thickness. The natural question is "why should the ice thickness have an influence on the reactivity?" The answer can be found in the chemical desorption pumping process.

5.3.2.3 Chemical desorption pumping process

Figure 5.28 shows DED of mass 28 during the exposure of H atoms on 2.5 ML of CO ice and on 1.8 ML of H_2CO on the graphite substrate held at 10 K. Both DED experiments would suggest the presence of CD process on graphite of CO molecules. An overview of chemical desorption is shown in Table 5.4, where we have considered DED of different masses, in
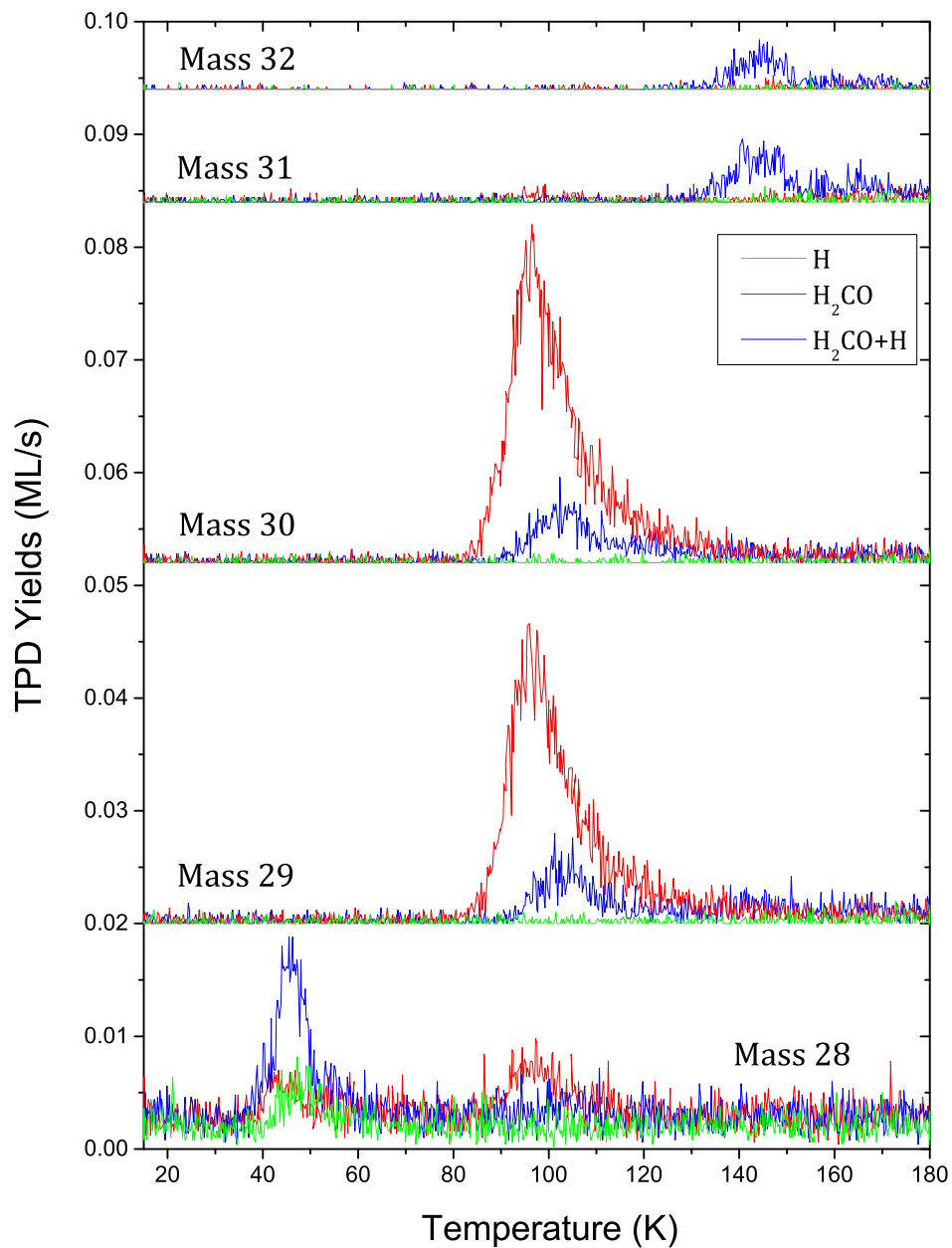
Figure 5.27: TPD traces for mass 28, 29, 30, 31, and 32 obtained after deposition on oxidized HOPG held at 10 K of: 1.8 ML of H_2CO (red curves), 1.8 ML of H_2CO + 3.6 ML of H (blue curves), and 3.6 ML of H (green curves). The TPD spectra are offset for clarity.
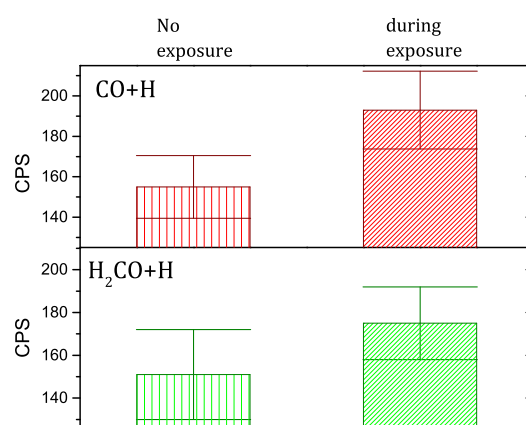
Figure 5.28: Mass 28 monitored with the QMS during the exposure of H atoms on 2.5 ML of CO ice (top panel) and on 1.8 ML of H_2CO (bottom panel) on the graphite substrate kept at 10 K.

Table 5.4: List of CD signal for different masses in $CO/H_2CO/CH_3OH+H$ experiments.

Experiments	Mass 28	Mass 29	Mass 30	Mass 31	Mass 32
			CD signal		
CO+H	Strong	No	No	No	No
H_2CO+H	Strong	Weak	Weak	No	No
CH_3OH+H	No	No	No	No	No

$CO/H_2CO/CH_3OH+H$ experiments.

Figure 5.29 shows the whole CO-H network leading from CO to CH_3OH and passing form the pivotal H_2CO molecule. We can sum up our finding considering three processes:

1. Methanol is formed via H_2CO hydrogenation. It is the only inert and stable (in the sense that it cannot be consumed by H atoms) molecule in the CO-H chemistry;

2. H_2CO can be both hydrogenated to form methanol or dehydrogenated to form CO. In the dehydrogenation process the chemical desorption can occur. Its efficiency could be high, probably around 40%.

3. CO can be hydrogenated to form formaldehyde but, even in this case, chemical desorption can occur, due to dehydrogenation reactions or due to H_2CO CD.

As we already discussed in the Sec. 4.3, chemical desorption depends strongly on the substrate and, recurring to this argument, we can explain the difference between our results and the results of *Watanabe et al.* (2004) and *Fuchs et al.* (2009). The balance of these processes depends on the ice thickness; in other words the balance of these processes depends on the possibility that reactions occur into the bulk or on the surface:

1. into the bulk, the chemical desorption occurring in the $CO-H_2CO$ system is not efficient. Gradually, the $CO-H_2CO$ system evolves toward a more stable system, that is CH_3OH.

2. on the surface, the chemical desorption occurring in the $CO-H_2CO$ system is efficient. Chemical desorption is continuously pumped and it leads to a loss of material. In this case the CH_3OH formation becomes less probable.

5.3.3 Preliminary results of CH_3OH and HCOOH irradiation with H/O atoms

In these section, we present preliminary[3] results on the reactivity of methanol (CH_3OH) and formic acid (HCOOH) with H or O atoms. These two molecules have been observed in

---

[3]We have obtained only qualitative results so far after testing the reactivity of CH_3OH and HCOOH.
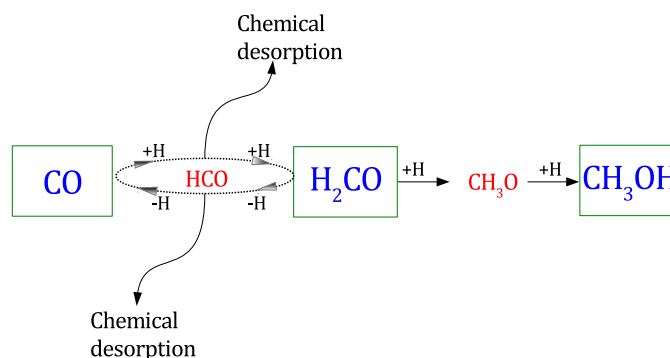
Figure 5.29: Scheme of the CO-H chemistry. The molecules in red are not detected in our experiments.

interstellar ices, and these experiments are intended to test their possible consumption routes. Experiments regarding CH_3OH are very trivial about the analysis: CH_3OH irradiations with H or O atoms produce no effects. Experiments were performed on oxidized graphite; CH_3OH ices are irradiated with different doses of H or O and TPDs spectra with or without irradiation are exactly alike. We can exclude solid-state consumption routes for CH_3OH: the importance of this finding will be illustrated in the astrophysical conclusions. On the other hand, formic acid presents a more lively surface chemistry. Figure 5.30 displays results after irradiation of 1.5±0.5 ML of HCOOH with 4.2±1 ML of H. First of all, we remind that formic acid is detected mainly via mass 29 and also via masses 46, 45, 44, and 28, while methanol is detected via mass 31 as well as via masses 32, 15, and 29 (see Sec. 2.2.2.1). By comparing blue and red curves in Figure 5.30, we notice that

$$1.5\,ML\ \ HCOOH = Mass\,29\,(red) > Mass\,29\,(blue) = HCOOH + 0.45{\times}Mass\,31\,(CH_3OH)$$

with

$$\frac{Mass\,29}{Mass\,31} = 0.45$$

being the cracking factor of methanol. We can conclude that a part of the deposited formic acid is consumed. By looking at the products, we notice in TPDs performed after H-irradiation a peak of mass 18 coming from H_2O desorption, a peak of mass 28 (between 30 and 60 K) due to CO desorption, and evident peaks of masses 31 and 32 due to methanol desorption. Finally a minor peak of mass 44 (between 70 and 100 K) could be due to CO_2 desorption. In summary

$$HCOOH + H \to H_2O\,+\,HCO$$
$$\to HCO + H \Rightarrow CO\,+\,CH_3OH.$$
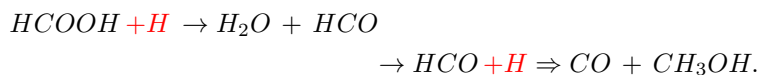
HCOOH+O experiments are presented in Figure 5.31. In this case, we still see consumption of HCOOH, and the products are limited to H_2O and CO_2. We reiterate that through these experiments (HCOOH+H/O) we provide only qualitative estimations of HCOOH+H/O reactivities and we are able to suggest only roughly branching ratios and reaction barriers. In particular, to estimate the reaction barrier we compare the rate of consumption ($k_{HCOOH+H}$) of HCOOH ($k_{HCOOH+X}$)(irradiated both with H and O) with the rate of consumption of CO and H_2CO (k_{CO+O} and k_{H_2CO+O})irradiated with O atoms:

$$k_{CO+O} \ll k_{HCOOH+X} < k_{H_2CO+O}$$

hence, since the following relation is valid for the activation barrier:

$$630K = E_{CO+O} \gg E_{HCOOH+X} > E_{H_2CO+O} = 335K,$$

we can conclude that $E_{HCOOH+X} \approx$450±100 K.
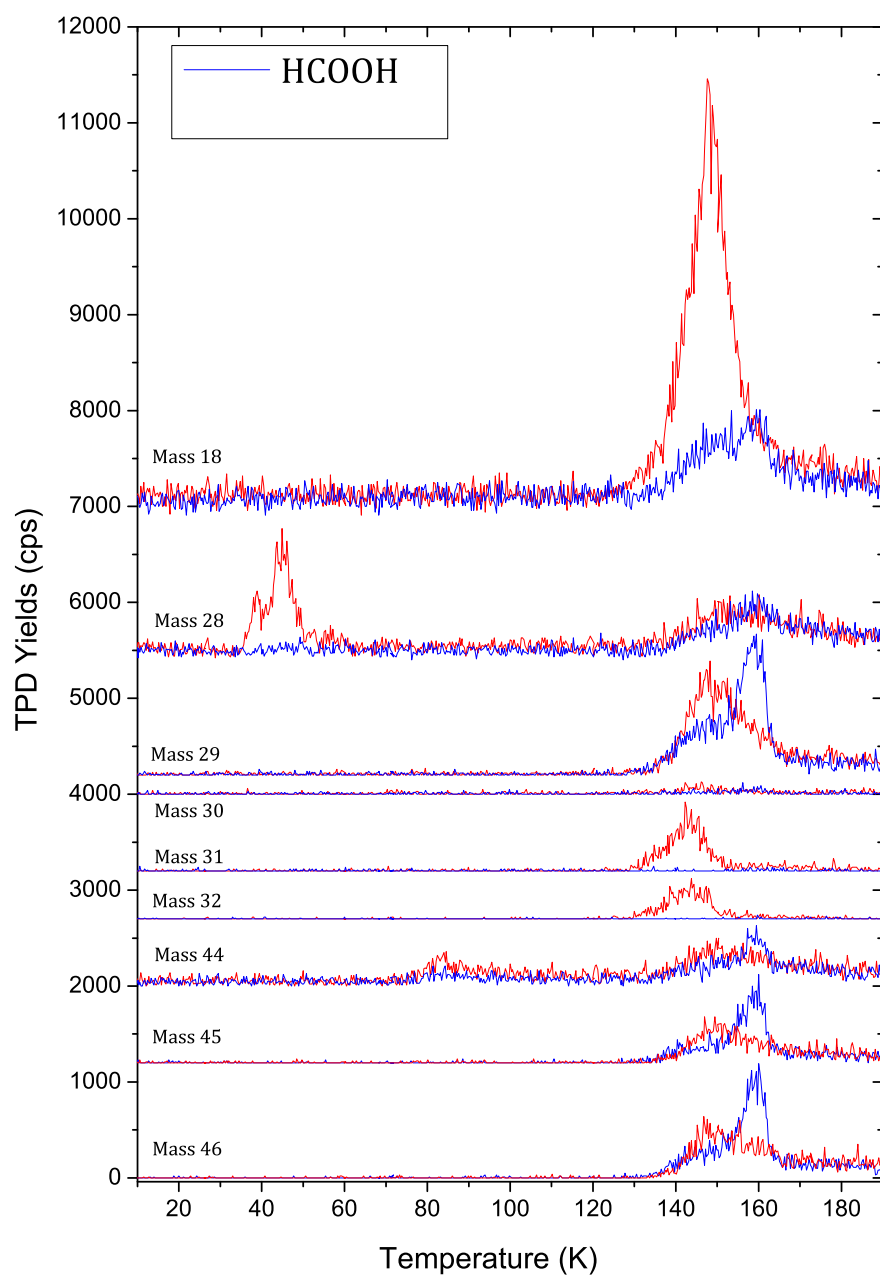
Figure 5.30: TPD curves of different masses after deposition of 1.5±0.5 ML of HCOOH (blue curves) and irradiation of 1.5±0.5 ML of HCOOH with 4.2±1 ML of H (red curves) on oxidized graphite held at 10 K.
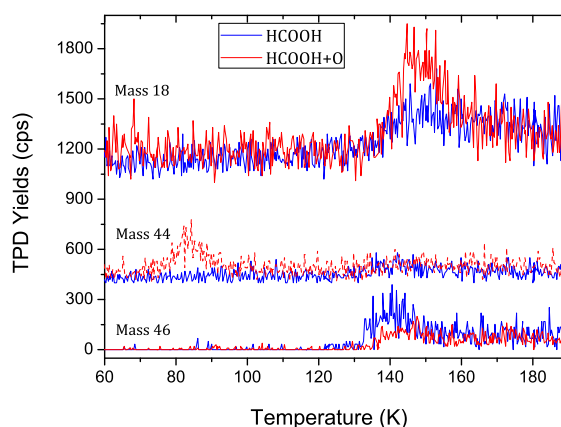
Figure 5.31: TPD curves of different masses after deposition of 1.5±0.5 ML of HCOOH (blue curves) and irradiation of 1.5±0.5 ML of HCOOH with 2±0.3 ML of O (red curves) on oxidized graphite held at 10 K.

Bibliography

5.01 Aikawa, Y., Kamuro, D., Sakon, I., Itoh, Y., Terada, H., Noble, J. A., Pontoppidan, K. M., Fraser, H. J., Tamura, M., Kandori, R., Kawamura, A., Ueno, M., *AKARI observations of ice absorption bands towards edge-on young stellar objects*, Astronomy and Astrophysics, Volume 538, id.A57, 12 pp. (2012)

5.02 Amiaud, L., Fillion, J. H., Baouche, S., Dulieu, F., Momeni, A., and Lemaire, J. L., *Interaction of D_2 with H_2O amorphous ice studied by temperature-programed desorption experiments*, The Journal of Chemical Physics, Volume 124, Issue 9, pp. 094702-094702-9 (2006)

5.03 Atkins, P., & de Paula, *Physical Chemistry*, Eighth Edition, Published in Great Britain by Oxford

5.04 Atkinson, R., *Atmospheric chemistry of VOCs and NO_x*, Atmospheric Environment, Volume 34, Issue 12, pp. 2063-2101 (2000)

5.05 Bartram, M. E. and Koel, B. E., *The Molecular adsorption of NO_2 and this formation of $N_2 0_3$ on Au(111)*, Surface Science, Volume 213, pp. 137-156 (1989)

5.06 Blagojevic, V., Petrie, S. and Bohme, D. K., *Gas-phase syntheses for interstellar carboxylic and amino acids*, Monthly Notices of the Royal Astronomical Society, Volume 339, Issue 1, pp. L7-11 (2003)

5.07 Caselli, P., Stantcheva, T., Shalabiea, O., Shematovich, V. I. and Herbst, E., *Deuterium fractionation on interstellar grains studied with modified rate equations and a Monte Carlo approach*, Planetary and Space Science, Volume 50, Issue 12-13, pp. 1257-1266 (2002)

5.08 Caux, E., Ceccarelli, C., Vastel, C., Castets, A., Baluteau, J.P., and Gry, C., *Large Atomic Oxygen Abundances observed towards Molecular Clouds*, The Promise of the Herschel Space Observatory. Eds. G.L. Pilbratt, J. Cernicharo, A.M. Heras, T. Prusti, and R. Harris. ESA-SP 460, p. 223 (2001)

5.09 Chaabouni, H., Minissale, M., Manicò, G., Congiu, E., Noble, J. A., Baouche, S., Accolla, M., Lemaire, J. L., Pirronello, V., and Dulieu, F., *Water formation through O_2 + D pathway on cold silicate and amorphous water ice surfaces of interstellar interest*, The Journal of Chemical Physics, Volume 137, Issue 23, pp. 234706-20 (2012)

5.10 Charnley, S.B., and Kaufman, M.J., *Carbon Dioxide in Star-forming Regions*, The Astrophysical Journal, Volume 529L, Issue 2, pp. L111-L114 (2000)

5.11 Congiu, E., Chaabouni, H., Laffon, C., Parent, P., Baouche, S. and Dulieu, F., *Efficient surface formation route of interstellar hydroxylamine through NO hydrogenation. I. The submonolayer regime on interstellar relevant substrates*, The Journal of Chemical Physics, Volume 137, p. 054713 (2012a)

5.12 Congiu, E., Fedoseev, G., Ioppolo, S., Dulieu, F., Chaabouni, H., Baouche, S., Lemaire, J.L., Laffon, C., Parent, P., Lamberts, T., Cuppen, H. M. and Linnartz, H., *NO Ice Hydrogenation: A Solid Pathway to NH_2OH Formation in Space*, The Astrophysical Journal, Volume 750, Issue 1, article id. L12, 4 pp. (2012b)

5.13 Cook, G. A., and Lauer, C. M., *Oxygen*, In Clifford A. Hampel. The Encyclopedia of the Chemical Elements. New York: Reinhold Book Corporation. pp. 499-512. LCCN 68-29938. (0.2) (1968)

5.14 Cuppen, H.M., Ioppolo, S., Romanzin, C., and Linnartz, H., *Water formation at low temperatures by surface O_2 hydrogenation II: the reaction network*, Physical Chemistry Chemical Physics, Volume 12, p. 12077 (2010)

5.15 Dulieu, F., Amiaud, L., Congiu, E., Fillion, J.-H., Matar, E., Momeni, A., Pirronello, V. and Lemaire, J. L., *Experimental evidence for water formation on interstellar dust grains by hydrogen and oxygen atoms*, Astronomy and Astrophysics, Volume 512, p. A30 (2010)

5.16 van Dishoeck, E. F., Helmich, F. P., de Graauw, T., Black, J. H., Boogert, A. C. A., Ehrenfreund, P., Gerakines, P. A., Lacy, J. H., Millar, T. J., Schutte, W. A., Tielens, A. G. G. M., Whittet, D. C. B., Boxhoorn, D. R., Kester, D. J. M., Leech, K., Roelfsema, P. R., Salama, A., and Vandenbussche, B., *A search for interstellar gas-phase CO_2. Gas: solid state abundance ratios*, Astronomy and Astrophysics, Volume 315, pp. L349-L352 (1996)

5.17 Fateley, W. G., Bent, H. A. and Crawford, B., *Infrared Spectra of the Frozen Oxides of Nitrogen*, The Journal of Chemical Physics, Volume 31, pp. 204-217 (1959)

5.18 Fuchs, G. W., Cuppen, H. M., Ioppolo, S., Romanzin, C., Bisschop, S. E., Andersson, S., van Dishoeck, E. F., and H. Linnartz, *Hydrogenation reactions in interstellar CO ice analogues. A combined experimental/theoretical approach*, Astronomy and Astrophysics, Volume 505, Issue 2, pp.629-639 (2009)

5.19 Fulvio, D., Sivaraman, B., Baratta, G., Palumbo, M. and Mason, N., *Novel measurements of refractive index, density and mid-infrared integrated band strengths for solid O_2, N_2O and NO_2: N_2O_4 mixtures*, Spectrochimica Acta, 2009, Volume 72, p. 1007 (2009)

5.20 Garrod, R. T., and Pauly, T., *On the Formation of CO_2 and Other Interstellar Ices*, The Astrophysical Journal, Volume 735, p. 15 (2011)

5.21 Gerakines, P. A., Schutte, W. A., and Ehrenfreund, P., *Ultraviolet processing of interstellar ice analogs. I. Pure ices.*, Astronomy and Astrophysics, Volume 312, p. 289 (1996)

5.22 Gerakines, P. A., Whittet, D. C. B., Ehrenfreund, P., Boogert, A. C. A., Tielens, A. G. G. M., Schutte, W. A., Chiar, J. E., van Dishoeck, E. F., Prusti, T., Helmich, F. P., and de Graauw, Th., *Observations of Solid Carbon Dioxide in Molecular Clouds with the Infrared Space Observatory*, The Astrophysical Journal, Volume 522, p. 357 (1999)

5.23 Gibb, E. L., Whittet, D. C. B., Boogert, A. C. A., and Tielens, A. G. G. M., *Interstellar Ice: The Infrared Space Observatory Legacy*, The Astrophysical Journal Supplement Series, Volume 151, p. 35 (2004)

5.24 Goumans, T. P. M., Uppal, M. A., & Brown, W. A., *Formation of CO_2 on a carbonaceous surface: a quantum chemical study*, Monthly Notices of the Royal Astronomical Society, Volume 384, 1158 (2008)

5.25 de Graauw, T., et al., *SWS observations of solid CO_2 in molecular clouds*, Astronomy and Astrophysics, Volume 315L.345D (1996)

5.26 Halfen, D., Apponi, A. J. and Ziurys, L. M., *Evaluating the N/O Chemical Network: The Distribution of N_2O and NO in the Sagittarius B2 Complex*, The Astrophysical Journal, Volume 561, p. 244 (2001)

5.27 Hartmann, D., Wallace, J., Limpasuvan, V., Thompson, D. and Holton, J., *Can ozone depletion and global warming interact to produce rapid climate change?*, Proceedings of the National Academy of Science, Volume 97, Issue 4, pp. 1412-1417 (2000)

5.28 Hasegawa, T. I., Herbst, E., & Leung, C. M. 1992, *Models of gas-grain chemistry in dense interstellar clouds with complex organic molecules*, The Astrophysical Journal Supplement Series, Volume 82, p. 167 (1992)

5.29 d'Hendecourt, L. B., and Jourdain de Muizon, M., *The discovery of interstellar carbon dioxide*, Astronomy and Astrophysics, Volume 223, p. L5 (1989)

5.30 Herbst, E., and Leung, C.M., *Effects of large rate coefficients for ion-polar neutral reactions on chemical models of dense interstellar clouds*, Monthly Notices of the Royal Astronomical Society, Volume 222, p. 689H (1986)

5.31 Hiraoka, K., Yamashita, A., Yachi, Y., Aruga, K., Sato, T., and Muto, H., *Ammonia formation from the reactions of H atoms with N atoms trapped in a solid N_2 matrix at 10-30 K*, The Astrophysical Journal, Volume 443, p. 363 (1995)

5.32 Hiraoka, K., Hiraoka, K., Ohashi, N., Kihara, Y., Yamamoto, K., Sato, T., and Yamashita, A., *Formation of formaldehyde and methanol from the reactions of H atoms with solid CO at 10-20 K*, Chemical Physics Letters, Volume 229, p. 408-414 (1994)

5.33 Hiraoka, K., Sato, T., Sato, S., Sogoshi, N., Yokoyama, T., Takashima, H., Kitagawa, S., *Formation of Formaldehyde by the Tunneling Reaction of H with Solid CO at 10 K Revisited*, The Astrophysical Journal, Volume 577, p. 265 (2002)

5.34 Hidaka, H., Watanabe, M., Kouchi, A., and Watanabe, N., *FTIR study of ammonia formation via the successive hydrogenation of N atoms trapped in a solid N_2 matrix at low temperatures*, Physical Chemistry Chemical Physics, (Incorporating Faraday Transactions), Volume 13, p. 15798 (2011)

5.35 Honrath, R. E., Peterson, M. C., Guo, S., Dibb, J. E. and Shepson, P. B. and B. Campbell, *Evidence of NO_x Production Within or Upon Ice Particles in the Greenland Snowpack*, Geophysical Researchs Letter, Volume 26, pp. 695-698 (1999)

5.36 Ioppolo, S., Cuppen, H. E., Romanzin, C., van Dishoeck, E. F. and Linnartz, H., *Laboratory evidence for efficient water formation in interstellar ices*, The Astrophysical Journal, Volume 686, pp. 1474-1479 (2008)

5.37 Ioppolo, S., Palumbo, M. E., Baratta, G. A., and Mennella, V., *Formation of interstellar solid CO_2 after energetic processing of icy grain mantles*, Astronomy and Astrophysics, Volume 493, p. 1017 (2009)

5.38 Ioppolo, S., Fedoseev, G., Lamberts, T., Romanzin, C., and Linnartz, H., *SURFRESIDE2: An ultrahigh vacuum system for the investigation of surface reaction routes of interstellar interest*, Review of Scientific Instruments, Volume 84, Issue 7, pp. 073112-073112-13 (2013)

5.39 Ioppolo, S., Fedoseev, G., Minissale, M., Congiu, E., Dulieu, F., and Linnartz, H., , *Solid state chemistry of nitrogen oxides - Part II: surface consumption of NO*, Physical Chemistry Chemical Physics, Volume 16, Issue 18, pp. 8270-8284 (2014b)

5.40 Jamieson, C. S., Mebel, A. M., and Kaiser, R. I., *Investigating the Formation of Intermediates in the Reactions of Carbon Dioxide (CO_2) with Suprathermal Oxygen and Nitrogen Atoms*, The Astrophysical Journal Supplement Series, Volume 163, p. 184 (2006)

5.41 Jacox, M.E. and Thompson, W.E., *The infrared spectroscopy and photochemistry of NO_3 trapped in solid neon*, The Journal of Chemical Physics, Volume 129, p. 204306 (2008)

5.42 Jing, D., He, J., Brucato, J., De Sio, A. and Tozzetti, L. and Vidali, G., *On Water Formation in the Interstellar Medium: Laboratory Study of the O+D Reaction on Surfaces*, The Astrophysical Journal, Volume 714L, p. 9J (2011)

5.43 Jones, A. E., Weller, R., Anderson, P. S., Jacobi, H. W., Wolff, E. W., Schrems, O. and H. Miller, *Measurements of NO_x emissions from the Antarctic snowpack*, Geophysical Researchs Letter, Volume 28, Issue 8, pp. 1499-1502 (2001)

5.44 Joshi, P.R., Zins E. L., and Krim, L., *The NO and non-energetic OH radical reactivity: characterization and reaction scheme* Monthly Notices of the Royal Astronomical Society, Volume 419, p. 1713 (2012)

5.45 Knez, C., Boogert, A. C., Pontoppidan, K. M., Kessler-Silacci, J., van Dishoeck, E. F., Evans, N. J.II, Augereau, J.-C., Blake, G. A., and Lahuis, F., *Spitzer Mid-Infrared Spectroscopy of Ices toward Extincted Background Stars*, The Astrophysical Journal, Volume 635, p. L145 (2005)

5.46 Laffon, C., Lasne, J., Bournel, F., Schulte, K., Lacombe, S., and Parent, P., *Photochemistry of carbon monoxide and methanol in water and nitric acid hydrate ices: A NEXAFS study*, Physical Chemistry Chemical Physics, Volume 12, Issue 36, p. 10865 (2010)

5.47 Listz, H. and Turner, B., *Microwave detection of interstellar NO*, The Astrophysical Journal, Volume 224, L73-L76 (1978)

5.48 Martín, S., Mauersberger, R., Martín-Pintado, J., García, Burillo, S. and Henkel, C., *First detections of extragalactic SO_2, NS and NO*, Astronomy and Astrophysics, 2003, Volume 411, pp. L465-L468 (2003)

5.49 Millar, T., Farquhar, P. and Willacy, K., *The UMIST Database for Astrochemistry 1995*, Astronomy and Astrophysics Supplement Series, Volume 121, p. 139 (1997)

5.50 Mallard, W.G., Westley, F., Herron, J.T., Hampson, R.F., and Frizzel, D.H., *NIST Chemical Kinetics Database Version 6.0*, National Institute of Standards and Technology, Gaithersbyrg (MD) (2004)

5.51 Minissale, M., Congiu, E., Baouche, S., Chaabouni, H., Moudens, A., Dulieu, F., Manicò, G., and Pironello, V. *Formation of nitrogen oxides via NO + O_2 gas-solid reaction on cold surfaces*, Chemical Physics Letters, Volume 565, p. 52-55 (2013a)

5.52 Minissale, M., Congiu, E., Baouche, S., Chaabouni, H., Moudens, A., Dulieu, F., Cazaux, S., Accolla, M., Manicò, G., and Pironello, V., *Quantum Tunneling of Oxygen Atoms on Very Cold Surfaces*, Physical Review Letter, Volume 111, p. 053201 (2013b)

5.53 Minissale, M., Congiu, E., Manicò, G., Pironello, V., and Dulieu, F., *CO_2 formation on interstellar dust grains: a detailed study of the barrier of the CO+O channel*, Astronomy and Astrophysics, Volume 559, pp. A49-57 (2013c)

5.54 Minissale, M., Congiu, E., and Dulieu, F., *Oxygen diffusion and reactivity at low temperature on bare amorphous olivine-type silicate*, The Journal of Chemical Physics, Volume 140, p. 074705 (2014a)

5.55 Minissale, M., Fedoseev, G., Congiu, E., Ioppolo, S., Dulieu, F., and Linnartz, H., *Solid state chemistry of nitrogen oxides - Part I: surface consumption of NO*, Physical Chemistry Chemical Physics, Volume 16, Issue 18, pp. 8257-8270 (2014b)

5.56 Minissale, M. and Dulieu, F., *Influence of surface coverage on the chemical desorption process*, The Journal of Chemical Physics, Volume 141, Issue 1, p. 014304 (2014c)

5.57 Miyauchi, N., H. Hidaka, T. Chigai, A. Nagaoka, N. Watanabe, and A. Kouchi, *Formation of hydrogen peroxide and water from the reaction of cold hydrogen atoms with solid oxygen at 10 K*, Chemical Physics Letter, Volume 456, p. 27 (2008).

5.58 Noble, J. A., Dulieu, F., Congiu, E., and Fraser, H. J., *CO_2 Formation in Quiescent Clouds: An Experimental Study of the CO + OH Pathway*, The Astrophysical Journal, Volume 735, Issue 2, pp. 121-127 (2011)

5.59 Noble, J. A., Congiu, E., Dulieu, F. and Fraser, H. J., *Thermal desorption characteristics of CO, O_2 and CO_2 on non-porous water, crystalline water and silicate surfaces at submonolayer and multilayer coverages*, Monthly Notices of the Royal Astronomical Society, 2012, Volume 421, pp. 768-779 (2012)

5.60 Nummelin, A., Whittet, D. C. B., Gibb, E. L., Gerakines, P. A., and Chiar, J. E., *Solid Carbon Dioxide in Regions of Low-Mass Star Formation*, The Astrophysical Journal, Volume 558, p. 185 (2001)

5.61 Oba, Y., Watanabe, N. Kouchi, A., Hama, T., and Pironello, V., *Formation of Carbonic Acid (H_2CO_3) by Surface Reactions of Non-energetic OH Radicals with CO Molecules at Low Temperatures*, The Astrophysical Journal, Volume 722, p. 1598 (2010)

5.62 Oba, Y., Watanabe, N., Hama, T., Kuwahata, K., Hidaka, H. and A. Kouchi, A., *Water Formation through a Quantum Tunneling Surface Reaction, OH + H_2, at 10 K*, The Astrophysical Journal, Volume 749, p. 67O (2012)

5.63 Oliveira, J. M., van Loon, J. Th., Sloan, G. C., Indebetouw, R., Kemper, F., Tielens, A. G. G. M., Simon, J. D., Woods, P. M., and Meixner, M. *Ice chemistry in massive young stellar objects: the role of metallicity*, Monthly Notices of the Royal Astronomical Society, Volume 411, p. L36 (2011)

5.64 Ootsubo, T., Usui, F., Kawakita, H., Ishiguro, M., Furusho, R., Hasegawa, S., Ueno, M., Watanabe, J., Sekiguchi, T., Wada, T., Ohyama, Y., Oyabu, S., Matsuhara, H., Onaka, T., Nakagawa, T., and Murakami, H., *Detection of Parent H_2O and CO_2 Molecules in the 2.5-5 mum Spectrum of Comet C/2007 N3 (Lulin) Observed with AKARI*, The Astrophysical Journal Letters, Volume 717, Issue 1, pp. L66-L70 (2010)

5.65 Palumbo, M. E., Baratta, G. A., Brucato, J. R., Castorina, A. C., Satorre, M. A., and Strazzulla, G., *Profile of the CO_2 bands produced after ion irradiation of ice mixtures*, Astronomy and Astrophysics, Volume 334, pp. 247-252 (1998)

5.66 Raut, U., and Baragiola, R., *Solid-State CO Oxidation by Atomic O: A Route to Solid CO_2 Synthesis in Dense Molecular Clouds*, The Astrophysical Journal Letters, Volume 737, Issue 1, article id. L14, 5 pp. (2011)

5.67 Ridley, J., Walega, B. D., Montzka, F., Grahek, E., Atlas, F., Flocke, V., Stroud, J. Deary, A., Gallant, H., Boudries, J., Bottenheim, K., Anlauf, D., Worthy, A., Sumner, B.S. and Shepson, P., *Is the Arctic surface layer a source and sink of NO_x in winter/spring?*, Journal of Atmospheric Chemistry, Volume 36, pp. 1-22 (2000)

5.68 Roser, J. E., Vidali, G., Manicò, G., and Pironello, V. *Formation of Carbon Dioxide by Surface Reactions on Ices in the Interstellar Medium*, The Astrophysical Journal, Volume 555, pp. L61-64 (2001)

5.69 Schwalke, U., Parmeter, J. E., and Weinberg, W. H., *Vibrational spectra of chemisorbed NO_2 and condensed N_2O_4 on the Ru(001) surface*, The Journal of Chemical Physics, Volume 85, pp. 4036-4042 (1986)

5.70 Shimonishi, T., Onaka, T., Kato, D., Sakon, I., Ita, Y., Kawamura, A., and Kaneda, H. *Spectroscopic observations of ices around embedded young stellar objects in the Large Magellanic Cloud with AKARI*, Astronomy and Astrophysics, Volume 514, pp. A12-24 (2010)

5.71 Stirling, A., Papai, I., Mink, J., and Salhub, D.R., *Density functional study of nitrogen oxides*, The Journal of Chemical Physics, Volume 100, Issue 4, pp. 2910-2923 (1994)

5.72 Suess, H. E., and Urey, H. C., *Abundances of the Elements*, Reviews of Modern Physics, Volume 28, Issue 1, pp. 53-74 (1956)

5.73 Talbi, D., Chandler, G. S., and Rohl, A. L., *The interstellar gas-phase formation of CO_2 - Assisted or not by water molecules?* , Chemical Physics, Volume 320, Issue 2-3, pp. 214-228 (2006)

5.74 Toon, O. and Tolbert, N., *Spectroscopic evidence against nitric acid trihydrate in polar stratospheric clouds*, Nature, Volume 375, Issue 6528, pp. 218-221 (1995)

5.75 Toon, O. and Turco, R., *Polar stratospheric clouds and ozone depletion*, Scientific American, Scientific American, Volume 264, pp. 68-74 (1991)

5.76 Tsuji, T., Yamamura, I., and Sorahana, S., *AKARI Observations of Brown Dwarfs. II. CO_2 as Probe of Carbon and Oxygen Abundances in Brown Dwarfs*, The Astrophysical Journal, Volume 734, Issue 2, pp. 73-81 (2011)

5.77 Watanabe, N. and Kouchi, A., *Efficient formation of formaldehyde and methanol by the addition of hydrogen atoms to CO in H_2O-CO ice at 10 K*, The Astrophysical Journal, Volume 571, pp. L173-L176 (2002)

5.78 Watanabe, N, Nagaoka, A, Shiraki, T, and Kouchi, A., *Hydrogenation of CO on Pure Solid CO and CO-H_2O Mixed Ice*, The Astrophysical Journal, Volume 616, Issue 1, pp. 638-642 (2004)

5.79 Watson, A. J., Donahue, T. M., Stendman, D. H., Knollenberg, R. G., Ragent, B., and Blamont J., *Oxides of nitrogen and the clouds of Venus*, Geophysical Research Letters, Volume 6, pp. 743-746 (1979)

5.80 Whittet, D. C. B., Gerakines, P. A., Tielens, A. G. G. M., Adamson, A. J., Boogert, A. C. A., Chiar, J. E., de Graauw, Th., Ehrenfreund, P., Prusti, T., Schutte, W. A., Vandenbussche, B., and van Dishoeck, E. F. *Detection of Abundant CO_2 Ice in the Quiescent Dark Cloud Medium toward Elias 16*, The Astrophysical Journal, Volume 498, Issue 2, pp. L159-L16 (1998)

5.81 Woodruff, D. P., and Delcher, T. A., *Modern Techniques of Surface Science*, 2nd edn. Cambridge: Cambridge University Press (1994)

5.82 World Health Organization, *Health Aspects of Air Pollution with Particulate Matter,Ozone and Nitrogen Dioxide*, January 2003, Bonn, Germany

5.83 Ziurys, L. M., Apponi, A. J., Hollis, J. M., and Snyder, L. E., *Detection of interstellar N_2O: A new molecule containing an N-O bond*, The Astrophysical Journal, Volume 436, pp. L181-L184 (1994)

5.84 Ziurys,L. M., McGonagle, D., Minh, Y., and Irvine, W. M., *Nitric oxide in star-forming regions - Further evidence for interstellar N-O bonds*, The Astrophysical Journal, Volume 373, pp. 535-542 (1991)

5.85 *Naturally occurring isotope abundances: Commission on Atomic Weights and Isotopic Abundances report for the International Union of Pure and Applied Chemistry*, Pure and Applied Chemistry, 1998, Volume 70, p. 217

6

Astrophysical conclusion and perspectives

La noche está estrellada,
y tiritan, azules, los astros, a lo lejos.

"Poema 20"
Pablo Neruda

Far above the Moon
Planet Earth is blue
And there's nothing I can do.

"Space Oddity"
David Bowie

In this thesis we have reviewed some important results of recent experimental investigations relative to physical-chemical processes occurring on cold surfaces. The main part of these results can be framed in an astrophysical context, particularly in astrochemisty, where they could be relevant to help astronomers understand the formation of interstellar ices, the increase of molecular complexity, and the equilibrium between gas and solid phase. In the following we will present briefly the astrophysical context in which we apply our findings, and we will discuss their influence on the physical-chemistry of molecular clouds.

6.1 Astrophysical conclusion

6.1.1 Astrophysical context

More than eighty years ago, Robert Julius Trumpler noted that the brightness of the more distant open clusters was lower than expected, and the stars appeared more red (*Trumpler* 1930). He supposed that something in the space between stars and us weakened starlight, by an amount proportional to the distance it travelled, so that light from more distant clusters was extinguished more than that from nearby clusters. This hypothesis was revealed to be true. Space among stars is not empty, observations show that it is filled with rarefied gas, dust particles, magnetic field, and relativistically moving electrons, protons and other atomic nuclei. Such diffuse matter is called the Interstellar Medium (ISM). The total mass of the ISM in the Milky Way is about 10% of the visible mass of Galaxy; 99% is made of gas, intermixed with it there is a 1% consisting of tiny dust grains. The ISM is present in different phases (see Table 6.1) characterized by different densities and temperatures, that depend on the physical

and chemical characteristics of the gas and dust and on the physical condition which lead to condensation in clouds. To simplify the description, interstellar clouds may be subdivided in

Table 6.1: List of different components of an interstellar cloud, with the respective temperature, density of particle and mass in SMU (solar mass unity).

Phase	T_g (K)	density (cm^{-3})	M ($10^9 M_\odot$)
Molecular	20 - 30	10^3 - 10^6	≈ 2.5
Cold neutral medium	50 - 100	10 - 50	> 6.0
Warm neutral medium	8000	0.2 - 0.5	≈ 2.8
Ionized warm medium	8000	0.2 - 0.5	≈ 1.5
Warm coronal gas	10^6	0.003	-

two main types:

- Diffuse clouds (density $\leq 10^2$ cm^{-3}), in which UV photons penetrate. The UV radiation causes the breaking of complex molecules (Gas is composed above all of H_2, CO and CH) and inhibits the formation of ice mantle in the dust (substantially silicate and a-Carbon)

- Dense clouds, (density $\approx 10^4$ cm^{-3}) in which photons do not penetrate. In these clouds molecules more complex than H_2, CO and CH can form, as for example formaldehyde, alcohols and so on up to HC_9N. The fact that photons do not penetrate permits the formation of ice mantles on dust grains.

Moreover it must be clarified that cloud morphology changes continuously; its density varies (in the range of million of years) from dense to diffuse and vice versa, because of different energy budgets from surrounding environments:

1. clouds tend to expand and become more diffuse when radiation pressure is larger than gravity;

2. clouds tend to contract and become more dense when radiation pressure is smallar than gravity;

3. cloud collapses (in certain conditions fragmentation occurs, see *Cabrit* (1994) and *Bate* 2000) and star formation begins when radiation pressure is not strong enough to prevent gravitational collapse (the Jeans instability is reached *Jeans* 1902).

It is know that 1% of the ISM mass is in the form of dust grains, with sizes ranging from nanometric to micrometric. For several decades, dust grains were thought to be only passive and annoying entities present towards any astrophysical objects that astronomers wanted to observe. Only in the 1946, Oort and van de Hulst (*Oort&Hulst* 1946) revealed the real nature of dust, showing that dust grains could be a powerful interstellar catalyst. Actually today around 200 molecular species have been identified in interstellar space[1], ranging in complexity from molecular hydrogen (H_2), which is by far the most common molecule in space, through other familiar ones, such as water, hydrogen cyanide (HCN), nitrous oxide (N_2O), and ethanol (CH_3CH_2OH), to esoteric carbon-chains known as cyano-polyynes, the biggest known of which is $HC_{11}N$. Although most of the molecules detected in the interstellar clouds appear to be formed via sequences of gas-phase reactions (*Smith et al.*, 2004; *Herbst*, 2001), this is not true for all species in all types of sources: the presence of dust grains is crucial to synthesis of these species. Grains both shield molecules from stellar ultraviolet light that would otherwise disrupt the chemical bonds and provide a surface on which atoms, radicals, and molecules can congregate and interact. A well studied example is the formation of molecular hydrogen from precursor hydrogen atoms adsorbed in cold surfaces.

Today the formation of several other molecules by surface reactions has been studied. Among them there are carbon dioxide, water, formaldehyde, methanol and carbonic acid (*Hage*

---

[1]An updated and well referred list of detected molecules can be found at *http* : *//en.wikipedia.org/wiki/List_of_interstellar_and_circumstellar_molecules*

et al. 1998; *Zheng&Kaiser* 2007). Laboratory studies have shown that not only simple molecules can be made in this way but elaborate molecules (yet to be detected in space) that may be important in the origin of life itself. Among the molecules of biochemical interest already detected in the Sagittarius B2 cloud, near the center of the Galaxy, is glycolaldehyde ($C_2H_4O_2$), a simple sugar that can combine with other molecules to form more complex sugars i.e. ribose and glucose. Ribose is a building block of nucleic acids such as RNA and DNA, which carry the genetic code of living organisms. One observation also suggests the presence of glycine, the simplest amino acid (a chemical unit of proteins), in Sag B2 (*Kuan at al.*, 2003), even if we have to say that such a detection has not been yet confirmed by other observations.

6.1.2 O diffusion

In Sec. 4.1.3 we have deduced O-atom diffusion coefficients on different surfaces (see Table 4.1 for details). Aside from the diffusion mechanism at play, we have found the a very efficient diffusive process exists; this has an impact on the chemistry occurring at the surface of dust grains. In fact, either the formation of some species may be enhanced, or at least the relative abundances of the final products affected. The implications for solid-state astrochemistry are of major importance. It was usually thought that the chemistry was mostly driven by H diffusion, and therefore the final products were mostly hydrogen saturated species such as H_2O, NH_3, CH_4, and CH_3OH. We can affirm that O addition chemistry is competitive with H additions because of the comparable budget of O atoms and H atoms in dense and UV protected interstellar environments (*Caselli et al.* 2002). An important example of how O-atom mobility can modulate the abundances of key species of ices in dense quiescent molecular clouds is the case of the H_2O : CO_2 ratio. Most of the molecular variety observed in interstellar ices has long been considered the outcome of H-atom addition reactions involving O, O_2, O_3, CO, N, and NO. Water, for example, is the final and most stable species of all the chemical networks between H and O, O_2 and O_3, which justifies its role as the most abundant ice in the Universe. If the reactive partner of H is CO, then CH_3OH is obtained via a series of successive hydrogenations. On the other hand, if H is the only mobile species able to scan the entire surface of the grain (*Matar et al.* 2008), it may be difficult to explain the abundance of CO_2, the second most abundant condensed species. Even if CO_2 can be formed via energetic processes by irradiating ice mixtures of H_2O and CO with UV photons or ions (*Ioppolo et al.* 2009; *Laffon et al.* 2010, and reference therein), these processes are less efficient in dense core of molecular clouds, and CO_2 can only be formed via non-energetic mechanisms, i.e., the reactions CO + OH, CO + O, and H_2CO + O. If these chemical routes leading to CO_2 involved only species which are not mobile at 10 K, then CO_2 formation would be greatly hindered by the rate of accretion and the high mobility of H atoms, which are able to reach CO, OH, and O long before these species can meet to form carbon dioxide. Our present and previous works introduce strong arguments to suggest that O atoms too are mobile at very low temperatures. This implies that the formation rate of CO_2 in dense clouds is governed by a balance between the accretion rate of H atoms and the diffusion rate of O atoms on the surface of dust grains. We carried out some calculations to show the evolution of the relative abundances of H atoms and O atoms on the surfaces of dust grains and - assuming that both species are mobile at low temperatures - how this balance can affect the chemistry within interstellar clouds of various densities. In fact, different environments are characterized by different densities; the abundances of species in the gas phase change and this entails a change in the accretion time-scales of particles on dust grains. In diffuse clouds, hydrogen is mainly present in its atomic form and is by far the most abundant atomic species. In dark clouds, hydrogen is mainly present in its molecular form, so H atoms become a rather rare reactant, with [H] : $[H_2]= 10^{-3}$ (*Li&Goldsmith* 2003). The number density of H atoms is mostly governed by the destruction of H_2 due to cosmic rays. This value, almost independent of the density of the cloud, is of the order 1 H cm^{-3}. On the other hand, the [O] : $[H_2]$ ratio remains approximately constant (10^{-4}), thus the number of atomic O, unlike H, is proportional to the density of the cloud (see, for example, Table 1 in *Caselli et al.* (2002)). For a cloud with number density of 10^4 cm $^{-3}$, the [H] : [O] ratio is 1 : 0.75, while for
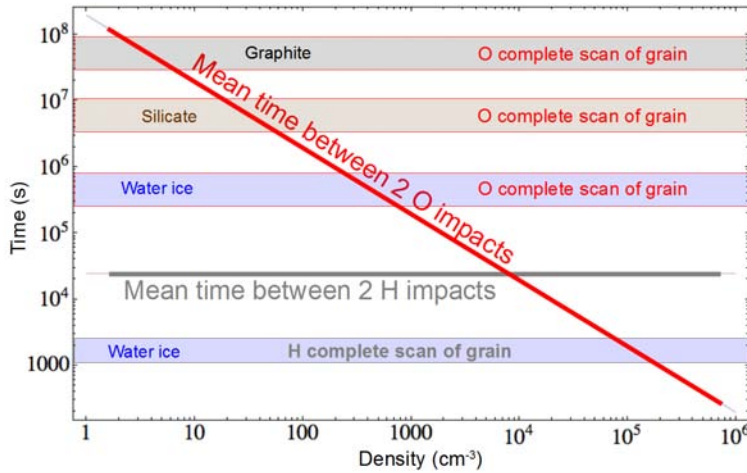
Figure 6.1: From *Congiu et al.* 2014. Time intervals between two impacts of H and O, and the times employed to scan a whole grain (shaded horizontal bands) on various surfaces of interest are plotted as a function of the density of the cloud. The time interval between two arrivals of H is constant, as the density of H atoms remains rather constant regardless of the density of the medium, while the abundance of O atoms increases with cloud density.

a denser cloud with a density of 10^5 cm $^{-3}$, the [H] : [O] ratio is 1 : 7. Therefore, for very dense clouds, O is the most abundant species in atomic form, can accrete on grains and, provided the O atoms are mobile, can subsequently react with other species before these become fully saturated by H-additions. The accretion rates of H atoms and the diffusion coefficients of O are then the key factors to be compared in order to determine at what density of the medium oxidation reactions become comparable to H atom additions. Figure 6.1 shows the time interval between two impacts of particles of the same species (H or O) on a single dust grain, as a function of the density n of the cloud. The time intervals between the two arrivals are derived from the actual particle flux of a given species. The interstellar flux of a species accreting on dust grains can be calculated as follows:

$$\Phi_x = \frac{1}{4}\, n_x\, v_x \tag{6.1}$$

where n_x is the density of species x in the gas phase and $v_x = (8\, k_B\, T\ /\ \pi\, m_x)^{0.5}$ is its mean velocity. Φ_x is thus expressed in particles cm $^{-2}$ s $^{-1}$. For our calculation, we can approximate the dust grains to spheres with a typical radius $r=0.1$ mm, with accessible surface area $A = 4\,\pi\,r^2$. The time interval between the impacts of two particles is then:

$$t = \left(\frac{n_x\, v_x\, A}{4}\right)^{-1} \tag{6.2}$$

The grey solid line in Figure 6.1 represents the time interval between the impact of two hydrogen atoms, calculated by assuming a constant density of H atoms, $n_H=$ 2.3 cm $^{-3}$ (*Li&Goldsmith* 2003). The density of O atoms is proportional to the density of the clouds, n, namely, $n_O=$ 5 $\times 10^{-4}\, n$. The time interval between the arrival of two O atoms is displayed as a red solid line, which clearly shows that the arrival of oxygen atoms becomes more frequent (shorter time between the two impacts) with the increasing density of the cloud. The grey and red lines cross at a density n of around 10^4 cm $^{-3}$. This suggests that for cloud densities of $\approx 10^4$ cm $^{-3}$ the accretion rates of H and O are comparable, and, given that both species can diffuse, oxidation reactions on the grains may play a role, although H-atom additions are still dominant due to the higher mobility of H. In Figure 6.1 we also indicate the mean time O atoms need to complete a scan of all the adsorption sites on the surface of one typical grain as used above, with radius = 0.1 μm and 10^6 absorption sites (10^{15} sites cm^{-2}). The mean times needed for a complete scan of the grain surface were calculated for a surface temperature of 10 K by using the diffusion constants k of O atoms on each substrate presented in this work,

taking into account that $k = 10^{-15}$ cm^2 s^{-1} corresponds to one jump per unit time. For H atoms, the mean time for scanning the entire surface of water ice was derived by the energy barrier for diffusion of 255 K (at 10 K) given by *Matar et al.* (2008). It is interesting to observe the intersection occurring at $n = 10^5$ cm^{-3} between the red line and the band giving the mean time H atoms employ to scan the whole surface of the grain. This implies that at cloud densities of $\approx 10^5$ cm^{-3} or greater, the diffusion and accretion rates of H atoms are smaller than the accretion rate of O atoms. Therefore, in very dense clouds, oxygen atoms may become the dominant reaction partner, able to react with CO and produce CO$_2$, as well as reacting with H to produce OH. Since H atoms are rare in this environment, OH will not be readily transformed into water via hydrogenation, and the hydroxyl radical is likely to react with the abundant CO molecules to form CO$_2$.

6.1.3 Chemical Desorption

For a long time the role of dust as interstellar catalyst has been well recognized. On the contrary, mechanisms that allow the formed species on the surface to populate the gas phase are still poorly known. This is a real paradox and issue of modern astrochemistry: to reconcile almost non-observable solid phase dust catalysis to observable products in the gas phase. In Sec. 1.1.3, we have listed some of the processes leading to gas phase release of adsorbed species. In particular three types of non-thermal desorption can be considered: photodesorption, sputtering, and chemical desorption. This last has been discussed in depth in Sec. 4.3. Here we try to pinpoint what is the impact of CD on the chemistry of ISM. To estimate the impact of chemical desorption on the gas phase composition of astrophysical environments, we used a theoretical model (*Cazaux et al.* (2010); *Meijerink et al.* (2012)), by adding CD yields derived from the experiments presented in Sec. 4.3 (*Dulieu et al.* 2013; *Minissale&Dulieu* 2014). In this sense, we quantify the direct impact of the chemistry on dust on the gas phase. For some reactions occurring on the surface, an important amount of the formed species are ejected in the gas phase. Therefore, within the parameter range at which these reactions dominate the chemistry on the dust surface, an important contribution in the gas phase is expected. Figure 6.2 displays the calculated efficiencies of the conversion rate of gas
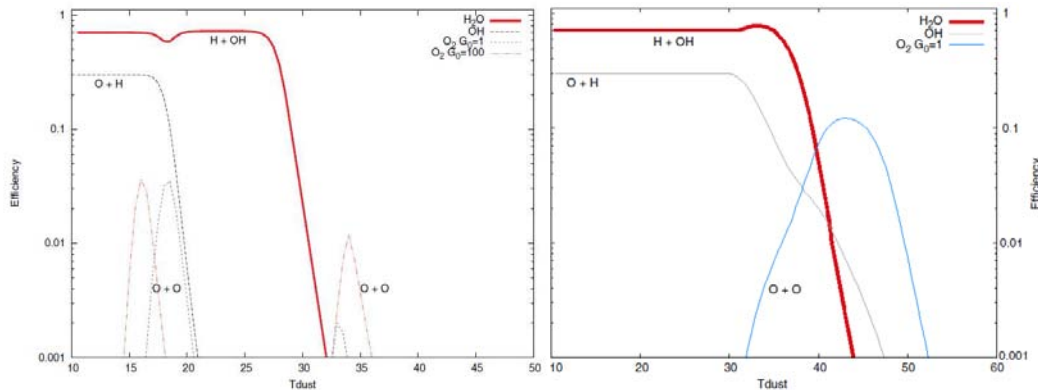
Figure 6.2: Efficiency of chemical desorption as a function of dust temperature. This efficiency represents the fraction of oxygen released into the gas as OH, H$_2$O and O$_2$. The first three reactions are computed for a UV field of G$_0$=1, while the final three are for G$_0$=100. The binding energy of O atoms is 1100 K on the left panel and 1800 K on the right panel.

phase atomic oxygen into another gas phase species (OH, H$_2$, and O$_2$) by the use of grain surface chemistry. In *Dulieu et al.* (2013) efficiency has been calculated for binding energy of E$_{Oxygen}$=1100 K (left panel of Figure 6.2). The formation efficiency is on the order of 30% for OH (below 15 K) and 70% for water (below 25 K). For O$_2$, there are two main temperature ranges where desorption into the gas phase is important. The first one, located around 17 K, has an efficiency of about 4%, while the second one, located around,35 K, has an efficiency of 0.2%. If a strong UV field is considered in our calculations, then the species on the surface can be photo-dissociated and reform. We consider a strong radiation filed

(G_0=100, which corresponds to 100 times the ambient UV radiation field), and show that the efficiency of O_2 formation is increased by a factor of 5. On the other hand, the formation of OH and H_2O is unchanged. In the right panel of Figure 6.2 we have calculated efficiency for binding energy of E_{Oxygen}=1800 K, that is the value found in Sec. 4.2. Even in this case the formation efficiency is on the order of 30% for OH and 70% for water, while for O_2 efficiency has a value of 12 %. Moreover the T_{dust} dependence is somewhat different: water and OH efficiency are zero at 44 K and 48 K (instead of 33 K and 21 K), and O_2 efficiency has no longer two peaks, but only one that falls down at zero at around 52 K. By comparing the formation rates of species via gas or dust routes, we note that the formation of OH (and water) on dust surfaces dominates by 12 (9) orders of magnitude the gas phase route for a gas at 100 K, while this becomes of 0 (2) for a gas at 500 K. These estimations are made considering the dust temperature in the range (0-15 K for left panel and 0-31 K for right panel) for OH and (0-25 K for left panel and 0-30 K for right panel) for water (for calculation details see *Dulieu et al.* (2013)). Searches of O_2 with ground based telescopes and space missions such as SWASS and ODIN indicated that O_2 has a widespread low abundance. O_2 remained unseen allowing to derive some upper limits $X(O_2) \leq 10^{-7}$ (*Goldsmith et al.* 2000; *Pagani et al.* 2003). However, while recent Hershel observations confirmed the general trend that O_2 has very low abundances (detection of O_2 towards rOph, $X(O_2) \approx 10^{-8}$, *Liseau et al.* (2012)), one isolated high abundance of O_2 has been reported towards ORION (*Goldsmith et al.* 2011). This high abundance has been attributed to the presence of warm dust, or to shocks. In this work, our model shows an alternative efficient way to form O_2 in the gas phase through chemical desorption from dust. This efficiency is important only for very specific conditions (T_{dust},30-40 K and high UV field), which could explain why the detection of O_2 is seen only in isolated cases. We note that a single variation of one of model parameters (i.e. O atom binding energy) produces a substantial change in model results, and thus of their astrophysical interpretation. In other words, the prediction power of a theoretical model lies, for a big part, on the right choice of (experimental) physical-chemical parameters, and not only on model degree of sophistication.

Finally we want to stress that the existence of CD not only impacts the chemical composition of our Universe, but affects the way stars form. Actually in regions where stars are forming, the presence of dust dramatically influences the gas phase composition, changing the abundances of molecules available to cool the gas. Therefore, a cloud that undergoes gravitational collapse to form a star will cool more or less rapidly, depending on the available coolants, and this impacts the efficiency and characteristics (mass, binarity) of star formation.

6.1.4 H/C/N/O chemical network

In Chapter 5, we have presented many reactions pointing out their final products and their efficiency. Here we report a list of reactions studied in this thesis by providing products and energy barrier. We have not been able to find a precise value of energy barrier in all the studied reactions, but we provide anyhow an estimation.

6.1.4.1 Interstellar ices

Thanks to infrared observations we know that interstellar dust grains are covered with a ice mantle formed in molecular clouds. Temperatures in these regions can be as low as 10 K, allowing molecules that collide with grains to form an icy mantle. Thereafter, atoms undergo thermal motion across the surface, eventually forming bonds with other atoms. This results in the formation of water and other molecules (i.e. carbon dioxide, carbon monoxide, methanol, ammonia). The composition of interstellar ice varies along the line of sight of different objects and Table 6.3 lists abundances of interstellar ices (CO, CO_2, and CH_3OH) expressed as percentages of the H_2O abundance. We note that

1. carbon dioxide is the most common and abundant types of ice after water. It presents an abundance $N(CO_2/H_2O) \approx 30$ in all objects.

2. carbon monoxide has very variable abundance ranging from 12 to 47 % of H_2O abundances.

Table 6.2: List of reactions (their final products and their efficiency) studied in this thesis.

Reactants	Products	Energy Barrier			Reference
		kJ/mol	meV	K	
O+H	OH		bl		*Dulieu et al.* (2010)
OH+H	H_2O		bl		*Dulieu et al.* (2010)
O_2+H	O_2H		bl		*Chaabouni et al.* (2012)
O_2H+H	H_2O_2		bl		*Chaabouni et al.* (2012)
O_2H+H	2 OH		bl		*Chaabouni et al.* (2012)
O_3+H	O_2+OH		bl		*Mokrane et al.* (2009)
O+O	O_2		bl[a]		*Minissale et al.* (2013, 2014)
O_2+O	O_3		bl[a]		*Minissale et al.* (2013b, 2014a)
N+N	N_2		bl[a]		*This work*
CO+2H	H_2CO		vh		*This work*
CO+O	CO_2	5.24	54.3	630	*Minissale et al.* (2013c)
H_2CO+2 H	CO+4H		s		*This work*
H_2CO+2 H	CH_3OH		s		*This work*
H_2CO+O	CO_2+H_2	2.79	28.9	335	*Minissale et al.* (2014s)
CH_3OH+H	–		vh		*This work*
CH_3OH+O	–		vh		*This work*
HCOOH+H	H_2O+CO+CH_3OH		s		*This work*
HCOOH+O	H_2O+CO_2		s		*This work*
NO+H	NH_2OH		bl		*Congiu et al.* (2012)
NO+N	N_2+ NO_2 + O_3		s		*Minissale et al.* (2014b)
NO+O	NO_2		bl		*Minissale et al.* (2014b)
NO+O_2	NO_2	1.66	17.2	200	*Minissale et al.* (2013a)
NO+O_3	NO_2		small		*Minissale et al.* (2014b)
NO_2+H	NH_2OH+H_2O		bl		*Ioppolo et al.* (2014b)
NO_2+N	N_2O + O_3		high		*Ioppolo et al.* (2014b)
NO_2+O	NO+O_3		high		*Ioppolo et al.* (2014b)
NO+NO	$(NO)_2$		bl		*Minissale et al.* (2013a, 2014b)
NO+NO_2	N_2O_3		bl		*Minissale et al.* (2013a, 2014b)
NO_2+NO_2	N_2O_4		bl		*Minissale et al.* (2013a, 2014b)

[a] These reactions should be barrierless, and we estimate an upper limit of 150 K. [b] For some experiments we are not able to give a precise evaluation of the barrier; we use *bl* (barrierless) for reactions with barrier (E_b) smaller than 150 K, *s* (small) for 150≤E_b ≤500 K, *h* (high) for 500≤E_b ≤800 K, *vh* (very high) for E_b >800 K

3. methanol presents low abundances (< 6) with unexpected peak at 30 % of H_2O ices.

How to explain these abundances? To give an answer to this question, we have to know how these molecules are formed and consumed.

CO_2: its high abundances observed in interstellar ices are explained through some solid-phase reactions. Energetic formation processes leading to efficient formation of CO_2 include irradiation of CO ices (pure or mixed with H_2O) with photons, charged particles or electrons (*Ioppolo et al.* 2009; *Laffon et al.* 2010). On the other hand, *Whittet et al.* (1998) invoke chemical pathways occurring without the addition of energy to explain the CO_2 detection in those interstellar environments where a lack of UV photons forbids ice processing (i.e., molecular cloud Taurus). To date, three (non energetic) pathways are considered:

a CO+OH → CO_2+H

b CO+O → CO_2

c H_2CO+O → CO_2+H_2
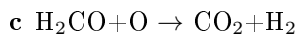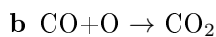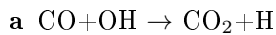
Noble et al. (2011) and *Oba et al.* (2011) showed experimentally the CO_2 formation through reaction (a), but no consistent values were obtained for the activation barrier (barrier between 0 and 400 K). *Roser et al.* (2001) and *Raut&Baragiola* (2011) successfully showed that the formation of CO_2 is possible through reaction (b). Recently in *Minissale et al.* (2013b)

Table 6.3: Abundances of interstellar (CO, CO_2, and CH_3OH) ices expressed as percentages of the H_2O abundance. Data are based on infrared spectroscopy of *Whittet et al.* (2011) and references therein[a]. Each value is obtained by averaging observations of different interstellar objects (Dark clouds, low-mass YSO, and high-mass YSO). *y* (yes) and *n* (not) indicate evidence for thermal processing of ices.

Species	Relative abundance				
Species	Field Stars	Low-mass YSOs		High-mass YSOs	
	–	y	n	y	n
H_2O			100		
CO_2	30.7±9.2	27.1±4.5	34.3±4.3	16.7±4.1	27.4±3.9 [b]
CO	26.0±15.1	14.4±6.1	47.2±14.9	11.9±11.2	25.0±2.5 [b]
CH_3OH	<6.7±3.1	<5.4±3.4	<5.7±4.3[c]	<9.9±7.4	11.1±4.0 [b]

[a] *Whittet et al.* 2011 and references therein: *Boogert et al.* (2000, 2008); *Pontoppidan et al.* (2003, 2004, 2008); *Bottinelli et al.* 2010; *Cook et al.* (2011); *Zasowski et al.* 2009; *Chiar et al.* (1996, 1998); *Thi et al.* (2002, 2006); *Gerakines et al.* 1999; (13) *Öberg et al.* 2011; *Graham 1998*; *Gibb et al.* (2004). [b] This value has been obtained by considering only an object; [c] the average has been obtained by counting out two objects with $N(CH_3OH/H_2O)\approx30$;

we confirmed these results, and we estimated an activation barrier of about 600 K. Finally in *Minissale et al.* (2014s) we have studied reaction (c) by showing that also reaction (c) can efficiently form CO_2 in the ISM. Up to know there is a lack of knowledge on efficient reaction routes able to consume CO_2, except for irradiation of energetic cosmic rays not very likely to occur in molecular clouds.

CO: its abundance is explained only via gas-phase reactions and subsequent accretion on dust grains (*Glover et al.* 2013); up to now, it is known that solid-phase reactions are at a certain degree able to consume CO (i.e. to form CO_2 or CH_3OH).

CH_3OH: CH_3OH is formed via four CO hydrogenations (with a total energy barrier > 800 K/k_b, *Fuchs et al.* 2009), leading to the formation of two unstable radicals, HCO and CH_3O, and one stable molecule, namely, H_2CO. This process can occur only in very H-atom-rich environments (see Sec. 5.3.2). CH_3OH can be formed through energetic processing of icy mantles (*Hudson&Moore* 1999; *Ioppolo et al.* 2009, and references therein). As for CO_2, no efficient routes of consumption are known.

Abundances of Table 6.3 can be explained on the basis of formation and consumption routes. H_2O, CO, CO_2, and CH_3OH are the principle molecules in the solid phase of the H-C-O system. In this system we have three inputs (species arriving from the gas-phase): H, O, and CO (in red in Figure 6.3). By combining two by two inputs we obtain: H-O→H_2O, H-CO→CH_3OH, O-CO→CO_2 (broad arrow in Figure 6.3). This is true only in first approx-
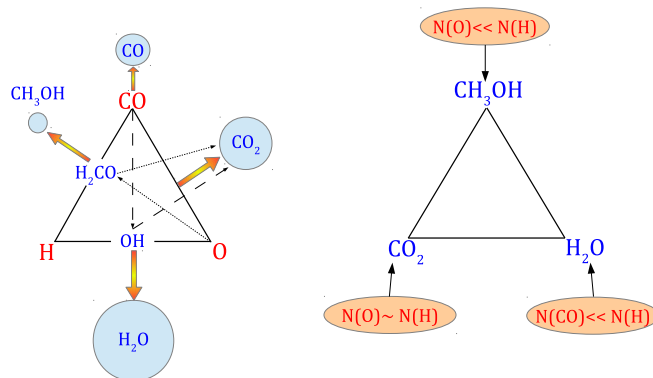
Figure 6.3: Simple schemes of ices formation in ISM. Species are denoted in red and in blue if they are in the gas-phase and in the solid-phase respectively.

imation; in fact OH and H_2CO break the symmetry of the system. Reaction (a) (CO+OH) does not influence very much H_2O formation, due to the abundance of H atoms and the

barrierless reactions leading to H_2O formation; on the other hand reaction (c) (H_2CO+O) and the large CO hydrogenation energy barrier could hinder CH_3OH formation, and favor CO_2 formation. In other words, except for H-rich environments CH_3OH formation is not a very likely event. These considerations can be summarized up as follows (right panel of Figure 6.3):

1. $N(CO_{gas}) \ll N(H_{gas})$ and $N(CO_{gas}) < N(O_{gas})$ favors H_2O_{ice}

2. $N(O_{gas}) \approx N(H_{gas})$ favors CO_{2-ice}

3. $N(O_{gas}) \ll N(H_{gas})$ favors CH_3OH_{ice}

From an astrophysical point of view, these conditions would suggest that a segregation of interstellar ices may develop (see Figure 6.4); the first condition is met when the dust cools down, at $40 < T_{dust} < 25$ K. Under this regime, CO cannot stick while O atoms are able to stick on dust ($E_{b-CO} \approx 1000K < 1500K \approx E_{b-O}$). Hydrogen is prevalently in its atomic form and it is able to hydrogenate O atoms to form water ices; neither CH_3OH nor CO_2 can be formed. At $T_{dust} < 15$ K all species stick. Part of the hydrogen is in molecular form ($N(H_{2-gas})$ increases), thus $N(H_{gas})$ decreases and the second condition is satisfied. These two conditions basically explain observations of ices in field stars and low-mass YSOs, where water and carbon dioxide are the most abundant ices. The third condition is met only in some peculiar cases. Actually, this condition requires that, at least locally, $N(H_{2-gas})$ decreases to favor the $N(H_{gas})$ increase. In high-mass YSOs the high photon fluxes could cause photodissociation of H_2. This produces a temporary increase of $N(H_{gas})$ and thus conditions for CH_3OH formation. In other words, indirect photochemistry increases CH_3OH abundance in high-mass YSOs. This schematic scenario is quite coherent with observations of interstellar ices; in fact, it seems that a sort of depth (i.e., age) segregation exists between the three most abundant ices (H_2O, CO_2, CO) (Gibb et al. 2004; Öberg et al. 2011) water tends to be concentrated in the layers forming the inner (and older) part of the mantles, while CO_2 and CO abundance increases in the outer (and more recent) layers.

6.2 Perspectives

6.2.1 Ice growth: MonteCarlo Model

The growth of ice mantle can be simulated by using a microscopic Monte Carlo (MMC) method. Atoms and molecules (essentially H/O/CO) accrete on dust from the gas-phase and their rates of accretion vary over time simulating interstellar evolution. In collaboration with S. Cazaux (University of Groningen) and V. Cobut (University of Cergy-Pontoise) we are developing a MMC to study the ice mantle growth. The model is very similar to the one used in *Cuppen&Herbst* (2007) or *Cazaux et al.* (2010), but it differs essentially in two points: (1) massive use of experimental data; (2) continuous comparison with experimental results. We assume that the physics acting on interstellar ices is the same of the physics we observe in the laboratory. Hence, we think that a MMC has to reproduce laboratory results in order to provide reliable predictions. The match between theoretical and observational data (scheme in Figure 6.5) should be improved by increasing the degree of model sophistication and using a different "physics", as the more consistent physics adopted, the more reliable the match will be. For this reason, first of all, we will implement in our MMC all the experimental results that we have found (i.e. activation barriers for reaction, energy barriers for diffusion, CD efficiencies, binding energies), and subsequently we will test the physics used in the model by comparing model results with experimental data. Model parameters are tuned to find a reasonable match. Only after determining that the model can reproduce the experimental values it will be used for predicting physical chemical properties of the ISM and for drawing astrophysical conclusion (see scheme b in Figure 6.5). One way for comparing model results with experimental data could be reproduce experimental TPDs with MMC as shown in Figure 6.6. In this case, the parameters we have to adjust, to find a good match is the addition of binding energies and the transition from monolayer to multilayer desorption.
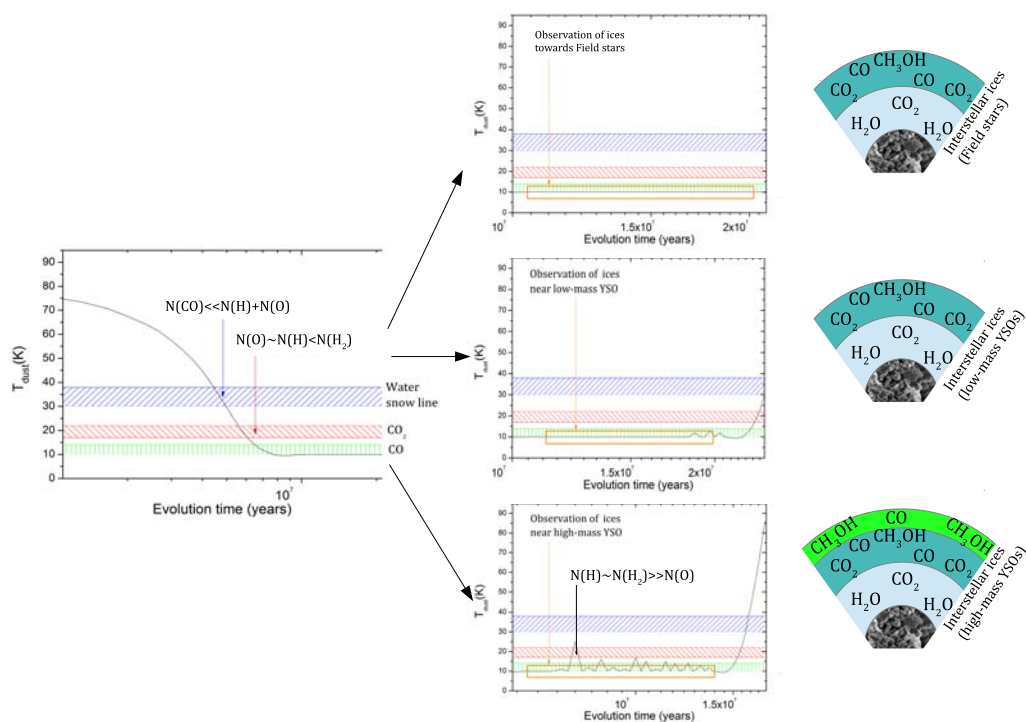
Figure 6.4: Temperature of dust as a function of evolution time for ices in molecular clouds towards field stars, and ices observed near low-mass YSOs and high-mass YSOs. Pinstriped zones indicate, respectively H_2O, CO_2, and CO snow-lines. Colored arrows indicate moments at which each condition is met (see text). On the right side schematic representation of interstellar ices for their respective regions of observation.
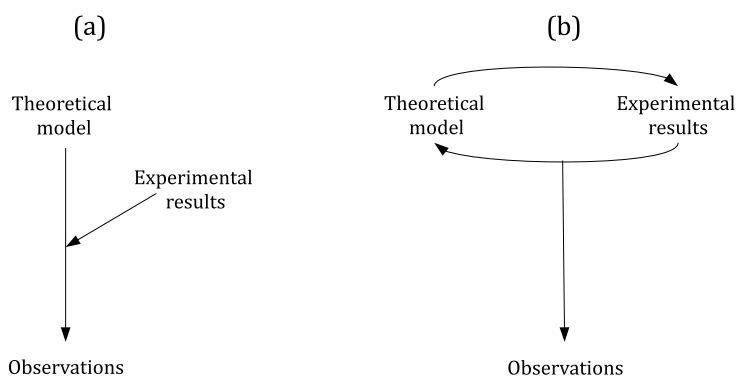
Figure 6.5: Schematic representation of classical a MMC approach sequence (a) and our own MMC for deriving physical chemical properties of ISM (b).
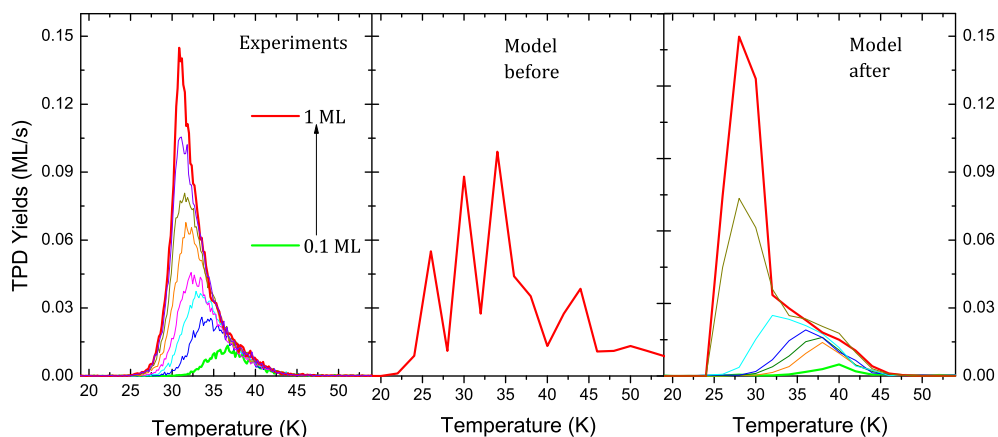
Figure 6.6: Comparison between TPDs of O_2 obtained experimentally (panel at left) and through two different versions (central panel, preliminary version; panel at right, improved version) of the MMC model.

Once TPDs of different molecules and simple reactivity cases are checked, the MMC model could also be used to study the properties of icy mantles.

6.2.2   Further perspectives

1. *Comparison of O-atom isotopic diffusion*: the use of an isotope of the O atom (i.e., $^{18}O_2$) could give further experimental constraints about the O atoms diffusion and could help to demonstrate the mass effect predicted in *Alben et al.* (1980).

2. *N-atom and C-atom diffusion*: N and C atoms could reveal mobility properties similar to those of O atoms. If we scale the diffusion for these atoms, on the basis of their polarizability alone - the main parameter for physisorption - there is a reasonable range of temperatures (5-20 K) where the mobility of O, C and N is activated. For this reason, the production of O, C, and N bearing molecules can grow, avoiding saturated chemical traps. This could also be one of the mechanisms leading to complex nonvolatile organic compounds observed in meteorites, such as amino acids.

3. *Molecular complexity, H-C-N-O*: in Chapter 5 we presented many reactions by using not more than a 3-dimensional matrice of species (H-C-O, H-N-O). What molecule can be formed using a 4-dimensional matrices?

4. *Phase transition, from gas to solid and viceversa*: the gas and solid phases are almost sealed off and a bridge between them would help to understand chemistry and dynamics of the ISM. Some key questions already stand on robust pillars, but some other questions are still open:

   - What are the parameters ruling the phase transition?

   - What is the energy distribution of desorbing molecules (thermal and non-thermal)?

   - How phonons dissipation occurs?

Un jour.
Un jour, bientôt peut-être.
Un jour j'arracherai l'ancre qui tient mon navire loin des mers.

"Peintures" in L'espace du dedans
Henri Michaux

Bibliography

6.01 Alben, J. O., Beece, D., Bowne, S. F., Eisenstein, L., Frauenfelder, H., Good, D., Marden, M. C., Moh, P. P., Reinisch, L., Reynolds, A. H., and Yue, K. T., *Isotope Effect in Molecular Tunneling*, Physical Review Letter, Volume 44, p. 1157 (1980)

6.02 Bate, M., *Star Formation*, *http://www.astro.ex.ac.uk/people/mbate/Research/SF.html*, (2000)

6.03 Cabrit, S. *Molecular Clouds and Star Evolution*, in Star Formation and Techniques in Infrared and mm-Wave Astronomy. T.P. Ray & S.V.W. Beckwith eds. Springer-Verlag, Berlin, pp. 1-48 (1994)

6.04 Caselli, P., Stantcheva, T., Shalabiea, O., Shematovich, V. I. and Herbst, E., *Deuterium fractionation on interstellar grains studied with modified rate equations and a Monte Carlo approach*, Planetary and Space Science, Volume 50, Issue 12-13, pp. 1257-1266 (2002)

6.05 Cazaux, S., Cobut, V., Marseille, M., Spaans, M., and Caselli, P. *Water formation on bare grains: When the chemistry on dust impacts interstellar gas*, Astronomy and Astrophysics, Volume 522, p. A741 (2010)

6.06 Chaabouni, H., Minissale, M., Manicò, G., Congiu, E., Noble, J. A., Baouche, S., Accolla, M., Lemaire, J. L., Pirronello, V., and Dulieu, F., *Water formation through O_2 + D pathway on cold silicate and amorphous water ice surfaces of interstellar interest*, The Journal of Chemical Physics, Volume 137, Issue 23, pp. 234706-20 (2012)

6.07 Cuppen, H., and Herbst, E., *Simulation of the Formation and Morphology of Ice Mantles on Interstellar Grains*, The Astrophysical Journal, Volume 668, Issue 1, pp. 294-309 (2007)

6.08 Congiu, E., Minissale, M., Baouche, S., Chaabouni, H., Moudens, A., Cazaux, S., Manicò, G., Pirronello, V., and Dulieu F., *Efficient diffusive mechanisms of O atoms at very low temperatures on surfaces of astrophysical interest*, Faraday Discussion 168 (2014)

6.9 Dulieu, F., Amiaud, L., Congiu, E., Fillion, J.-H., Matar, E., Momeni, A., Pirronello, V. and Lemaire, J. L., *Experimental evidence for water formation on interstellar dust grains by hydrogen and oxygen atoms*, Astronomy and Astrophysics, Volume 512, p. A30 (2010)

6.10 Fuchs, G. W., Cuppen, H. M., Ioppolo, S., Romanzin, C., Bisschop, S. E., Andersson, S., van Dishoeck, E. F., and H. Linnartz, *Hydrogenation reactions in interstellar CO ice analogues. A combined experimental/theoretical approach*, Astronomy and Astrophysics, Volume 505, Issue 2, pp.629-639 (2009)

6.11 Gibb, E. L., Whittet, D. C. B., Boogert, A. C. A., and Tielens, A. G. G. M., *Interstellar Ice: The Infrared Space Observatory Legacy*, Astrophysical Journal Supplement, Volume 151, p. 35 (2004)

6.12 Goldsmith, P. F. et al.*Herschel Measurements of Molecular Oxygen in Orion*, The Astrophysical Journal, Volume 737, p. 96 (2011)

6.13 Goldsmith, P. F. et al. *O_2 in Interstellar Molecular Clouds*, The Astrophysical Journal Letter, Volume 539, p. L123 (2000)

6.14 Hage, W., Liedl, K. R., Hallbrucker, A., and Mayer, E., *Carbonic acid in the gas phase and its astrophysical relevance*, Science, Volume 279, Issue 5355, pp. 1332-5 (1998)

6.15 Ioppolo, S., Palumbo, M. E., Baratta, G. A., and Mennella, V., *Formation of interstellar solid CO_2 after energetic processing of icy grain mantles*, Astronomy and Astrophysics, Volume 493, p. 1017 (2009)

6.16 Ioppolo, S., Fedoseev, G., Minissale, M., Congiu, E., Dulieu, F., and Linnartz, H., , *Solid state chemistry of nitrogen oxides - Part II: surface consumption of NO*, Physical Chemistry Chemical Physics, Volume 16, Issue 18, pp. 8270-8284 (2014b)

6.17 Herbst, E., *The Chemistry of Interstellar Space*, Chemical Society Reviews, Volume 30, pp. 168-176 (2001)

6.18 Hudson, R. L., and Moore, H. M., *Laboratory Studies of the Formation of Methanol and Other Organic Molecules by Water+Carbon Monoxide Radiolysis: Relevance to Comets, Icy Satellites, and Interstellar Ices*, Icarus, Volume 140, p. 451 (1999)

6.19 Jeans, J. H., *The Stability of a Spherical Nebula*, Philosophical Transactions of the Royal Society of London. Series A, Containing Papers of a Mathematical or Physical Character, Volume 199, pp. 1-53 (1902)

6.20 Kuan, Y.-J., Charnley, S. B., Huang, H.-C., Tseng, W.-L., and Kisiel, Z., *Interstellar Glycine*, The Astrophysical Journal, Volume 593, pp. 848-867 (2003)

6.21 Laffon, C., Lasne, J., Bournel, F., Schulte, K., Lacombe, S., and Parent, P., *Photochemistry of carbon monoxide and methanol in water and nitric acid hydrate ices: A NEXAFS study*, Physical Chemistry Chemical Physics, Volume 12, Issue 36, p. 10865 (2010)

6.22 Li, D., and Goldsmith, P. F., *Massive Quiescent Cores in Orion. I. Temperature Structure*, The Astrophysical Journal, Volume 585, pp. 823 (2003)

6.23 Liseau, R. et al. *Multi-line detection of O_2 toward r Ophuichi A*, Astronomy and Astrophysics Volume 541, p. A73 (2012)

6.24 Matar, E., Congiu, E., Dulieu, F., Momeni, A., and Lemaire, J. L., *Mobility of D atoms on porous amorphous water ice surfaces under interstellar conditions*, Astronomy and Astrophysics, Volume 492, Issue 1, pp. L17-L20 (2008)

6.25 Meijerink, R., Cazaux, S., and Spaans, M. *Enhanced H_2O formation through dust grain chemistry in X-ray exposed environments*, Astronomy and Astrophysics, Volume 537, p A102 (2012)

6.26 Minissale, M., Congiu, E., Baouche, S., Chaabouni, H., Moudens, A., Dulieu, F., Manicó, G., and Pirronello, V. *Formation of nitrogen oxides via NO + O_2 gas-solid reaction on cold surfaces*, Chemical Physics Letters, Volume 565, p. 52-55 (2013a)

6.27 Minissale, M., Congiu, E., Baouche, S., Chaabouni, H., Moudens, A., Dulieu, F., Cazaux, S., Accolla, M., Manicò, G., & Pirronello, V., Physical Review Letter, Volume 111, p. 053201 (2013b)

6.28 Minissale, M., Congiu, E., Manicò, G., Pirronello, V., and Dulieu, F., *CO_2 formation on interstellar dust grains: a detailed study of the barrier of the CO+O channel*, Astronomy and Astrophysics, Volume 559, pp. A49-57 (2013c)

6.29 Minissale, M., Congiu, E., and Dulieu, F., *Oxygen diffusion and reactivity at low temperature on bare amorphous olivine-type silicate*, The Journal of Chemical Physics, Volume 140, pp.074705 (2014a)

6.30 Minissale, M., Fedoseev, G., Congiu, E., Ioppolo, S., Dulieu, F., and Linnartz, H., *Solid state chemistry of nitrogen oxides - Part I: surface consumption of NO*, Physical Chemistry Chemical Physics, Volume 16, Issue 18, pp. 8257-8270 (2014b)

6.31 Minissale, M., and Dulieu, F., *Influence of surface coverage on the chemical desorption process*, The Journal of Chemical Physics, Volume 141, Issue 1, p. 014304 (2014c)

6.32 Minissale, M., Baouche, S., Chaabouni, H., Congiu, E., Moudens, A., and Dulieu, F., *Solid-state formation of CO2 via the H2CO + O reaction*, submitted to Astronomy and Astrophysics (2014s)

6.33 Mokrane, H., Chaabouni, H., Accolla, M., Congiu, E., Dulieu, F.,Chehrouri, M., and J. L. Lemaire, *Experimental Evidence for Water Formation Via Ozone Hydrogenation on Dust Grains at 10 K*, The Astrophysical Journal, Volume 705, pp. L195 (2009)

6.34 Noble, J. A., Dulieu, F., Congiu, E., and Fraser, H. J., *CO_2 Formation in Quiescent Clouds: An Experimental Study of the CO + OH Pathway*, The Astrophysical Journal, Volume 735, Issue 2, pp. 121-127 (2011)

6.35 Oba, Y., Watanabe, N., Kouchi, A., Hama, T., and Pirronello, V., *Experimental studies of surface reactions among OH radicals that yield H_2O and CO_2 at 40-60 K*, Physical Chemistry Chemical Physics, vol. 13, issue 35, p. 15792 (2011)

6.36 Öberg, K. I., Boogert, A. C. A., Pontoppidan, K. M., van den Broek, S., van Dishoeck, E. F., Bottinelli, S., Blake, G., A., and Evans, N. J. II, *The Spitzer Ice Legacy: Ice Evolution from Cores to Protostars*, Astrophysical Journal, Volume 740, p. 109 (2011)

6.37 Oort, J. H., and van de Hulst, H. C., *Gas and smoke in interstellar space*, Bulletin Astronomical Institute Netherlands, Volume 10, p. 187 (1946)

6.38 Pagani, L. et al. *Low upper limits on the O_2 abundance from the Odin satellite*, Astronomy and Astrophysics, Volume 402, p. L77 (2003)

6.39 Raut, U., and Baragiola, R., *Solid-State CO Oxidation by Atomic O: A Route to Solid CO_2 Synthesis in Dense Molecular Clouds*, The Astrophysical Journal Letters, Volume 737, Issue 1, article id. L14, 5 pp. (2011)

6.40 Roser, J. E., Vidali, G., Manicò, G., and Pirronello, V. *Formation of Carbon Dioxide by Surface Reactions on Ices in the Interstellar Medium*, The Astrophysical Journal, Volume 555, pp. L61-64 (2001)

6.41 Smith, I. W. M., Herbst, E. , and Chang, Q., *Rapid neutral-neutral reactions at low temperatures: a new network and first results for TMC-1*, Monthly Notices of the Royal Astronomical Society, Volume 350, pp. 323-330 (2004)

6.42 Trumpler, R. J., *Preliminary results on the distances, dimensions and space distribution of open star clusters*, Lick Observatory Bulletin, Volume XIV, Number 420, pp. 154-188 (1930)

6.43 Whittet, D. C. B. , Cook, A. M., Herbst, E., Chiar, J. E., and S. S. Shenoy, *Observational constraints on methanol production in interstellar and preplanetary ices*, The Astrophysical Journal, Volume 742, pp. 28-38 (2011)

6.44 Whittet, D. C. B., Gerakines, P. A., Tielens, A. G. G. M., Adamson, A. J., Boogert, A. C. A., Chiar, J. E., de Graauw, Th., Ehrenfreund, P., Prusti, T., Schutte, W. A., Vandenbussche, B., and van Dishoeck, E. F. *Detection of Abundant CO_2 Ice in the Quiescent Dark Cloud Medium toward Elias 16*, The Astrophysical Journal, Volume 498, Issue 2, pp. L159-L16 (1998)

6.45 Zheng, W., and Kaiser, R. I., *On the formation of carbonic acid (H_2CO_3) in solar system ices*, Chemical Physics Letters, Volume 450, pp. 55-60 (2007)

Appendix A. Atomic and molecular term symbols

Atomic and molecular term symbols specify electronic energy levels of atoms and diatomic molecules, respectively. The form of the symbols imply Russell-Saunders coupling and consist of four parts: spin multiplicity, azimuthal angular momentum, total angular momentum, symmetry and parity. In the atomic case, the whole notation has the general form

$$^{2S+1}L(S, P, D, F, ...)_J \tag{6.3}$$

where

- L is the total orbital quantum number; The first 4 symbols of are S, P, D, F corresponding to a value of 0, 1, 2, 3;

- S is the total spin quantum number. 2S + 1 is the spin multiplicity;

- J is the total angular momentum quantum number.

For homonuclear diatomic molecules, or symmetric molecules with an inversion centre the following notation is used:

$$X(A, B, ..., a, b)^{2S+1}\Lambda(\Sigma, \Pi, \Delta, \Phi, ...)^{(+,-)}_{\Omega,(g,u)} \tag{6.4}$$

where

- $\Lambda(\Sigma, \Pi, \Delta, \Phi, ...)$ is the projection of the orbital angular momentum along the internuclear axis; Σ=0, Π=1, Δ=2, Φ=3, and so on;

- S is the total spin quantum number;

- Ω is the projection of the total angular momentum along the internuclear axis;

- $+,-$ indicates the reflection symmetry along an arbitrary plane containing the internuclear axis

- g,u indicates the parity (reflection through an inversion center). g means *gerade* (German for even), u means *ungerade* (odd).

- *X(A,B,...,a,b)* indicates the electronic states. X is for the ground state, excited states of the same multiplicity (i.e., having the same spin quantum number) are labelled in ascending order of energy with capital letters *A, B, C...*; excited states having different multiplicity than the ground state are labelled with lower-case letters *a, b, c...*

J and Ω are usually omitted in atomic and molecular orbital notations.

Appendix B. List of publications

1 *Water formation through O_2+D pathway on cold silicate and amorphous water ice surfaces of interstellar interest,*
H. Chaabouni, **M. Minissale**, G. Manicó, E. Congiu, J. Noble, S. Baouche, M. Accolla, J. L. Lemaire, V. Pironello, and F. Dulieu,
Journal of Chemical Physics, 137, 234706 (2012)

2 *Chemical desorption source of observable molecules in our Universe,*
F. Dulieu, E. Congiu, J. Noble, S. Baouche, H. Chaabouni, A. Moudens, **M. Minissale** and S. Cazaux,
Scientific Reports, Nature, 3, 1338 (2013)

3 *Formation of nitrogen trioxide and nitrogen dioxide via NO + O_2 gas-solid reaction on cold surfaces,*
M. Minissale, E. Congiu, S. Baouche, H. Chaabouni, A. Moudens, F. Dulieu, G. Manicó and V. Pironello,
Chemical Physics Letter, 565, 52 (2013)

4 *Quantum tunneling of oxygen atoms on very cold surfaces,*
M. Minissale, E. Congiu, S. Baouche , H. Chaabouni, A. Moudens, F. Dulieu, M. Accolla, S. Cazaux, G. Manicó, and V. Pironello,
Physical Review Letters, 111, 053201, (2013)

5 *CO_2 formation on interstellar dust grains: a detailed study on the barrier of the CO+O channel,*
M. Minissale, E. Congiu, G. Manicó, V. Pironello, and F. Dulieu,
Astronomy and Astrophysics, 559, A49, (2013)

6 *Efficient diffusive mechanisms of O atoms at very low temperatures on surfaces of astrophysical interest,*
E. Congiu, **M. Minissale**, S. Baouche, S. Cazaux, H. Chaabouni, G. Manicó , A. Moudens, V. Pironello, and F. Dulieu,
Faraday Discussion 168 "Astrochemistry of Dust, Ice and Gas" (2014)

7 *Oxygen diffusion and reactivity on bare silicate interstellar grains,*
M. Minissale, E. Congiu, and F. Dulieu,
Journal of Chemical Physics, 140, 074705, (2014)

8 *Nitrogen chemistry on cold surfaces - Part I: The surface consumption of NO,*
M. Minissale, G.S. Fedoseev, E. Congiu, S. Ioppolo, F. Dulieu, and H. Linnartz,
Physical Chemistry Chemical Physics, 16, 8257 (2014)

9 *Nitrogen chemistry on cold surfaces - Part II: The surface consumption of NO_2,*
S. Ioppolo, G.S. Fedoseev, **M. Minissale**, E. Congiu, F. Dulieu, and H. Linnartz,
Physical Chemistry Chemical Physics, 16, 8270 (2014)

10 *Influence of surface coverage on the chemical desorption process,*
M. Minissale, and F. Dulieu,
Journal of Chemical Physics, 141, 014304 (2014)

11 *CO_2 formation via solid state H_2CO+O reaction,*
M. Minissale, E. Congiu, S. Baouche, H. Chaabouni, and F. Dulieu,
submitted to A&A

List of Acronyms

AMU : Atomic Mass Unit

ASW : Amorphous Solid Water

CD : Chemical Desorption

Cps : Counts per second

DED : During Exposure Desorption (or Detection)

EID : Electron impact desorption

ER : Eley-Rideal

ESD : Electron-stimulated desorption

FIR : Far InfraRed

FL : Focal Length

FT : Fourier Transform

FUV : Far UltraViolet

HAM : Hot-Atom Mechanism

HOPG : Highly Ordered Pyrolytic Graphite

IR : InfraRed

ISM   : InterStellar Medium

LERMA : Laboratoire d'Etudes du Rayonnement et de la Matière en Astrophysique et Atmosphères

LH : Langmuir-Hinshelwood

MCT : Mercury Cadmium Telluride

ML : MonoLayer

OFHC : Oxygen-Free High thermal Conductivity

p-np : porous - not porous

QMS : Quadrupole Mass Spectrometer

RAIRS : Reflection Absorption InfraRed Spectroscopy

TD : Thermal desorption

TDS : Temperature Desorption Spectroscopy

TPD : Temperature Programmed Desorption

UHV : Ultra High Vacuum

UV : UltraViolet

Acknowledgements

A thesis is not the result of only one person's work (mine) but that of many people. Clearly not all of them have contributed in the same way, by plotting a graph or writing a formula. Many of these have been very helpful in non-working times and for extra-working reasons, but it does not mean they were less crucial to who I am, and what this thesis is.

These lines could not start with anyone else other than *François Dulieu*. Without him, I would probably still be drafting the first chapter. He was my supervisor, but also a colleague and a friend giving and asking for advice. Then, it is the turn of the seraphic *Emanuele Congiu*, who had to hear my chatter, in the laboratory and in the office, on the train and on soccer fields. So much time spent with him to have any doubts of his "genius". I want to thank *Valerio Pirronello* and *Giulio Manicò*, whose distance has certainly decreased the number of contacts, but certainly not their intensity. I thank my referees *Stephen Price* and *Pascal Parneix* for their wise counsel and for the pleasant words used to describe my work. With them, I would like to thank the rest of the jury of my thesis (*Paola Caselli*, *Cécile Engrand* and *Olivier Pluchery*) for not having asked bad questions during the defense. Thanks, from the bottom of my heart, to *Stephanie Cazaux*, one of the few people with whom to work with seriously becomes synonymous of fun. She was able to make me work when I would have probably preferred to be partying or drinking in a pub. I would also like to thank *Henda Chaabouni*, whose constant presence has often helped me in the deafening silence of the laboratory. Then *Saoud Baouche* that I cannot forget on one hand for the skillful mastery with bolts and connections, and on the other hand for the curses due to broken pumps or American screw stripped. Next is *Audrey Moudens*, with her delicious cakes, cakes that I missed even more at the time of the thesis redaction when I desperately needed more sugar. Fortunately, *Henri Lemaître* was able to make up for this lack, thanks to interesting discussion and by raising the alcohol content in our office. I have to thank Stephan Diana, for his help with computers, as well as *Eric Somson, François Lachevre*, and *Gilles Remy* for the debates over crêpes and cafes about French culture, movies and football.

I also thank all the people with whom I had the pleasure to work and/or discuss with: *Harold Linnartz, Sergio Ioppolo, Gleb Fedoseev, Jennifer Noble, Patrice Theulé, Maria Elisabetta Palumbo, Giuseppe Baratta, Rosario Brunetto, Gianni Strazzulla, Emmanuel Dartois, Jean-Christophe Loison, Lisseth Gavillan, Demian Marchione* and all the colleagues from the LASSIE network, the Observatory of Paris, and in particular, *Michel Perault, Valerie Audon, Dominique Lopes, Jean-Michel Krieg*, and *Darek Lis*.

Then, I want to thank my "Parisian" roommates (family not by birth but by adoption): *Roberto, Ciampa, Luca Palma Gentlemen, Bruno, Martina, Ventura* and *Giusy* (along with *Ethan&Franc*). My "Parisian" friends with whom I have not shared the apartment but

A fool sees not the same tree as the wise man sees.

"The Marriage of Heaven and Hell"
William Blake

Remerciements

niqué : *Loretta&Carlos*, la petite *Arianna, Daniele Meo, Vito Paul, Elodie&Peppe, Ciccio, Lorenzo, Silvia, Ripul, Marie, Claire, Karan, Cecilia, Vito*, et *Hector*. Les amis « Neuvilliens »: les café-chimistes *Elisa, Fabio, Carlotta*, et *Matthea* ; et les britanniques *Matteo et Marie*. Les amis du foot : *Matthieu* et tous les autres « Creteilliens ». Les amis de l'aviron : *Erwan, Georgia, Alisee* et *Céline*.

Enfin, une grande pensée va à : *Pippo&Franca*, mon frère *Ture*, mon frère *Alfio* et ma belle soeur *Roberta* pour leur confiance et leur soutien moral ; et enfin merci *Susanna* que, malgré moi, j'ai dû "supporter" au cours de la préparation de ce manuscrit, mais qui obstinément me soutenait dans mes moments de déncouragement.

Avec le temps...
Avec le temps, va, tout s'en va
On oublie les passions et l'on oublie les voix

"Avec le temps"
Léo Ferré

Ringraziamenti

È bello doppo il morire vivere anchora.

Bernardino Corio,
attribuzione incerta